Lehigh University
Lehigh Preserve

Theses and Dissertations

2014

Investigations into Convective Deposition from Fundamental and Application-Driven Perspectives

Alexander L. Weldon
Lehigh University

Follow this and additional works at: http://preserve.lehigh.edu/etd

 Part of the Chemical Engineering Commons

Recommended Citation
Weldon, Alexander L., "Investigations into Convective Deposition from Fundamental and Application-Driven Perspectives" (2014). *Theses and Dissertations.* Paper 1667.

This Dissertation is brought to you for free and open access by Lehigh Preserve. It has been accepted for inclusion in Theses and Dissertations by an authorized administrator of Lehigh Preserve. For more information, please contact preserve@lehigh.edu.

Investigations into Convective Deposition from Fundamental and Application-Driven Perspectives

by

Alexander L. Weldon

Presented to the Graduate and Research Committee
of Lehigh University
in Candidacy for the Degree of
Doctor of Philosophy
in
Chemical Engineering

Lehigh University
May 2014

Copyright by Alexander L. Weldon
2014

Certificate of Approval

Approved and recommended for acceptance as a dissertation in partial fulfillment of the requirements of the degree of Doctor of Philosophy.

_____
Date

_____
James F. Gilchrist, Ph.D.
Dissertation Advisor

_____
Accepted Date

Committee Members:

_____
James F. Gilchrist, Ph.D.
Committee Chair

_____
Manoj K. Chaudhury, Ph.D.
Committee Member

_____
Xuanhong Cheng, Ph.D.
Committee Member

_____
Mark A. Snyder, Ph.D.
Committee Member

Acknowledgements

Special thanks to my dissertation advisor, James F. Gilchrist for his invaluable insight and quick wit throughout my doctoral research. Also, thank you to the Chemical Engineering department at Lehigh University, and especially my committee members: Professors Chaudhury, Cheng, Klein, and Snyder. The Gilchrist lab has been a constant source of companionship and support throughout the years—in particular, Pisist Kumnorkaew was essential in helping me to hit the ground running in my research. In addition, the graduate student population as a whole has made my time at Lehigh fun and productive. I thank you all.

Also, I would like to recognize my friends, family, and girlfriend Megan for their support through the long grind of graduate school. They have all endured long nights in the lab, and an uncertain timeline, to a greater or lesser degree. In addition, athletics have kept me sane and balanced while completing my dissertation, and I would like to acknowledge all the individuals with whom I have trained and completed throughout the years. These include the athletes of South Mountain Crossfit and Crossfit Lehigh Valley, the Endurance Multisport Extreme Team, other graduate students at Lehigh, and a host of others who shall go unnamed.

With regards to specific studies, I would like to acknowledge those who helped make our successes possible.

Matching Constituent Fluxes for Convective Deposition of Binary Suspensions (Chapter 3)

Pisist Kumnorkaew (CHE, Lehigh) and I carried out this study with the advice and support of James F. Gilchrist (CHE, Lehigh). Polystyrene nanoparticles were prepared by the Emulsion Polymers Institute at Lehigh University. In addition, we gratefully acknowledge the support of the National Science Foundation under award number 0828426. P.K. is grateful for the support of the Royal Thai Scholarship.

Enhanced Colloidal Monolayer Assembly via Vibration-Assisted Convective Deposition (Chapter 3)

Tanyakorn Muangnahpoh and I carried out this study with the advice and support of James F. Gilchrist (CHE, Lehigh). Polystyrene nanoparticles were prepared by the Emulsion Polymers Institute at Lehigh University. This material is based upon the work supported by the National Science Foundation Scalable Nanomanufacturing Program under Grant No. 1120399. T.M. gratefully acknowledges support through the Royal Thai Scholarship Program.

Instability-Driven Streak Formation in Particle Convective Deposition (Chapter 4)

We greatly acknowledge the help of Midhun Joy for his invaluable and tireless support writing and debugging MATLAB scripts to aid in image analysis.

Drying Stress-Driven Cracking of Nanoparticle Thin Films (Chapter 5)

We greatly acknowledge enlightening conversations and a burgeoning partnership with Alex Routh (CHE, Cambridge). Polystyrene nanoparticles were prepared by the Emulsion Polymers Institute at Lehigh University.

Effect of Surface Nanotopography on Immunoaffinity Cell Capture in Microfluidic Devices (Chapter 6)

Bu Wang (MSE, Lehigh), Pisist Kumnorkaew (CHE, Lehigh) and I carried out this study with the advice and support of James F. Gilchrist (CHE, Lehigh) and Xuanhong Cheng (MSE, Lehigh). In addition, we are grateful for Makenzie Wolfe, Christopher Tibaldi, and Jonathan Longley's help in nanoparticle deposition, COMSOL simulation, and AFM imaging, respectively. Funding for the research is provided by National Science Foundation under Grant No. CBET-0828426 and by the Biosystems Dynamics Summer Institute 2009, 2010 sponsored by the Howard Hughes Medical Institute.

Fabrication of Macroporous Polymer Membranes through Binary Convective Deposition (Chapter 7)

Pisist Kumnorkaew (CHE, Lehigh) and Bu Wang (MSE, Lehigh) and I carried out this study with the advice and support of James F. Gilchrist (CHE, Lehigh) and Xuanhong Cheng (MSE, Lehigh). Polystyrene nanoparticles were prepared by the Emulsion Polymers Institute at Lehigh University. In addition, we gratefully acknowledge the support of the National Science Foundation under award number 0828426. Pisist Kumnorkaew is grateful for support under the Royal Thai Scholars program. Also we would like to thank Lehigh University and the Howard Hughes Medical Institute for their support of the Biosystems Dynamics Summer Institute at Lehigh University and specifically Sherwood Benavides, Colleen Curley, Jonathan Cursi, and Meaghan Phipps for their work through the summer 2010 BDSI program. We also thank Mark Snyder and Eric Daniels for their comments.

Table of Contents

List of Tables

List of Figures

Abstract

Crystalline particle coatings can provide critical enhancement to wide-ranging energy and biomedical device applications. One method by which ordered particle arrays can be assembled is convective deposition. In convective deposition, particles flow to a surface via evaporation-driven convection, then order through capillary interactions. This thesis will serve to investigate convective deposition from fundamental and application-driven perspectives.

Motivations for this work include the development of point-of-care diagnostic devices, macroporous membranes, and various energy applications. Immunoaffinity cell capture devices display enhanced diagnostic capabilities with intelligently varied surface roughness in the form of particle coatings. Relatedly, highly crystalline particle coatings can be used to template the fabrication of macroporous polymer membranes. These membranes display highly monodisperse pores at particle contact points. In addition, ordered areas of particles, acting as microlenses, can enhance LED performance by 2.66-fold and DSSC efficiency by 30%.

Previous research has targeted the formation of crystalline monolayers of particles. However, much insight can be gleaned from “imperfect” coatings. The analysis of submonolayer coatings, exhibiting significant void spaces, provides insight as to the specific mechanisms and timescales for flow and crystallization. A pair of competing deposition modes, termed ballistic and locally-ordered, enables the

intelligent design of experiments and enables significant enhancement in control of resultant thin film morphology.

Surface tension-driven particle assembly is subject to a number of native instabilities and macroscale defects that can irreversibly compromise coating uniformity. These include the formation of three-dimensional “streaks,” where surface tension-driven flow spurs on the nucleation of large imperfections. These imperfections, once nucleated, exhibit a feedback loop of dramatically enhanced evaporation and resultant flow. In addition, thick nanoparticle coatings, subject to enormous drying stresses, exhibit highly uniform crack formation and spacing in an attempt to minimize system energy. Both these imperfections yield insight on convective deposition as a fundamental phenomenon, and intelligent design of experiments moving forward. Cracking can be suppressed through layer-by-layer particle assembly, whereas streaking can be controlled via several significant process enhancements.

Process enhancements include the addition of smaller constituent, as packing aids, to suspension, the application of lateral vibration, and the reversal of relevant surface tension gradients. The transition from unary to binary suspensions represents a significant improvement to convective deposition as a process. Nanoparticles act as packing, and flow, aids, wholly suppress macroscale defects under ideal conditions. A relative deficiency or excess of nanoparticles can generate complex coating morphologies including multilayers and transverse stripes. The application of lateral vibration to convective deposition allows the assembly of monolayer particle coatings under a larger range of operating conditions and at a faster rate. Macroscale defect

formation can increased through an enhancement of the natural condition, where evaporative cooling generates a thermal gradient in drying droplets. Conversely, these defects can be suppressed with a reversal of this gradient, which will reverse the direction of surface tension-driven recirculation.

These fundamental developments in understanding, and associated process enhancements, are critical in current efforts to scale up convective deposition. As convective deposition evolves from laboratory-scale batch experiments to continuous, large scale, coatings, repeatability and robustness, as well as an ability to controllably change thin film morphology, will be essential.

Chapter 1

Introduction

1.1: Summary

This doctoral thesis serves to present fundamental and application-driven research on particle convective deposition. Convective deposition in its base case, as well as contrasting deposition modes relating to a competition of timescales for particle assembly and flow, are described in the analysis of submonolayer coatings (Chapter 2). Fundamental process enhancements include the additional of nanoparticle packing aids as well as the application of lateral oscillatory vibration to enhance thin film order and packing density (Chapter 3). Coating nonuniformities, what can go "wrong," yield a greater understanding of the convective deposition process and allow more intelligent process enhancement efforts. Induced thermal, and surface tension, gradients can enhance native instabilities and nucleate macroscale three-dimensional "streaks" which catastrophically compromise thin film uniformity (Chapter 4). Additionally, drying stresses in nanoparticle thin films can induce highly monodisperse crack formation and spacing (Chapter 5). This work also serves to show the robustness of convective deposition in enabling biomedical and materials device technologies. Crystalline

particle thin films can be used to control, and enhance, surface roughness in immunoaffinity cell capture devices (Chapter 6). Additionally, codeposited polymer and oxide particles enable the development of macroporous polymer membranes with highly monodisperse pore size (Chapter 7). Finally, future enhancements, directions, and areas of interest are quickly summarized (Chapter 8).

1.2: Motivations

Ordered particle layers and thin films have found enormous use recently in industries spanning a huge array of fields. Fields impacted include photonics, [2-5] lithography,[4,6,7] ceramics,[8] sensors,[9-11] diagnostic platforms,[12-15] membranes,[16-19] and biocompatible surfaces.[9,20] Methods for assembling particle layers range from electrophoretic particle assembly[21] and optical tweezers[22] to spin coating[23] and vertical deposition, also known as dip coating[24-27]. One method for the deposition of uniform particle layers is rapid convective deposition. Here, evaporation of the liquid phase of a suspension drives fluid to flow into a thin film where particles align on a surface due to either capillary forces or increased volume fraction.[24,28-32] Rapid convective deposition can deposit morphologies including submonolayers, monolayers, and multilayers of particles ranging from 10 nm to multiple microns. Spherical particles are typically deposited, but the process is by no means limited in this respect. Nor is the process limited to suspensions with only a single particle constituent. Depositing smaller particles enhances the packing and crystallinity of thin films. A huge variety of suspensions can be deposited as well. So long as the liquid phase can be made to evaporate and partially wets the substrate, any liquid can be used and similarly particles with a huge range of compositions and properties can be deposited. Aside from the robustness in suspensions that can be deposited, convective deposition has strong potential for scaling up to continuous processes. Experiments described henceforth typically deposit films 1” in width by ~1.5” in width in a batch process using 10 μl concentrated suspension atop a glass slide. With a continuous suspension addition

system, or ever just a larger batch experiment, and a larger substrate there are no foreseeable scientific limits to the scalability of this process.

The pairing of convective deposition with device-oriented applications is longstanding. Recently, prior work initiated with investigations of the effect of varying blade angle and deposition speed to control deposited morphology.[2] This work is within the spectrum of enhancing optical technologies. InGaN Quantum Well LEDs benefit from the addition of a microlens array coating. Convective deposition was a natural fit to accomplish this end, and iterative studies developed and perfected these game-changing innovations.[2,33-43] Here, convective deposition was used to consecutively deposit Polystyrene (PS), then SiO_2 microspheres. The PS particles are melted in order to form a close-packed microlens array of partially buried SiO_2 microspheres. This microlens array of SiO_2 particles acts to enhance the light extraction efficiency of the InGaN QW LEDs.[2] Notable enhancements include a 2.66-fold increase in integrated photoluminescence, with peak photoluminescence enhanced by 2.7-fold. In addition, these devices exhibit a 219% increase in light output power.

Further recent enhancements in optical technologies have been developed for use in dye-sensitized solar cells (DSSCs).[44] Here, convective deposition is used in a similar, through contrasting, manner. With LEDs, the objective is to maximize the amount of light transmitted out of the device. Conversely, with solar cells, the objective is to maximize the amount of light entering the device. Kumnorkaew and Joy (Gilchrist, Snyder, Lehigh) have shown that a convectively deposited microlens array can enhance the efficiency of DSSCs. The additions of convex and concave microlens arrays have

shown efficiency improvements of up to 30%. Dye-sensitized solar cells, though relatively inexpensive and easy to make, are often criticized for their low efficiencies. With these sorts of microlens array enhancements, DSSCs could quickly grow to become a more competitive technology.

Convective deposition has also been used to enable various biomedical device technologies. The development of immunoaffinity cell capture devices[12] as well as macroporous polymeric membranes[16] will be discussed at length in Chapters 6 and 7, respectively.

1.3: Evaporation and Capillary-Driven Particle Assembly

Convective deposition proceeds through a pair of sequential phenomena. Fluid and particles flow from the bulk suspension to a thin film region atop the substrate due to evaporation-driven convection. In this thin film region, fluid continues to evaporate. As the fluid level drops below the height of individual particles, particles lock into crystalline arrays due to capillary interactions and surface energy minimization.

Evaporation-driven flow is a well-understood phenomenon, and convective deposition shares strong similarities with the "coffee-ring" effect.[45,46] Coffee stains display characteristic ring-like structures as opposed to homogenous particle distributions. This is a result of enhanced evaporation at the droplet edge, which drives particle flow to a thin film region (Figure 1.1). In this thin film, continuing evaporation causes particles to lock into close-packed structures due to capillary forces. This is sometimes deemed the "cheerio effect," as particles pack in order to minimize surface energy, and fluid deflection, in the system.[47,48] The comparison in that the few remaining cheerios in a bowl will cluster in order to minimize the surface deflection in their liquid system.

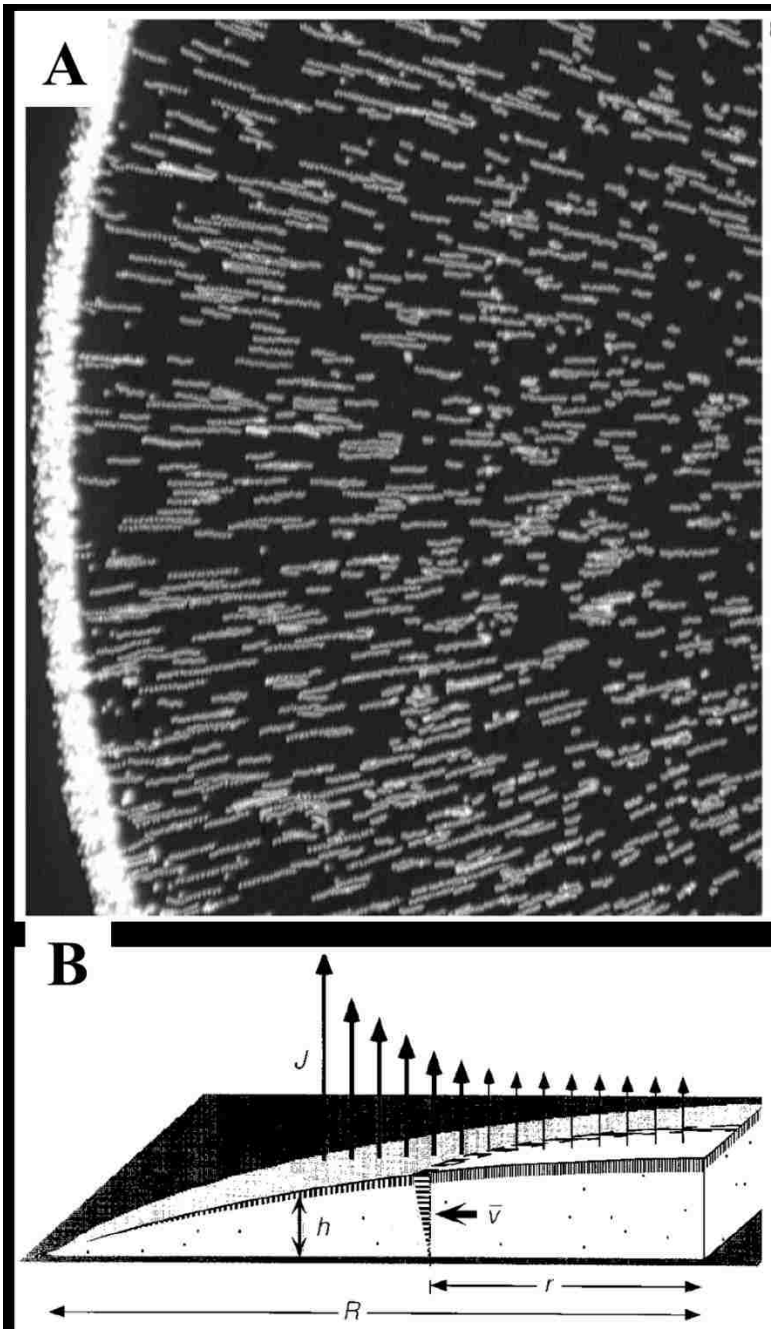

Figure 1.1: Demonstration of the "coffee ring" effect, (A) where evaporation drives particle flow to the outside edge of a droplet. Characteristic "ring-like" morphologies result. (B): Diagram showing enhanced evaporation at the edge of a drying droplet. Reprinted from Deegan et al., 1997.

Particles in a drying thin film are subject to a variety of forces (Figure 1.2).[49,50] These forces can dramatically affect particle motion, and pull it in competing directions. Electrostatics will repel particles from one another and their substrate. Gravity will force the particles downwards. Drag forces will resist particle flow through a medium. Finally capillary forces cause particles to contact one another and lock into crystalline, low energy, arrays. As solvent evaporates, capillary forces dominate the system.

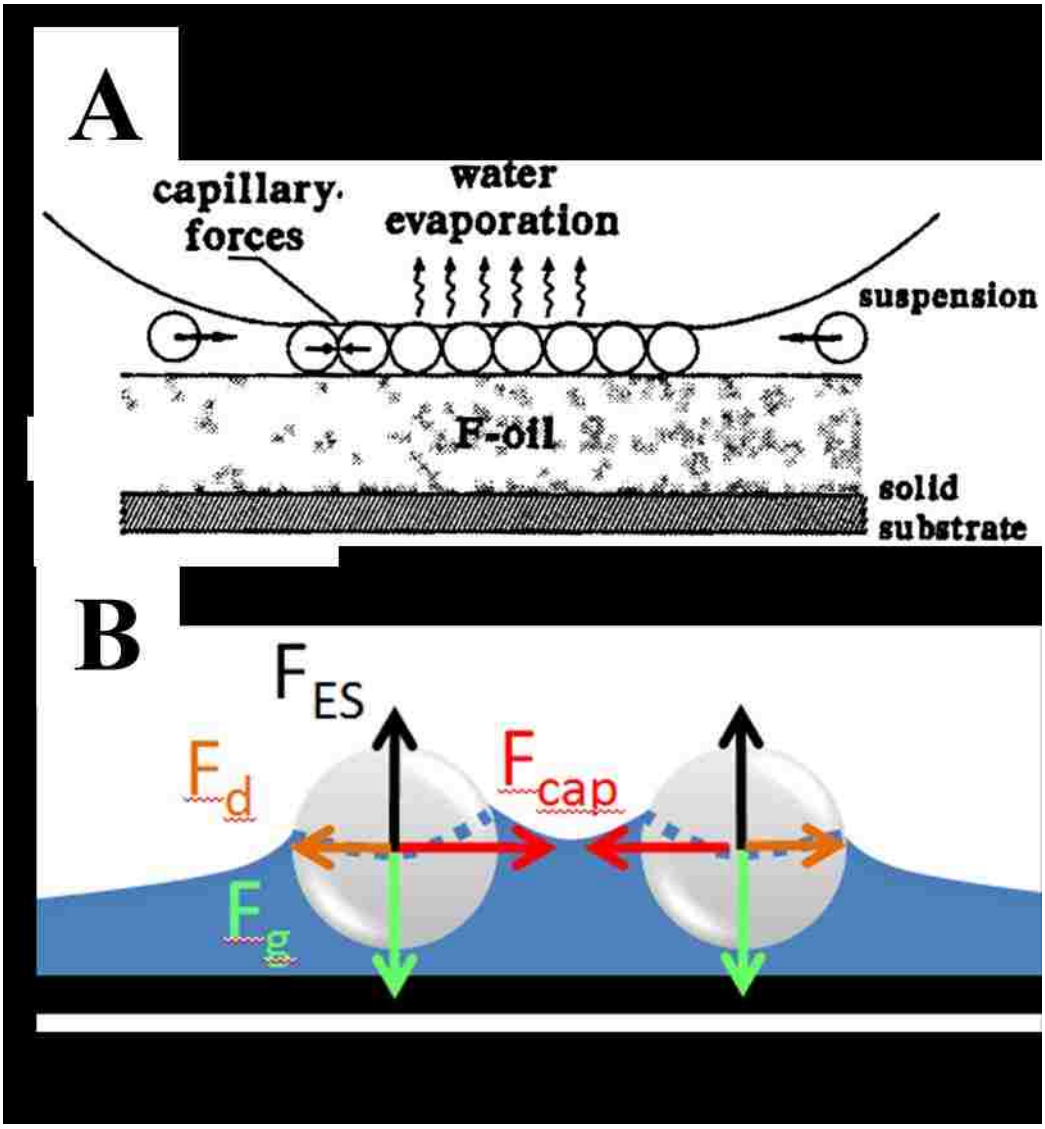

Figure 1.2: (A) Illustration demonstrating particle ordering due to capillary interactions and evaporation-driven flow. Reprinted from Lazarov et al., 1994. (B) Schematic showing the competing forces involved in clustering particles. F_{ES} refers to electrostatics, which repel particles from one another and the substrate. F_d describes drag forces resisting particle motion. F_g represents gravitational forces. Finally F_{cap} depicts capillary interactions. These forces dominate the system as the solvent evaporates and draw particles together.

1.4: Preliminary Studies and Expansion

This dissertation will expand upon previous convective deposition research.[2,51] Previous work has investigated the effects of particle size, blade angle α, and hydrophobically/hydrophilically-coated deposition blades in the deposition of single component suspensions.[2] These parameters can be used to controllably deposit submonolayer, monolayer, and multilayer particle thin films. Also, the addition of smaller particles in suspension has been shown to significantly impact coating morphology and order.[51] While the relation between larger and smaller components is complex, complementary concentrations show an ability to significantly improve coating consistency, crystallinity, and packing density. These studies will be expanded upon as needed and as is relevant in the following chapters.

Convective deposition as a method for particle coating is developing rapidly, and thus is replete with opportunities for development. Process enhancement opportunities include developments to improve coating consistency and order as well as to scale-up and provide enhanced control. In parallel, convective deposition is a complex process. Thus, in addition to "improving" the technology, significant fundamental understanding can be generated as to the methodology behind enhancements, as well as the propensity for defects and instabilities. Additionally, convective deposition, as a robust particle coating technology, stands to simply and consistently improve a variety of device and materials technologies.

1.5: References

1. Kumnorkaew P, Ee Y, Tansu N, Gilchrist JF. Investigation of the deposition of microsphere monolayers for fabrication of microlens arrays. *Langmuir*. 2008;24(21):12150-12157.

2. Kumnorkaew P, Ee Y, Tansu N, Gilchrist JF. Investigation of the deposition of microsphere monolayers for fabrication of microlens arrays. *Langmuir*. 2008;24(21):12150-12157.

3. Tessier PM, Velev OD, Kalambur AT, Rabolt JF, Lenhoff AM, Kaler EW. Structured metallic films for optical and spectroscopic applications via colloidal crystal templating. *Adv. Mater.* 2001;13(6):396-400.

4. Haes AJ, Haynes CL, Van Duyne RP. Nanosphere lithography: Self assembled photonic and magnetic materials. *Mater Res Soc*. 2001;636:D4.8.1-D4.8.6.

5. Im SH, Lim YT, Suh DJ, Park OO. Three-dimensional self-assembly of colloids at a water-air interface: A novel technique for the fabrication of photonic bandgap crystals. *Adv Mater*. 2002;14(19):1367-1369.

6. Haynes CL, Van Duyne RP. Nanosphere lithography: A versatile nanofabrication tool for studies of size-dependent nanoparticle optics. *J Phys Chem B*. 2001;105(24):5599-5611.

7. Zhang YJ, Wang XH, Wang YX, Liu HL, Yang JH. Ordered nanostructures array fabricated by nanosphere lithography. *J Alloys Compd*. 2008;452(2):473-477.

8. Harris DJ, Hu H, Conrad JC, Lewis JA. Patterning colloidal films via evaporative lithography. *Phys Rev Lett*. 2007;98(14):148301-1-4.

9. Koyama K, Yamaguchi N, Miyasaka T. Antibody-mediated bacteriorhodopsin orientation for molecular device architectures. *Science*. 1994;256(5173):762-5.

10. Velev OD, Kaler EW. In situ assembly of colloidal particles into miniaturized biosensors. *Langmuir*. 1999;15(11):3693-3698.

11. Yi DK, Kim MJ, Turner L, Breuer KS, Kim DY. Colloid lithography-induced polydimethylsiloxane microstructures and their application to cell patterning. *Biotechnol Lett*. 2005;28(3):169-173.

12. Wang B, Weldon AL, Kumnorkaew PK, Xu B, Gilchrist JF, Cheng X. Effect of surface nanotopography on immunoaffinity cell capture in microfluidic devices. *Langmuir*. 2011;27(17):11229-11237.

13. Han WJ, Allio BA, Foster DG, King MR. Nanoparticle coatings for enhanced capture of flowing cells in microtubes. *ACS Nano*. 2010;4(1):174-180.

14. Tuttle PV, Rundell AE, Webster TJ. Influence of biologically inspired nanometer surface roughness on antigen-anti body interactions for immunoassay-biosensor applications. *Int J Nanomedicine*. 2006;1(4):497-505.

15. Hughes AD, King MR. Use of naturally occurring halloysite nanotubes for enhanced capture of flowing cells. *Langmuir*. 2010;26(14):12155-12164.

16. Weldon AL, Kumnorkaew PK, Wang B, Cheng XC, Gilchrist JF. Fabrication of macroporous polymeric membranes through binary convective deposition. *Acs Applied Materials & Interfaces*. 2012;4(9):4532-4540.

17. Boudreau LC, Kuck JA, Tsapatsis M. Deposition of oriented zeolite A films: In situ and secondary growth. *Journal of Membrane Science*. 1999;152(1):41-59.

18. Bohaty AK, Abelow AE. Nanoporous silica colloidal membranes suspended in glass. *J Porous Mater*. 2011;18(3):297-304.

19. Yuan Y, Burckel DB, Atanassov P, Fan H. Convective self-assembly to deposit supported ultra-thin mesoporous silica films. *Journal of Materials Chemistry*. 2006;16(48):4637-4641.

20. Zhang YJ, Wang SP, Eghtedari M, Motamedi M, Kotov NA. Inverted-colloidal-crystal hydrogel matrices as three-dimensional cell scaffolds. *Adv Funct Mater*. 2005;15(5):725-731.

21. Hayward RC, Saville DA, Aksay IA. Electrophoretic assembly of colloidal crystals with optically tunable micropatterns. *Nature*. 2000;404(6773):56-59.

22. Biancaniello PL, Crocker JC. Line optical tweezers instrument for measuring nanoscale interactions and kinetics. *Rev Sci Instrum*. 2006;77:113702-113702-10.

23. Jiang P, McFarland MJ. Wafer-scale periodic nanohole arrays templated from two-dimensional nonclose-packed colloidal crystals. *J Am Chem Soc*. 2005;127(11):3710-3711.

24. Prevo BG, Kuncicky DM, Velev OD. Engineered deposition of coatings from nano- and micro-particles: A brief review of convective assembly at high volume fraction. *Colloids and Surfaces A-Physicochemical and Engineering Aspects*. 2007;311(1-3):2-10.

25. Dimitrov AS, Nagayama K. Continuous convective assembling of fine particles into two-dimensional arrays on solid surfaces. *Langmuir*. 1996;12(5):1303-1311.

26. Shimmin RG, DiMauro AJ, Braun PV. Slow vertical deposition of colloidal crystals: A langmuir-blodgett process? *Langmuir*. 2006;22(15):6507-6513.

27. Diao JJ, Hutchison JB, Luo GH, Reeves ME. Theoretical analysis of vertical colloidal deposition. *J Chem Phys*. 2005;122(18):184710-1-184710-5.

28. Prevo BG, Velev OD. Controlled, rapid deposition of structured coatings from micro- and nanoparticle suspensions. *Langmuir*. 2004;20(6):2099-2107.

29. Prevo BG, Fuller JC, Velev OD. Rapid deposition of gold nanoparticle films with controlled thickness and structure by convective assembly. *Chemistry of Materials*. 2005;17(1):28-35.

30. Xiao J, Attinger D, Bhardwaj R. Manufactured self-assembled coatings of micro- and nano-particles by controlled evaporation of drops and thin films. *Proc SPIE 8031*. 2011;8031.

31. Luo H, Cardinal CM, Scriven LE, Francis LF. Ceramic nanoparticle/monodisperse latex coatings. *Langmuir*. 2008;24(10):5552-5561.

32. Brewer DD, Allen J, Miller MR, et al. Mechanistic principles of colloidal crystal growth by evaporation-induced convective steering. *Langmuir*. 2008;24(23):13683-13693.

33. Ee YK, Kumnorkaew P, Arif RA, Gilchrist JF, Tansu N. Enhancement of light extraction efficiency of InGaN quantum well LEDs using SiO2 microspheres. . 2007.

34. Ee Y, Arif RA, Tansu N, Kumnorkaew P, Gilchrist JF. Enhancement of light extraction efficiency of InGaN quantum wells light emitting diodes using SiO(2)/polystyrene microlens arrays. *Appl Phys Lett*. 2007;91(22):221107-1-3.

35. Ee YK, Kumnorkaew P, Arif RA, Tong H, Gilchrist JF, Tansu N. Comparison of numerical modeling and experiments of InGaN Quantum well light emitting diodes with SiO2 / polystyrene microlens arrays. . 2008.

36. Ee YK, Kumnorkaew P, Arif RA, Gilchrist JF, Tansu N. Size effects of SiO2 / polystyrene microspheres in the enhancement of light extraction efficiency of InGaN Quantum well LEDs. . 2008.

37. Ee YK, Arif RA, Kumnorkaew P, Gilchrist JF, Tansu N. Optimization and fabrication of III-nitride light-emitting diodes with self-assembled colloidal-based convex microlens arrays. . 2008.

38. Ee YK, Kumnorkaew P, Arif RA, Tong H, Gilchrist JF, Tansu N. Enhancement of light extraction efficiency of InGaN quantum well light-emitting diodes with polydimethylsiloxane concave microstructures. . 2009.

39. Ee YK, Kumnorkaew P, Arif RA, Tong H, Gilchrist JF, Tansu N. The use of polydimethylsiloxane concave microstructure arrays to enhance light extraction efficiency of InGaN quantum wells light-emitting diodes. . 2009.

40. Ee Y, Kumnorkaew P, Arif RA, Tong H, Gilchrist JF, Tansu N. Light extraction efficiency enhancement of InGaN quantum wells light-emitting diodes with polydimethylsiloxane concave microstructures. *Optics Express*. 2009;17(16):13747-13757.

41. Ee Y, Kumnorkaew P, Arif RA, et al. Optimization of light extraction efficiency of III-nitride LEDs with self-assembled colloidal-based microlenses. *Ieee Journal of Selected Topics in Quantum Electronics*. 2009;15(4):1218-1225.

42. Li X, Song R, Ee Y, Kumnorkaew P, Gilchrist JF, Tansu N. Light extraction efficiency and radiation patterns of III-nitride light-emitting diodes with colloidal microlens arrays with various aspect ratios. *IEEE Photonics Journal*. 2011;3(3):489-499.

43. Li X, Zhu P, Liu G, et al. Light extraction efficiency enhancement of III-nitride light-emitting diodes by using 2-D close-packed TiO2 microsphere arrays. *Journal of Display Technology*. 2013;9(5):324-332.

44. Joy M, Kumnorkaew PK, Snyder MA, Gilchrist JF. Internal microlenses for dye-sensitized solar cells. *to be Submitted*.

45. Deegan RD, Bakajin O, Dupont TF, Huber G, Nagel SR, Witten TA. Capillary flow as the cause of ring stains from dried liquid drops. *Nature*. 1997;389(6653):827-829.

46. Deegan RD. Pattern formation in drying drops. *Physical Review E*. 2000;61(1):475-485.

47. Vella D, Mahadevan L. The "cheerios effect". *American Journal of Physics*. 2005;73(9):817-825.

48. Larmour IA, Saunders GC, Bell SEJ. Sheets of large superhydrophobic metal particles self-assembled on water by the cheerios effect. *Angewandte Chemie-International Edition*. 2008;47:5043-5045.

49. Denkov ND, Velev OD, Kralchevsky PA, Ivanov IB, Yoshimura H, Nagayama K. Two-dimensional crystallization. *Nature*. 1993;361:26.

50. Lazarov GS, Denkov ND, Velev OD, Kralchevsky PA. Formation of two-dimensional structures from colloidal particles on fluorinated oil substrate. *Journal of the Chemical Society, Faraday Transactions*. 1994;90(14):2077-2083.

51. Kumnorkaew P, Gilchrist JF. Effect of nanoparticle concentration on the convective deposition of binary suspensions. *Langmuir*. 2009;25(11):6070-6075.

Chapter 2

Background: Convective Deposition and Assembled Morphologies

2.1: Introduction and Background

This work serves to further develop and understanding of the fundamental physics at work in convective deposition.[1] There are many adaptations in technique that enhance the formation of uniform crystalline particle thin films—these adaptations are wildly useful to enhance device optimization and reliability.[1-3] However, this study strips back those process enhancements[4-7] to take convective deposition to its base case. These experiments look to elucidate the mechanisms involved in the deposition of unary 1 μm SiO_2 microsphere suspensions, specifically looking at the deposition of submonolayer thin films. "Submonolayer" particle thin films are coatings with incomplete particle coverage—some amount of void space populates interstices between deposited particles. This contrasts with "monolayers," where a substrate is completely covered with a single crystalline array of particles, and "multilayers," where layers of particles stacked atop one another yield thicker coatings (Figure 2.1).

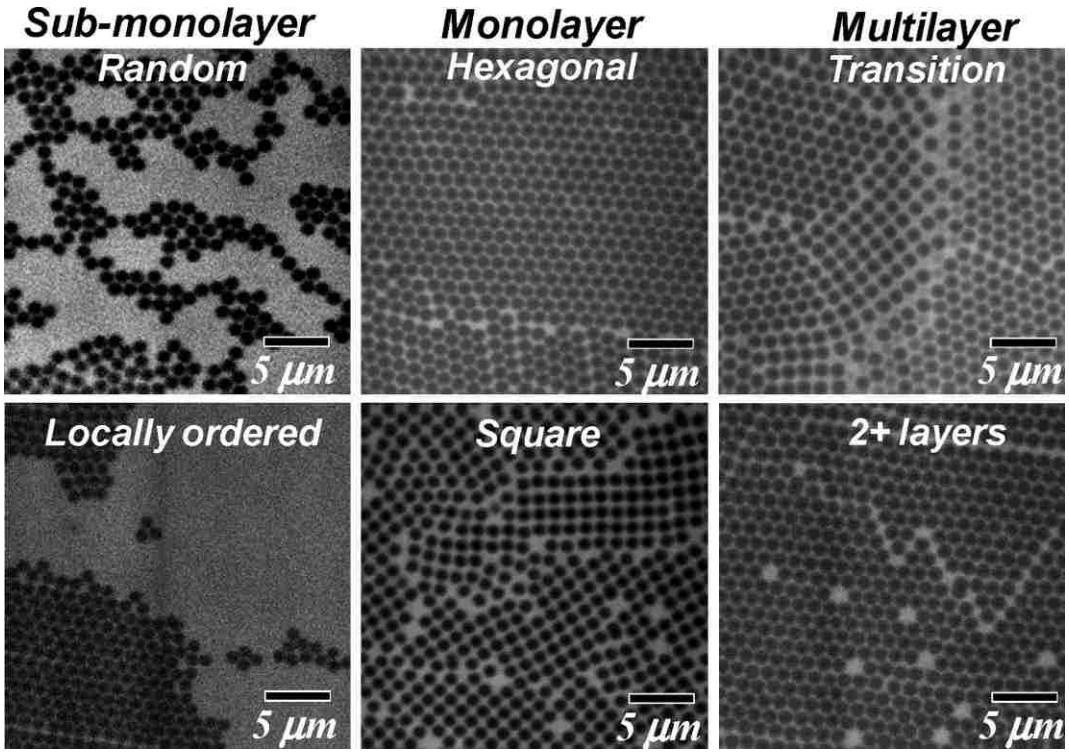

Figure 2.1: Three resulting thin film morphologies are submonolayer, monolayer, and multilayer depositions. Various microstructures may exist, including random and locally ordered morphologies in the submonolayer regime, hexagonal and square close-packed monolayer crystals, and transition regions separating various microstructures formed in 3D. (Reprinted from Kumnorkaew et al., *Langmuir* 2008)[1]

The principle of controllably depositing particles from suspension is not a new concept. Dimitrov and Nagayama provide seminal work as to the controllable deposition of a particle monolayer.[8] For a single-component suspension, they derived the relationship between volume fraction and deposition speed for an advancing crystal on a substrate. This mass balance results from calculating the amount of solvent to remove from the bulk suspension in order to yield a thin liquid layer of particles of equal height to the particle diameter. For a hexagonally ordered monolayer:

$$v_{mono} = \frac{J_e \beta}{2a\left(\phi^D\right)} \frac{\phi}{(1-\phi)} \tag{2.1}$$

v_{mono} is substrate velocity and equal to the velocity of the advancing monolayer crystal front, J_e is solvent flux, 2a is microsphere diameter, ϕ and ϕ^D are suspension volume fraction in solution and within the deposited thin film respectively, and β describes particle-surface interactions. Assumptions in implementing this equation include that the bulk suspension volume fraction equals particle volume fraction near the advancing crystal front and that when particle-surface interactions are strongly repulsive $\beta \approx 1$.

Convective deposition has been heavily scrutinized and undergone major process development recently. Velev et al provide significant enhancement to the scalability and versatility of the process.[9] They show contrasting submonolayer, monolayer, and multilayer morphologies, and provide an ability to control resultant morphology through changing volume fraction.[10] Other enhancements include the ability to assemble antireflective silica coatings[11] as well as the influence of applied

electric fields on coating thickness.[12] Modeling research has been significant, both in analysis of fluid flow streamlines[13] and surface pressure[14] in the suspension meniscus.

2.2: Materials and Methods

2.2.1: Suspension Preparation

The primary colloid suspension used in this work is prepared by dispersing silica microspheres (Fuso Chemical Co, Japan) having a density of 2.2 g/cm^3, an average diameter of $2a_{micro}$ = 1.01 ± 0.02 μm, and a zeta potential of −48 mV ± 1 mV in deionized (DI) water with a volume fraction ϕ_{micro}. The suspension is dispersed using a sonic dismembrator (model 550, Fisher Scientific, Pittsburgh, PA) for 10 min and is stirred for 30 min. (Fisher Scientific, model 550). When applicable (Chapters 3, 5, 7), a separate colloidal suspension of diameter $2a_{nano}$ = 100 nm polystyrene (PS) having a zeta potential of −59 mV ± 1 mV prepared at ϕ_{nano} = 0.35 in DI water (supplied by the Emulsion Polymer Institute at Lehigh University) is combined with the silica solution to achieve the desired suspension composition

2.2.2: Substrate Preparation

Plain glass microslides (76 × 25 × 1 mm^3, Fisher PA) are used as deposition blades, and glass coverslips (40 × 24 × 0.25 mm^3, Fisher PA) are used as substrates for all samples. All glassware is cleaned by immersion in Piranha solution, 5:1 v/v sulfuric acid/hydrogen peroxide, for 30 min. The cleaned glassware is rinsed with DI water until no residual acid remains and is then immersed in DI water until use. The bottom edge of the glass deposition blade is made hydrophobic with a thin coating of parafilm (Fisher PA). The contact angles on bare glass and on the hydrophobic surface are measured to be 10 and 105°, respectively, by imaging a 10 μL stationary droplet on the surface.

2.2.3: Convective Deposition of Particle Suspensions

Under convective deposition, particles flow to the leading edge of the meniscus via evaporative forces, and are drawn to the three-phase contact line near the thin film region. As particles flow into this thin film region, they are deposited and can form highly-crystalline structures through capillary interactions. Convective deposition experiments are carried out as shown in Figure 2.2. A suspension meniscus is pinned atop a glass substrate, by a hydrophobically-coated deposition blade. A linear motor is used to translate the substrate and draw out a thin film. Blade angle, α, is variable depending on experimental conditions, and is directly observed and calibrated using a digital camera (Dinolite AM311S). The volume of colloid suspension for each experiment is 10 μL unless otherwise noted. Ambient temperature and humidity are controlled in each study and will be described in the appropriate chapter.

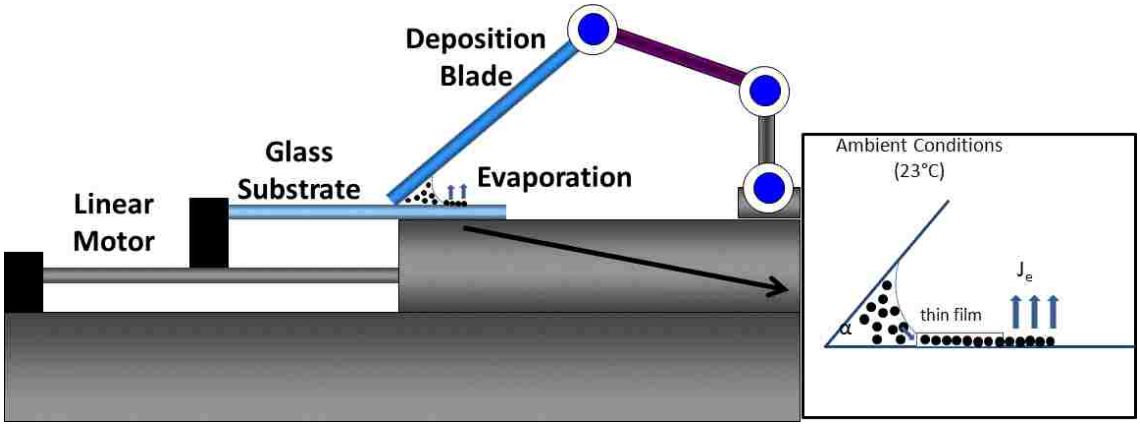

Figure 2.2: Schematic showing rapid convective deposition experimental setup with the inset highlighting the evaporating meniscus and thin film. The deposition blade is stationary while the glass substrate translates to the right.

2.2.4: Microstructural Analysis

Deposited monolayers are observed directly using scanning electron microscopy (SEM) and confocal laser scanning microscopy. A Hitachi 4300 field emission SEM is used to observe particle array microstructure. Prior to SEM imaging, the sample is coated with iridium. Confocal laser scanning microscopy (VTeye, Visitech International) is used to observe the microstructure after rewetting the layer with an aqueous solution of 8 mM Rhodamine B for imaging; this rewetting does not disturb the microstructure. The sample is scanned at 30 fps while translating at 100 μm/s across the microscope objective. This allows for the scanning of large regions of the sample (▬ 60 000 microspheres) to evaluate the microstructure of those microspheres in contact with the substrate as described above.

The two quantitative parameters most often used to characterize particle thin films are Ψ_6, the local bond order, and ρ, the relative microsphere substrate coverage. ρ is simply defined as the ratio, viewing a particle array from above, of particle-covered area to total sample area. Thus the theoretical maximum value of $\rho = \pi/(12)^{1/2} = 0.907$ which would describe a perfectly crystalline array of monodisperse spheres. Local bond order, Ψ_6, describes the crystallinity of the sample. It describes the relative orientation of particles in a plane around a central particle and achieves its maximum value when each particle has six nearest neighbors, each at a 60° relative to the central particle and its neighbors. Ψ_6 is calculated through those angles θ between each particle of interest i and its neighbors j (Equation 2.2). Prior to computation, vectors r_{ij} are determined for all nearest neighbors n. $\Psi_6 = 1$ is a perfect crystal, and $\Psi_6 \geq 0.8$ is

considered to be highly ordered for a polycrystalline morphology and is reported as the average over a larger number of microspheres, N,

$$\psi_{6,ave} = \frac{1}{N}\sum_{k=1}^{N}\frac{1}{n}\sum_{j=1}^{n} exp\left[6i\theta\left(r_{ij}\right)\right] \tag{2.2}$$

This equation is critical, and is used extensively, in the following analysis. A schematic classification of particles within a deposited thin film, based on Ψ_6 and ρ, is given in Figure 2.4.

2.3: Motivations and Previous Work

This study is prompted by the presence of two contrasting submonolayer morphologies (Figure 2.3). Depending on experimental conditions, namely blade angle, α, submonolayers can exhibit random packing or locally-ordered particle "islands." Confocal videography, not shown, confirms the presence of two very different modes of deposition. Where the resultant particle thin film is "random," under low blade angles, particles appear to flow to the crystal front relatively independent of one another. Where the resultant particle thin film exhibits "local ordering," particles form well-ordered clusters prior to reaching the crystal front. Those clusters flow in as units, then reorder and pack into an evolving thin film. For classification, particles flowing independently, and unpacked, from their neighbors are termed to be in a "ballistic" deposition mode, whereas particles under the converse condition are termed to be in a "locally ordered" deposition mode. "Ballistic" deposition is seen under lower blade angles, whereas "locally ordered" deposition is evident when α is large. Note that this "ballistic" mode is highly dissimilar from the classical ballistic motion of objects moving through a fluid as a result of an initial applied force—this term is purely used to aid in ease of understanding through familiarity.

From previous work, it is clear that blade angle plays an enormous role in deposited thin film characteristics. This is at odds with, or at least extends, the previous convention wisdom in convective deposition as presented by Dimitrov and Nagayama (Equation 2.1).[15] This equation is insufficient to fully describe the convective deposition process,

as will be highlighted with the following. Figure 2.3 shows that control over the monolayer deposition velocity extends much farther than these parameters would suggest.

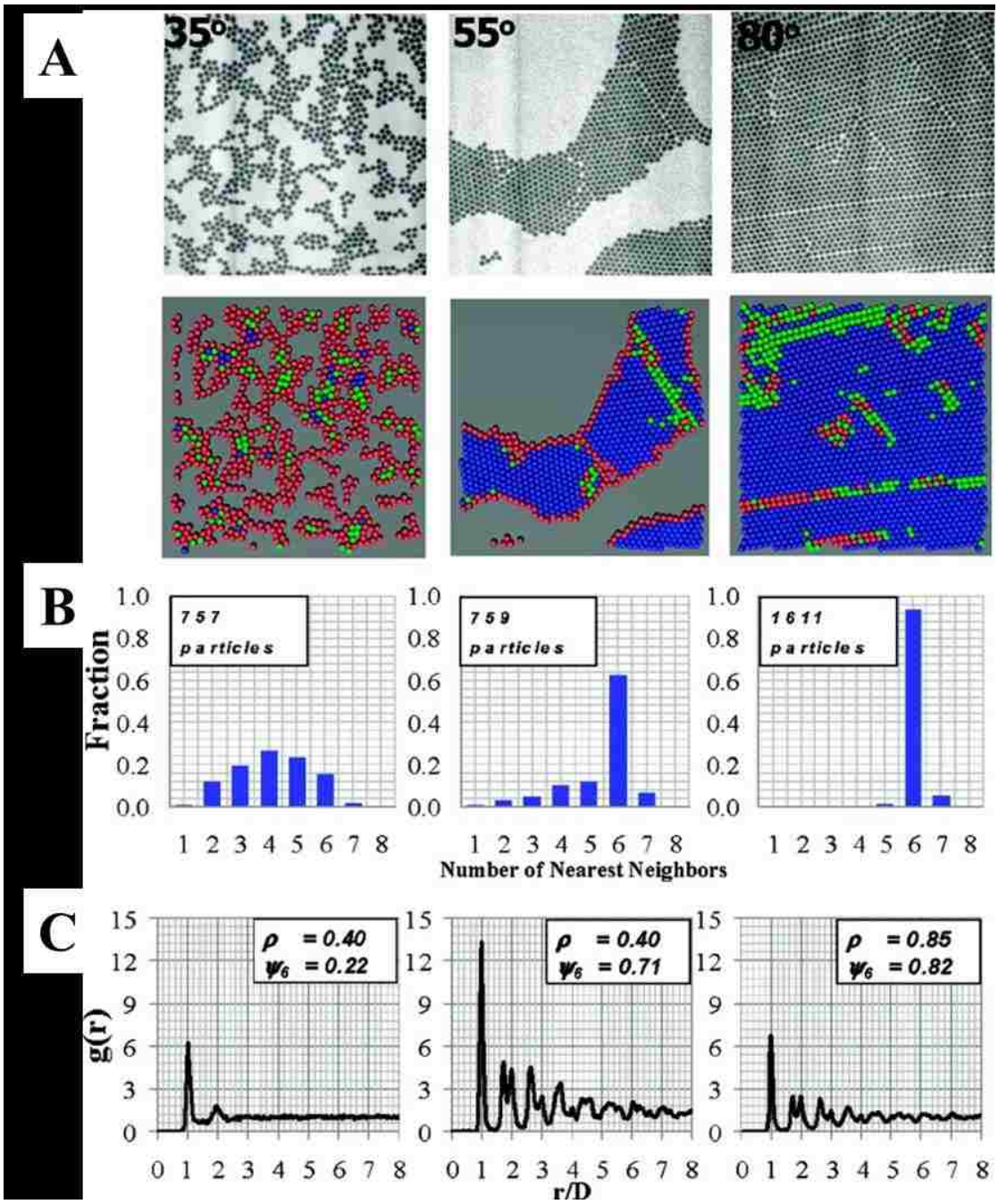

Figure 2.3: Microstructure analysis of thin films generated by varying blade angle, with constant deposition speed of 60 μm/sec. (A) Images and particles identified for α = 35°, 55°, and 80°. (B) Number of nearest neighbor and (C) radial distributions for each case. Whereas different deposition parameters can result in the same morphology, the microstructure depends on the blade angle. For v_{mono} (right), a highly ordered crystal is formed at higher blade angles. (Reprinted from Kumnorkaew et al., *Langmuir* 2008)

Figure 2.3 holds all deposition parameters constant except for blade angle. Figure 2.3A shows that, from a purely qualitative perspective, there is a gross trend in thin film morphologies. At a deposition speed of 60 μm/sec, a blade angle of 35° yields a random submonolayer packing, 55° yields a locally ordered submonolayer, and 80° yields a highly-ordered monolayer. Thus, while $v_{mono}(80°) = 60$ μm/sec, this is untrue at lower blade angles. Figure 2.4 provides clarification on the color-coding in Figure 2.3B. To summarize, blue and green particles have six nearest neighbors, and blue particles are highly ordered whereas green particles are less so. Green particles often indicate defects and grain boundaries. Red particles have fewer than six nearest neighbors and indicate high levels of disorder. Figure 2.3B and Figure 2.3C clearly show the differences in layer quality through crystallinity, packing and nearest neighbor quantifications. Figure 2.3B shows that the monolayer crystal is near-exclusively in a hexagonally close-packed (HCP) arrangement, while the locally ordered submonolayer, $\alpha = 55°$, is primarily HCP with the edges compromising the thin film crystallinity to some degree. In contrast, the randomly-packed submonolayer shows much less-pronounced trends in the nearest neighbor distribution. Figure 2.3C looks at thin film g(r) distributions as well as crystallinity and packing density. 55°and 80° samples clearly show g(r) corresponding with HCP particle arrays. The important contrast in these microstructural characterization plots is in the submonolayer comparisons. While both randomly-packed and locally-ordered thin films exhibit similar packing, $\rho = 0.40$, their crystallinity, Ψ_6, contrast greatly—$\Psi_6(35°) = 0.22$ whereas $\Psi_6(55°) = 0.71$. Obviously, thin film crystallinity will be most sensitive to randomly-packed versus

locally-ordered morphologies, as the adjacent and crystalline particles will vary greatly. Figure 2.5, adapted from Kumnorkaew et al., 2008,[1] highlights previous work specifically targeting the monolayer condition, but also highlighting submonolayer and multilayer regimes. Figure 2.5 provides the basis for the following investigations varying submonolayer morphologies and the transitions therewithin.

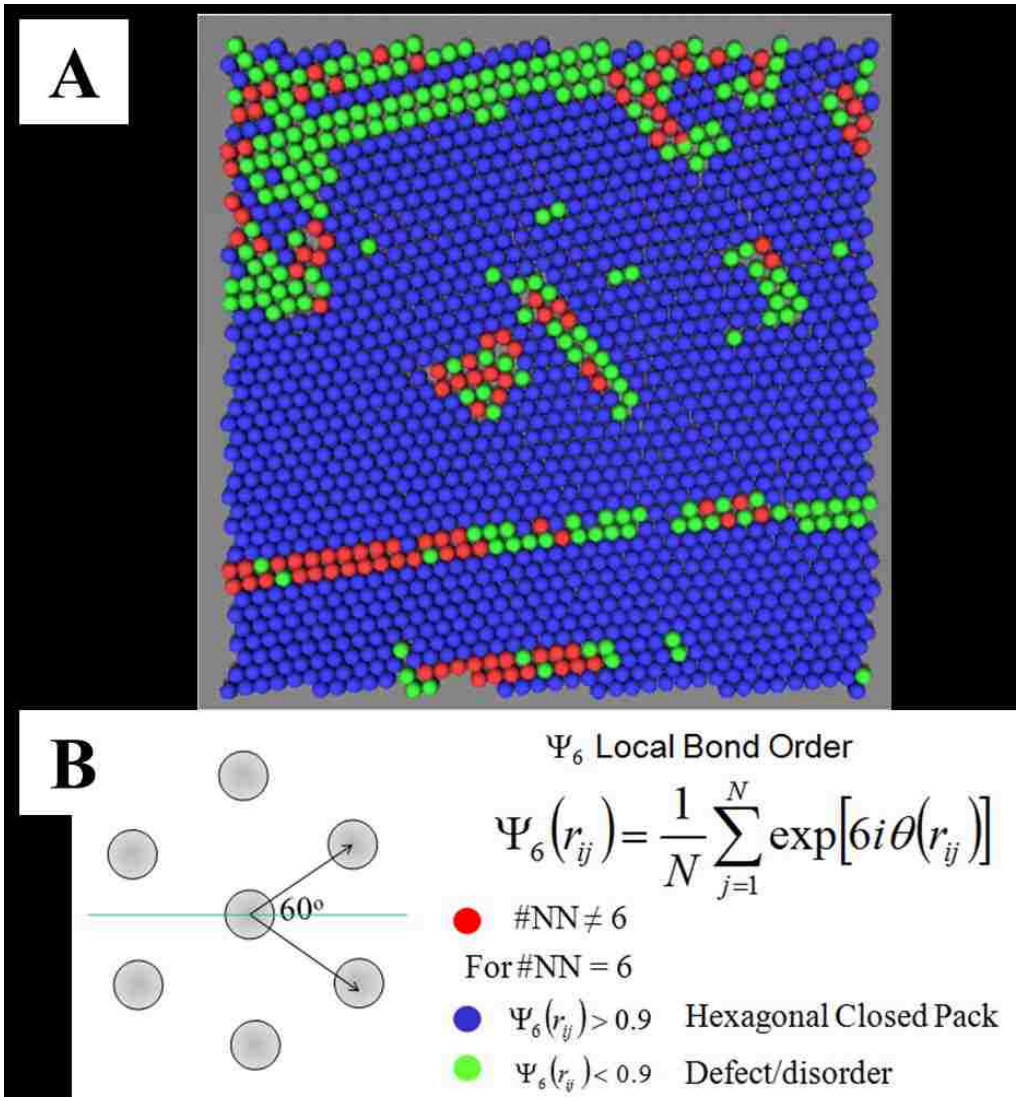

Figure 2.4: Short summary of particle color coding to guide the eye with regards to highly ordered and defect regions. (A) Example rendered experimental thin film. (B)Blue particles have six nearest neighbors and are highly crystalline. Green particle have six nearest neighbors but lower crystallinity—green particles often indicate defects or grain boundaries. Red particles are highly disordered, with fewer than 6 nearest neighbors.

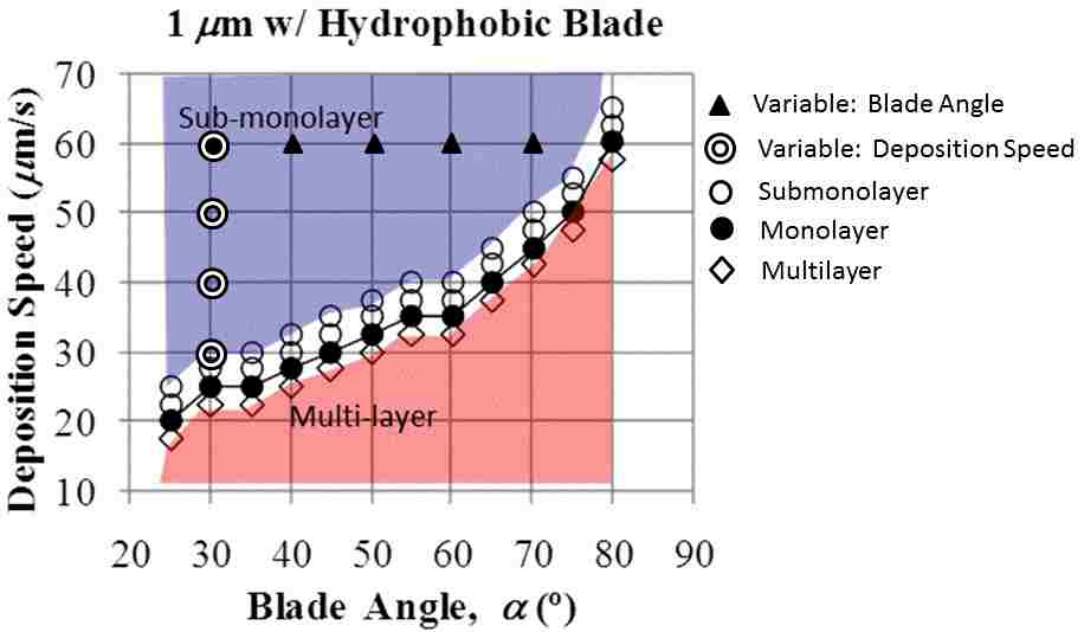

Figure 2.5: Convective deposition results from Kumnorkaew et al., 2008 highlighting the effects of changing blade angle and deposition speed. A fine transition at the monolayer condition (black circles) separates the submonolayer regimes (faster deposition speeds, lower blade angles) from the multilayer regime (slower deposition speeds, higher blade angles). This plot also highlights the forthcoming studies, that serve to elucidate changing submonolayer morphologies through changing deposition speed and blade angle. (Adapted from Kumnorkaew et al., *Langmuir* 2008)

This study will serve to further elucidate the submonolayer trends at play across this range of deposition speeds and blade angles. Initial phase diagrams (example, Figure 2.5) present a focus on the monolayer condition, without much focus on subphases/transitions within the submonolayer and multilayer regimes. Preliminary results (Figure 2.3), highlighting a pair of submonolayer deposition modes and resultant thin films, suggest that this regime has the potential to be quite inhomogeneous and complex. The submonolayer phase will be studied with an emphasis on changing "ballistic" to "locally ordered" dynamics as evidenced through resultant thin films over varying conditions.

2.4: Further Investigations into the Submonolayer Morphology

As shown in Figure 2.5, the submonolayer regime will be investigated through a pair of parallel methodologies. In an effort to pinpoint the effects of blade angle and deposition speed, these parameters will be varied independently. As a basic extension of Figure 2.5, in general higher speeds and lower blade angles decrease overall packing and increase submonolayer characteristics. Intuitively, this speed dependence makes sense. Under faster deposition speeds, fewer particles will have time to flow to the substrate and order. Conversely, slower deposition speeds will yield increasingly thick particle coatings.[3] The effects of blade angle are more complex. Increasing blade angle will yield increasing droplet radius of curvature (Figure 2.6), as described by Equation 2.3.[1] Varying droplet characteristics under different blade angles will influence the extended profile of the drawn out thin film as well as surface pressure within the droplet. Note that, in the following experiments, the bottom of the deposition blade will always be hydrophobically treated.

$$R = \left[\frac{W}{V}\left(\frac{cos^2\theta}{tan(\alpha/2)} - \cos\theta \sin\theta - \frac{\pi}{2} + \theta + \frac{\alpha}{2}\right)\right]^{-0.5} \quad (2.3)$$

One explanation of these contrasting deposition modes is the competition between various fluidic timescales. Under convective deposition, particles flow to the deposition front, sometimes crystallizing before reaching it. An empirically-driven hypothesis of the two varying modes is that contrasting timescales dominate under changing blade angle. At low blade angles, the timescale for flow could be much smaller than that for crystallization. Thus particles reach the crystalline front prior to

ordering. In contrast, under higher blade angles the timescale for flow could be larger than that for crystallization. Thus, in this case, particles have time to organize prior to reaching the crystal front.

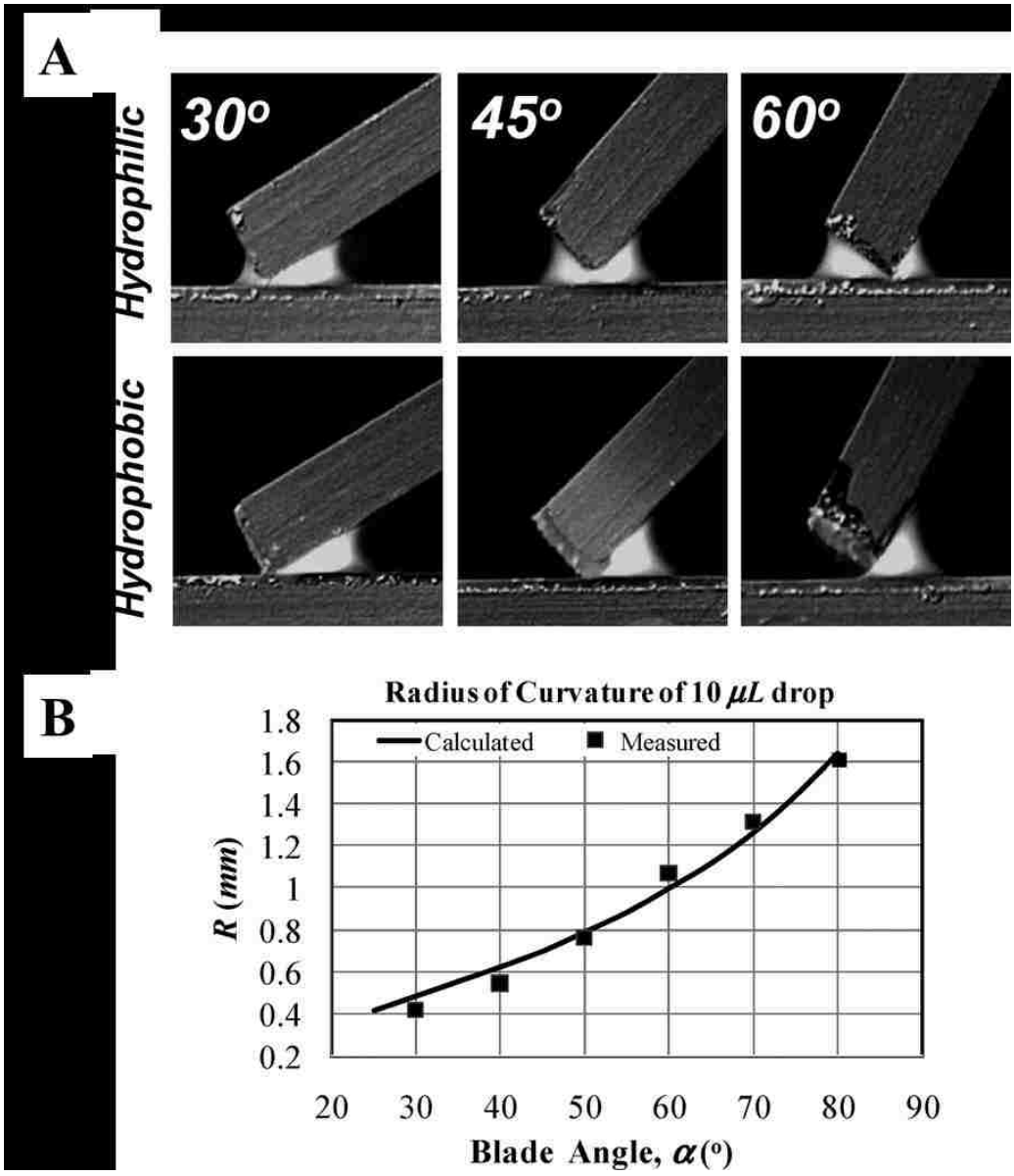

Figure 2.6: Radius of curvature shown as a function of contact angle. (A) Images of meniscus curvature (hydrophilic, top; hydrophobic, bottom). (B) Comparison between measured values and Equation 2.3 (Reprinted from Kumnorkaew et al., *Langmuir* 2008).

2.4.1: Gross Trends and Morphologies

Qualitatively, the following images show sample frames scanned showing two series, one at 30° under an array of speeds (Figure 2.7), the other at 60 μm/sec with varying blade angle (Figure 2.8). As a reminder, Ψ_6 = local bond order and particle color coding methodology is described in Figure 2.4.

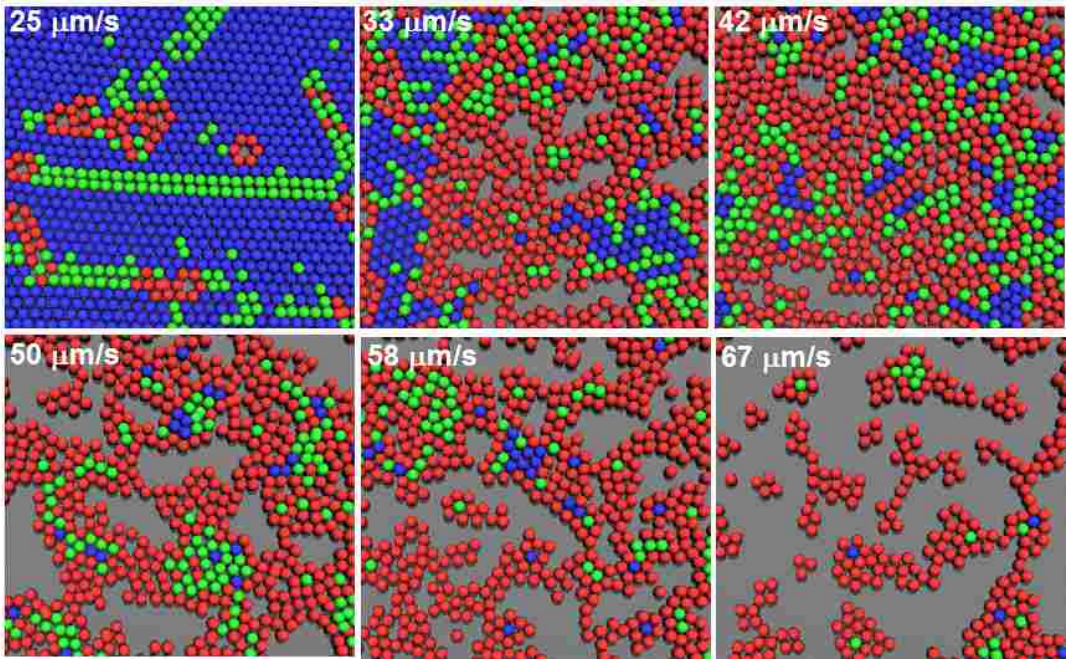

Figure 2.7: Representative images of convectively deposited thin films with a constant blade angle of 30° and speed varying from 25-67 μm/s. Blue particles have six nearest neighbors and $\Psi_6 > 0.9$. Green particles have six nearest neighbors and $\Psi_6 < 0.9$. Red particles have fewer than six nearest neighbors.

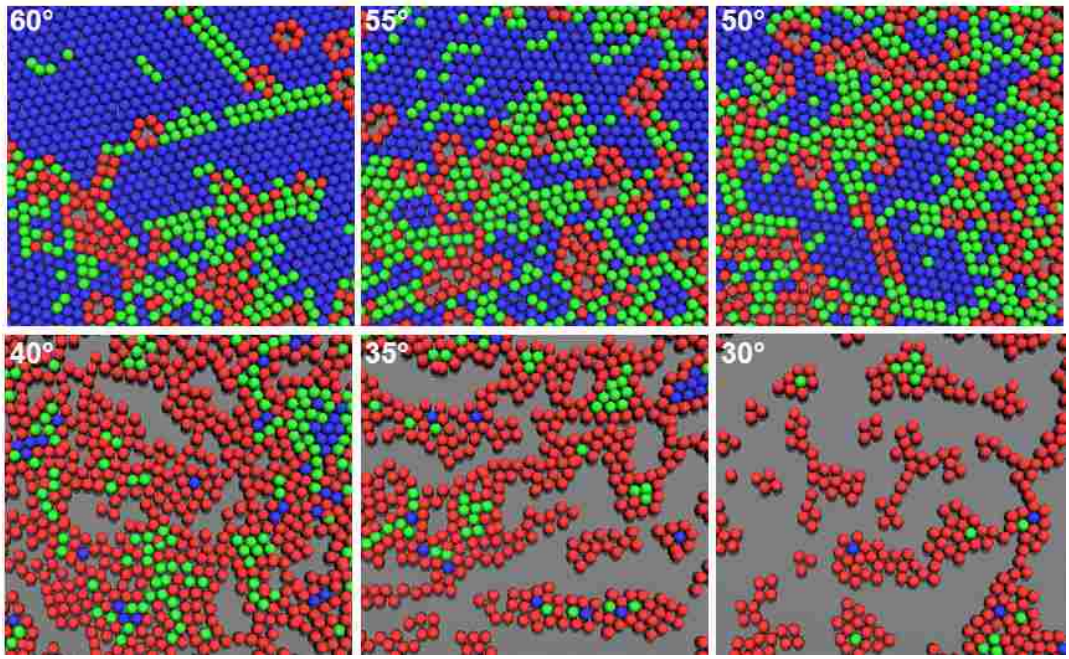

Figure 2.8: Representative images of convectively deposited thin films with a constant deposition speed of 60 μm/sec and blade angle varying from 60-30°. Blue particles have six nearest neighbors and $\psi_6 > 0.9$. Green particles have six nearest neighbors and $\psi_6 < 0.9$. Red particles have fewer than six nearest neighbors.

Figure 2.7 holds blade angle constant under varying deposition speed. Thus the series moves "vertically" through the phase diagram presents in Figure 2.5. A deposition speed of 25 μm/sec corresponds to the monolayer condition, and the previously mentioned trends are qualitatively validated in the presented image series. As the deposition speed is increased, samples show increasing submonolayer characteristics. 33 42 μm/sec and 42 μm/sec still exhibit relatively high particle density, but as the data moves "farther" from the monolayer condition, 50, 58, and 67 μm/sec deposited particle coatings become increasingly sparse. The data behaves somewhat "as expected," with a monotonic decay in particle density, under a blade angle of 30°.

Figure 2.8 highlights similar transitioning morphologies under constant deposition speed and varying blade angle. At 60 μm/sec, a relatively "fast" deposition speed, a complete range of morphologies presents itself between 30° and 60°. Under large blade angles, 60°, 55°, and 50°, thin films are relatively densely packed, with increasing amounts of disorder following decreasing blade angle. Under low blade angles of 40°, 35° and 30°, submonolayers are increasingly sparse. Coating morphology was quite consistent, albeit different, under "high" and "low" blade angles. Under high blades angles, submonolayer thin film morphology showed a higher level of order, and was characterized by many large crystalline "islands." Under low blade angles, submonolayers were randomly packed, and showed a much lower degree of order. These results parallel those presented in Figure 2.3 quite strongly, namely that two contrasting "deposition modes" yield very different resultant submonolayer

morphologies. The data truly becomes interesting in the intermediate regime, near a blade angle of 45° (Figure 2.9). Under this condition, both morphologies are presented in an alternating "striped" format. Figure 2.9 presents imagery of both locally-ordered and randomly-packed regions. Looking forward to crystallinity and packing data of submonolayer thin films, there is significant spread to data at intermediate blade angles as compared to stable "high" and "low" blade angle conditions.

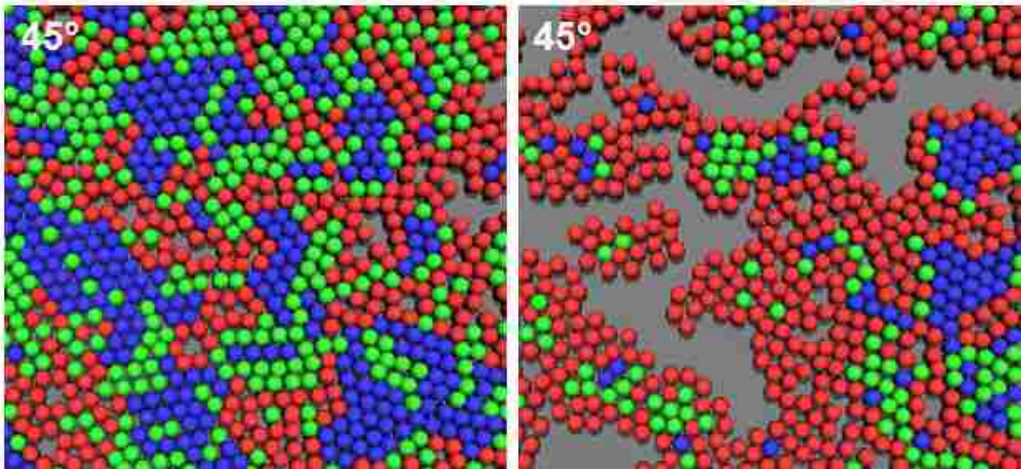

Figure 2.9: Snapshot of the "intermediate blade angle" deposition regime. This coating, deposited at 60 μm/sec, most likely undergoes both "ballistic" and "locally ordered" deposition, and definitely exhibits both "high blade angle," ordered, and "low blade angle," disordered, resultant morphologies.

2.4.2: Submonolayer Morphological Characterization: Quantitative Analysis

Paralleling and expanding upon these qualitative snapshots and trends, Figures 2.10 and 2.11 present a quantitative parametric study of the submonolayer regime. Figure 2.10 holds blade angle constant, and presents thin film crystallinity, Ψ_6, and packing density, ρ, with varying deposition speed. Figure 2.11 presents a converse organization of the data—Ψ_6 and ρ with constant deposition speed, varying blade angle.

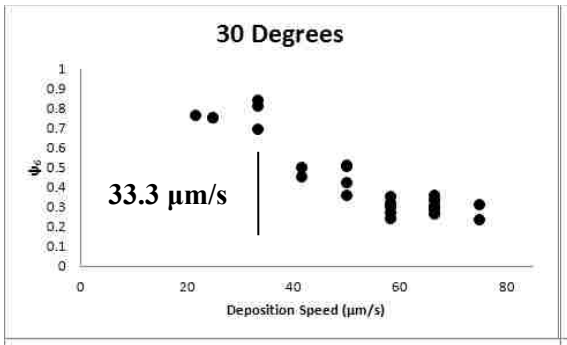
30 Degrees
33.3 µm/s
Deposition Speed (µm/s)

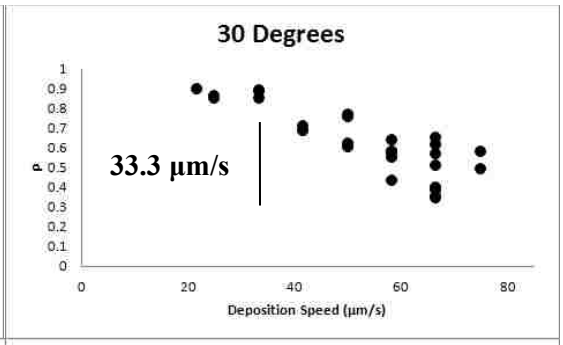
30 Degrees
33.3 µm/s
Deposition Speed (µm/s)

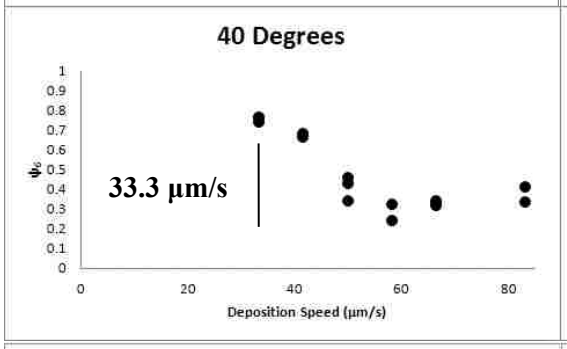
40 Degrees
33.3 µm/s
Deposition Speed (µm/s)

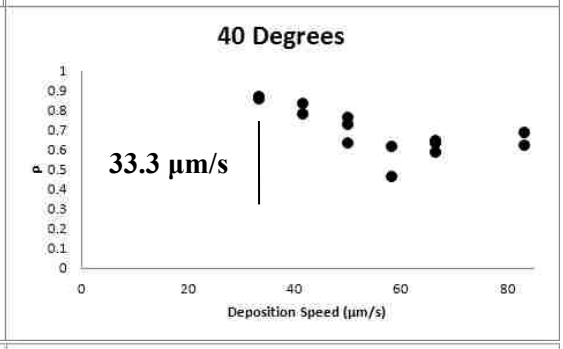
40 Degrees
33.3 µm/s
Deposition Speed (µm/s)

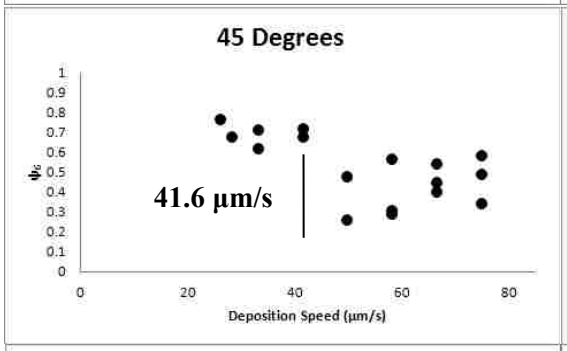
45 Degrees
41.6 µm/s
Deposition Speed (µm/s)

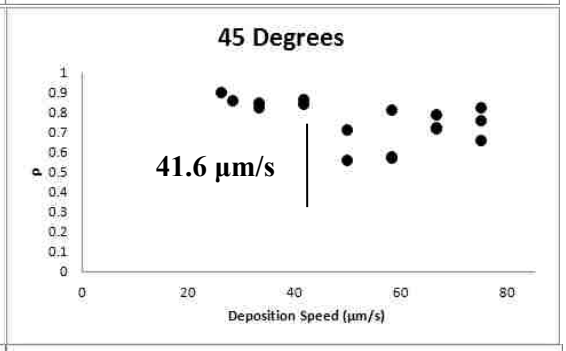
45 Degrees
41.6 µm/s
Deposition Speed (µm/s)

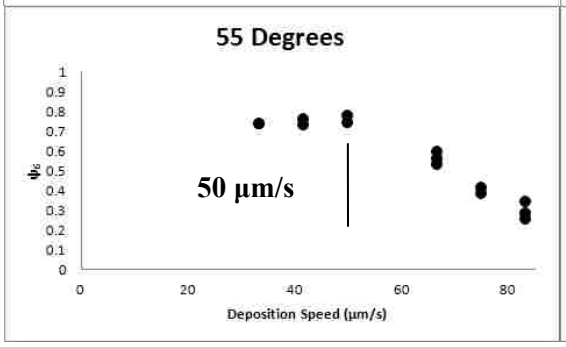
55 Degrees
50 µm/s
Deposition Speed (µm/s)

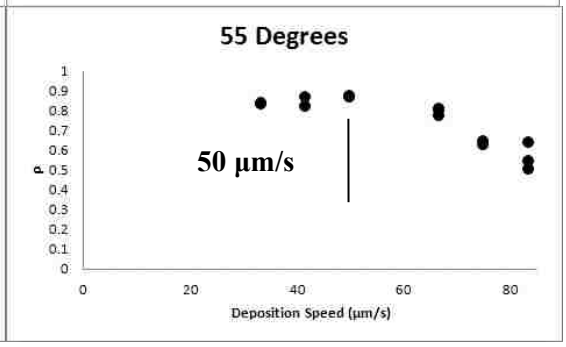
55 Degrees
50 µm/s
Deposition Speed (µm/s)

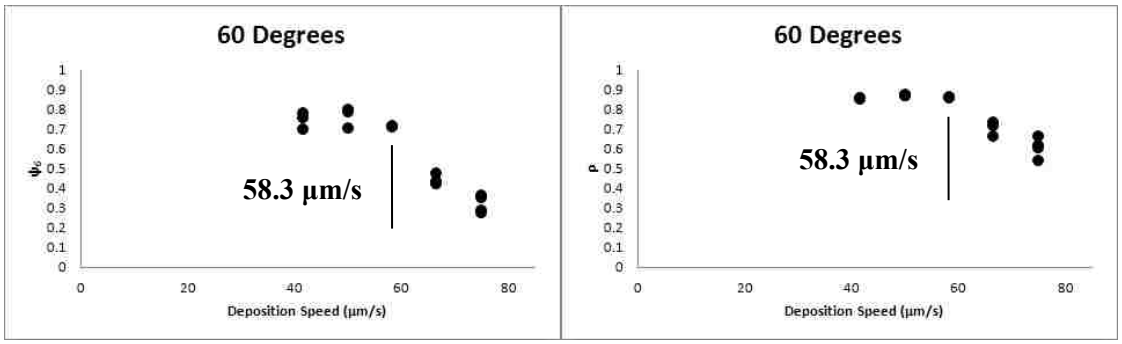

Figure 2.10: In-depth characterization of the submonolayer regime holding blade angle constant while varying deposition speed. Thin film crystallinity, Ψ_6, and packing density, ρ, are averaged and quantified via image analysis of 90-100 separate images from a high speed confocal microscope. Note that the initial high crystallinity/packing plateau at lower deposition speeds corresponds to multilayer, then monolayer, morphologies. The transition point into the submonolayer condition, evidenced by a drop in crystallinity and packing density, is highlighted in each plot. Note that, as expected and shown through previous results (Figure 2.5), higher blade angles correspond to a higher monolayer-submonolayer transition point.

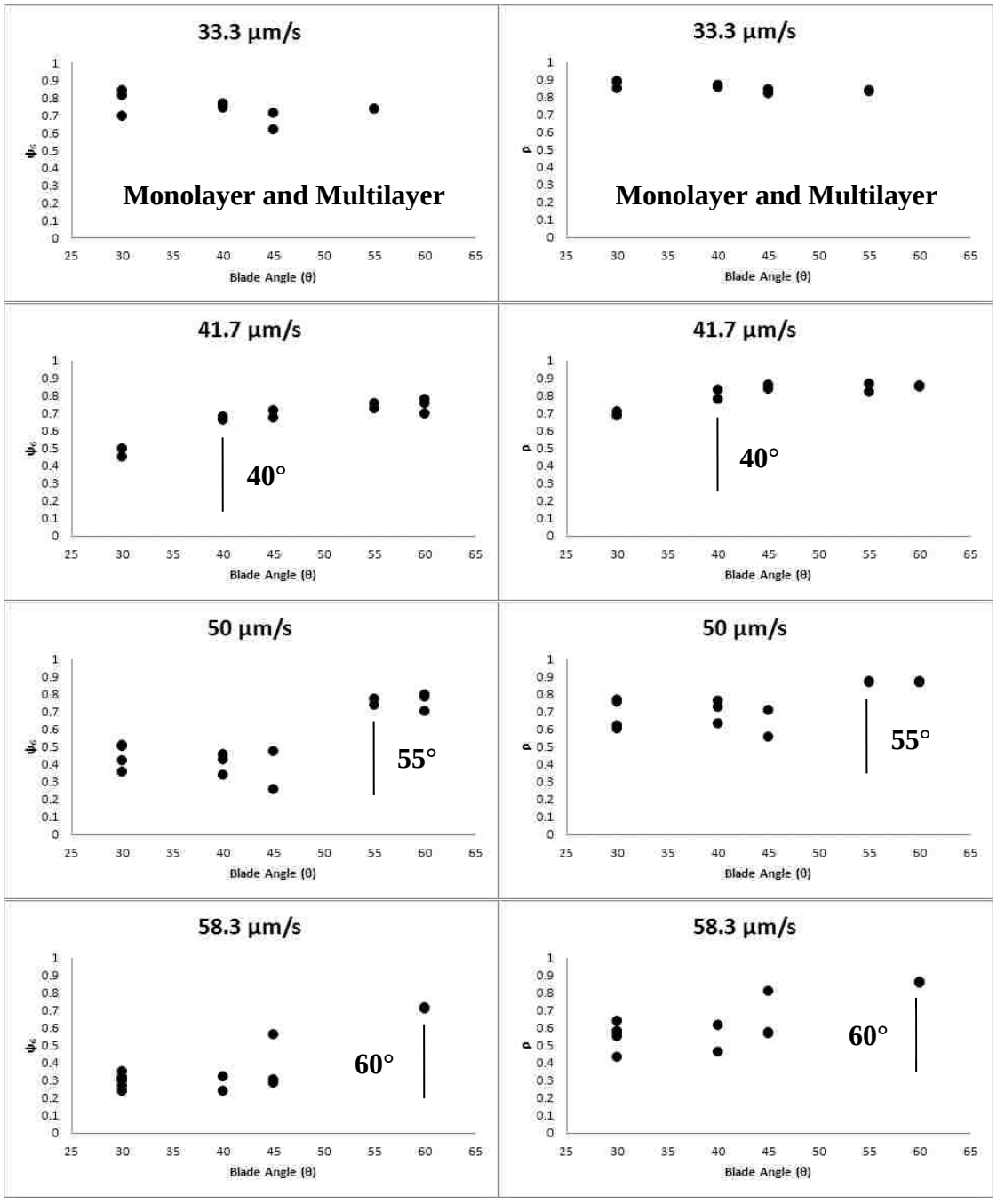
33.3 µm/s
Monolayer and Multilayer
33.3 µm/s
Monolayer and Multilayer
41.7 µm/s
40°
41.7 µm/s
40°
50 µm/s
55°
50 µm/s
55°
58.3 µm/s
60°
58.3 µm/s
60°
Blade Angle (θ)

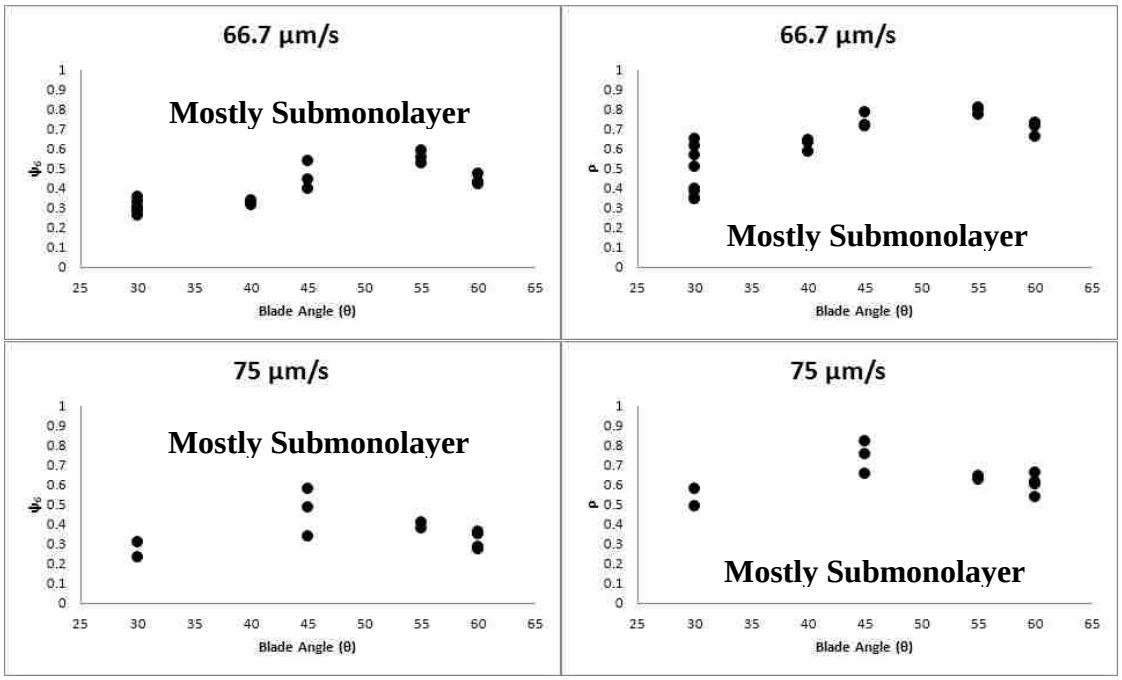

Figure 2.11: In-depth characterization of the submonolayer regime holding deposition speed constant while varying blade angle. Thin film crystallinity, Ψ_6, and packing density, ρ, are averaged and quantified via image analysis of 90-100 separate images from a high speed confocal microscope. Note that plateaus at higher relative blade angles are in reality a transition from monolayer to multilayer morphologies. The transition point into the monolayer condition, evidenced by increased crystallinity and packing density, is highlighted in each plot. Note that, as expected and shown through previous results (Figure 2.5), faster deposition speeds yield increasingly submonolayer morphologies and an increasingly higher blade angle transition threshold.

Figure 2.10, an organization by blade angle, helps show clear trends with changing deposition speed. This multilayer to monolayer plateau, and transition to a submonolayer morphology, is in line with the observed trends in Figure 2.5. Note that this data series was run under different humidity conditions vs. Kumnorkaew et al., 2008, and the specific magnitudes in this study should stand alone, whereas qualitative trending should be similar. These data are a composite of 90-100 averaged individual images collected via high speed confocal microscopy. Frames typically exhibit 400-1400 particles depending on thin film morphology—thus data from 60,000-120,000 individual particles are averaged to yield each data point. Within these confocal scans, the focal plane is limited to the first layer of particles atop a substrate. Thus the bottom layer in a multilayer and the single layer in a monolayer will have obvious similarities. Packing density, ρ, under these contrasting conditions, will be near identical. However, Ψ_6 is very sensitive to small changes in particle ordering—thus there is an increasing spread in Ψ_6 with multilayer morphology.

Across the blade angles presented in Figure 2.10, the data exhibits clear drops from the monolayer into the submonolayer regime. As expected, these final monolayer conditions preceding the submonolayer condition increase with increasing blade angle—the monolayer-submonolayer transition points are 33.3 μm/sec(30°), 33.3 μm/sec(40°), 41.6 μm/sec(45°), 50 μm/sec(55°), and 58.3 μm/sec(60°). In line with the previous discussion of varying submonolayer morphologies and deposition modes, it is essential to contrast "low," "moderate," and "high" blade angle conditions. At 30° and 40°, Ψ_6 and ρ highlight a strongly ordered condition at 33.3 μm/sec, then clear

monotonic decreases over the ~30 μm/sec. At that point the data plateaus into a sparsely packed submonolayer. At 55° and 60°, there are strongly ordered conditions at moderate deposition speeds followed by monotonic drops in Ψ_6 and ρ that appear quite linear within the range of deposition speeds investigated.

At 45°, the multilayer/monolayer to submonolayer transition follows the same trend. However, there is a significant increase in spread to the intermediary-blade angle data. Higher deposition speeds show large variation in Ψ_6 and ρ. These data do not exhibit the monotonic or linear trends that are evident at both "high" and "low" blade angles. The competition between locally ordered and randomly packed submonolayer morphologies, and similarly contrasting deposition modes, generates a larger degree of thin film nonuniformity. These data strongly corroborate the qualitative snapshots presented in Figure 2.9. It is also interesting to note that these data exhibit much higher packing and crystallinity, at relatively faster deposition speeds, versus "high" and "low" blade angle conditions.

Figure 2.11 organizes the same quantitative Ψ_6 and ρ data by deposition speed in an attempt to elucidate further patterns with changing blade angle. These data, trending across both deposition "modes" serve to provide valuable insight, especially with regards to morphological limitations within the spread of investigated deposition parameters. Once more the transition points trend as expected (Figure 2.5), with the monolayer/submonolayer "transition point" increasing with higher deposition speed. The slowest deposition speed, 33.3 μm/sec, yields multilayer and monolayer thin films under all investigated blade angles. The extremely high packing density of these films,

paired with high but varying crystallinity, indicates the deposited thin films are mostly multilayer. A slightly higher deposition speed, 41.7 μm/sec, shows the first coatings that cross into the submonolayer regime. The lowest blade angle, 30°, generates a submonolayer while 40° and beyond generate more highly packed thin films. Moderate speeds of 50 and 58.3 μm/sec show clear transitions from submonolayer to monolayer/multilayer morphologies, with transition points of 55 and 60° respectively. These submonolayers exhibit significant spread in Ψ_6 and ρ, with this spread particularly pronounced at an intermediate blade angle (45°). Finally, under the fastest deposition speeds (66.7 μm/sec, 75 μm/sec), most resultant thin films are submonolayer. These data show complex trends, and thus it would be a mistake to draw further conclusions without addition support.

2.5: Conclusions and Impact

These forays into the submonolayer regime are highly enlightening, and an extremely useful complement to previous work.[1] It is clear that both blade angle and deposition speed play a role in the control of transitions into and out of the submonolayer regime, as well as varying morphologies therewithin. Figure 2.11 shows that, in contrast with, and extending, Equation 2.1, convective deposition significantly depends on blade angle. Figure 2.10 shows changing dynamics with blade angle with deposition speed held constant. It complements preliminary confocal videography and imagery that indicate the presence of two contrasting submonolayer morphologies and deposition modes. Under lower blade angles, coatings assume "random" submonolayer morphology, where particles are relatively disordered. These results are corroborated by confocal videography showing particles flowing to the crystal front seemingly "independent" of one another. Figure 2.10 shows that, under low blade angles, deposition speed yields significant control over resultant morphologies. In contrast, higher blade angles yield coatings where submonolayers assume a locally-ordered morphology. Again, these results are complemented by confocal videography that shows pre-formed crystalline islands of particles flowing to the crystal front. Under higher blade angles, thin film crystallinity and packing fraction are once again well-controlled. A competition between these "high blade angle" and "low blade angle" submonolayer morphologies is seen at the intermediate condition. Qualitatively, these intermediate coatings exhibit stripes of locally-ordered and random

submonolayer morphologies. Quantitatively, these data exhibit significant spread, and show nonmonotonic and nonlinear trends in Ψ_6 and ρ.

This study is quite important moving forwards. Previous work into the convective deposition of particle monolayers is carried out, almost exclusively, with a 45° blade angle.[1,4,5] These studies show obvious successes. However in light of the competitive deposition modes at this intermediate blade angle, future studies can take on a more intelligent design of deposition parameters. These data show a higher degree of coating regularity at higher and lower blade angles. Technically, it is easier to carry out experiments with smaller blade angles—the suspension meniscus more easily wets both blade and substrate. In light of the results presented in this chapter, instability and defect-related work, already vulnerable to non-uniformity, are carried out at a blade angle of 30°. These results, presented in Chapters 4 and 5, elucidate the dynamics at play in increasing complex systems—carrying out these experiments at a lower blade angle thus minimizes excess variability.

2.6: References

1. Kumnorkaew P, Ee Y, Tansu N, Gilchrist JF. Investigation of the deposition of microsphere monolayers for fabrication of microlens arrays. *Langmuir*. 2008;24(21):12150-12157.

2. Wang B, Weldon AL, Kumnorkaew PK, Xu B, Gilchrist JF, Cheng X. Effect of surface nanotopography on immunoaffinity cell capture in microfluidic devices. *Langmuir*. 2011;27(17):11229-11237.

3. Weldon AL, Kumnorkaew PK, Wang B, Cheng XC, Gilchrist JF. Fabrication of macroporous polymeric membranes through binary convective deposition. *Acs Applied Materials & Interfaces*. 2012;4(9):4532-4540.

4. Kumnorkaew P, Gilchrist JF. Effect of nanoparticle concentration on the convective deposition of binary suspensions. *Langmuir*. 2009;25(11):6070-6075.

5. Kumnorkaew P, Weldon AL, Gilchrist JF. Matching constituent fluxes for convective deposition of binary suspensions. *Langmuir*. 2010;26(4):2401-2405.

6. Muangnapoh T, Weldon AL, Gilchrist JF. Enhanced colloidal monolayer assembly via vibration-assisted convective deposition. *Applied Physics Letters*. 2013;103:181603-1-181603-4.

7. Prevo BG, Fuller JC, Velev OD. Rapid deposition of gold nanoparticle films with controlled thickness and structure by convective assembly. *Chemistry of Materials*. 2005;17(1):28-35.

8. Dimitrov AS, Nagayama K. Steady-state unidirectional convective assembling of fine particles into 2-dimensional arrays. *Chemical Physics Letters*. 1995;243(5-6):462-468.

9. Prevo BG, Kuncicky DM, Velev OD. Engineered deposition of coatings from nano- and micro-particles: A brief review of convective assembly at high volume fraction. *Colloids and Surfaces A-Physicochemical and Engineering Aspects*. 2007;311(1-3):2-10.

10. Prevo BG, Velev OD. Controlled, rapid deposition of structured coatings from micro- and nanoparticle suspensions. *Langmuir*. 2004;20(6):2099-2107.

11. Prevo BG, Hwang Y, Velev OD. Convective assembly of antireflective silica coatings with controlled thickness and refractive index. *Chemistry of Materials*. 2005;17(14):3642-3651.

12. Kleinert J, Kim S, Velev OD. Electric-field-assisted convective assembly of colloidal crystal coatings. *Langmuir*. 2010;26(12):10380-5.

13. Jerrim LB, Velev OD. Deposition of coatings from live yeast cells and large particles by "convective-sedimentation" assembly. *Langmuir*. 2009;25(10):5692-5702.

14. Xiao J, Attinger D, Bhardwaj R. Manufactured self-assembled coatings of micro- and nano-particles by controlled evaporation of drops and thin films. *Proc SPIE 8031*. 2011;8031.

15. Dimitrov AS, Nagayama K. Steady-state unidirectional convective assembling of fine particles into 2-dimensional arrays. *Chemical Physics Letters*. 1995;243(5-6):462-468.

Chapter 3

Binary Convective Deposition

3.1: Introduction and Previous Work

Tuned polydispersity in colloidal suspensions is increasingly used in applications to control film morphology during drying,[1,2] fabricate crystals of various periodicities,[3] and study the effects of differing species on suspension rheology.[4,5] Polydispersity refers not only to the size distribution in a given suspension, but also to the variability in particle shape, density, internal morphology, and surface chemistry.[6] Suspension polydispersity commonly stems from the variability in nucleation and growth rates and from particles formed via aggregation. Heteroaggregation and depletion flocculation are classic examples of tuned polydispersity.[4,7] Novel combinations of particles of tuned size and surface polydispersity have been used to form aggregates with specified properties.[8] Long-studied particle-sorting processes including fractionation and other phoretic analyses focus on reducing polydispersity.

Convective deposition is a method of growing popularity in altering surface morphology and chemistry.[9] Convective deposition is the process by which a suspension meniscus is drawn across a substrate with well-ordered particle layers

deposited as the contact line advances. The fundamental science continues to elucidate novel aspects of convective deposition related to suspension properties and fluid mechanics;[10-14] however, the role of polydispersity on convective deposition is still unclear.[15] Binary suspensions of differently sized particles have found use in the fabrication of 2D and 3D colloidal crystals where smaller constituents fill the interstitial regions between larger species.[14,15] Deposited binary suspension layers are very useful for altering surfaces' optical properties.[16,17] Binary suspensions with polydispersity in properties other than size have been minimally explored, though most combinations of materials will probably result in highly heterogeneous deposited layers. The exception to this is the higher degree of uniformity in polymer and microsphere binary suspensions where the elastic stresses aid assembly.[13]

One significant enhancement to convective deposition is the transition from unary to binary suspensions, where nanoparticles paired with microspheres enhance packing and resultant thin film uniformity. These enhancements are particularly useful in application enhancement, where thin film crystallinity and high two-dimensional packing maximize device performance while minimizing variability. In addition, pairing oxide microspheres alongside polymer nanoparticles gives enormous flexibility in the fabrication of composites. After codeposition, either component can be selectively removed through etching or heat treatment. This can enable the formation of highly-ordered single component microsphere thin films as well as uniform nanoporous structures.[18]

Initial forays into the field show that the specific ratio of microsphere to nanoparticle volume fractions is crucial in attaining maximum uniformity.[15] In particular, the addition of nanoparticles suppresses gross-scale defects that can result from thermal gradient-induced flow near the evaporative flux. In addition, stepping outside these ideal conditions can yield the formation of complex macroscale morphologies (Figure 3.1).

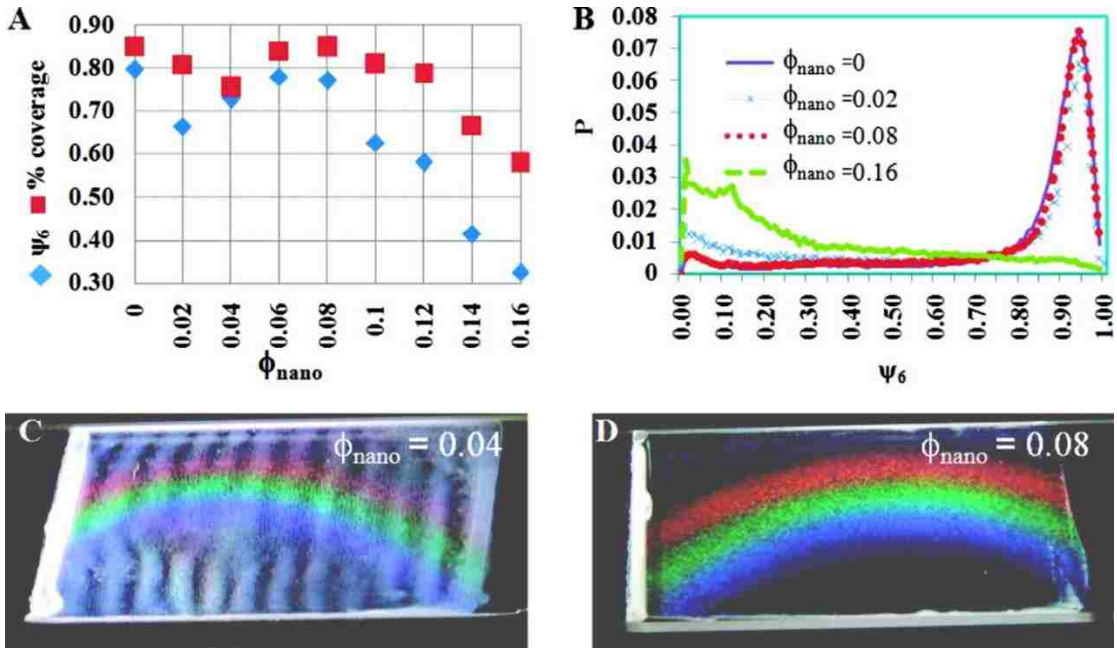

Figure 3.1: (A) Surface microstructure as evaluated by measuring substrate density, ρ, and surface crystallinity; $\Psi_{6,ave}$ is a function of nanoparticle volume fraction (See Chapter 2 for details). The optimum structure is recovered at ϕ_{nano}= 0.08 and produces the largest, most, coherent thin films. (B) Probability distribution of Ψ_6 plotted for ϕ_{nano} = 0, 0.02, 0.08, and 0.16 shows similarities in microstructure for ϕ_{nano}= 0 and ϕ_{nano}= 0.08, and ϕ_{nano}= 0.16 has few crystalline domains. (C, D) Images of samples show the variability of the deposition due to the addition of nanoparticles. At ϕ_{nano}= 0.04 (C), films exhibit variations in thickness from brighter stripes of crystalline monolayer to darker stripes of pure nanoparticles without microspheres. For ϕ_{nano}= 0.08 (D), a continuous monolayer covers the entire substrate. Adapted from Kumnorkaew et al., 2009.

Figure 3.1 describes the microstructure and morphology of convectively developed binary thin films. Here, 1 μm SiO_2 microspheres are codeposited with 100 nm polystyrene nanoparticles. Figure 3.1A provides a parametric study of thin film crystallinity and packing fraction with varying volume fraction of nanoparticles alongside 20% v/v SiO_2. This plot shows that nanoparticle addition can be useful or detrimental, depending on experimental parameters, in convective deposition. At excessively low or high relative nanoparticles volume fraction, thin film crystallinity, Ψ_6, and packing fraction, ρ, decrease in value. However, under optimal conditions, ϕ_{nano} = 0.06, 0.08 (v/v), thin film crystallinity and density regain their initial high values. Figure 3.1B shows the probability distribution of finding microspheres with increasing amounts of order under varying nanoparticle conditions. This highlights the fact that under excessively "high" values of ϕ_{nano}, few to no highly-ordered particles regions are apparent. Conversely, microsphere probability densities at moderate volume fraction, ϕ_{nano} = 0.08, match those of the unary case. Finally, in the lower intermediate regime, ϕ_{nano} = 0.02, there is a balance between highly and minimally-ordered regions.

Macroscopically, a few sample images are shown in Figure 3.1C and Figure 3.1D. Figure 3.1C highlights an interesting striped morphology under lower relative nanoparticle volume fraction. While this is interesting, and the striping appears somewhat uniformly spaced, these gross nonuniformities will severely less overall crystallinity and packing fraction. In addition, any variance in thickness would cripple applications that take advantage of uniform 2D particle coatings. Figure 3.1D shows a highly-ordered and uniform thin film coating under ideal conditions of ϕ_{micro} = 0.20 and

ϕ_{nano} = 0.08. In addition, the degree to which nanoparticles bury microspheres, in crystalline regions, varies with relative nanoparticle concentration (Figure 3.2).

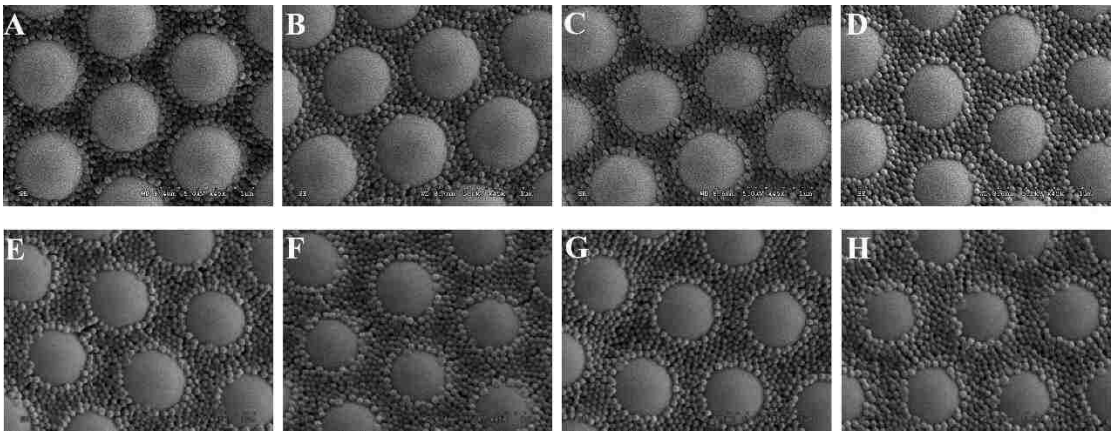

Figure 3.2: SEM images of the deposited microstructure where nanoparticles partially bury microspheres. All samples are created from solutions ϕ_{micro}= 0.2 and ϕ_{nano}= 0.02 (A), 0.04 (B), 0.06 (C), 0.08 (D), 0.10 (E), 0.12 (F), 0.14 (G), and 0.16 (H). Neighboring microspheres are in contact, and nanoparticles fill the interstitial regions up to a height less than the diameter of the microsphere. Adapted from Kumnorkaew et al., 2009.

Figure 3.2 presents crystalline regions under each nanoparticle volume fraction. It is important to note that, while nonideal nanoparticle pairing may yield global drops in Ψ_6 and ρ, those samples still exhibit some highly-ordered regions. These data show that, in those regions, increasing nanoparticle concentration in suspension yields increased nanoparticle filling around deposited microspheres. This increasing coverage with concentration is roughly linear (not presented here).

Previous work sets the stage for further adaptations to the convective deposition process, and specifically the use and design of binary suspensions. While these results are novel and enlightening, there is little theory to support this "optimal" nanoparticle volume fraction. These follow-up studies on the use of binary suspensions in convective deposition will 1) shed some light on how and why this optimal nanoparticle concentration exists, 2) analyze the position of nanoparticles in submonolayer binary films, and 3) present yet another substantial innovation with addition of vibration to binary convective deposition.

3.2: Steady Convective Deposition Expansion and Theory

This study extends previous work on the versatility of binary convective deposition, namely the addition of a nanoparticle packing aid.[15] It expands upon the involved dynamics by considering relative constituent fluxes during deposition. Prior work showed that nanoparticle addition, at optimum volume fraction ϕ_{nano}, to a suspension allows the coating of a much larger homogeneous monolayer than would be allowed in the unary case. With suboptimal ϕ_{nano}, stripes of alternating morphologies form perpendicular to the direction of the advancing meniscus; with superoptimal ϕ_{nano}, surface crystallinity degrades or forms other morphologies such as multilayers and stripes. In deposited layers, microspheres are partially buried within a nanoparticle multilayer, and the degree of exposed microspheres depends on ϕ_{nano}. At high ϕ_{nano}, depletion destabilizes microspheres and forms a gel that cannot be deposited uniformly. This work provides a mechanism that describes optimal deposition concentration ratios and the formation of stripes and other morphologies through unbalanced deposition fluxes. This allows for the tuning of binary suspension properties to match species' flux and deposit uniform monolayers. Here, nanoparticle influence is expanded across microsphere volume fractions $0 < \phi_{micro} \leq 0.24$. In addition, it will be demonstrated that varying ϕ_{micro}, under constant ϕ_{nano}, influences resultant morphology but does not influence the degree of microsphere burial.

3.2.1: Suspension Preparation

The primary colloid suspension used in this work is prepared by dispersing silica microspheres (Fuso Chemical Co, Japan) having a density of 2.2 g/cm^3, an average

diameter of $2a_{micro}$ = 1.01 ± 0.02 μm, and a zeta potential of −48 mV ± 1 mV in deionized (DI) water with a volume fraction ϕ_{micro}. The suspension is dispersed using a sonic dismembrator (model 550, Fisher Scientific, Pittsburgh, PA) for 10 min and is stirred for 30 min. (Fisher Scientific, model 550). A separate colloidal suspension of diameter $2a_{nano}$ = 100 nm polystyrene (PS) having a zeta potential of −59 mV ± 1 mV prepared at ϕ_{nano} = 0.35 in DI water (supplied by the Emulsion Polymer Institute at Lehigh University) is combined with the silica solution to achieve the desired suspension composition.

3.2.2: Deposition

The experimental setup is as described in the unary case (Chapter 2). All experiments were performed at roughly 50% relative humidity and 24 °C. The deposition blade angle is fixed at 45°, positioned approximately 10 μm above the substrate, and observed directly using a digital camera (Dinolite AM311S). The volume of colloid suspension for each experiment is 10 μL. Other experimental parameters, as well as microstructural characterization, are described in Chapter 2.

3.2.3: Relative Fluxes

As shown in chapter two, Dimitrov and Nakayama[19] derived the relationship between volume fraction and deposition speed, in a single-component suspension, for an advancing crystal on a substrate. For a hexagonally ordered monolayer:

$$v_{mono} = \frac{J_e \beta}{2a(\phi^D)} \frac{\phi}{1-\phi} \tag{3.1}$$

Where v_{mono} is the substrate velocity and is equal to the velocity of the advancing monolayer crystal front, J_e is the solvent flux, $2a$ is microsphere diameter, ϕ and ϕ^D are

the suspension volume fraction in solution and within the deposited thin film, respectively, and β describes particle−surface interactions.

The volume fraction of an ordered monolayer immersed in liquid at the same height $2a$ is ϕ^D, which is the deposited microsphere volume fraction. A simple geometric relationship gives ϕ^D:

$$\phi^D = \frac{\pi \int_{-a}^{a} (a^2 - x^2) dx}{2\sqrt{3}a^3} = \pi/3\sqrt{3} \tag{3.2}$$

In binary suspensions where smaller constituents percolate through the interstitial spaces between larger particles, referred henceforth as nanoparticles and microspheres respectively, a few modifications to this model are necessary. First, we assume that deposition dynamics of a microsphere monolayer primarily relate to microsphere properties (ϕ_{micro}, a_{micro}). However, when considering the final microstructure of microsphere monolayers embedded within a nanoparticle layer, as shown in Figure 3.3, nanoparticle flux into the layer is as significant as microsphere flux. As the layer reaches maximum packing and jams near the microsphere crystallization front, J_e changes and the local free surface curvature, solvent surface area, and effective suspension viscosity become nontrivial. However, these physical changes affect the deposition process comparatively little as compared to the relative microsphere and nanoparticle fluxes into the layer. In binary depositions resulting in high-quality microsphere monolayers, nanoparticles almost entirely bury microspheres. Uniform deposition is possible only with balanced constituent fluxes. If nanoparticles exactly fill to a height of $2a$ at the top of the microspheres, relative volume fraction of each species, directly related to the ratio of constituent fluxes into the thin film, is

$$\frac{\phi_{nano}^{D}}{\phi_{micro}^{D}} = \frac{J_{nano}}{J_{micro}} = \frac{\left(1-\pi/\left(3\sqrt{3}\right)\right)P}{\pi/\left(3\sqrt{3}\right)} \tag{3.3}$$

Where $\phi_{nano}{}^{D}$ and $\phi_{micro}{}^{D}$ are deposited nanoparticle and microsphere volume fractions respectively, J_{nano} and J_{micro} are nanoparticle and microsphere fluxes respectively, and P is the packing fraction of nanoparticles in the interstitial region between hexagonally ordered microspheres. High nanoparticle confinement inhibits crystallization; for jammed nanoparticles[20,21] with diminishing nanoparticle size, $a_{nano}/a_{micro} \rightarrow 0$ and $P \approx 0.64$. For finite-sized nanoparticles, P may be significantly lower because of confinement. As seen in Figure 3.3, nanoparticles do not completely bury microspheres, instead residing at a height $h/a = 0.725$ above the microsphere equator. Hence, the ratio of deposited nanoparticles to microspheres is

$$\frac{J_{nano}}{J_{micro}} = \frac{\left(1-\pi\int_{-a}^{0.725a}(a^2-x^2)dx\right)P}{\pi\int_{-a}^{0.725a}(a^2-x^2)dx} \approx 0.32 \tag{3.4}$$

The constituent flux ratio is exactly the volume fraction ratio of species; consequently, when $J_{nano} \approx 0.32 J_{micro}$, nanoparticle and microsphere fluxes into the thin film are matched appropriately for binary depositions. Note that this result is largely independent of a_{nano}. The degree of burial depends weakly on ϕ_{nano},[15] and across observed degrees of burial this results in less than 5% error in this calculation.

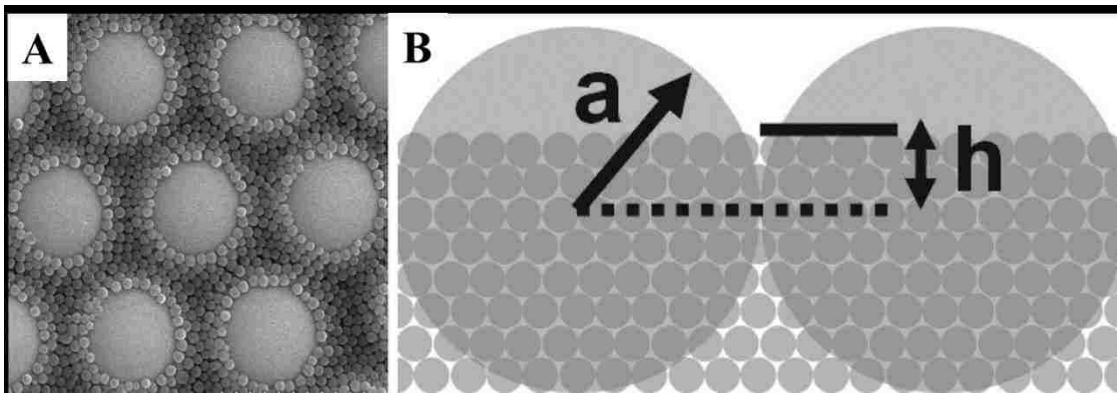

Figure 3.3: (A) Nanostructure of nanoparticles surrounding microspheres in a well-ordered array. (B) Sketch of the local geometry and relative burial of microstructures. The nanoparticles do not completely bury the microspheres, covering only to h/a = 0.725.

Ideal and nonideal matched J_{nano} and J_{micro} combinations are explored in Figure 3.4 in terms of their control over thin film morphology under otherwise ideal conditions. Under ideal monolayer-deposition conditions (Figure 3.4A), the fluxes are balanced through the relation proposed in Equation 3.4, and the thin film is filled with the appropriate number of particles for steady deposition. When nanoparticle flux is insufficient (Figure 3.4B), the moving front of the nanoparticles lags behind that of the advancing microsphere crystal front. The result is instability where the liquid layer pins on the deposited particles and interacts with binary morphology or the microsphere monolayer. Thus, a stick−slip periodic motion is possible, which results in stripes forming perpendicular to the deposition direction; these have features similar to those seen with monodisperse suspensions.[11,22-25] Packing of microspheres in the transition regions from single to multilayer morphologies likely follows that seen in monodisperse suspension depositions.[26,27] Any monodisperse suspensions with an additional nonvolatile species at high enough concentration can potentially undergo the same transition. The distance between stripes may correlate with the degree of mismatch between fluxes; this is seen qualitatively in experiments but is not quantified. Finally, when the nanoparticle flux exceeds that necessary to fill the microsphere interstitial region (Figure 3.4C), nanoparticles force this region to expand. This expansion comes about in two ways. Microspheres separate as nanoparticles inhibit crystallization and a submonolayer is formed or microspheres pack vertically to transition to multilayer morphology. If the nanoparticle concentration is insufficient to fill the multilayer voids,

layer morphology will oscillate between the monolayer and multilayer regions. Experiments within these three situations are summarized below.

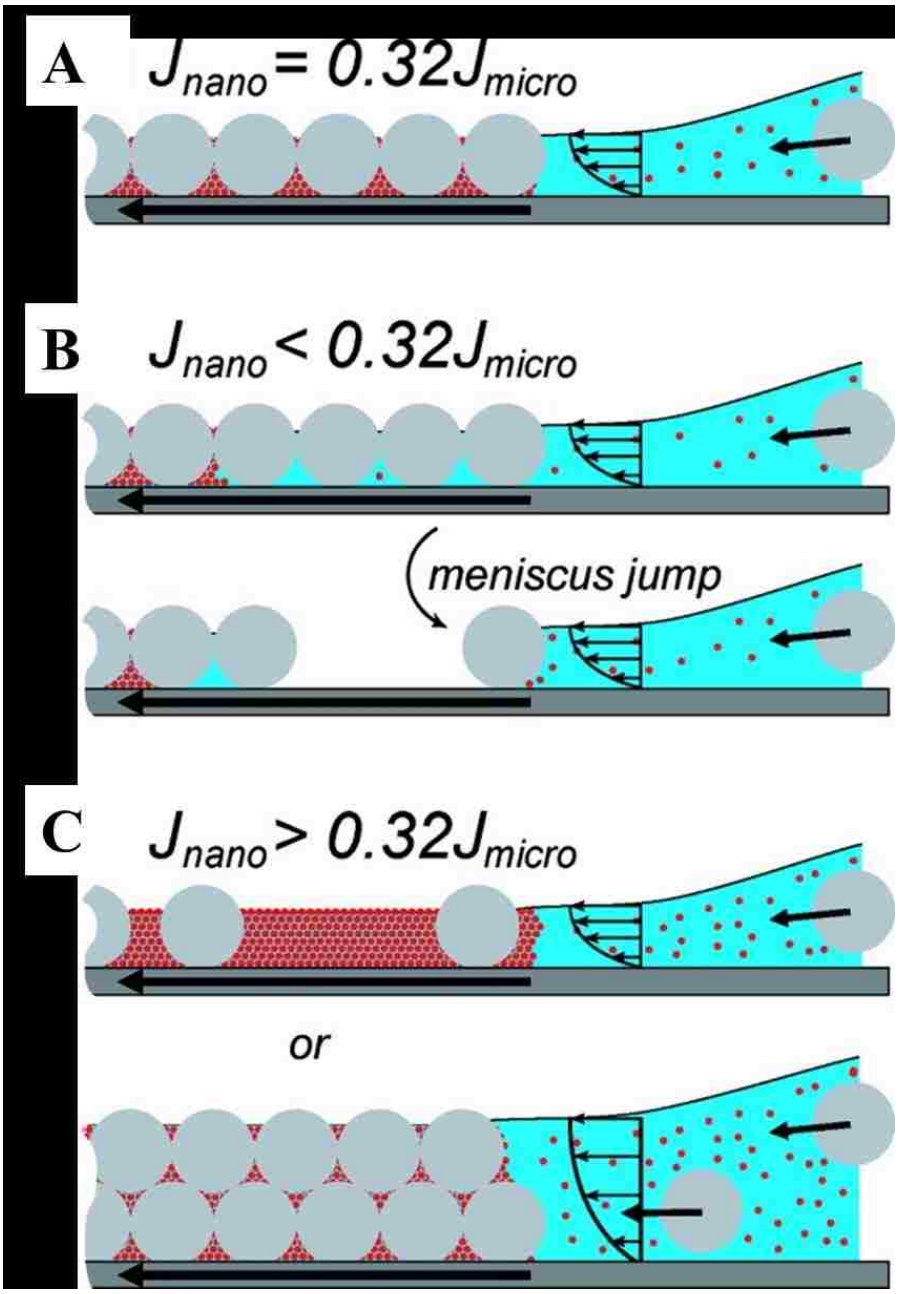

Figure 3.4: Description of matched fluxes and resulting layer morphologies. (A) When the nanoparticles and microspheres have complementary concentrations, steady monolayer deposition occurs. (B) For a lower-than-optimal nanoparticle concentration, instability arises and causes the advancing meniscus to jump. (C) For higher-than-optimal nanoparticle concentration, the interstitial region between microspheres must increase by either spreading the microspheres or forming a multilayer. Instability between monolayer and multilayer morphologies can also occur.

3.3: Steady Convective Deposition - Experimental Results

First baseline monolayer deposition speeds of monodisperse microsphere suspensions, $0.12 \leq \phi_{micro} \leq 0.24$, are established to quantify the relationship between v_{mono} and ϕ_{micro} (Figure 3.5). This quantification closely parallels the relationship given in Equation 3.1. It is difficult to produce large monolayer regions with $\phi_{micro} \leq 0.12$ in part because of the experimental protocol of depositing a finite volume of suspension; lower ϕ_{micro} experiments result in deposition areas too small for the determination of optimum conditions. However, previous studies successfully show the continuation of this trend at lower ϕ_{micro}.[26] Optimum v_{mono} values shown in Figure 3.5 are used for binary deposition with corresponding ϕ_{micro}. This assumption has been validated through select binary deposition trials with varying deposition speed.

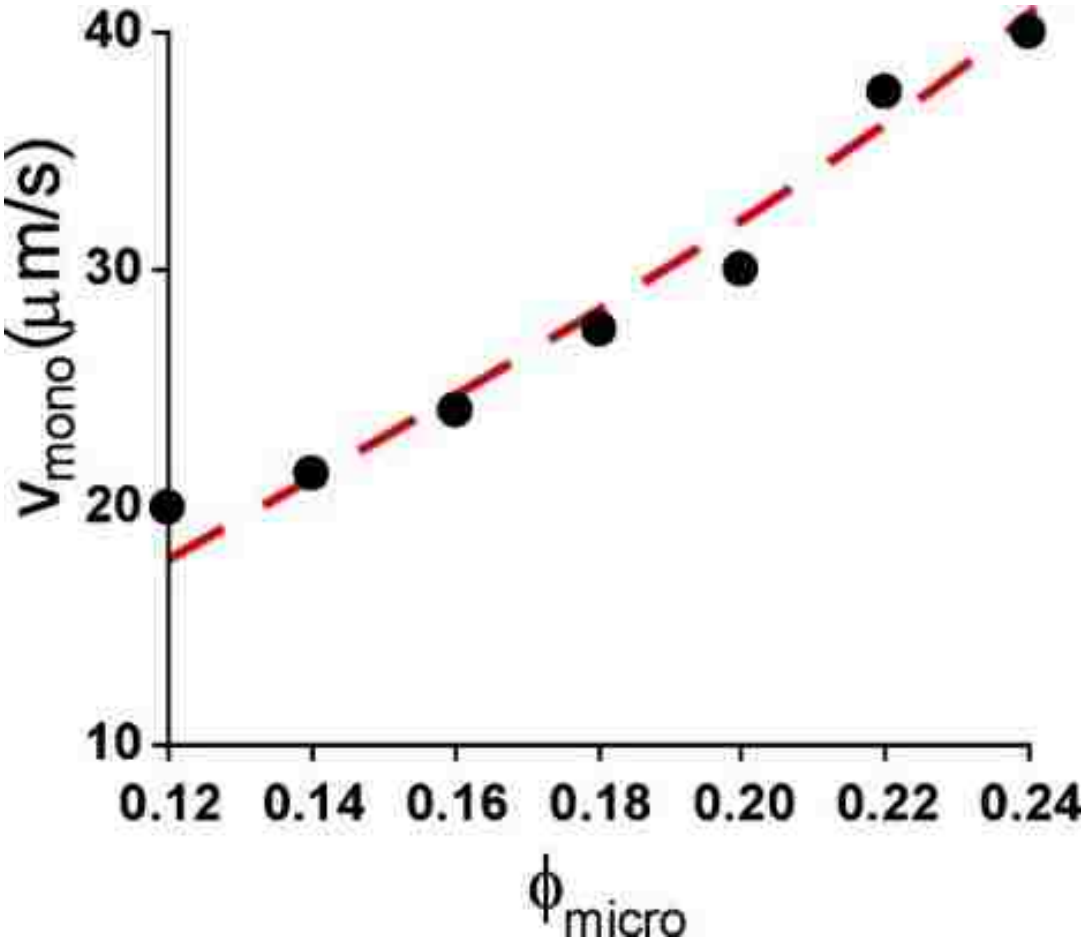

Figure 3.5: Plot of monolayer deposition velocity, v_{mono}, vs ϕ_{micro}. The data follows the trend given by Equation 3.1.

The morphology of microsphere depositions can be further tuned with the addition of moderate ϕ_{nano}. Optimized binary suspension depositions have larger uniform regions as compared with unary depositions as well as fewer defects and smaller edge multilayer regions. As in prior studies,[12,15] Ψ_6 and ρ quantify the quality of monolayer microstructure and coverage (Figure 3.6). Optimization of ϕ_{nano} for ϕ_{micro} = 0.12, 0.16, 0.20, and 0.24 yields a maximum Ψ_6 and ρ for each ϕ_{micro}. With increasing ϕ_{micro}, optimum ϕ_{nano} increases. These data correlate with morphological observations; henceforth, the respective ϕ_{nano} for each ϕ_{micro} producing a maximum Ψ_6 or ρ will be referred to as optimum ϕ_{nano}, $\phi_{nano}^*(\phi_{micro})$. Experimentally obtained optimum concentrations are found to be $\phi_{nano}^*(0.12) = 0.04$, $\phi_{nano}^*(0.16) = 0.055$, $\phi_{nano}^*(0.20) = 0.065$, and $\phi_{nano}^*(0.24) = 0.07$. For each ϕ_{micro}, $\phi_{nano} < \phi_{nano}^*$ produces stripes of alternating monolayer and submonolayer regions whereas $\phi_{nano} > \phi_{nano}^*$ produces low-quality samples of either general disorder or alternating monolayer and multilayer bands.

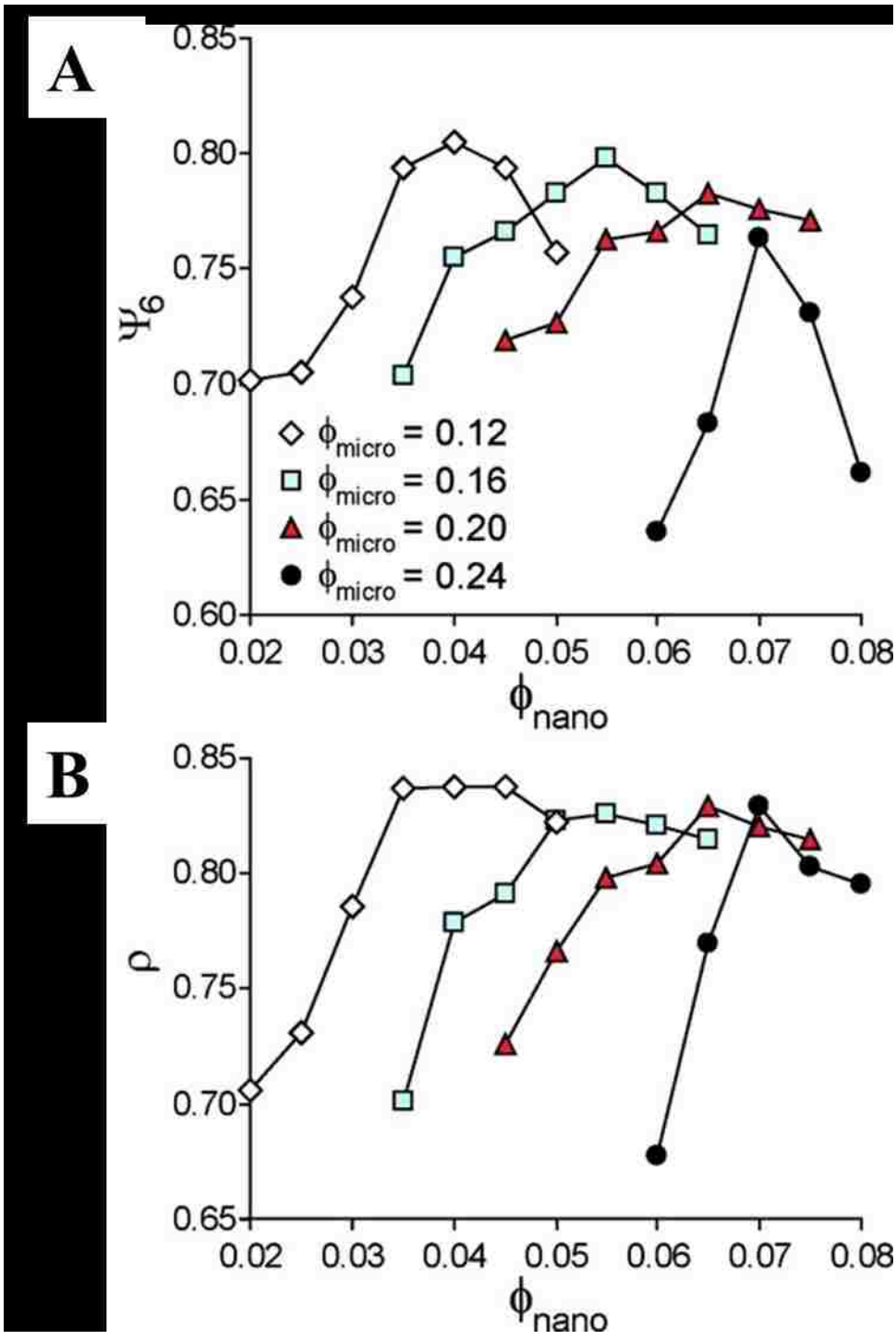

Figure 3.6: (A) Surface crystallinity, Ψ_6, and (B) percent coverage, ρ, versus ϕ_{nano} for ϕ_{micro} = 0.12, 0.16, 0.20, and 0.24. Optimal ϕ_{nano} maximizing $\Psi_6$and ρ exists for each ϕ_{micro}.

Optimal Ψ_6 and ρ for each ϕ_{nano}^* show a slight downward trend suggesting that binary suspensions with lower ϕ_{micro} produce more uniform layers. This variation relates directly to the number of crystalline defects and suggests that the crystal domain size is larger for lower ϕ_{micro}. For monodisperse samples under optimum conditions with varying deposition speeds and blade angles, Ψ_6 and ρ were essentially constant.[12] It is also clear that at higher ϕ_{micro}, Ψ_6 and ρ are more sensitive to nanoparticle concentration. This sensitivity plays an important role in the choice of processing conditions. Also, the slopes of Ψ_6 and ρ verses ϕ_{nano} are steeper with $\phi_{nano} < \phi_{nano}^*$ than with $\phi_{nano} > \phi_{nano}^*$. This increased sensitivity of Ψ_6 and ρ at $\phi_{nano} < \phi_{nano}^*$ is a result of insufficient nanoparticle flux (Figure 3.4B) as compared with that of microspheres. Sample patchiness with $\phi_{nano} < \phi_{nano}^*$ obviously yields lower-than-optimum percent coverage and heterogeneity of surface morphology and, with a correspondingly higher number of layer/void transition regions, a decreased overall layer crystallinity as well. The smaller magnitudes of the decreases in Ψ_6 and ρ with $\phi_{nano} > \phi_{nano}^*$ are explained through the same reasoning except that void spaces are replaced with multilayer regions. Only the microsphere layer in contact with the substrate is imaged for analysis; thus the difference between a monolayer and the bottom of a multilayer is small except in the mono- to multilayer morphological transition regions. The same argument for the absence of crystallinity at void/monolayer interfaces holds for monolayer/multilayer boundaries, which often exhibit square packing, and explains the Ψ_6 reduction. The relatively smaller magnitude of this reduction stems from the larger relative size of multilayer regions versus their void counterparts. The percent coverage, however, drops only slightly from the

maximum ρ at ϕ_{nano}^{*} with a higher nanoparticle concentration. This stems from the fact that the only real decrease in the coverage of these $\phi_{nano} > \phi_{nano}^{*}$ samples with multilayer region samples occurs at the monolayer/multilayer boundaries; there is no $\phi_{nano} > \phi_{nano}^{*}$ analog to the void interior with submonolayer patchiness.

Figure 3.7 summarizes experimental trials of varying ϕ_{nano} and ϕ_{micro} and compares them to the theoretical prediction of ϕ_{nano}^{*} from Equation 3.4. Each experimental datum is shaded with its respective Ψ_6. Note that Ψ_6 was calculated through the computational analysis of large-deposition-length scans; $\phi_{micro} \leq 0.04$ yielded only short-range (less than 0.5 cm) depositions. In short depositions, striping would not necessarily be apparent, and even in high-quality monolayers, the data lacks statistically viable quantification. Those samples $\phi_{micro} < 0.12$ have a qualitatively high-quality (HQ) monolayer microstructure though they no longer follow the flux balance and instead form monolayers only with $\phi_{nano} = 0.04$. Samples at $\phi_{nano} = 0.03$ show stripes, and samples at $\phi_{nano} = 0.05$ produce poor-quality depositions. It is unclear why this ϕ_{nano} plateau exists from low to moderate ϕ_{micro}. Perhaps these samples never reach steady deposition conditions. At $\phi_{micro} = 0.12$, the data transitions follow our prediction from Equation 3.4 of proportionally increasing ϕ_{micro} with ϕ_{nano}. This prediction is an upper limit based on the maximum possible random packing and results in a slight mismatch between experiments and predictions at $\phi_{micro} = 0.24$. Below our theoretical line, where $\phi_{nano} < \phi_{nano}^{*}$, Ψ_6 drops because of striping from insufficient nanoparticle flux. For $\phi_{nano} > \phi_{nano}^{*}$, Ψ_6 is suboptimum but remains high as previously discussed. At

very high ϕ_{nano}, for all ϕ_{micro}, (not shown) depletion results and the resulting gel cannot be convectively deposited uniformly.

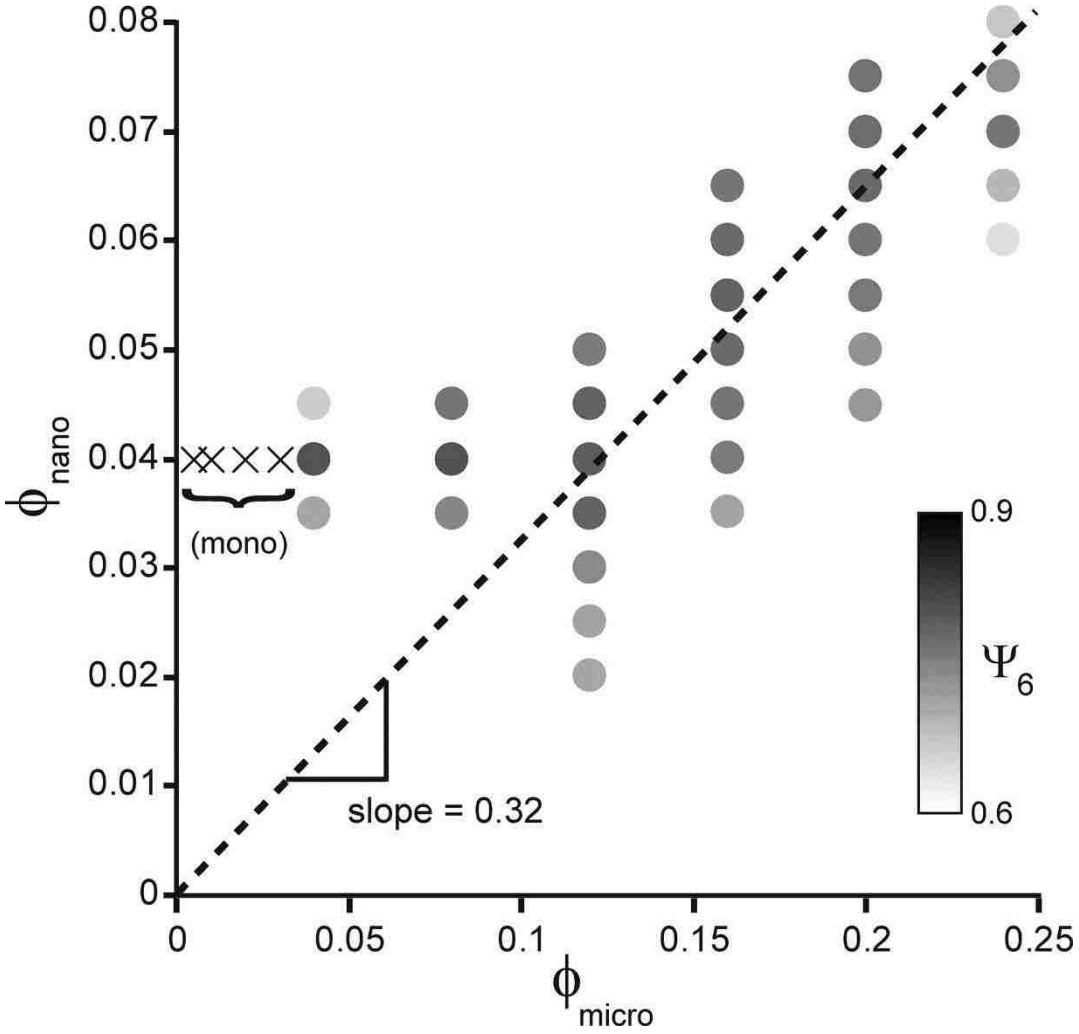

Figure 3.7: ϕ_{nano} vs ϕ_{micro} where each datum is shaded by its relative Ψ_6. Darker points are more crystalline. X's indicate monolayer depositions at low ϕ_{micro} where monolayer regions are too short for robust crystallinity analysis. The dashed line, from Equation 3.4, predicts the concentration ratio when constituent deposition fluxes are matched.

Thus far this discussion has focused on tuning ϕ_{nano} for a given ϕ_{micro}. Likewise, for a given ϕ_{nano} and deposition rate, changing ϕ_{micro} alters the surface morphology. Figure 3.8 shows SEM images of long-range morphology and short-range microstructure for $\phi_{nano} = \phi_{nano}^{*}(0.20) = 0.06$, v = 30 μm/s (v_{mono} = 30 μm/s for ϕ_{micro} = 0.20), and ϕ_{micro} = 0.04, 0.08, 0.12, 0.16, 0.20, and 0.24. From the ideal conditions shown in Figure 3.8E, decreasing ϕ_{micro} reduces ρ by forming microsphere-free patches with only small streaks of assembled nanoparticles. For ϕ_{micro} = 0.16 and 0.12, v_{mono}= 20 and 12.5 μm/s, respectively; the submonolayer formed at these relatively higher deposition speeds supports the assumption that deposition quality is dictated by microsphere size and concentration. At ϕ_{micro} = 0.24, regions of microsphere multilayers form. Monolayer regions, albeit less prolific under nonoptimal conditions, have exactly the same microstructure across these samples and thus demonstrate that the degree of microsphere burial is independent of ϕ_{micro}.

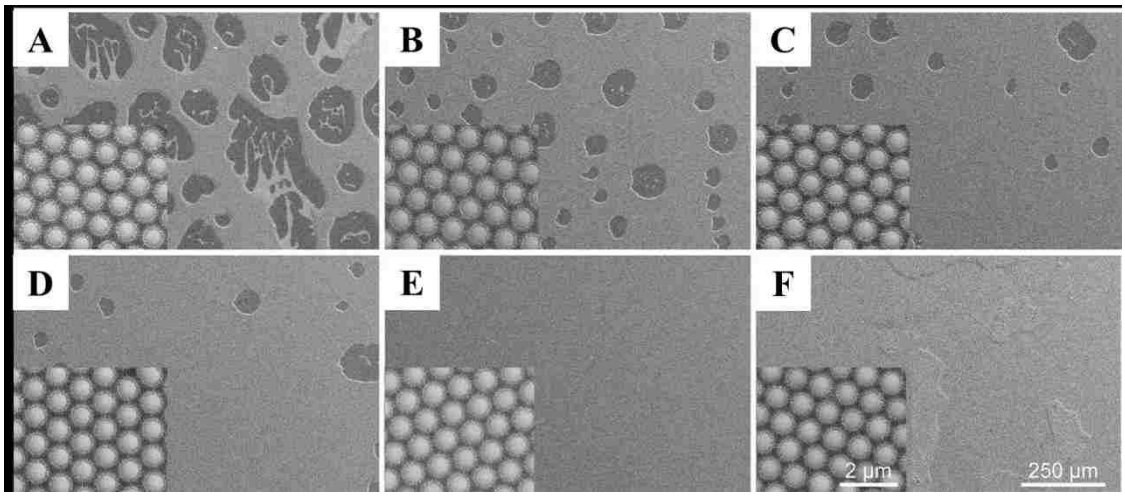

Figure 3.8: SEM images of depositions with ϕ_{micro} = 0.04 (A), 0.08 (B), 0.12 (C), 0.16 (D), 0.20 (E), and 0.24 (F) at ϕ_{nano} = 0.06 and v = 30 µm/s. A well-ordered monolayer with high Ψ_6 and ρ is formed at ϕ_{micro} = 0.20, submonolayer morphologies are formed at ϕ_{micro} < 0.20, and multilayer morphologies are formed at ϕ_{micro} > 0.20. Locally, the degree of microsphere burial by nanoparticles is constant in regions of well-ordered microsphere monolayers.

3.4: Steady Convective Deposition - Conclusions and Impact

The morphology and microstructure of convectively deposited binary microsphere−nanoparticle suspensions are controlled through relative constituent fluxes, the ratio of which directly relates to the ratio of the volume fractions. The theoretical optimum nanoparticle concentration predicted is $\phi_{nano}^{*} = 0.32\phi_{micro}$, which is verified through the quantitative analysis of thin film quality with $\Psi_6$and ρ at various ϕ_{nano} and ϕ_{micro}. Experiments resulting in the deposition of well-ordered microsphere monolayers from binary suspensions occur at $\phi_{nano} \approx \phi^{*}_{nano}$. With $\phi_{nano} < \phi_{nano}^{*}$, instability causes the monolayer to jump. With $\phi_{nano} > \phi_{nano}^{*}$, insufficient interstitial space for nanoparticles causes microsphere spreading and disorder, multilayer formation, or a combination of these two phenomena. Tuning ϕ_{nano} and ϕ_{micro} toward optimal monolayer deposition conditions enhances the field of convective deposition both from intellectual and application-driven standpoints. From a fundamental scientific standpoint, this work builds on the literature[15] by demonstrating a greater understanding of the role and relation of species flux during deposition in the tuning of alternate morphologies and nano- and microscale particle interactions. From an application-driven standpoint, the ability to deposit longer and more uniform layers as well as the ability to control the morphology precisely is invaluable. The reason for this enhancement is not immediately clear. In practice, the addition of nanoparticles may be considered to be a deposition aid. Limitations and questions raised with this research include the further explanation of binary suspension behavior at low ϕ_{nano} and ϕ_{micro} as well as how depositions of polydisperse suspensions will behave. We explore unary and

binary suspensions, with our binary constituents being an order of magnitude different in size. This begs the question of how ternary and higher-order suspensions would behave under deposition when intermediately sized particles do not fit within interstices and similarly how a truly large distribution of particle sizes would behave.

3.5: Low ϕ_{nano} Condition - Introduction

A follow-up study on the low ϕ_{nano} condition, as presented in Figure 3.4A, is presented. When there is a nanoparticle deficiency, binary convective deposition appears more likely to exhibit "stick-slip" motion. As the suspension "slips," it leaves behind a void space, and under some conditions the spacing of these void regions can be uniform (Figure 3.1C). It is important to note, contrasting Figure 3.1C and 3.1D, optically clear regions in these samples are of high order. In contrast, the cloudy "white" bands are submonolayer regions that exhibit void spaces. This submonolayer microstructure compromises the opalescence of the thin film. It is important to note that this macroscale banding, resulting from stick-slip motion, is composed of many small void pockets. By no means does the entire 2.54 cm wide meniscus jump millimeters on a micron-scale initiation point. Also, it is important to note that the point of matched nanoparticle and microsphere fluxes is to maximize layer uniformity and consistency. Forcing this experimental system into "non-ideal" conditions will compromise that uniformity and consistency to some degree. However, even in the midst of complex thin film morphologies and inconsistencies, these data can yield valuable understanding on the overall mechanisms at play.

3.6: Low ϕ_{nano} Condition - Experimental Results

The following study will provide insight into this low, relative, nanoparticle flux condition using optical, fluorescence, and electron microscopy. As shown previously, 20% 1 μm SiO_2 and 8% 100 nm polystyrene are in a matched flux condition that yields thin films with high packing density and crystallinity. In particular, the distribution of nanoparticles within the deposited thin film, and how that distribution correlates with void spacing, is of interest. As such, these results primarily highlight the submonolayer condition. In particular, submonolayer coatings with 20/2, 20/4, 20/6, and 20/8 relative volume fractions will be evaluated under near identical experimental conditions to the aforementioned studies. As a process enhancement, 100 nm PS were replaced with fluorescent SiO_2 nanoparticles, synthesized in-house, of comparable size. Silica nanoparticles are synthesized through a Stöber process as described previously.[28] To complement the standard ammonia-catalyzed hydrolysis reaction, SiO_2 was functionalized with (3-Aminopropyl)triethoxysilane (APTES), Isothiocyanate, then Rhodamine B.

3.6.1: 20% Microspheres / 2% Nanoparticles (v/v)

Firstly, the lowest relative nanoparticle flux condition, 20% 1μm SiO_2, 2% 100 nm fluorescent SiO_2, is presented. Under this submonolayer condition, scanning electron microscopy demonstrates clear evidence of void-space banding (Figure 3.9). Here, bands of larger void spaces separate regions of higher order and particle density.

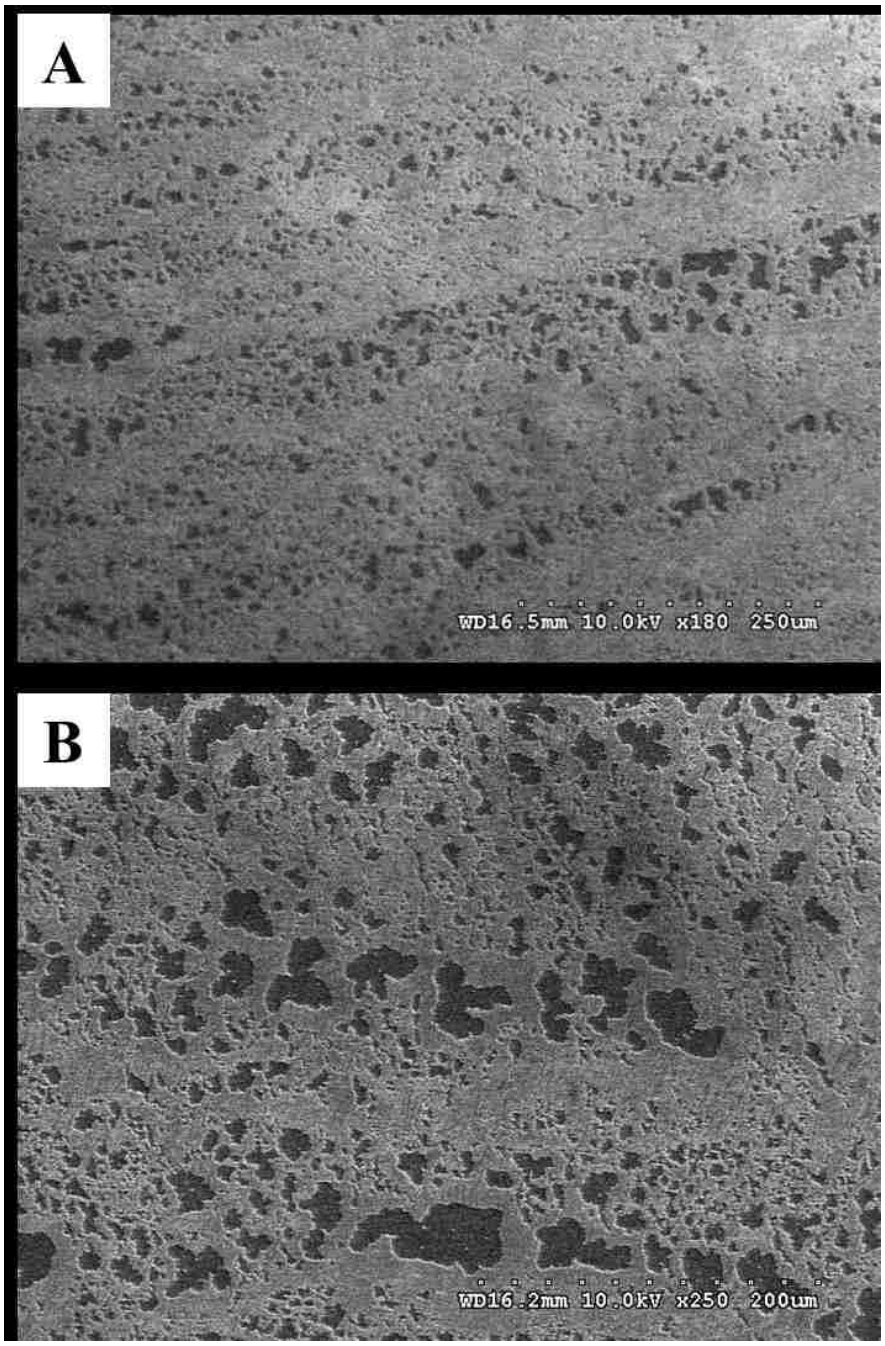

Figure 3.9: Scanning electron microscopy (SEM) images of convectively deposited thin films from a 20% (v/v) 1 μm SiO_2, 2% 100 nm SiO_2 suspension. This coating was deposited at 67 μm/sec in order to force the thin film into the submonolayer regime. Note the clear banding of void spaces at (A) 180x and (B) 250x. These void spaces are attributed to stick-slip motion of the deposition

Having observed gross void spacing banding, indicating the suspension "slipping" or jumping across the substrate, it is of particular interest where nanoparticles are and are not found within these coatings. It is hypothesized that nanoparticles, acting as a packing aid, are depleted in the deposition process. Under a relative nanoparticle concentration threshold, the suspension is more likely to "slip" and form these void bands. Of course there will be some lateral movement and equilibration of nanoparticles, so this depletion will be formed in a band , rather than a series of randomly isolated voids. Next, microscale SEM microscopy data are presented to show the relative distribution and placement of nanoparticles under this low relative nanoparticle concentration condition (Figure 3.10). Note that the trailing edge to the void spaces, where the coating "slips," shows no nanoparticles, whereas the leading edge, where the coating "sticks" and redeposit, does exhibit nanoparticles. It does appear that nanoparticles are depleted at this leading edge. When the suspension begins to re-deposit, the coating exhibits size-dependent separation, with nanoparticles preferentially located at the outside edge.[29] It is also interesting to note that some isolated nanoparticles, whereas few to no microspheres, are in fact deposited within the void region.

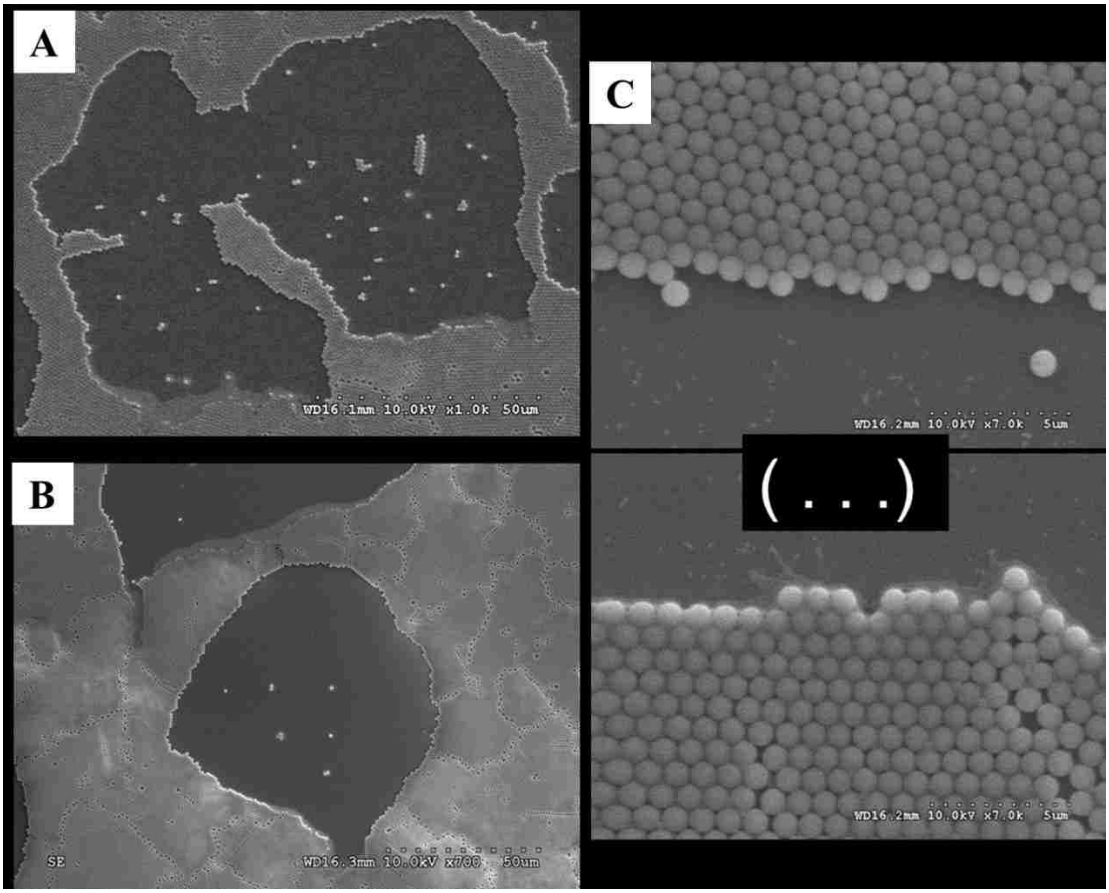

Figure 3.10: SEM Micrographs highlight the spatial distribution of nanoparticles in 20/2 convectively deposited submonolayer thin films at (A) 1000x and (B) 700x. All micrographs are deposited "down" the page. Note that the leading edge, where the coating "sticks" shows a re-distribution of nanoparticles, whereas the trailing edge, where the coating "slips" is devoid of nanoparticles. (C) The right pair of images highly the trailing (top) and leading (bottom) boundaries of a void pocket omitting the void space itself. Also, note that a small amount of nanoparticles are deposited in the "void" space, but these void spaces do not exhibit the characteristic close-packed structure of a convectively deposited particle thin film.

Figures 2.11 and 2.12 use fluorescence microscopy to highlight nanoparticle distribution in deposited thin films. Figure 3.11 shows the leading edge after a void space, but then more importantly shows the large number of microscale crystalline defects, and how closely those defects correlate with regions devoid of nanoparticles. It is enlightening to note that the line and point defects show minimal fluorescence—no nanoparticles. This supports the previous studies showing that nanoparticle addition increases thin film crystallinity. In a deficient nanoparticle condition, crystalline defects seem correlated with depleted nanoparticle regions.

Figure 3.12 shows the trailing edge of a void space, then subsequently the lateral edge of that void. Through a series of images, it becomes clear that the beginning of that void correlates strongly with a depleted nanoparticle condition. While SiO_2 microspheres are still close-packed, they appear devoid of nanoparticles. As the void progresses, and starts to close, nanoparticles begin to deposit once more. Note that the transition between a growing and shrinking void correlates exactly with the transition from unary to binary convective deposition.

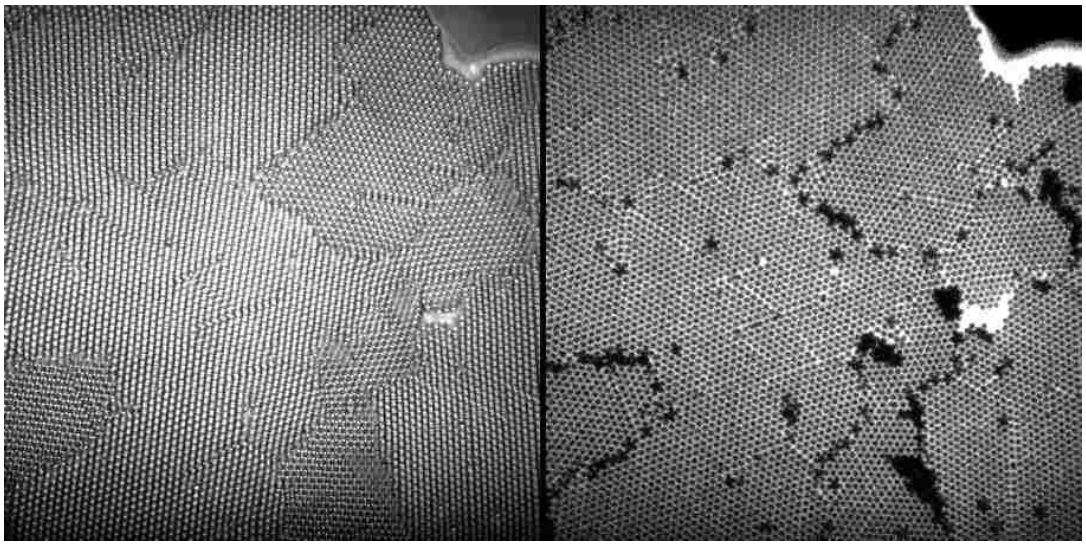

Figure 3.11: Optical (left) and fluorescence (right) micrographs highlighting nanoparticle distribution at the leading edge of a void space and in the bulk thin film. These coatings are deposited from a 20/2 suspension under submonolayer conditions. Note that nanoparticles re-deposit prior to microsphere/binary deposition. Also, note that crystalline line and point defects highly correlate with microscale depletions in nanoparticle concentration.

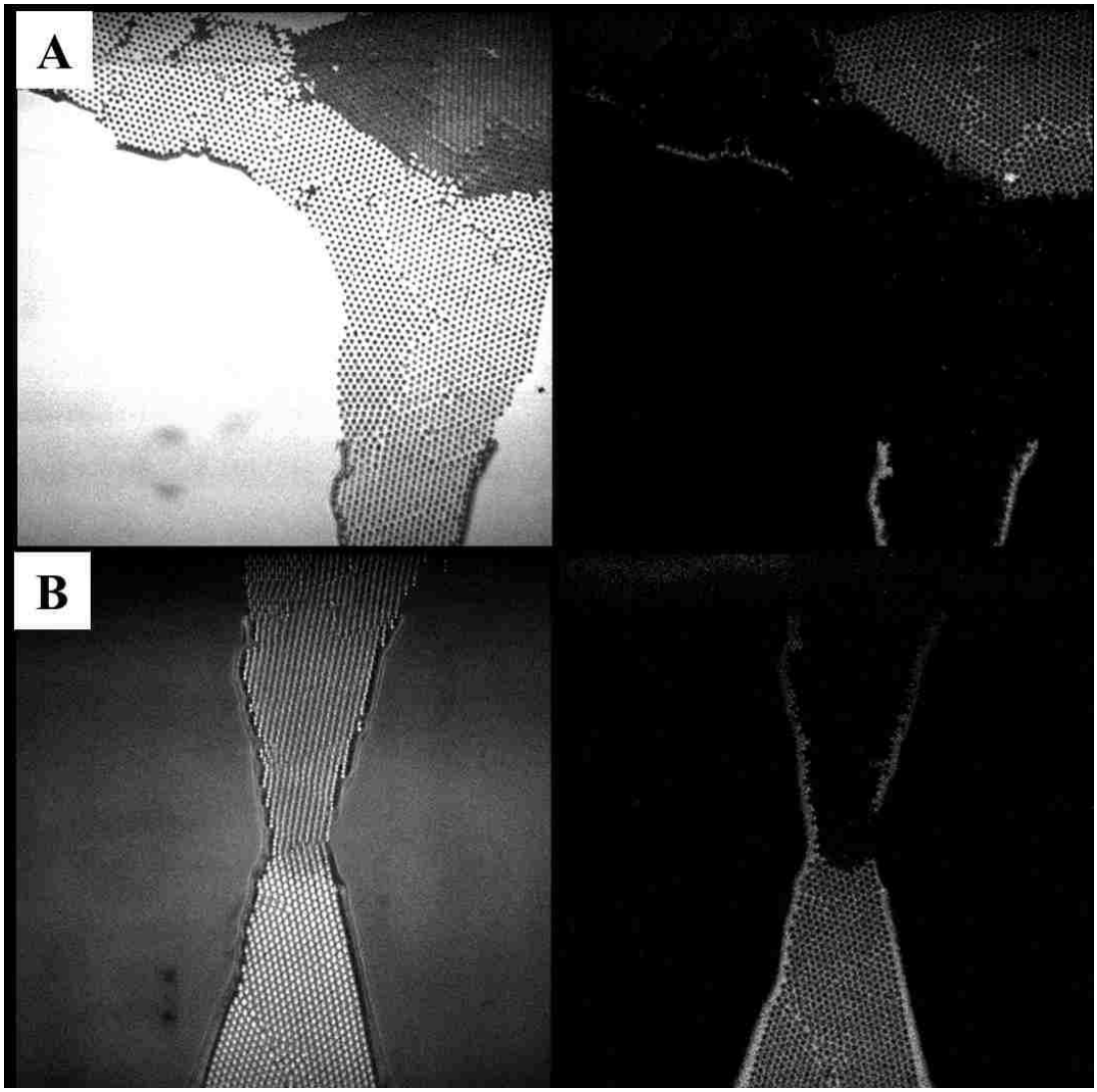

Figure 3.12: Optical (left) and fluorescence (right) micrographs highlighting nanoparticle distribution at (A) the trailing edge of a void space and (B) along the lateral edge of a void. These coatings are deposited from a 20/2 suspension under submonolayer conditions. Note that the coating is devoid of nanoparticles directly before is "slips." Along the edge of the void, nanoparticle deposition correlates strongly with the closing of the void.

3.6.2: 20% Microspheres / 4% Nanoparticles (v/v)

Having shown initial trends in nanoparticle distribution with severely depleted, 20/2 (v/v) microsphere/nanoparticle suspensions, higher suspension nanoparticle concentrations are investigated. With double the volume of nanoparticles, 20/4 depositions show significantly more nanoparticles under scanning electron microscopy (Figure 3.13). However, void spaces, and banding, share strong similarities with the 20/2 condition. The trailing edges of voids exhibit very few nanoparticles, while size-dependent separation is evident at voids' leading edges. Also, under these conditions, there are "enough" nanoparticles such that an increase in nanoparticle thin film thickness near the re-deposited microspheres in clearly evident. These data will be further supported with results at higher nanoparticle concentrations.

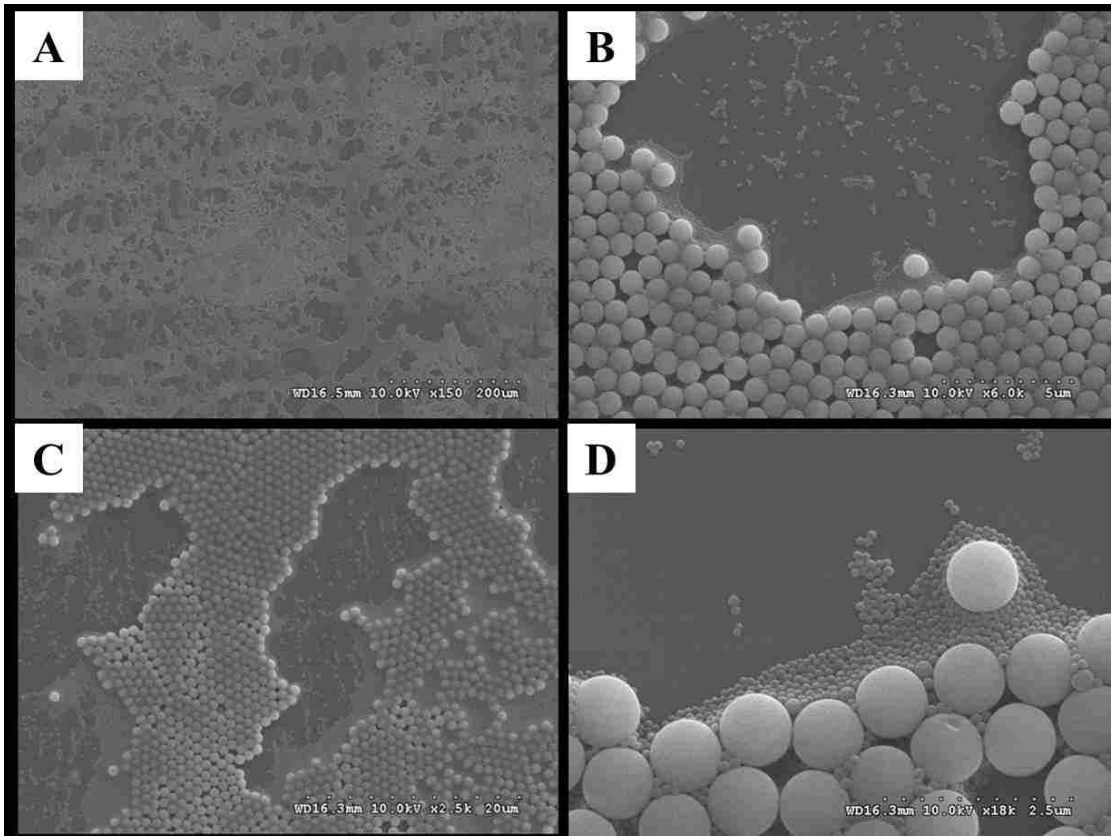

Figure 3.13: SEM micrograph of convectively deposited 20/4 microsphere/nanoparticle (v/v) suspension. (A), (C) Note the continuing macroscale clustering of void regions, where the coating "sticks" and "slips" roughly along a lateral band. Note that, again, (B) the trailing edges to void spaces have few nanoparticles, whereas (D) the leading edges show nanoparticle re-deposition ahead of microsphere or binary deposition. Also, it has become increasingly evident that nanoparticle thickness will trend upward to the re-depositing microsphere thin film.

Paired optical and fluorescence microscopy provide further insight into the 20/4 condition, and parallel the low-nanoparticle condition (Figure 3.14). Once more, gross nanoparticle deposition is evident near the leading void edge. A complex series of binary morphologies are observed post-void. Microscale crystalline defects are highlighted by nanoparticle deficiencies, with these defects especially pronounced near the trailing void edge. Also, as will continue to evidence itself with progressively higher nanoparticle conditions, immediately following size-dependent nanoparticle deposition, microspheres can be deposited alone. There appears to be a relevant timescale before complementary binary deposition has re-established.

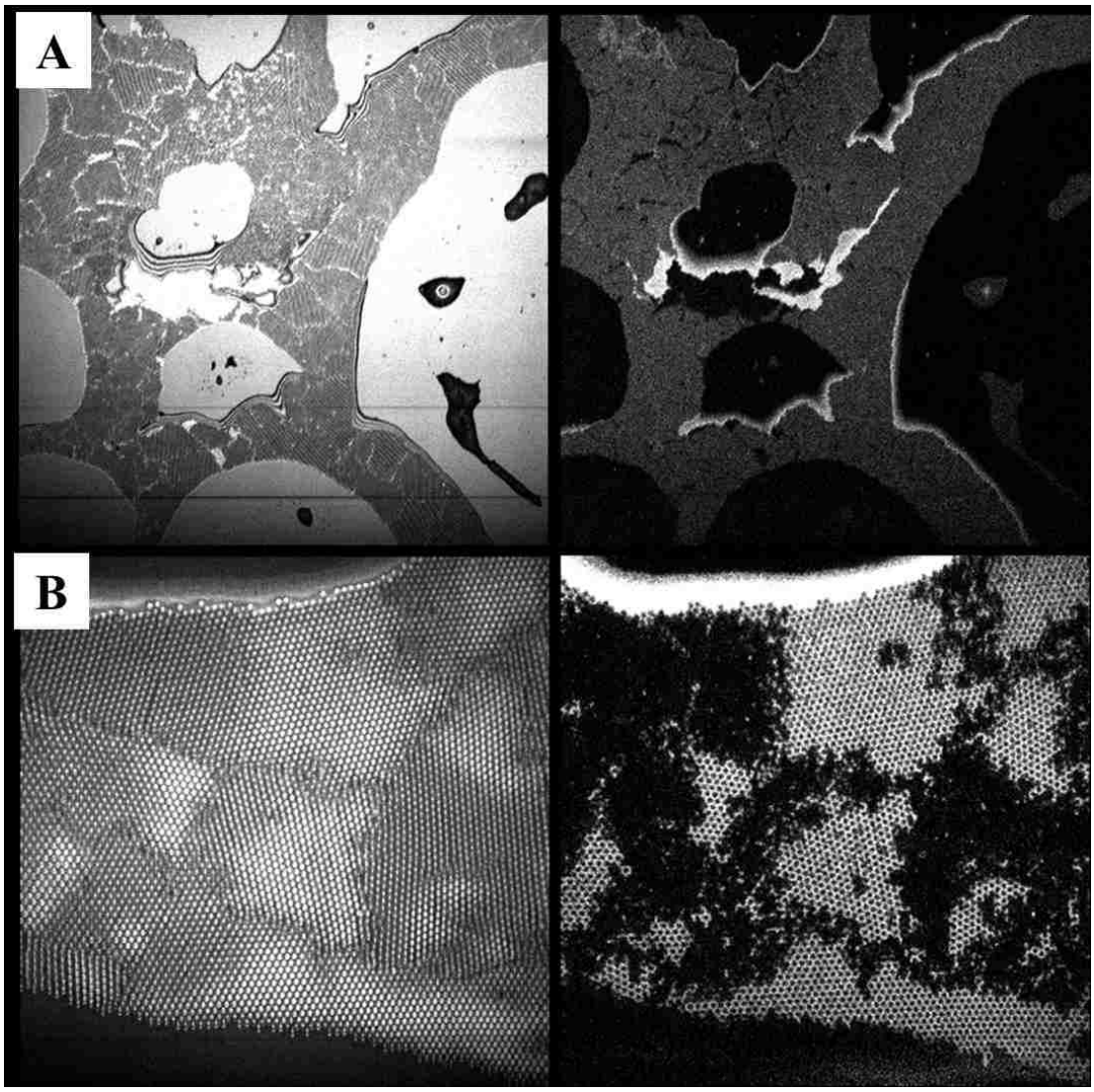

Figure 3.14: Optical (left) and fluorescence (right) micrographs highlighting nanoparticle distributions with respect to void spaces. These coatings are depositing from a 20/4 suspension under submonolayer conditions. (A) Note that the coating is devoid of nanoparticles directly before it "slips." Along the edge of the void, nanoparticle deposition correlates strongly with the closing of the void. (B) Also, in some cases, the size-dependent separation of nanoparticles near the closing of a void seems linked with nanoparticle depletion in the subsequent redeposited binary thin film.

3.6.3: 20% Microspheres / 6% Nanoparticles (v/v)

Further increasing nanoparticle concentration, the next series of experiments concern convectively deposited 20/6 binary suspensions. There is a stark transition in the morphology of the deposited submonolayer thin films with higher nanoparticle concentration. The evident void bands are now much more strongly pronounced, with individual void connected through regions of binary deposition (nanoparticles and microspheres). One can easily envision a meniscus of suspension sticking and slipping across the substrate. Voids exhibit significantly increased nanoparticle filling, though void leading edges still show a significantly higher concentration of nanoparticles relative to their trailing counterpart. Also, progressively increasing nanoparticle thin film height, leading up the re-deposition of microspheres at the leading void edge, is quite evident with higher nanoparticle concentration.

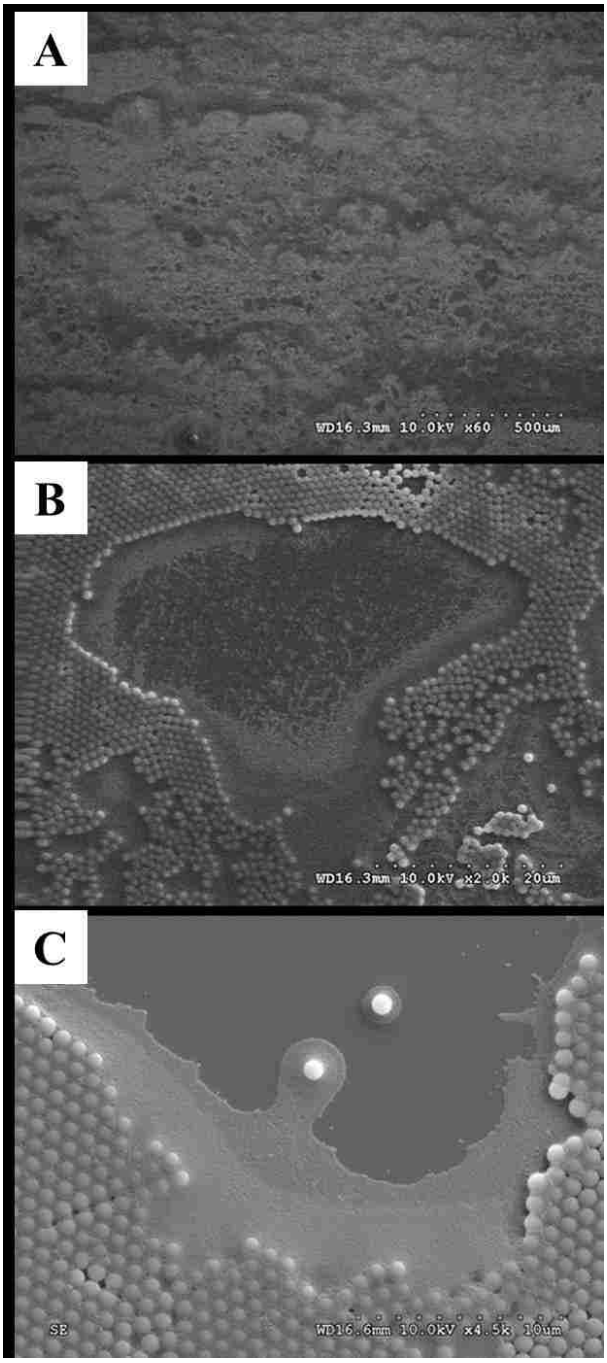

Figure 3.15: Scanning electron micrographs highlighting some features of deposited submonolayer 20/6 (v/v) microsphere/nanoparticle suspensions. Note that, in contrast to the lower nanoparticle concentration condition, (A) banding is composed of continuous, binary regions as well as contiguous void spaces. (B), (C) Voids exhibit significantly more nanoparticles, though the previously established trends remain in place.

Paired fluorescence and optimal microscopy yield less novel insight on the continuing effects of increased nanoparticle concentration, and serve primarily as an extension of previous results (Figure 3.16). At the microscale, imagery looks quite similar to lower Φ_{nano} conditions, expanding upon the aforementioned trends. At the gross scale void regions look quite similar, with larger amounts of nanoparticles near the leading than the trailing border. In addition, occasionally the same sorts of behavior to 20/4 manifests at the leading edge, where nanoparticle deposition precedes a unary deposition of microspheres. Also, as expected, there is a larger volume of nanoparticles near that leading void edge as compared with conditions under lower nanoparticle volume fractions.

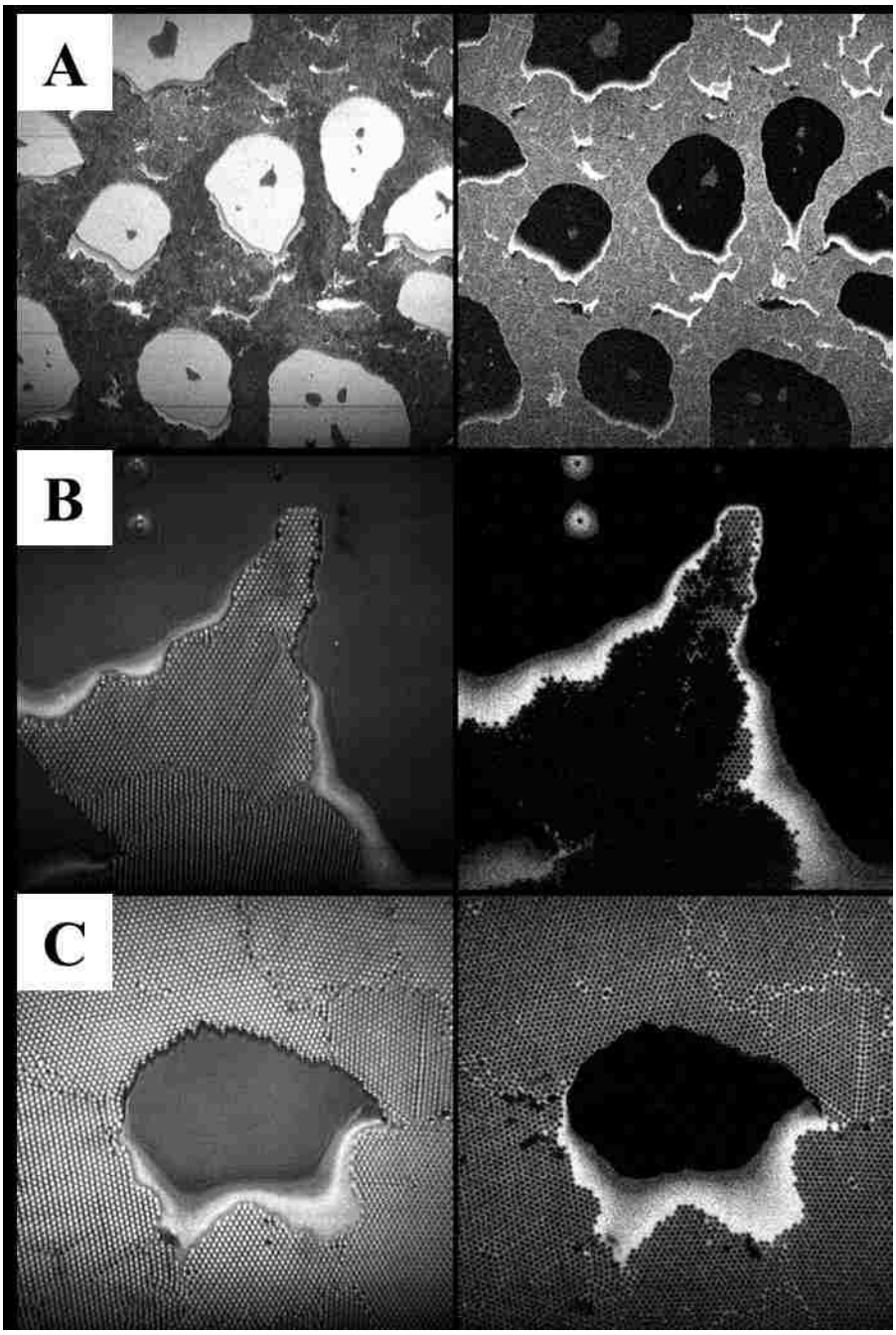

Figure 3.16: Optical (left) and fluorescent (right) micrographs of convectively deposited submonolayer thin films at 20% 1μm microspheres, 6% 100 nm nanoparticles. (A), (C) These samples expand upon the previous trends, where similar distributions of nanoparticles are seen within the voids, only to a larger degree. (B) Also, there is still some tendency for microsphere-only regions directly following unary nanoparticle buildup.

3.6.4: 20% Microspheres / 8% Nanoparticles (v/v)

Finally, for comparison, a few results are presented at the matched constituent flux condition of 20% microspheres, 8% nanoparticles (Figure 3.17). Note that these experiments are still carried out in the submonolayer regime, via increased deposition speed, for the purpose of showing the distribution of nanoparticles in void spaces. Note that, in general, void spaces show significantly more nanoparticle filling. At the gross scale, in many cases even as microspheres "slip," nanoparticles are still deposited. This begins to highly the complementary "high Φ_{nano}" condition presented in Figure 3.4. These experiments show that the aforementioned nanoparticle distribution is not purely a product of unmatched microsphere:nanoparticle fluxes.

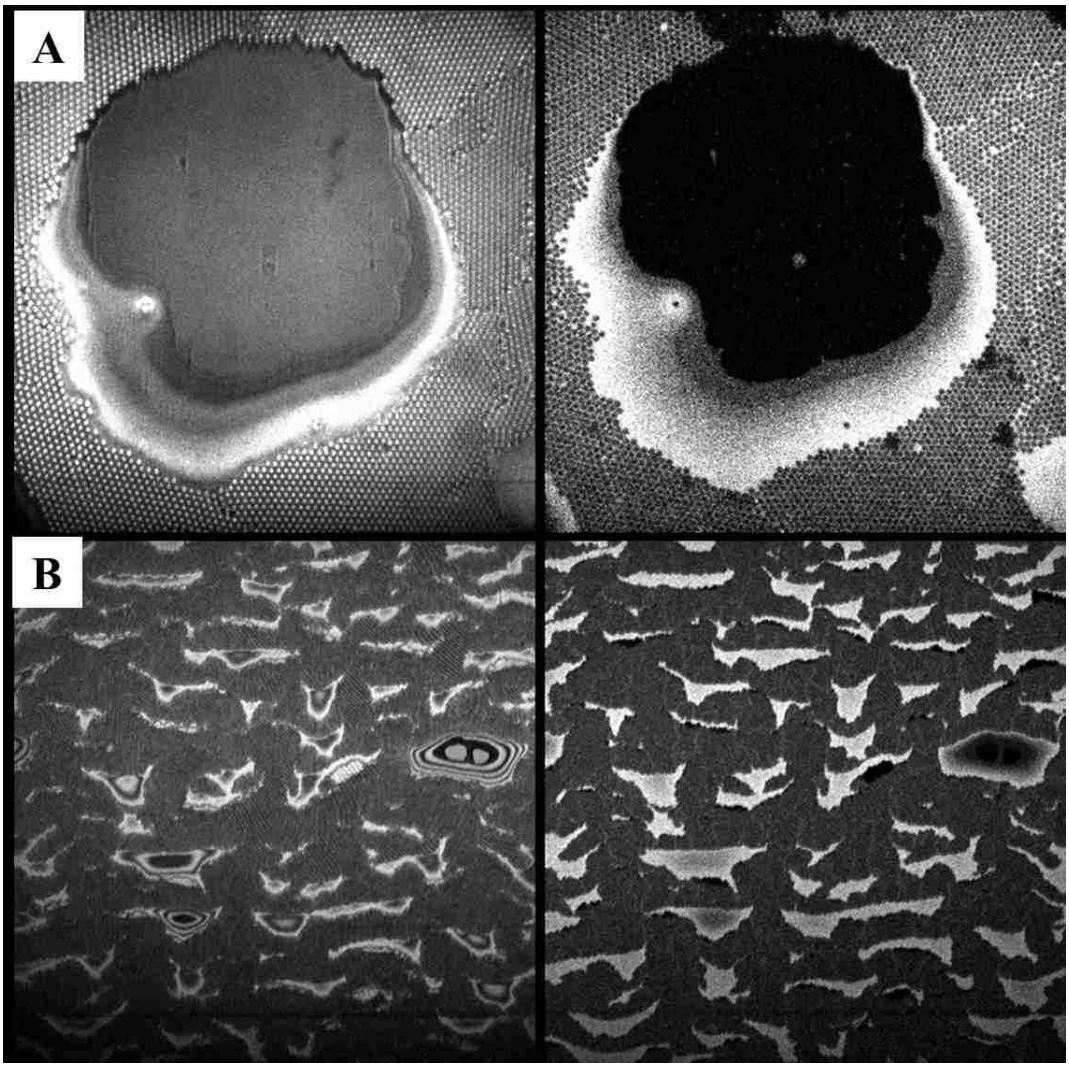

Figure 3.17: Optical (left) and fluorescent (right) micrographs of convectively deposited submonolayer thin films at 20% 1 μm microspheres, 8% 100 nm nanoparticles. (A) Here, the fluxes of each component are matched. (B) Thusly, regions void of microspheres still exhibit high concentrations of nanoparticles. In regions that are truly "void," the previous trends are still apparent, where there are significantly more nanoparticles at the leading versus the trailing void boundary.

3.7: Low ϕ_{nano} Condition – Conclusions and Impacy

These experiments expand upon the low nanoparticle condition as presented earlier in the chapter. Convective deposition is used to deposit submonolayers from suspensions with 20% 1 μm SiO_2 microspheres, 2, 4, 6, and 8% 100 nm SiO_2 nanoparticles. Note that these particles were synthesized in house and were functionalized with Rhodamine for complementary fluorescence analysis. These experiments clearly show the behavior of nanoparticles with respect to the "stick slip" motion of the coating suspension and resultant void spaces. When the suspension "slips," at the void trailing edge, there is a clear dearth of nanoparticles. As the suspension "sticks," at the leading edge of the void, nanoparticles codeposit with microspheres. Size dependent separation is apparent, and a clear growing thin film of nanoparticles precedes microsphere deposition. At the macroscale, these experiments show the formation of submonolayer "bands" of void spaces, separating regions with higher order. Finally, these results highlight further interesting conditions, including the tendency of nanoparticle re-deposition to precede the closing of void spaces and for nanoparticle re-deposition to spur on a unary microsphere deposition until the system reequilibrates and binary deposition resumes.

3.8: Enhanced Colloidal Monolayer Assembly via Vibration-Assisted Convective Deposition - Introduction

Here, a substantial enhancement of the convective deposition process is presented in the addition of periodic vibration in the direction of substrate motion. The schematic diagram, shown in Figure 3.18, is similar to that for traditional convective deposition except for the added ability to oscillate the substrate along the deposition direction (Figure 3.18). The original motivation for this work was to investigate how noise would affect convective deposition and whether vibration would thwart efforts to scale up this process in a commercial setting. Investigation into the stability of vibrating, falling, films is a classic problem.[30-32] Recent studies have used vibration to influence colloidal assembly.[33,34] Notably, work by Wei and coworkers[35] demonstrates that vibration of a monolayer of particles confined in a vertical soap film can anneal defects with a logarithmic coarsening profile; however, the time scales in this work are inappropriately long for convective deposition due to the short particle residence time in the thin film and associated scale-up limitations.

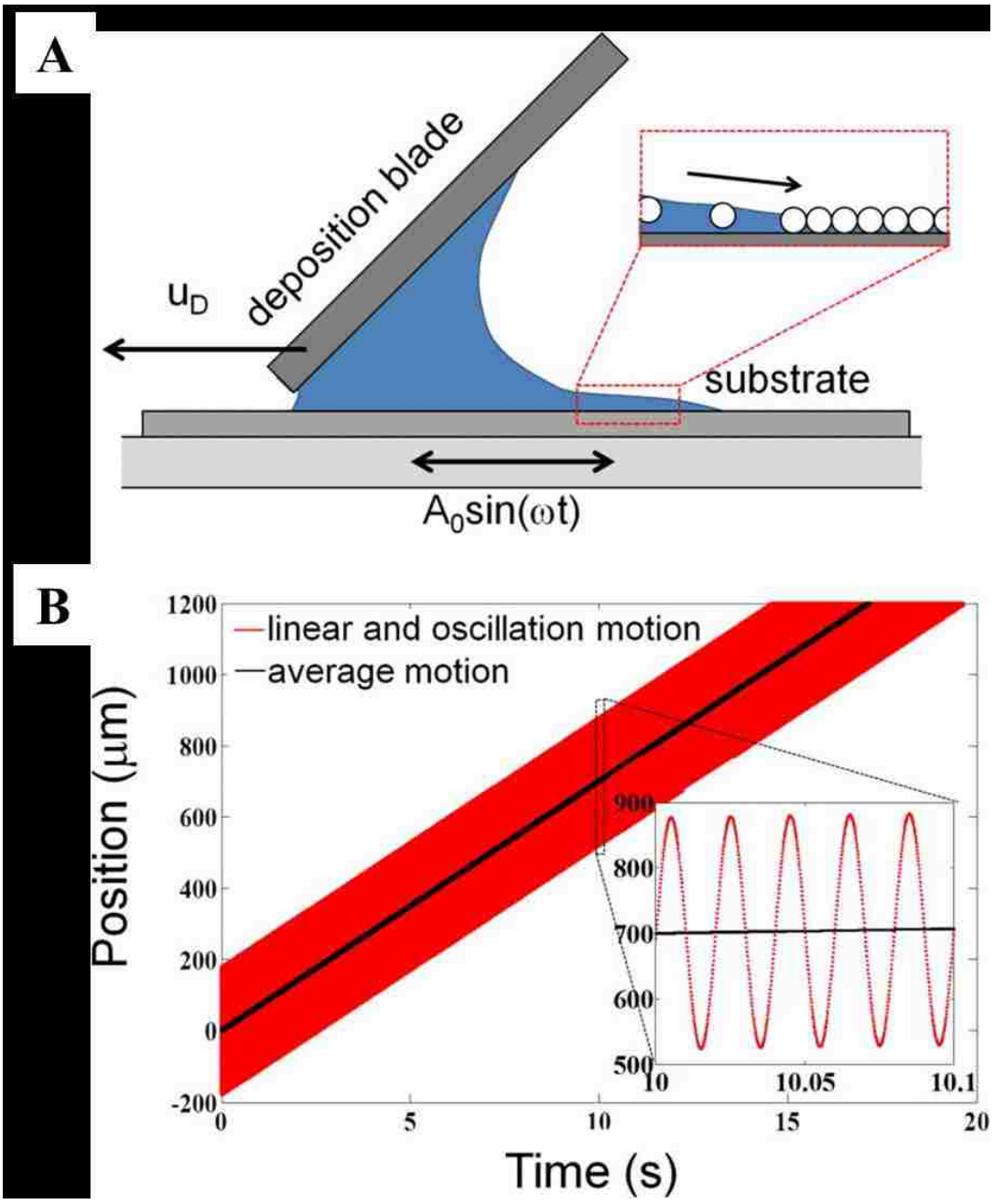

Figure 3.18: (A) Schematic diagram of experimental setup showing deposition apparatus with a substrate motion highlighted and (B) a graph of substrate motion.

The addition of vibration provides intriguing results that show enhanced convective deposition through increased viable deposition speeds, enhanced robustness of the deposition process through transition to a monolayer-deposition window, and resultant higher packing and order of deposited monolayers. These enhancements occur over a large range of vibration frequencies and amplitudes. While flow kinematics have likely evolved beyond simple explanation, phenomenological understanding of these changing properties is hypothesized.

Suspension and substrates are prepared as described in Section 3.2 and Chapter 2, respectively. This enhanced experimental setup is shown in Figure 3.18. The apparatus is contained within a humidity-controlled environment, where all experiments are performed at 20% relative humidity and 24 °C. The blade angle is set at 45° approximately 10 μm above the substrate. The motion of the substrate is controlled through a linear motor (Harvard Instruments Co. Ltd.), while a mechanical driver (PASCO SF-9324) and waveform generator (Agilent 3320A) are used to control periodic oscillation. The position of the substrate is given by $x=u_D t+A_0 \sin\omega t$, where u_D is the apparent deposition velocity of the substrate andA_0 and ω are the amplitude and frequency of vibration. The relative velocity and acceleration of the sinusoidal motion scale are $A_0\omega$ and $A_0\omega^2$, respectively.

Thin film characterization is performed as described in Chapter 2. Here, monolayers exhibit $\rho \geq 0.8$ and $\Psi_6 \geq 0.575$, while submonolayers have densities $\rho < 0.8$. Multilayer depositions are identified through direct imaging of multiple layers and increased light reflectance.

Glass substrates were coated using variable deposition velocity, $0 \leq u < 90$ μm/sec, vibration amplitude, $0 \leq A_0 < 300$ μm, and frequency $1 \leq \omega \leq 50$ Hz. Similar to traditional convective deposition (effectively where $A_0 = 0$),[36] relatively large areas are easily coated with a small amount of solution in a uniform fashion, shown on a coated glass slide, under optimum conditions (Figure 3.19A). At the macroscopic scale, three qualitative observations are apparent with even the smallest vibration amplitudes sampled ($A_0 > 10$ μm). First, the quality of coated substrates appears more uniform and over a larger area versus those coated with constant velocity convective deposition. Second, buildup of particles along coating edges and the formation of multilayer streaks in the deposition direction are minimized with the vibration frequencies sampled. Third, although not investigated thoroughly for this study, substrates of variable hydrophobicity can be coated easily. Traditionally, convective deposition is limited to highly wettable substrates. Already, vibration-assisted convective deposition has been used to coat substrates with water contact angles up to 80°, including GaN, polyethylene terephthalate, and Fluorine-doped Tin Oxide (FTO). Although these effects are not quantified, they are readily apparent when using this technique in application.

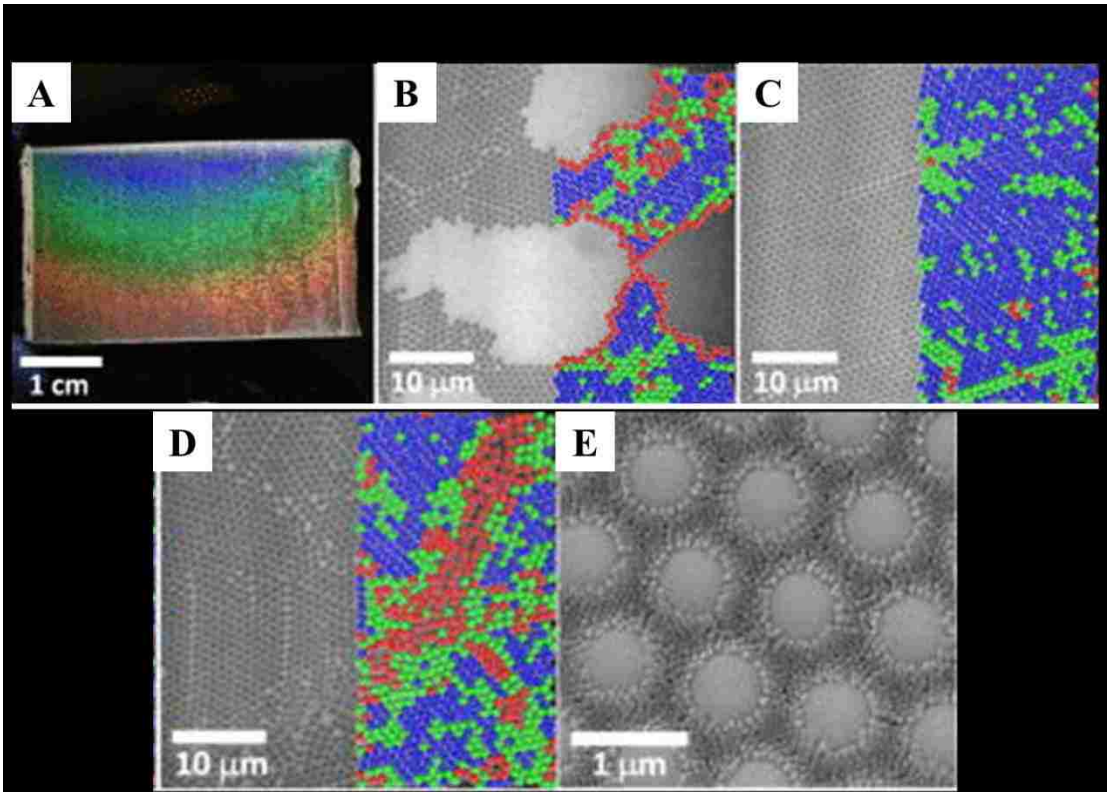

Figure 3.19: Examples of coatings at $\omega = 50$ Hz and $A_0 = 248\ \mu$m. Typical macroscopic coating using vibration-assisted convective deposition is shown in (A). The morphologies that result are submonolayer (B), monolayer (C), and multilayer depositions (D), shown as optical images partnered with analysis where blue particles are ordered, red particles have fewer than 6 nearest neighbors, and green particles have 6 nearest neighbors with asymmetric neighbor locations. SiO_2 microspheres are surrounded by and packed within polystyrene nanoparticles (E).

3.9: Enhanced Colloidal Monolayer Assembly via Vibration-Assisted Convective Deposition - Experimental Results

Similar to traditional convective deposition, three mesoscale surface morphologies are observed: particle submonolayers, monolayers, and multilayers (Figure 3.19A-2.19D). Depending on experimental conditions, samples may be comprised of a single morphology or may exhibit all three, deposited in a periodic manner in the direction of deposition. Locally, microspheres are in contact with one another and the interstitial regions between particles are filled with nanoparticles. Experimental conditions are tuned such that microspheres and nanoparticle are codeposited; neither component will be deposited alone and void spaces have neither microspheres nor nanoparticles.[36,37]

Significant enhancements resulting from the addition of vibration are exhibited in the phase diagram (Figure 3.20). Non-vibrated samples, exactly replicating traditional convective deposition, on the y-axis show that a single monolayer condition exists. The addition of vibration yields two primary effects. First, for all A_0 sampled, the monolayer deposition speed is increased. It can be interpreted that the effective length, l, of the thin film is increased similar to that seen in laterally vibrated evaporating droplets of water, where the evaporation is enhanced near the contact line. Second, there is a wide monolayer deposition range of conditions. For $\omega = 1$ Hz, a small region spanning less than 10 μm/s results in monolayer coatings near 20 μm; at high amplitude, no long range monolayer deposition condition exists. At $\omega = 10$ Hz, results are similar to $\omega = 1$ Hz, but the range of monolayer deposition rates is roughly twice as large. For

higher frequencies, the range of conditions resulting in monolayer depositions increases drastically and is no longer limited to small amplitude vibration. With $\omega = 20\,\text{Hz}$ and $\omega = 50\,\text{Hz}$, increases/decreases to deposition speed by as much as $\sim 50\%$ do not necessarily transition deposition conditions beyond the monolayer regime, suggesting the mode of deposition has drastically changed.

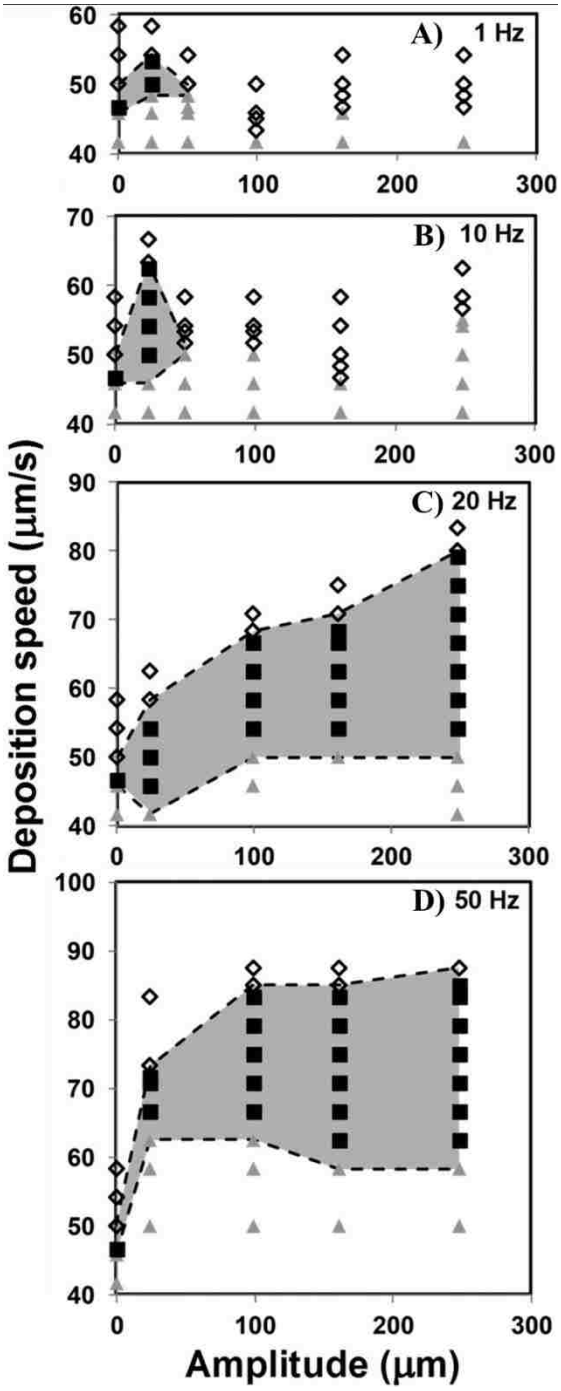

Figure 3.20: Phase diagrams show the resulting morphology as a function of changing amplitude, A_0, and deposition speed for $\omega = 1$, 10, 20, and 50 Hz. Open diamonds represent submonolayer deposition, black squares are monolayer conditions, and grey triangles are multilayer depositions. The operating conditions for monolayer deposition are shaded in grey to guide the eye.

Through dimensional analysis, one can consider the relative effects of inertia, surface tension, and viscosity. The Reynolds number, $Re=\rho uL/\mu$, relating inertial to viscous forces increases roughly 100-fold with vibration addition. However, it is still no more than $O(10^{-2})$ and thus is far below instability conditions for thin film flow. The capillary number, $Ca=\mu u/\gamma$, relating viscous to surface force also increases by roughly 100-fold; however, it also remains extremely small at $O(10^{-4})$. The Weber number, $We=\rho A0\omega 2L2/\gamma$ is $O(10^{-3})$ when based on the millimeter scale radius of curvature of the droplet between the blade and substrate. Although drop breakup is associated with We roughly O(1), this amount of inertia is sufficient to alter the shape of a droplet. Here, the suspension interface likely deforms due to lateral acceleration. This deformation would create pressure variations within the thin film that significantly alter the flow profile. Particles sliding over the substrate may sustain lubrication with respect to the substrate, increasing the time which they can assemble before being brought into contact with the substrate through capillary force.

The two-dimensional packing density and local order in monolayer depositions are enhanced by vibration as well. Figure 3.21 shows compiled microstructural analyses. There is little variation in sample quality within the monolayer regime. In all samples, this vibration-induced reduction of deposition speed sensitivity results in smaller error bars. Particles likely have more relative time within the thin film to assemble before capillary forces pin the particles to the substrate. Further investigation is necessary to determine the specific changes in self-assembly within the thin film.

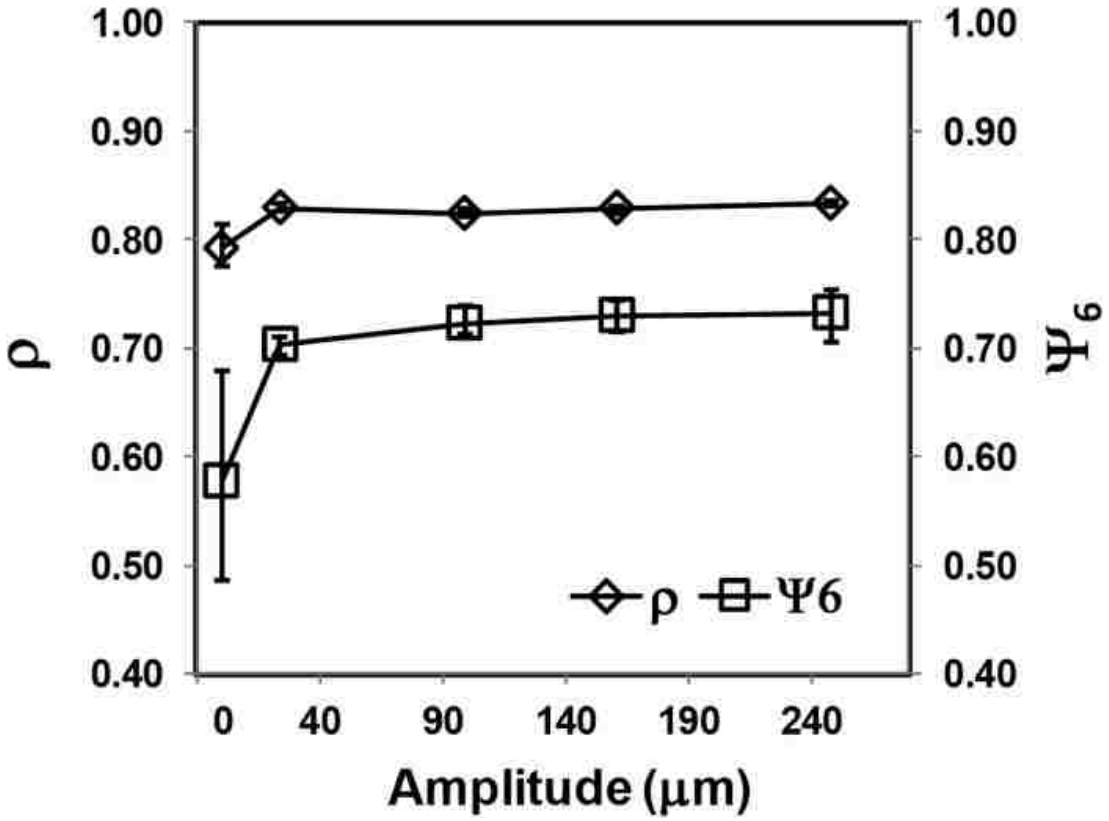

Figure 3.21: Surface density, ρ, and local order parameter, Ψ_6, as a function of vibration amplitude for $\omega = 50$ Hz. Surface density and order increase as compared to traditional convective deposition, $A_0 = 0$, and smaller error bars indicate less variability between samples.

3.10: Enhanced Colloidal Monolayer Assembly via Vibration-Assisted Convective Deposition – Conclusions and Impact

We have demonstrated a significant enhancement to particle convective deposition that increases surface density and local order of monolayers, increases viable deposition rate, and reduces the sensitivity of surface morphology to deposition speed without changing particle, solvent, or surface chemistry. No previous study has shown methodology to reduce the sensitivity of deposited morphologies to deposition speed. This relatively simple alteration to traditional convective deposition may also be extended to dip coating and other systems where assembly occurs in flowing thin films.

3.11: References

1. Harris DJ, Hu H, Conrad JC, Lewis JA. Patterning colloidal films via evaporative lithography. *Phys Rev Lett*. 2007;98(14):148301-1-4.

2. Harris DJ, Lewis JA. Marangoni effects on evaporative lithographic patterning of colloidal films. *Langmuir*. 2008;24(8):3681-3685.

3. Shevchenko EV, Talapin DV, Kotov NA, O'Brien S, Murray CB. Structural diversity in binary nanoparticle superlattices. *Nature*. 2006;439:55-59.

4. Gilchrist JF, Chan AT, Weeks ER, Lewis JA. Phase behavior and 3D structure of strongly attractive microsphere-nanoparticle mixtures. *Langmuir*. 2005;21(24):11040-11047.

5. Mohraz A, Weeks ER, Lewis JA. Structure and dynamics of biphasic colloidal mixtures. *Physical Review E*. 2008;77(6):060403-1-4.

6. Glotzer SC, Solomon MJ. Anisotropy of building blocks and their assembly into complex structures. *Nature Materials*. 2007;6(8):557-562.

7. Russel WB, Saville DA, Schowalter WR. A review of: "Colloidal dispersions". *Journal of Dispersion Science and Technology*. 1989;12(3-4):381-382.

8. Snyder CE, Yake AM, Feick JD, Velegol D. Nanoscale functionalization and site-specific assembly of colloids by particle lithography. *Langmuir*. 2005;21(11):4813-4815.

9. Velev OD, Gupta S. Materials fabricated by micro- and nanoparticle assembly - the challenging path from science to engineering. *Adv Mater*. 2009;21(19):1897-1905.

10. Brewer DS, Allen J, Miller MR, et al. Mechanistic principles of colloidal crystal growth by evaporation-induced convective steering. *Langmuir*. 2008;24(23):13683-13693.

11. Ghosh M, Fan F, Stebe KJ. Spontaneous pattern formation by dip coating of colloidal suspensions on homogeneous surfaces. *Langmuir*. 2007;23(4):2180-2183.

12. Kumnorkaew P, Ee Y, Tansu N, Gilchrist JF. Investigation of the deposition of microsphere monolayers for fabrication of microlens arrays. *Langmuir*. 2008;24(21):12150-12157.

13. Yang SY, Ryu I, Kim HY, Kim JK, Jang SK, Russell TP. Nanoporous membranes with ultrahigh selectivity and flux for the filtration of viruses. *Advanced Materials*. 2006;18(6):709-712.

14. Kitaev V, Ozin GA. Self-assembled surface patterns of binary colloidal crystals. *Adv Mater*. 2003;15(1):75-78.

15. Kumnorkaew P, Gilchrist JF. Effect of nanoparticle concentration on the convective deposition of binary suspensions. *Langmuir*. 2009;25(11):6070-6075.

16. Tessier PM, Velev OD, Kalambur AT, Rabolt JF, Lenhoff AM, Kaler EW. Assembly of gold nanostructured films templated by colloidal crystals and use in surface-enhanced raman spectroscopy. *Journal of the American Chemical Society*. 2000;122(39):9554-9555.

17. Prevo BG, Fuller JC, Velev OD. Rapid deposition of gold nanoparticle films with controlled thickness and structure by convective assembly. *Chemistry of Materials*. 2005;17(1):28-35.

18. Weldon AL, Kumnorkaew PK, Wang B, Cheng XC, Gilchrist JF. Fabrication of macroporous polymeric membranes through binary convective deposition. *Acs Applied Materials & Interfaces*. 2012;4(9):4532-4540.

19. Dimitrov AS, Nagayama K. Steady-state unidirectional convective assembling of fine particles into 2-dimensional arrays. *Chemical Physics Letters*. 1995;243(5-6):462-468.

20. Jaeger HM, Nagel SR. Physics of the granular state. *Science*. 1992;255(5051):1523-1531.

21. Song C, Wang P, Makse HA. A phase diagram for jammed matter. *Nature*. 2008;453(7195):629-632.

22. Lee JA, Meng L, Norris DJ, Scriven LE, Tsapatsis M. Colloidal crystal layers of hexagonal nanoplates by convective assembly. *Langmuir*. 2006;22(12):5217-5219.

23. Snyder MA, Lee JA, Davis TM, Scriven LE, Tsapatsis M. Silica nanoparticle crystals and ordered coatings using lys-sil and a novel coating device. *Langmuir*. 2007;23(20):9924-9928.

24. Abkarian M, Nunes J, Stone HA. Colloidal crystallization and banding in a cylindrical geometry. *J Am Chem Soc*. 2004;126(19):5978-5979.

25. Ray MA, Kim H, Jia L. Dynamic self-assembly of polymer colloids to form linear patterns. *Langmuir*. 2005;21(11):4786-4789.

26. Prevo BG, Velev OD. Controlled, rapid deposition of structured coatings from micro- and nanoparticle suspensions. *Langmuir*. 2004;20(6):2099-2107.

27. Meng L, Wei H, Nagel A, Wiley BJ, Scriven LE, Norris DJ. The role of thickness transitions in convective assembly. *Nano Letters*. 2006;6(10):2249-2253.

28. Wang B, Weldon AL, Kumnorkaew P, Xu B, Gilchrist JF, Cheng X. Effect of surface nanotopography on immunoaffinity cell capture in microfluidic devices. *Langmuir*. 2011;27(17):11229-11237.

29. Yamaki M, Higo J, Nagayama K. Size-dependent separation of colloidal particles in 2-dimensional convective self-assembly. *Langmuir*. 1995;11(8):2975-2978.

30. Baikov VI, Listrov AT, Shabunina ZA. Stability of a film flowing down along an oscillating surface. *Journal of Engineering Physics*. 1982;43(6):1413-1418.

31. Bauer RJ, Vonkerczek CH. Stability of liquid-film flow down an oscillating wall. *Journal of Applied Mechanics-Transactions of the Asme*. 1991;58(1):278-282.

32. Weinstein SJ, Baumlin JM, Servant J. The propagation of surface waves in flow down an oscillating inclined plane. *Aiche Journal*. 1993;39(7):1113-1123.

33. Rudenko OV, Korobov AI, Korshak BA, Lebedev-Stepanov PV, Molchanov SP, Alfimov MV. Self-assembly of colloidal particle ensembles in an acoustic field. *Nanotechnologies in Russia*. 2010;5(7-8):469-473.

34. Alvarez M, Friend JR, Yeo LY. Surface vibration induced spatial ordering of periodic polymer patterns on a substrate. *Langmuir*. 2008;24(19):10629-10632.

35. Wei QH, Cupid DM, Wu XL. Controlled assembly of two-dimensional colloidal crystals. *Appl Phys Lett*. 2000;77(11):1641-1643.

36. Kumnorkaew P, Weldon AL, Gilchrist JF. Matching constituent fluxes for convective deposition of binary suspensions. *Langmuir*. 2010;26(4):2401-2405.

37. Kumnorkaew P, Gilchrist JF. Effect of nanoparticle concentration on the convective deposition of binary suspensions. *Langmuir*. 2009;25(11):6070-6075.

Chapter 4

Instability-Driven Streak Formation During Convective Deposition

4.1: Introduction and Background

Convective deposition is a robust and scalable technique for the fabrication of particle thin films. Ordered particle thin films have wide-ranging applications including photonics,[1-5] biological technologies,[6-9] lithography,[3,10,11] and catalysis.[12] There are a wide variety of methods available to assemble particle thin films. These include epitaxy,[13,14] spin coating,[15,16] optical tweezers,[17] and electrophoretic assembly.[18] In general, increased order and thin film crystallinity maximizes device performance. Convectively deposited particle thin films, under ideal conditions, are highly uniform. Unfortunately, instability-driven "streaking" has plagued the field since its inception. Streaks, shown in Figure 4.1, are regions of thicker particle coatings that develop in the deposition direction. Streaks occur as a result of enhanced evaporation at the edge of the film in essentially all previous studies. However, native instabilities can spur on the nucleation of three-dimensional macroscale defects throughout the film that compromise thin film uniformity. Most groups have developed techniques, namely the

addition of nanoparticles[19,20] and surfactants[21] or applied mechanical vibration,[22] for the suppression of streaking. However, there has been very little rigorous analysis on how and why streaking occurs. Greater understanding of the nature of streaking and the instabilities at play should yield greater fundamental control in convective deposition. With current efforts to scale up convective deposition and other thin film technologies, it is essential that these instabilities are suppressed for continuous uniform operation. These efforts will be critical both from a process development standpoint and with device-oriented efforts to maximize quality, repeatability, and resultant performance.

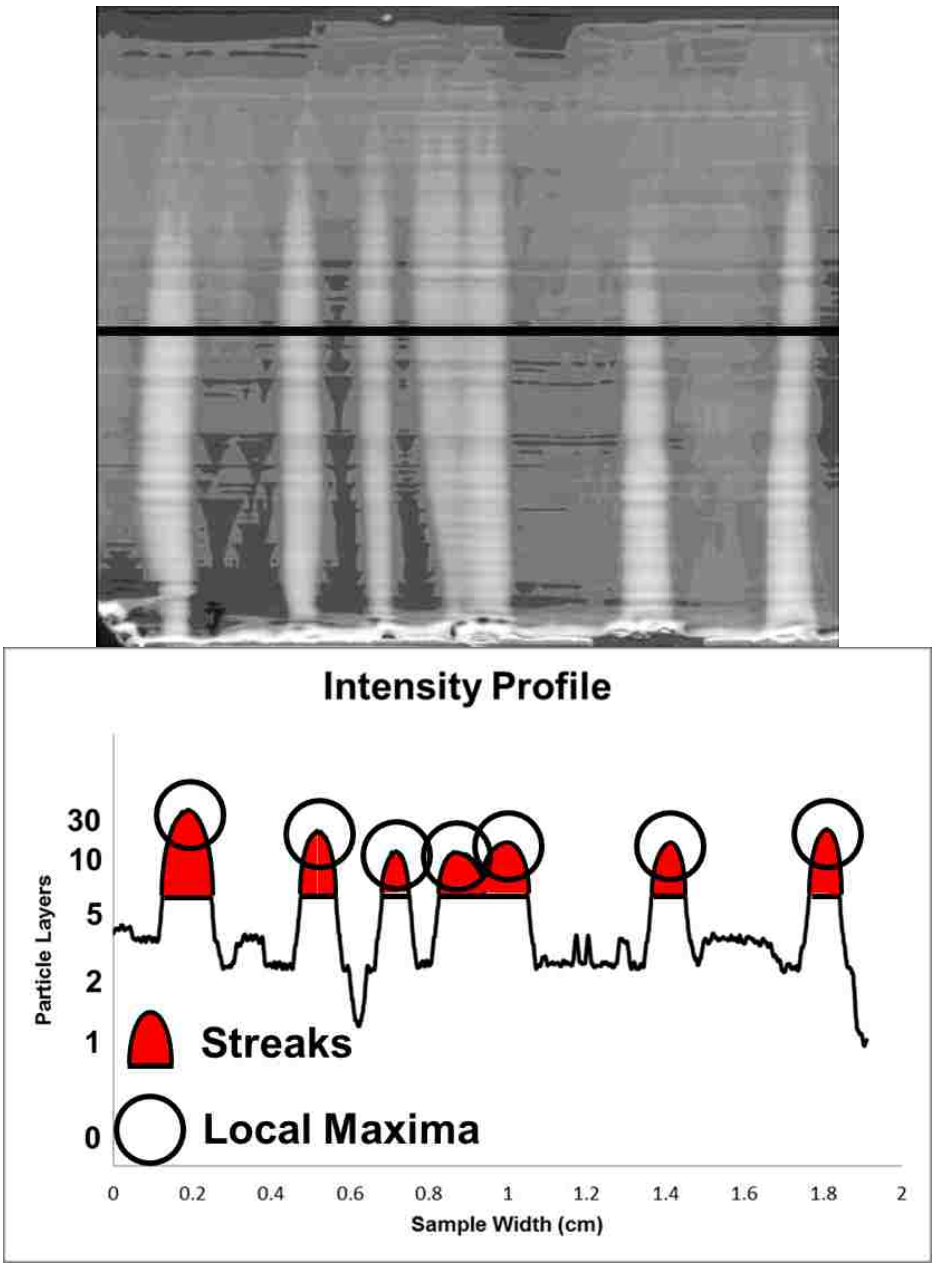

Figure 4.1: Instability-driven three-dimensional macroscale streaking can compromise thin film uniformity in convectively deposited particle coatings. These "streaks: extend in the deposition direction, and grow three-dimensionally, often to thicknesses of 30-50 particle layers. Automated image analysis can be used to characterize samples and delineate streaks from steady regions. In addition, local maxima can be used to delineate merging events. Here, a 7-particle threshold is used to identify streaks.

4.1.1: Relevant Interfacial Phenomena and Theory

A number of interfacial phenomena and instabilities such as Marangoni and contact line instabilities may be the cause of the streak formation. Marangoni instabilities and flows are driven by surface tension gradients, driving transport from regions of low to high surface tension. These surface tension gradients can be a result of compositional differences, temperature gradients, or surface characteristics. The classic example of a Marangoni flow, first characterized by James Thomson, is the tears of wine.[23] Alcohol has a lower surface tension than water. Alcohol also evaporates faster. As alcohol evaporates along the edge of a wine glass, those binary fluidic regions relatively increase in surface tension. These higher surface tension regions pull more strongly on the fluid and drive flow. As evaporation progresses, macroscale "tears" become pronounced along the thin film. In a contrasting example, Marangoni flows can be induced atop surfaces, for instance by varying surface tension via silanization.[24] These surfaces then can be used to direct droplet motion towards the higher surface tension regions. In addition, fingering-like behavior in spreading droplets.[25] These fingers grow and develop as a result of local undulations and concentration gradients that induce surface tension-driven flow.

As surface tension scales inversely with temperature, fluid will flow from high to low temperature regions. Rondelez et al., show the same fingering behavior, but in spreading fluids subjected to horizontal temperature gradients.[26,27] As expected, resulting from the surface tension gradient, fingers grow towards the cold region. Luo et al. use nanoparticles as tracking aids to study Marangoni flows in evaporating water

droplets.[28] This study closely parallels the experiments presented in this publication—Marangoni-driven fluid flow in an evaporating droplets is driven by a temperature, and corresponding surface tension, gradient.

In droplets and thin films, interfacial contact lines are prone to instabilities. These instabilities can grow and be suppressed in a complex series of fluidic feedback processes.[29] Contact line instabilities can result from Marangoni flows as well as gravitational forces. Extensive studies probe the behavior of contact lines in gravity-driven fluid flow.[30,31] In general, these studies place a droplet or thin film on an inclined plane. The droplet flows downward as a result of gravity and the three-phase contact line is analyzed. In many cases, contact line instability further develops into a series of fingers. In the vicinity of the spreading contact line, surface tension gradients can overwhelm stabilizing viscous and gravitational forces. As was briefly mentioned earlier, Marangoni flows also show contact line instabilities and fingering.[27,32,33] Thermal gradients or concentration gradients near the contact line will induce surface tension-driven flow and perturbations. Similarly to the gravitational case, fluid flows along induced thermal gradients and the corresponding three-phase contact line exhibit instabilities and perturbations. As the fluid flow profile develops, minor perturbations grow and nucleate fingering. It is important to note that fingering is an eventual and resultant behavior. Fingering "takes off" from small perturbations and instabilities that act as nucleation points in a developing feedback process.

4.1.2: Controlled Particle Assembly

In the convective deposition of particle suspensions, instabilities can be amplified through induced thermal gradients. These instabilities can nucleate macroscale defects. Most likely, it is the combination of instability and a nucleation event that creates a "streak" and comprises thin film crystallinity. This nucleation event could be a particle aggregate or a jamming event.[34] A microscale, three-dimensional, nucleation event such as this would exhibit enhanced evaporation and drive fluid flow. This, in combination with the aforementioned instabilities, could create a feedback loop and propel evolution of streaks.

Convective deposition is gaining popularity as a technique for the synthesis of crystalline particle thin films. Convective deposition uses surface tension and flow to drive particle assembly. In convective deposition, a concentrated particle suspension is dragged across a substrate and a thin film is drawn out. As the liquid phase evaporates, particles flow towards the three-phase contact line and are deposited on the substrate. Convective deposition shares very similar physics with the "coffee-ring" effect.[35-37] Evaporation is maximized at the outside of a drying droplet. Thus particles preferentially flow to the drying front and subsequently the surface. This results in dried "rings" with maximal concentration radially outward. Particles flow to the substrate due to evaporation-driven flow, then lock into a crystalline formation through capillary forces.

Dmitrov and Nakayama derive an equation describing the monolayer deposition condition based on a mass balance between the bulk and thin film regions.[38] They find that the monolayer deposition velocity is dependent on evaporative flux, J_e, particle

diameter, 2a, particle volume fraction in the bulk suspension, ϕ,[39] as well as the deposited thin film, ϕ^D, as well as a constant describing particle/surface interactions, β. $\beta \approx 1$ when particle surface interactions are strongly repulsive. This expression also assumes that the bulk suspension and advancing crystal front are of the same volume fraction.

$$v_{mono} = \frac{J_e \beta}{2a(\phi^D)} \frac{\phi}{(1-\phi)} \quad (4.1)$$

Evaporative flux induces the convection of particles to the drying front where they deposit on a surface. Evaporative flux plays an enormous role in the drying of colloidal suspensions. Purely by controlling the evaporation rate, Nagayama et al., 1992 control the number of particles that flow to a droplet edge and their surface. Using this methodology by covering their samples, thus changing local relative humidity, they tunably deposit monolayers, double layers, and trilayers.[40] In the following experiments, relative humidity is held constant. However, evaporative flux is changed by an increase in substrate and suspension temperature.

4.1.3: Theoretical Approach to Streaking Suppression and Enhancement

The following studies will tune stage temperature and withdrawal rate in order to control streaking (Figure 4.2). The probability of streaking is enhanced in thicker films. Slower withdrawal rates will yield thicker films as more particles have time to flow and pack in a given region. This changing deposition speed will mechanically tune film thickness. The number of particle layers dictated by the mechanical withdrawal rate will be related to evaporative flux and suspension characteristics. In addition, heating the substrate will enhance evaporative flux and also increase layer thickness.

Heating the substrate can also spur on recirculation and instabilities, and shows a strong ability to promote streaking. Changing stage temperature, T, as shown through the Clausius-Clapeyron relation, correlates with deposition speed. The Clausius-Clapeyron equation is used as an analog to describe the phase-transition between streaking and non-streaking morphologies. The inherent temperature component of this relation will directly affect vapor pressure in the suspension meniscus:

$$e^{-\frac{\Delta H_v}{RT}} \sim p^* \tag{4.2}$$

Increased vapor pressure in the system will turn force addition liquid into the vapor phase. Thusly the evaporative flux will increase

$$e^{-\frac{\Delta H_v}{RT}} \sim p^* \sim J_e \tag{4.3}$$

Increased evaporative flux near the three-phase contact will increase fluid and particle convective to the evaporative front. Keeping other experimental parameters static, increased particle flow into the thin film region will correlate with an increased thin film thickness, in terms of number of particle layers, n.

$$e^{-\frac{\Delta H_v}{RT}} \sim p^* \sim J_e \sim n \tag{4.4}$$

Obviously, an increased number of particle layers in the resultant coating will increase thin film height, h.

$$e^{-\frac{\Delta H_v}{RT}} \sim p^* \sim J_e \sim n \sim h \tag{4.5}$$

Finally, as previously shown, thin film thickness scales inversely with deposition speed.

$$e^{-\frac{\Delta H_v}{RT}} \sim p^* \sim J_e \sim n \sim h \sim \frac{1}{u} \tag{4.6}$$

In conclusion, the inverse of temperature, as an applied thermal gradient in these experiments, will scale will deposition speed.

$$e^{\frac{1}{T}} \sim u \tag{4.7}$$

Either increased applied thermal gradients or decreased deposition speed will increase thin film thickness. Alternatively, decreased applied thermal gradients or increased deposition speed will decreases coating thickness. This work concerns the application of heat in order to generate thicker thin films and spur on streaking. As a control, chilled substrates never exhibit streaking.

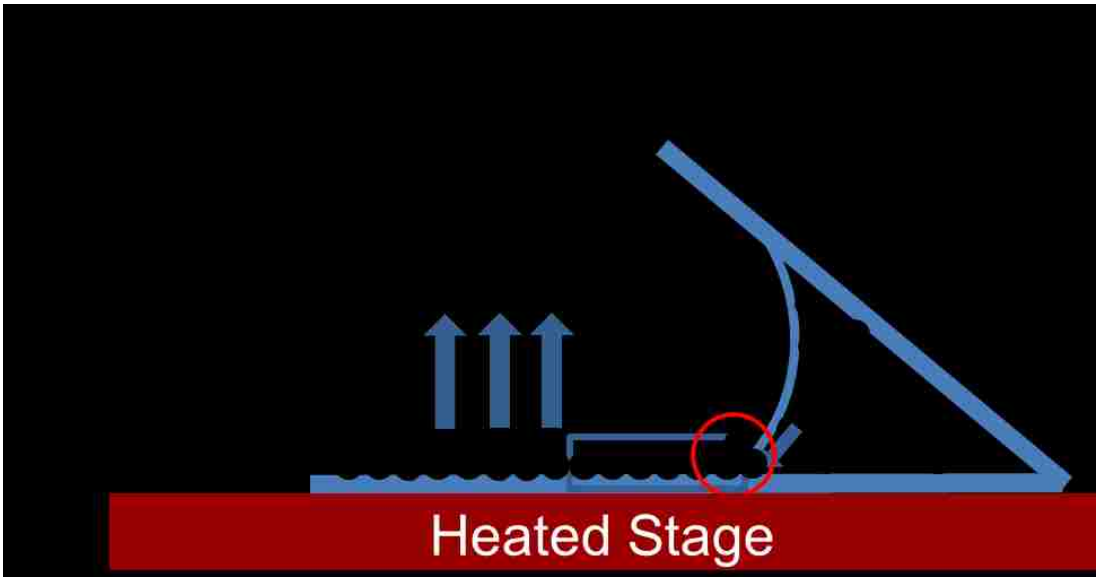

Figure 4.2: In order to tune streaking behavior, this study will vary deposition speed, or withdrawal rate, and applied thermal gradients. Withdrawal rate will mechanically tune thin film thickness and induce minor thermal gradients. Applied thermal gradients, due to a heated substrate, will change thin film thickness by increasing evaporative flux. Changing substrate temperature can induce large temperature gradients.

4.1.4: Motivation and Methodology in the Suppression of Macroscale Defects

Since Dmitrov and Nakayama's work, there have been extensive studies into convective deposition. Many of these efforts have been geared towards the maximization of thin film crystallinity and enabling relevant technologies. Initial studies used crystalline particle monolayers as microlens arrays for the enhancement of light extraction efficiency in InGaN/GaN Quantum Well Light Emitting Diodes (LEDs).[5] The addition of a microlens array of 1 μm SiO_2 is game changing in the field—these LEDs increased light output power of 219%. Within process development and fluid dynamics, changing blade angle and hydrophobicity are use a process optimization techniques in convective deposition. Using these techniques, submonolayer, monolayer, and multilayer thin films are controllably fabricated. This work also sets the stage for theoretical expansions within convective deposition—Equation 4.1 does not take these parameters into account.

Follow-up studies[19,20] show the effects of nanoparticles as a packing aid in the convective deposition of binary suspensions. The addition of nanoparticles significantly increases thin film uniformity, crystallinity, and packing—particle-layer crystallinity is maximized when microsphere and nanoparticle fluxes are matched. Additionally, nanoparticle addition completely suppresses the macroscale defects discussed in this work. More recently, the application of substrate and droplet vibration has been shown to further increase thin film quality.[22] Alternatively, suspension and deposition characteristics can be optimized to deposit varying complex morphologies including transverse striping.[20,41] Expanding upon these techniques, enhanced convective

deposition techniques have found use in wide-ranging applications including the fabrication of macroporous polymer membranes,[7] immunoaffinity cell capture devices,[6] and dye-sensitized solar cells.

4.2: Materials and Methods

4.2.1: Suspension Preparation

The colloidal silica suspension and substrates used in these experiments are prepared as detailed in Chapter 2. Samples are dispersed using a sonic dismembrator immediately prior to deposition so as to minimize aggregates in suspension.

4.2.2: Thermally-Controlled Stage

Convective deposition is performed atop a thermally-controlled stage in order to control the prevalence of streaking. A 6.5cm diameter anodized Aluminum disk is placed atop a Lin Kam TH600 the thermocouple-heated microscope stage. This stage is used to control glass coverslip temperature from 22-37°C. The Aluminum stage was fabricated on-campus, and anodization was performance by Hillock Anodizing (Philadelphia, PA). Stage temperature is monitored using a Fluke 62 Max+ IR thermometer calibrated for the anodized aluminum surface. For experiments requiring a chilled substrate, ice water was pumped through the temperature-controlled microscope stage using a KD Scientific double syringe pump. Alternatively, experiments were performed with the glass substrate atop a large, chilled, thermally-conductive platform.

4.2.3: Convective Deposition

The experimental setup for convective deposition parallels that described in Chapter 2, with the notable addition of a stage to apply thermal-gradients to the substrate.[5] Experiments were performed at 22°C ambient temperature and ~10% relative humidity. The deposition blade is fixed at an angle of 30° with respect to the

substrate. Batch experiments were carried out with 10 µl suspension. This blade angle is directly observed using a digital camera (Dinolite AM311S).

4.2.4: Novel Streaking Image Analysis Technique

Proper analysis of instability-driven streaking necessitated the development of a novel characterization technique. Upon fabrication, samples were optically scanned at 7200 dpi using an Epson Stylus CX3810 scanner. To provide maximal contrast versus deposited SiO_2 particles, thin films were scanned, feature-side down, with a blacked out room as the background. This technique allows an exacting intensity calibration that can be used to delineate regions of varying thickness throughout the sample (Figure 4.3). Resultant scanned images were evaluated using automated image analysis in MATLAB. Note that edge effects, where dramatically enhanced evaporative flux leads to streak-like behavior, and injection nonuniformities, were removed. Samples were analyzed throughout their length, and data at ¼, ½, and ¾ sample length are reported here in order to show streak progression.

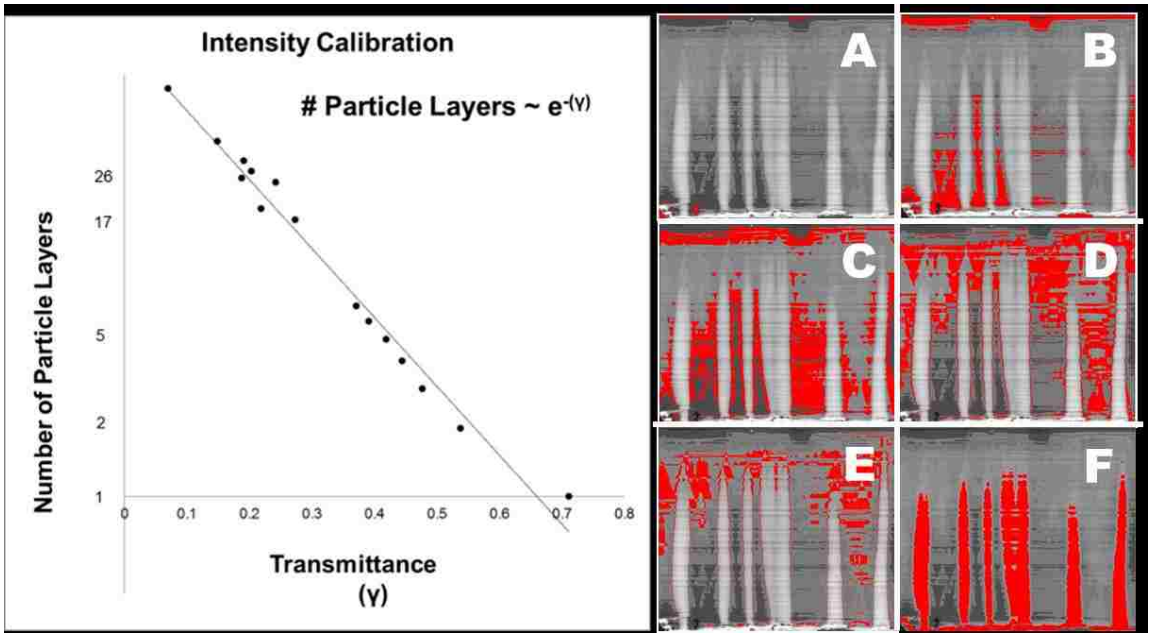

Figure 4.3: These robust image scanning and analysis techniques give particle-layer resolution. (Left) This intensity calibration curve shows the strong power law relation between transmittance through a given sample and number of particle layers (as verified through confocal microscopy). (Right) Here, a given sample is presented with Bare Glass regions (A), then monolayer (B), double layer (C), triple layer (D), four layer regions (E) highlighted. “Streaks” are defined as 7+ particle layers (F) in this study.

4.2.5: Novel Streaking Image Analysis Technique - Streaks vs. Local Maxima

Using automated image analysis in MATLAB, streak onset, prevalence, and size are characterized throughout each sample. 30-pixel (~100 μm) horizontal bands are analyzed. Across these line profiles, streaking is quantified through a pair of parameters—streaks and local maxima (Figure 4.1). "Streaks" are defined as any event crossing the 7-particle layers threshold. "Local Maxima" occur within a streak, particularly where streaks are merging, and refer to each peak within that sustained "streak."

4.3: Results and Discussion

There are multiple macroscale defects that can characterize convectively deposited particle thin films. To be clear, this work concerns the onset, prevalence, and behavior of three-dimensional streaks that grow and evolve in the deposition direction. These streaks, by rough analysis via confocal microscopy, reach a steady-state thickness of around 30-50 particle layers. It should be noted that streaks are macroscale defects, and visible optically. This study does not concern the prevalence of irregularities in the crystalline structure such as line and point defects.

Alternatively, samples can also be characterized by "striping" parallel to the dragging meniscus, transverse to the deposition direction. Striping stems from contact line depinning, "stick-slip" motion, as the suspension meniscus is dragged across the substrate[36,42,43]. Striping does not heavily influence the onset and progression of streaks and will not be further discussed here.

Marangoni instabilities share strong parallels with the streaking behavior seen in particle thin films as synthesized via convective deposition. Hosoi and Bush,[44] as well as Fanton and Cazabat,[45] find Marangoni wavelengths on the order of a millimeter. Their systems are dissimilar, both from one another and this convective deposition setup, but show global characteristics due to the nature of the instability. The imaging techniques presented here show resultant behavior, after the drying process is complete. That being said, changing thin film thickness can give some clues as to what sorts of fluidic behavior took place. Particles, suspended within the liquid phase, will be drawn into the thin film via evaporation-induced convection. Any rolls and periodicity to this

fluidic intermediary region will cause a gradient in particle deposition as there will be more particles in the "thicker" regions. It is important to note that it is in this thin film region, most likely, that micro and macroscale defects arise. There are extremely powerful forces at play in the thin film region. Capillary forces, quite strong as the liquid phase evaporates, will lock particles together in crystalline structures for energy minimization—as the thin film decreases in height the extremity of this thermal gradient will be maximized.

4.3.1: Streak Formation Mechanism

The cartoon presented in Figure 4.4 highlights progressions within the streak formation process. A uniform deposition under native conditions (Figure 4.4A) is subject to high wavelength instability (Figure 4.4B). This thin film exhibits enhancement evaporation and particle deposition in the vicinity of these three-dimensional nonuniformities (Figure 4.4C)—streaks nucleate and develop at these points (Figure 4.4D).

Paralleling Figure 4B, near the beginning of the deposited thin film there is evidence of high-wavelength instability in the 3-5 particle-layer range (not shown). These nucleation points quickly grow spatially while maintaining their thickness. These nucleation points, hypothesized as forensic evidence of instability within the thin film, also exhibit a wavelength ~1 mm. Keep in mind that this evidence of instability is a precursor to the 7+ particle layer streaks around which the following data will be centered. This evidence supports the theory that Marangoni flows, due to surface tension/temperature gradients, may contribute to macroscale defects like streaking.

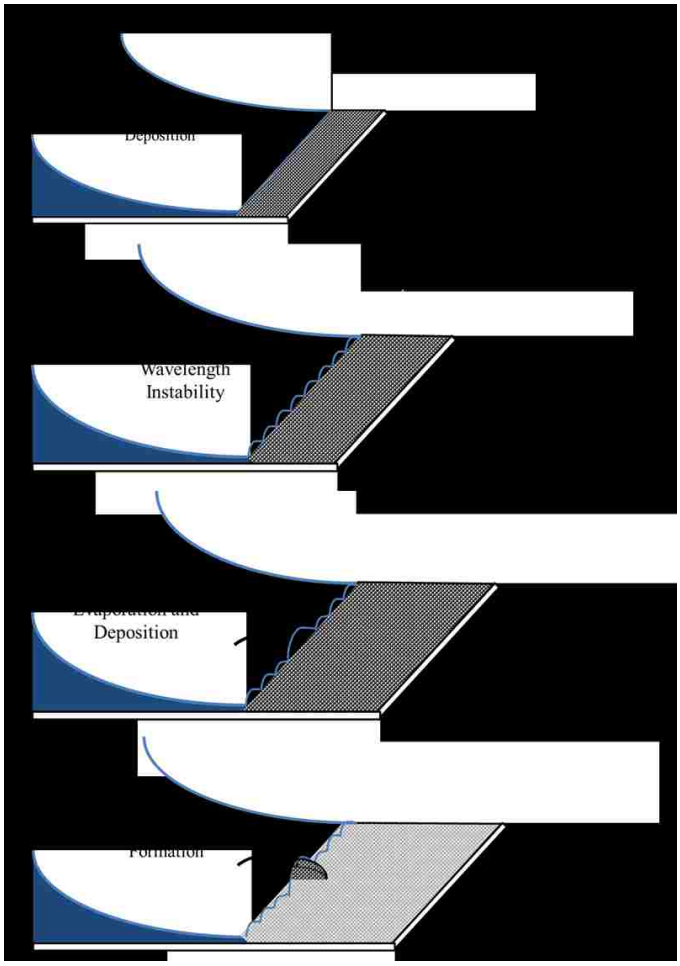

Figure 4.4: Schematic of streak formation process. (A) Base convective deposition yields uniform particle layers. (B) Native high wavelength instabilities arise. Limited forensic evidence of these instabilities (3-5 particle layers thick) is not shown. These nucleation sites have wavelength ~1 mm, which is similar to that found in representative studies on Marangoni instabilities. (C) Some instabilities will exhibit enhanced evaporation and particle deposition. (D) These three-dimensional nonuniformities initiate streak formation.

The theory surrounding these nucleation points (Figure 4.4B) is highly interesting. Looking at the above Figure, some nucleation points, resulting from high-wavelength instability, will further spur on the formation of thick macroscale "streaks." Again, streaks are defined here as regions with greater than seven particle layers. These instabilities, and fluid recirculation in the thin film region, require further initiation to form a streak. We hypothesize that this could come from some sort of jamming or suspension nonuniformity. In a jamming event, too many particles flow into the crystalline lattice and a three-dimensional feature forms. Alternatively, insufficient sonication, yielding a particle aggregate, or the presence of a dimer or trimer could yield a similar three-dimensional aberration, Such a feature will exhibit enhanced evaporative flux versus a planar crystal. As this feature presents itself, enhanced evaporation will cause a feedback loop. This enhanced evaporative flux will draw additional particles, which will further drive evaporation. This aberration, continuing to grow, will quickly develop into a streak. These sorts of jamming phenomena would be enhanced by increasing thin film thickness and recirculation.

4.3.2: Streak Onset

Figure 4.5 presents a phase diagram that demonstrates gross control over streak onset and prevalence with varying deposition speed and applied thermal gradient. These experiments characterize streaking after moderate development, in space and time, one quarter of the way through the sample length. Under ambient conditions, $\Delta T = 0^{\circ}C$, and with small applied thermal gradients $\Delta T = 4^{\circ}C$ and $7^{\circ}C$, deposition speed provides extensive control over streaking behavior. At faster speeds, with thinnest particle

coatings, streaking is suppressed. At slower speeds, with thinner particle coatings, streaks are increasingly prevalent. There is a clear transition from a suppression of streaking, to streaking with low wavelength, $\lambda_{Streak} > 5$ mm, to streaking with higher wavelength, $\lambda_{Streak} < 5$ mm. Also, at moderate temperature, the onset of streaking roughly follows an empirically optimized Clausius-Clapeyron trend.

In contrast, at high temperatures, $\Delta T = 10$, 12, and 15ºC within the speeds analyzed, there are no conditions where streaking is suppressed. In contrast, most conditions show highly levels of streaking, $\lambda_{Streak} < 5$ mm. It is worth noting once more that this phase diagram describes initial behavior in these samples. It describes the number of streaks at 25% of the sample length. Thus, under higher applied temperature gradients, the samples are characterized by extensive streaking immediately.

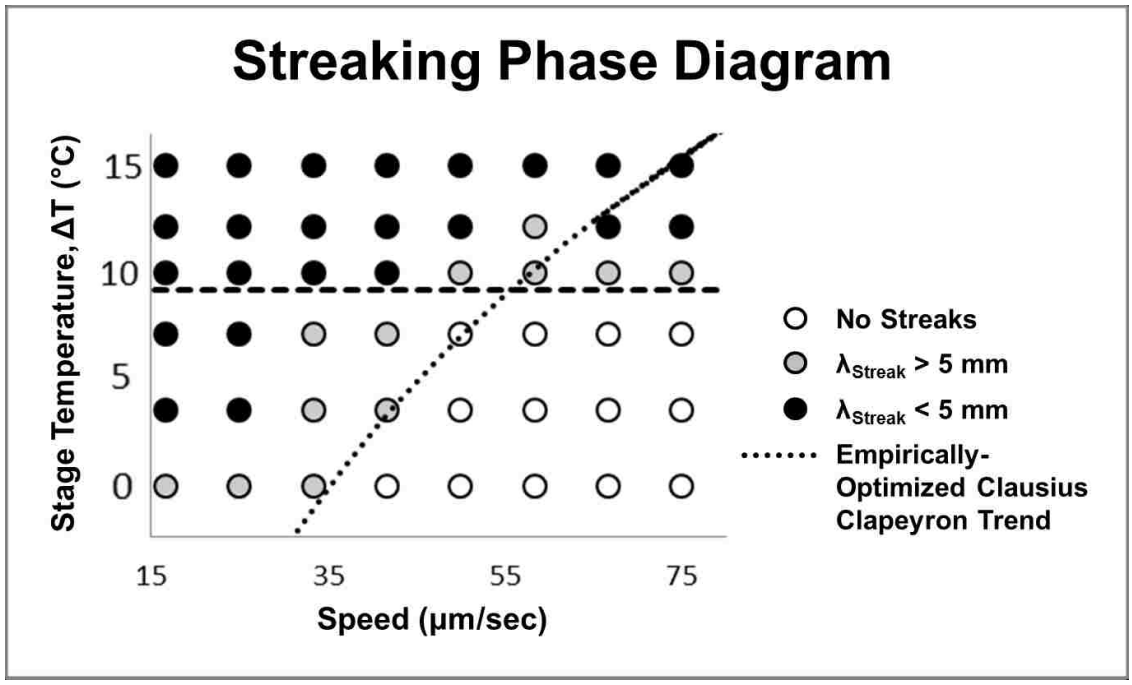

Figure 4.5: Phase diagram characterizing the existence and wavelength of streaking, λ_{Streak}, over an array of applied stage temperatures, ΔT, and deposition speeds. Conditions indicated by open circles indicate no streaking, while filled black circles indicate heavy streaking ($\lambda_{Streak} < 5$ mm). Intermediate conditions, $\lambda_{Streak} > 5$ mm, are indicated by filled grey circles. The dotted line presents a Clausius-Clapeyron fit, where $e^{\frac{1}{T}} \sim u$ (Equation 4.7) is optimized by a prefactor, that roughly parallels the No-Streaking boundary for lower temperatures. For more details see Section 4.1.3. Over the range of experimental conditions investigated, streaking could not be inhibited under greater induced thermal gradients.

4.3.3: Macroscale Defect Volume and Progression

In an effort to quantify the amount of each sample characterized by "streaking," the next series of plots present relative Streak Area, A, throughout the sample length. Streak Area, A, represents, for a particular line profile across a sample, the fraction of the sample falling above the seven-particle streaking threshold. Figure 4.6 presents, with increasing applied thermal gradients, the prevalence and evolution of streaking over a range of deposition speeds. Data are presented to show "initial" and "eventual" behavior, with data points at ¼ and ¾ sample length. Representative sample images are also provided to guide understanding.

The first row presents streaking onset, prevalence, and evolution without an applied thermal gradient. Corroborating Figure 4.5, at ¼ the sample length there is little to no streaking. However, as the samples progress, increasing area crosses the seven-particle layer threshold as "streaks." In all cases, the amount of streaking is relatively low, and none is observed at the fastest applied speeds. A small induced temperature gradient, $\Delta T = 4ºC$, shows only minor differences. In the early condition, at ¼ the sample length, increasing low amounts of streaking are seen at low deposition speeds. Throughout the sample length, a significantly higher probability of the samples exhibit streaking. That being said, the magnitude of streaking observed is fairly constant. With $\Delta T = 7ºC$, these trends become increasingly apparent, and are globally observed within the measured line profiles. Under this moderate thermal gradient, deposition speed provides a large amount of control. At faster speeds streaking is mostly suppressed. However, at slower speeds, there is a readily apparent upper bound to the streaking area

fraction that appears to evolve linearly with deposition speed. With a more amplified thermal gradient, $\Delta T = 10^{o}C$, there is a continued shift beyond that intermediary condition. The data still strongly follows the trend towards a lesser amount of streaking with increased deposition speed. However, having crossed this threshold presented in Figure 4.5, these data indicate less of an inability to suppress streaking. The curves are shifted up, indicating an increased amount of streaking across these samples. $\Delta T = 12^{o}C$ and $15^{o}C$ further these trends, and also highlight an increasing inability to suppress streaking and data scatter.

The positional analysis provides some insight regarding the kinetics and longtime behavior of instability-driven streaking in convective deposition. Samples, while depositing spatially as a growing thin film, give a record of the temporal evolution of fluid flow and instabilities quite linearly. The deposition is performed at a uniform rate. Thereby, data at any particular fraction of the total sample length will take place at the same fraction of the total time needed for deposition. Data is presented at ¼ and ¾ sample length. Under short timescales, instabilities have not had time to develop and generate streaking. However, data at ½ (not shown) and ¾ the sample length appear very similar in magnitude and behavior. Thus, this suspension volume and resultant sample length adequately describes stabilized, developed, behavior in the system. It appears that global behavior becomes constant after moderate timescales.

At low temperatures, only moderate streaking is seen, and experimental parameters yield a large amount of control of the system. That being said, with low temperatures, under the conditions evaluated, it is impossible to generate a sample

where more than 50% of the sample is characterized as a streak. Moderate temperatures give the greatest control. Changing deposition speed can wholly suppress streaking or yield samples where near 100% of sample exhibits streaking. Under high temperatures, as previously discussed, the likelihood for streaking becomes complex and less controlled.

At the highest temperatures, the data begin to look more like a scattershot with large amounts of streaking. This strongly supports the theory that thermal gradients, and resulting fluid flow, are at play in the onset and prevalence of streaking. With larger thermal gradients it is "easier" for streaks to nucleate and grow. To be clear, these increases in streak area are not due to extremely wide streaks forming—they are the result of an increasing frequency of streaks. Parallel plots examining the number of streaks under identical conditions show similar trends. In addition, identical analysis of the number of local maxima follows the same tendencies.

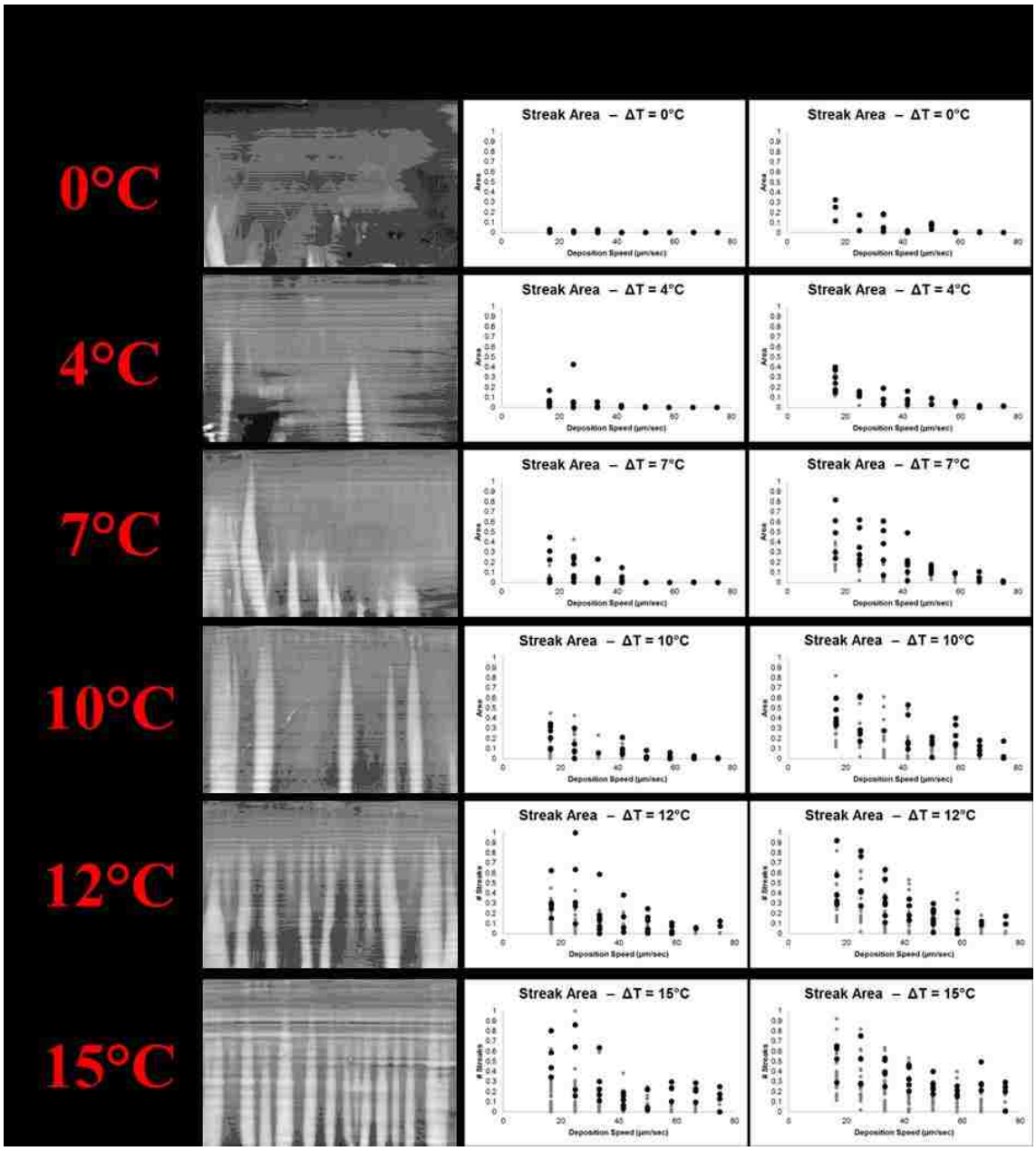

Figure 4.6: The prevalence, onset, and evolution of streaking behavior under ambient conditions and with applied thermal gradients. Data at progressively higher temperatures is overlaid on earlier data to highlight growing trends. Samples are analyzed under "initial" (¼ sample length) and "eventual" (¾ sample length) conditions. Samples were coated over a range of deposition speeds (withdrawal rates) ranging from 17 to 75 μm/sec, and $\Delta T = 0, 4, 7, 10, 12, 15°C$.

4.3.4: Characterization via Average Thin Film Thickness

Next, thin film thickness is used to glean further insight into the mechanism by which deposition speed and stage temperature affect streaking behavior (Figure 4.7). A simple mass balance based on the volume and volume fraction of suspension, as well as the size of the deposited thin film, yields an average coating thickness. This method is rudimentary, and assumes a uniform coating. As predicted, elevated stage temperature increases evaporative flux and thus thin film thickness. Also, as established, slowing the deposition speed will increase the number of particle layers. In this case, the thin film is withdrawn at a lower rate and thus more particles have the opportunity to flow to the substrate. The trendlines are empirically optimized Clausius-Clapeyron fits developed for each speed condition. The strong linearity in the effect of changing withdrawal rate is highly evident when these trendlines are scaled by their respective speeds. These curves collapse fairly strongly. It is important to note the scatter of the data under varying temperatures. While the curves collapse quite strongly, increased stage temperature yields a significant increase in the data scatter. This increase in scatter makes sense, as these thicknesses are global. They do not take into account the likelihood of a sample to exhibit streaking. However, increased temperature clearly shows an increase in the likelihood that a sample will exhibit streaking. The prevalence and behavior of streaks can throw off these rudimentary thin film thickness calculations where a uniform coating is assumed—thus the data indicates increased variability at high temperature.

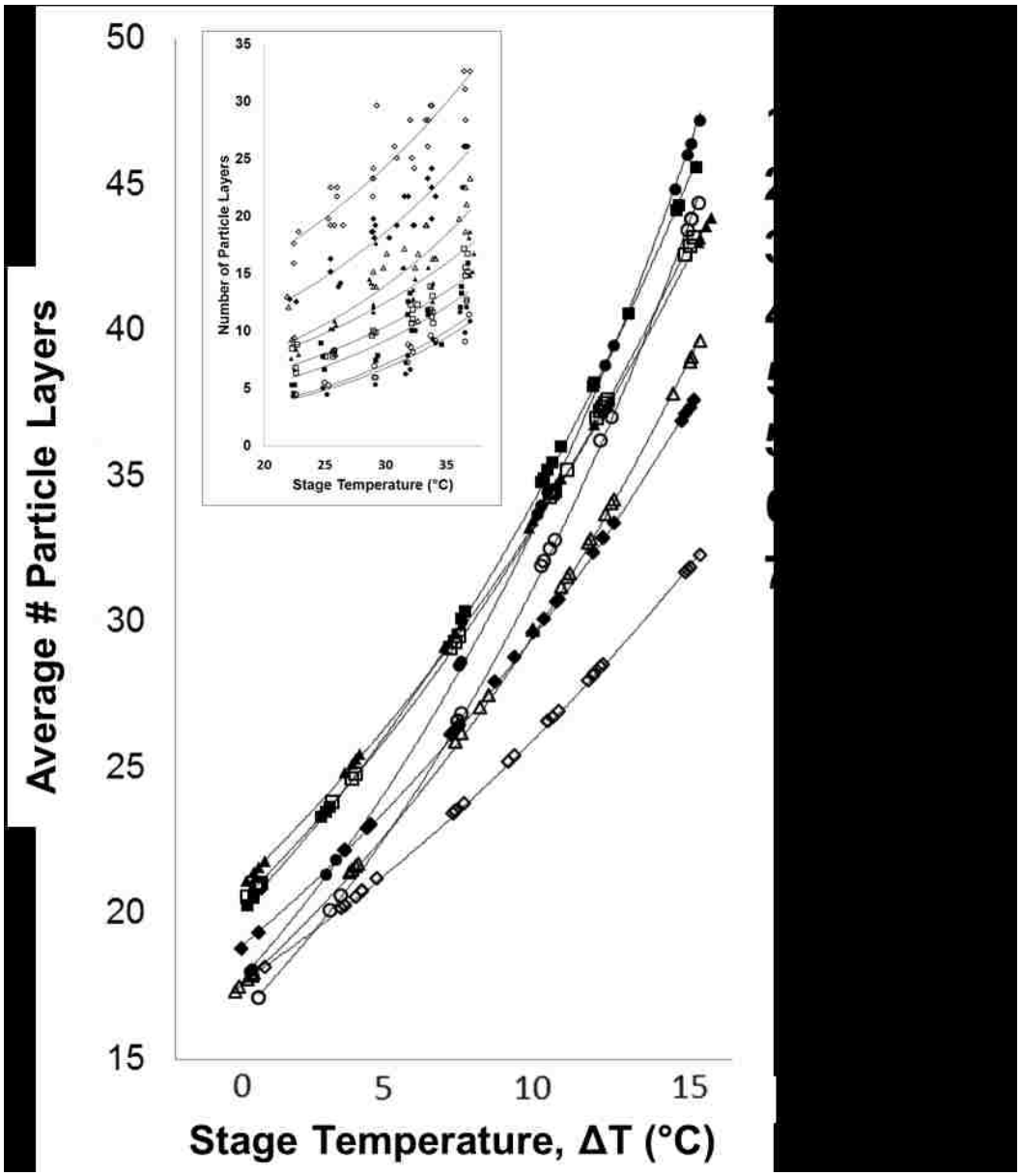

Figure 4.7: Average particle thin film thickness as calculated through a mass balance between suspension particle volume and volume fraction, as well as the deposited area. Note the collapsing trendlines as data series are scaled by their respective deposition speed. However, the data shows increased scatter with higher stage temperature. This scatter is most likely a result of the increased propensity for streaking with larger applied thermal gradients. The inset provides, raw, unscaled, data with trendlines.

4.3.5: Global Streaking Lifecycle and Probability

Qualitatively, streaking behavior falls into three broad categories: Formation, Combination, and Annihilation (Figure 4.8). Formation refers to the nucleation points for streaks (Figure 4.8A). These mesoscale points where the thin film crosses the seven-particle threshold will form the point from whence the streak will grow. These formation points are most likely successors of the initial Marangoni instability, or are at least points where a small defect has taken off within these vulnerable regimes. While these nucleation points often occur near the start of the sample, they are by no means restricted to that initial region—instead these nucleation points seem to follow an increase in thin film thickness. Additionally, within these thicker coating regions, as is clearly evident, oftentimes multiple streaks nucleate near to one another.

Streaks show a strong tendency to merge with their neighbors (Figure 4.8B). This is likely due to the complex and strong evaporative forces at play in the thin film regime. As three-dimensional macroscale defects form and grow, they drive enhanced evaporative flux. This enhanced evaporative flux draws addition fluid flow from nearby regions. This behavior is clear in the thinner coating areas "in-between" streaks. In addition, this enhanced evaporative flux will create a driving force and codependence between neighboring streaks. The complementary driving forces between adjacent streaks can cause these features to migrate towards one another and combine into a single resultant feature. Of course, as shown below, this migration can be skewed towards one or the other feature depending on its size and the complementary evaporative forces.

As an extension, less frequently these streaks can be annihilated (Figure 4.8C). In these cases, streaks terminate without an obvious combinatory event. There is less residual evidence, in the way of thicker progressively thicker or thinner coating regions, as to why a feature might terminate. In all likelihood, the aforementioned forces are still at fault. The evaporative forces due to adjacent features no doubt draw particles from the bulk suspension and thin film regime. Most likely through a combination of factors, including Marangoni and contact line instabilities, there is enough drive to divert particles significantly and cause the termination of a minority of streaks. No doubt the strong lateral forces from adjacent streaks feed into any momentary weakness and absorb incoming particles, thus "annihilating" their neighbor. Annihilation is a relatively low probability event, no doubt due to the strong evaporative feedback forces at play in the three-dimensional growth and maintenance of streaks.

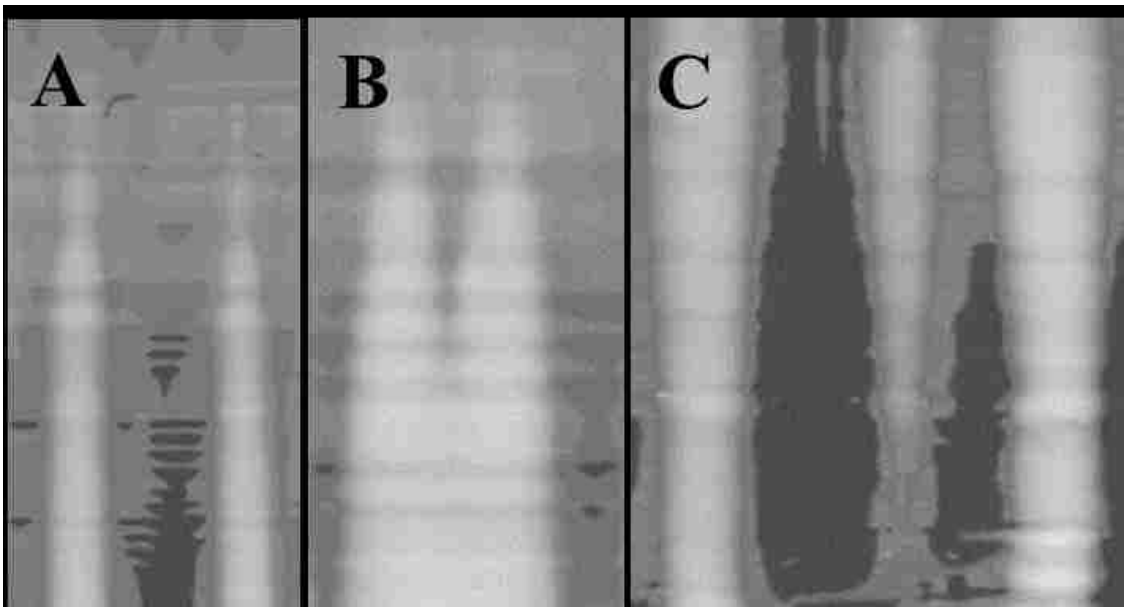

Figure 4.8: Streaking behavior can be roughly classified into a trio of categories: Formation, Combination, and Annihilation. (A) Two formation events, delineated by solid circles in the left image, describe the start of streaks. (B) A combinatory event, indicated by the dotted circle in the center image, occurs where streaks merge. (C) An annihilation event, indicated by the dashed circle in the right image, occurs where streaks terminate.

Finally, global streak life cycles were analyzed. Recall from Figure 4.1 the contrast between streaks and local maxima. Streaks are defined as any sustained event over the seven-particle threshold. Local maxima occur within a streaking event, typically where streaks are merging. In the following analysis, global streak characteristics are analyzed. Here, the probabilities of finding individual streaks with one local maximum, two local maxima, three local maxima, etc. are presented in Figure 4.9. It should be noted that these data truly are global, and represent over 200 samples and 6000 "streaks." Data presented are collected under every speed, temperature and position condition. These data fall along a very strong cubic power law fit. Note that the same trends are seen when data is separated by position, speed, and temperature—however, the rarer events become most clear with increasing amounts of data. This strong relation is particularly interesting in that it shows a global trend in the formation, combination, and dissolution of streaks. No matter the conditions, the probabilities of finding single and merging streaks are the same.

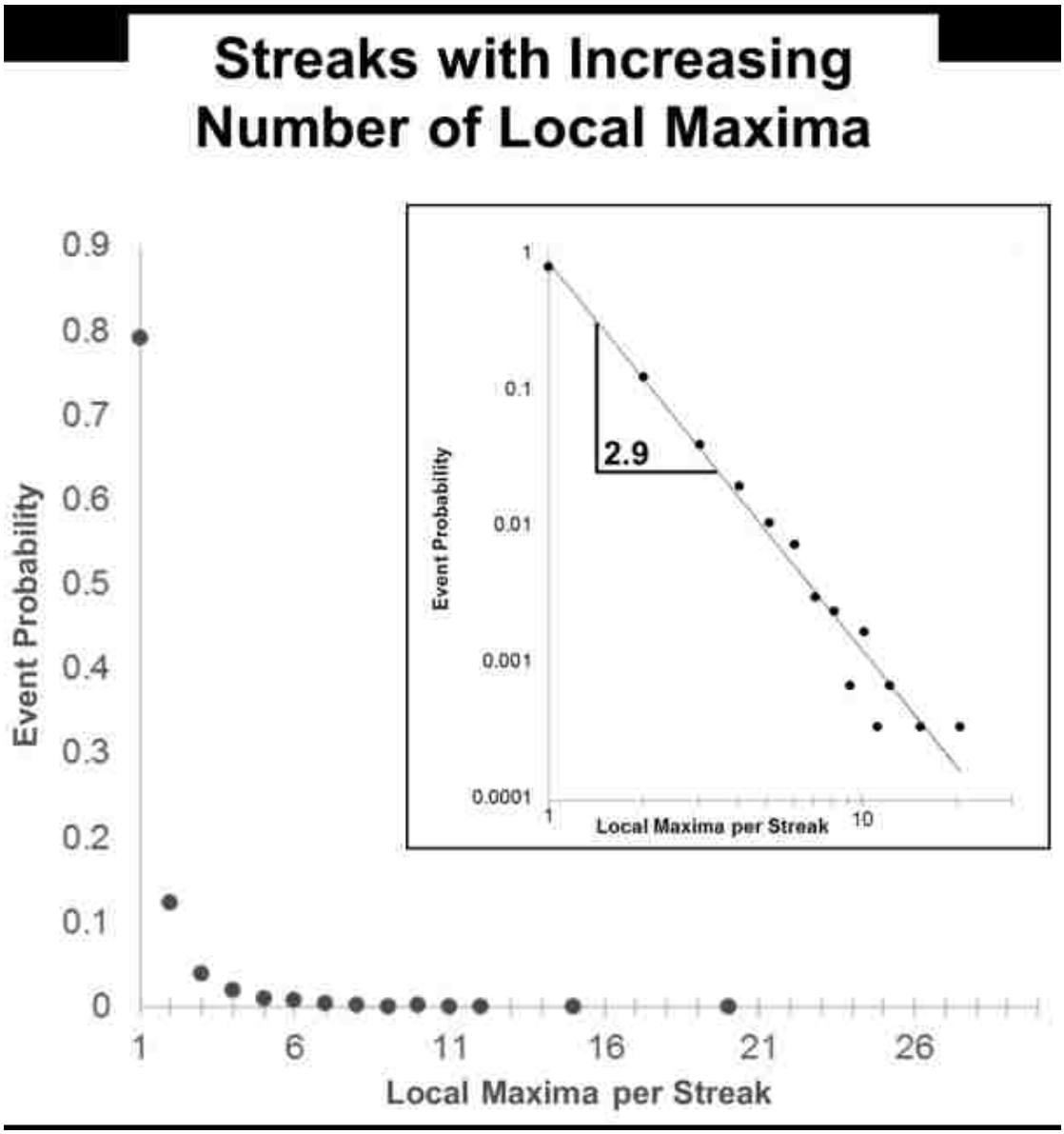

Figure 4.9: Compiled data across all temperature and speed conditions, as well as at ¼, ½, and ¾ sample length, of the probabilities of finding streak with one local maximum, two local maxima, three local maxima, etc. The outer plot uses linear scales, while the inset presents the data in a log-log format. The data very closely follows a cubic power law trend with slope -2.9. It is important to note that subsets of the data organized by temperature, speed, and position follow this same trend. It is also important to note that the scatter towards higher number of local maxima per streak indicate increasingly rare events. For example, only 14 of 6090 streaks analyzed exhibit eight local maxima.

4.3.6: Techniques for the Suppression of Macroscale Defects

This section serves as a small review of various techniques for the suppression of instabilities and resultant macroscale defects. While these techniques are effective for the suppression of streaks, there has been very little in the way of efforts to understand how and why streaking occurs, and by extension how and why these suppression techniques are so effective.

Specifically, nanoparticle and surfactant addition, as well as well as applied substrate vibration, are techniques that suppress streaking. The addition of nanoparticles to suspension dramatically improves thin film uniformity and microscale particle ordering.[19,20] These techniques, termed binary convective deposition, pair SiO_2 micospheres alongside polymer nanoparticles in suspension. With optimized relative volume fraction of each component, microspheres and nanoparticles flow into the thin film region with matched fluxes and pack very uniformly. Under optimal conditions, nanoparticles act as a packing aid and enhance thin film crystallinity and packing. The addition of surfactant also wholly suppresses streaking.[21,46] Most likely surfactants quell streaking by minimizing interfacial and surface tension-driven instabilities and effects. Again, under optimal conditions surfactants can be used to wholly suppress streaking. Finally, with scale-up in mind, the application of vibration to enhance convective deposition has recently been studied.[22] In these experiments, the substrate and suspension are vibrated. This draws out the suspension thin film enormously and again wholly suppresses streaking.

Two other notable techniques for the suppression of streaks are sonication and an applied thermal gradient. In all of the above-mentioned studies, suspensions are sonicated prior to deposition. A well-dispersed suspension relatively "free" of aggregates is necessary to minimize micro- and macroscale defects. In line with the theories presented here, ambient instabilities require some sort of nucleation point for a streak to begin. Even a small particle aggregate could sufficiently enhance evaporative forces to nucleate a streak. It is important to note that, while sonication does limit the prevalence of macroscale defects, it has not shown the capacity to wholly suppress streaking as have nanoparticle addition, surfactant addition, and induced vibration. In every experiment in this work, suspensions were sonicated prior to particle deposition.

One final technique that can be effectively used to suppress streaking is the application of a negative thermal gradient. In order to enhance streaking, throughout these experiments, a heated substrate was used to apply a positive thermal gradient. The application of a reverse thermal gradient through a chilled substrate completely eliminates streaking under the speed range investigated. These results support the theory that instabilities responsible for streaking are in fact a product of a positive thermal gradient and this natural condition can be enhanced. Under ambient conditions, evaporative cooling induces a positive thermal gradient. Thus the only experiments with a reverse, "negative," thermal gradient are those with a chilled substrate.

Ongoing research concerns the mechanism by which these techniques work to suppress instabilities and streaking. In particular, the interplays between these techniques should continue to elucidate the underlying mechanisms by which streaking

occurs. This greater understanding will maximize the ability to fabricate thin films with specified, defect-free, morphologies. A robust understanding and array of suppression techniques will be essential with continuing scale-up and device efforts.

4.4: Conclusions and Impact

Convective deposition is a robust technique for the fabrication of particle layers with uniform and targeted morphologies. However, in its base condition, convective deposition is highly prone to macroscale defects including transverse "streaking." This streaking arises from instabilities that are a product of thermal gradients through a thin film region. Even under ambient conditions, this thermal gradient exists as a result of evaporative cooling. While most convective deposition research teams have methods to suppress streaking, there has been very little in the way of systematic analysis of how and why streaks arise. Applying increasing thermal gradients, and varying deposition speed, this work systematically catalogues streaking prevalence, onset, and eventual behavior. Higher temperatures and thicker films very clearly show increasing amounts of streaking. Streak behavior can be classified as nucleation, combination, or annihilation. However, throughout samples and under all experimental conditions, the likelihood of streaks to merge and dissipate is highly uniform, fitting a cubic power law. This increased understanding of streaking will further enable the intelligent design of experiments so as to control morphology and suppress instabilities and macroscale defects as effectively as possible. In continuing technology development efforts where convective deposition enables optical and biomedical device technologies, control over particle crystallinity is essential. Obviously, as these technologies are scaled up and move toward production, macroscale defect suppression will become increasingly critical.

4.5: References:

1. Ee Y, Arif RA, Tansu N, Kumnorkaew P, Gilchrist JF. Enhancement of light extraction efficiency of InGaN quantum wells light emitting diodes using SiO2/polystyrene microlens arrays. *Appl Phys Lett*. 2007;91(22):221107-1-3.

2. Tessier PM, Velev OD, Kalambur AT, Rabolt JF, Lenhoff AM, Kaler EW. Structured metallic films for optical and spectroscopic applications via colloidal crystal templating. *Adv. Mater.* 2001;13(6):396-400.

3. Haes AJ, Haynes CL, Van Duyne RP. Nanosphere lithography: Self assembled photonic and magnetic materials. *Mater Res Soc*. 2001;636:D4.8.1-D4.8.6.

4. Im SH, Lim YT, Suh DJ, Park OO. Three-dimensional self-assembly of colloids at a water-air interface: A novel technique for the fabrication of photonic bandgap crystals. *Adv Mater*. 2002;14(19):1367-1369.

5. Kumnorkaew P, Ee Y, Tansu N, Gilchrist JF. Investigation of the deposition of microsphere monolayers for fabrication of microlens arrays. *Langmuir*. 2008;24(21):12150-12157.

6. Wang B, Weldon AL, Kumnorkaew PK, Xu B, Gilchrist JF, Cheng X. Effect of surface nanotopography on immunoaffinity cell capture in microfluidic devices. *Langmuir*. 2011;27(17):11229-11237.

7. Weldon AL, Kumnorkaew PK, Wang B, Cheng X, Gilchrist JF. Fabrication (error) of macroporous polymeric membranes through binary convective deposition. *J Mat Res*. 2012;4(9):4532-4540.

8. Zhang YJ, Wang SP, Eghtedari M, Motamedi M, Kotov NA. Inverted-colloidal-crystal hydrogel matrices as three-dimensional cell scaffolds. *Adv Funct Mater*. 2005;15(5):725-731.

9. Koyama K, Yamaguchi N, Miyasaka T. Antibody-mediated bacteriorhodopsin orientation for molecular device architectures. *Science*. 1994;256(5173):762-5.

10. Haynes CL, Van Duyne RP. Nanosphere lithography: A versatile nanofabrication tool for studies of size-dependent nanoparticle optics. *J Phys Chem B*. 2001;105(24):5599-5611.

11. Zhang YJ, Wang XH, Wang YX, Liu HL, Yang JH. Ordered nanostructures array fabricated by nanosphere lithography. *J Alloys Compd*. 2008;452(2):473-477.

12. Tessier PM, Velev OD, Kalambur AT, Rabolt JF, Lenhoff AM, Kaler EW. Assembly of gold nanostructured films templated by colloidal crystals and use in surface-enhanced raman spectroscopy. *Journal of the American Chemical Society*. 2000;122(39):9554-9555.

13. Lee W, Chan A, Bevan MA, Lewis JA, Braun PV. Nanoparticle-mediated epitaxial assembly of colloidal crystals on patterned substrates. *Langmuir*. 2004;20(13):5262-5270.

14. van Blaaderen A, Hoogenboom JP, Vossen DLJ, et al. Colloidal epitaxy: Playing with the boundary conditions of colloidal crystallization. *Faraday Discuss*. 2003;123(Pages 1-421):107-119.

15. Jiang P, McFarland MJ. Wafer-scale periodic nanohole arrays templated from two-dimensional nonclose-packed colloidal crystals. *J Am Chem Soc*. 2005;127(11):3710-3711.

16. Yang H, Jiang P. Scalable fabrication of superhydrophobic hierarchical colloidal arrays. *J Colloid Interface Sci*. 2010;352(2):558-565.

17. Biancaniello PL, Crocker JC. Line optical tweezers instrument for measuring nanoscale interactions and kinetics. *Rev Sci Instrum*. 2006;77:113702-113702-10.

18. Hayward RC, Saville DA, Aksay IA. Electrophoretic assembly of colloidal crystals with optically tunable micropatterns. *Nature*. 2000;404(6773):56-59.

19. Kumnorkaew P, Gilchrist JF. Effect of nanoparticle concentration on the convective deposition of binary suspensions. *Langmuir*. 2009;25(11):6070-6075.

20. Kumnorkaew P, Weldon AL, Gilchrist JF. Matching constituent fluxes for convective deposition of binary suspensions. *Langmuir*. 2010;26(4):2401-2405.

21. Kleinert J, Kim S, Velev OD. Electric-field-assisted convective assembly of colloidal crystal coatings. *Langmuir*. 2010;26(12):10380-5.

22. Muangnapoh T, Weldon AL, Gilchrist JF. Enhanced colloidal monolayer assembly via vibration-assisted convective deposition. *Applied Physics Letters*. 2013;103:181603-1-181603-4.

23. Thomson J. On certain curious motions observable on the surfaces of wine and other alcoholic liquours. *Philosophical Magazine*. 1855;10:330-333.

24. Daniel S, Chaudhury MK, Chen JC. Fast drop movements resulting from the phase change on a gradient surface. *Science*. 2001;291(5504):633-636.

25. Darhuber AA, Troian SM. Marangoni driven structures in thin film flows. *Physics of Fluids*. 2003;15(9):S9.

26. Brzoska JB, Brochard-Wyart F, Rondelez F. Exponential growth of fingering instabilities in spreading films under horizontal temperature gradients. *Europhysics Letters*. 1992;19(2):97-102.

27. Rondelez,J.B.Brzoska and F.Brochard-Wyart and F. Exponential growth of fingering instabilities of spreading films under horizontal thermal gradients. *EPL (Europhysics Letters)*. 1992;19(2):97.

28. Xu X, Luo J. Marangoni flow in an evaporating water droplet. *Applied Physics Letters*. 2007;91(124102):1-3.

29. Münch A, Wagner B. Contact-line instability of dewetting thin films. *Physica D*. 2005;209(1–4):178-190.

30. Joanny,S.M.Troian and E.Herbolzheimer and S.A.Safran and J.F. Fingering instabilities of driven spreading films. *EPL (Europhysics Letters)*. 1989;10(1):25-30.

31. Bertozzi AL, Brenner MP. Linear stability and transient growth in driven contact lines. *Physics of Fluids*. 1997;9(3):530-539.

32. Kataoka DE, Troian SM. A theoretical study of instabilities at the advancing front of thermally driven coating films. *Journal of Colloid and Interfacial Science*. 1997;192(2):350-362.

33. Cazabat AM, Heslot F, Troian SM, Carles P. Fingering instability of thin spreading films driven by temperature gradients. *Nature*. 1990;346(6287):824-826.

34. Shiba H, Onuki A. Jammed particle configurations and dynamics in high-density leonard-jones binary mixtures in two dimensions. *Progress of Theoretical Physics Supplement*. 2010;184:232-247.

35. Deegan RD, Bakajin O, Dupont TF, Huber G, Nagel SR, Witten TA. Capillary flow as the cause of ring stains from dried liquid drops. *Nature*. 1997;389(6653):827-829.

36. Deegan RD. Pattern formation in drying drops. *Physical Review E*. 2000;61(1):475-485.

37. Yunker PJ, Still T, Lohr MA, Yodh AG. Suppression of the coffee-ring effect by shape-dependent capillary interactions. *Nature*. 2011;476:308-311.

38. Dimitrov AS, Nagayama K. Steady-state unidirectional convective assembling of fine particles into 2-dimensional arrays. *Chemical Physics Letters*. 1995;243(5-6):462-468.

39. Prevo BG, Kuncicky DM, Velev OD. Engineered deposition of coatings from nano- and micro-particles: A brief review of convective assembly at high volume fraction. *Colloids and Surfaces A-Physicochemical and Engineering Aspects*. 2007;311(1-3):2-10.

40. Denkov ND, Velev OD, Kralchevsky PA, Ivanov IB, Yoshimura H, Nagayama K. Mechanism of formation of two-dimensional crystals from latex-particles on substrates. *Langmuir*. 1992;8(12):3183-3190.

41. Colosqui CE, Morris JF, Stone HA. Hydrodynamically driven colloidal assembly in dip coating. *Physical Review Letters*. 2013;110(18):188302-1-188302-5.

42. Adachi E, Dimitrov AS, Nagayama K. Stripe patterns formed on a glass-surface during droplet evaporation. *Langmuir*. 1995;11(4):1057-1060.

43. Ghosh M, Fan F, Stebe KJ. Spontaneous pattern formation by dip coating of colloidal suspensions on homogeneous surfaces. *Langmuir*. 2007;23(4):2180-2183.

44. Hosoi AE, Bush JWM. Evaporative instabilities in climbing films. *Journal of Fluid Mechanics*. 2001;442:217-239.

45. Fanton X, Cazabat AM. Spreading and instabilities induced by a solutal marangoni effect. *Langmuir*. 1998;14(9):2554-2561.

46. Prevo BG, Fuller JC, Velev OD. Rapid deposition of gold nanoparticle films with controlled thickness and structure by convective assembly. *Chemistry of Materials*. 2005;17(1):28-35.

Chapter 5

Cracking During Nanoparticle Thin Film Deposition

5.1: Introduction and Previous Work

This chapter concerns the convective deposition of multilayer nanoparticle thin films. These thin films display cracks in the deposition direction with highly monodisperse spacing. Varying thin film thickness correlates with increased drying stresses and complementary increased crack spacing. Uniform crack spacing from 2-160 μm are observed.

There is a strong interest in the controllable formation of defect-free nanoparticle thin films.[1-3] Extensive efforts have focused on the VOC-free formation of latex coatings.[4-6] There is a significant drive to move towards aqueous systems in order to minimize the environmental impact of these coatings. In addition, it is critical that the coatings be uniform upon drying. As such, significant efforts are underway to characterize varying deformation mechanisms and evolving stresses in these drying systems.[6-9] Typically, surfactants are used to enhance particle and suspension stability, as well as minimize macroscale defects and nonuniformities.[10-12] In particular,

nanoparticle films are susceptible to micro- to macroscale cracking—under some conditions these cracks can exhibit highly monodisperse spacing.[13-18]

Drying films can be explained through a number of different mechanisms. Recent experimental and modeling efforts have aimed to identify the predominant physics at play. The four proposed competing mechanisms in thin film formation and particle deformation are wet sintering, dry sintering, capillary deformation, and Sheetz's deformation.[4,8] Wet sintering centers around particle-fluid interactions while particle-air surface energy drives dry sintering. In capillary deformation, the curvature and applied pressure at the fluid-air interface drives particle interactions. Finally, Sheetz's deformation describes the flow of polymer particles to the air-fluid interface as a result of evaporation-induced convection—this polymer thin film will then limit evaporation.

The formation of latex films from bulk suspension is explained through three sequential steps.[7] Initially, the fluid evaporates and forces particles into a close-packed microstructure. Next, the plastic particles will deform as they contact one another and transition to an increasingly dense arrangement. Finally, polymer chains reptate and interdiffuse—a homogeneous, and mechanically stronger, film will result. Cracking is a result of these capillary forces. As the fluid evaporates, high pressure fluid generates tremendous drying stresses that compress the film.[14,17] Cracks form in order to minimize these stresses. Dufresne et al., validate these conclusions by showing that cracking films are wetted except at the cracks themselves.[19]

Routh et al., provide extensive modeling and theory to describe crack formation in nanoparticle thin films.[14] Solvent evaporation near the edge of a drying drop will lead

to a consolidation of particles and increased volume fraction. This will generate a pressure drop and increased fluid flow through the higher-density system. Solvent pressure in the system can be calculated through Darcy's Law:

$$\nabla P = -\frac{\mu}{k_p} u \tag{5.1}$$

Where μ is solvent viscosity, k_p is the permeability of a packed bed of particles, and u is the velocity of the fluid. Geometrically, the maximum capillary pressure for a monodisperse particle array will be:

$$P \sim \frac{10\gamma}{R} \tag{5.2}$$

This maximum capillary pressure is used to extrapolate a relaxation length scale, X, for the capillary pressure. Using the Carmen-Cozeny equation:

$$k_p = [2R^2(1-\phi^2)]/(75\phi^2) \tag{5.3}$$

With R referring to the particle radius and ϕ to the volume fraction. Finally, an expression for velocity can be expressed as an Evaporation rate, E with a scaled length to height ratio of the dried film. Thus characteristic velocity will be:

$$u^* = [\gamma/(3\eta_0 E)]^{1/4} E \tag{5.4}$$

With γ referring to the surface tension. Finally, substituting dispersion velocity, η_0 and these expressions into Darcy's Law, Routh et al., derive an expression for the relaxation length scale X.

$$X \sim \frac{20R(1-\phi)^2}{75\mu\phi^2}\left(\frac{3\eta_0\gamma^3}{E^3}\right)^{1/4} \tag{5.5}$$

Replacing this length scale with a capillary length will yield a characteristic pressure, which, scaled by Equation 5.2, yields a dimensionless pressure term which can characterize fluid flow through the higher volume fraction consolidated particle array.

$$P_{cap} = \frac{20}{75}\left(\frac{3\gamma\eta_0}{E}\right)^{1/2}\frac{R(1-\phi)^2}{\mu\phi^2 H} \tag{5.6}$$

Under intermediary capillary pressures, the formation of cracks is reversible. This means that fluid can flow as needed through the thin film to the compacted particle array. However, as capillary pressure reaches its maximum, defined by Equation 5.2, replacement fluid can no longer flow to compensate for that lost due to evaporation. It is this hydrodynamic length scale, the capillary pressure-driven distance the fluid must flow to compensate for that lost to evaporation, that controls the onset and evolution of cracking. In particular, capillary forces put the particle thin film under compression. As these stresses grow with increasing evaporation, the system seeks to minimize involved capillary forces and its energy. Upon the formation of "cracks," fluid recedes into either particle thin film and system energy relaxes. Cracks form with highly monodisperse spacing as a results of the characteristic hydrodynamic distance that fluid must flow upon the onset of cracks. Routh et al., scale crack spacing, y, by X, and find the following power law relation with P_{cap}:

$$\frac{y}{X} = 0.07{P_{cap}}^{-0.8} \tag{5.7}$$

While Routh et al. expect the trend to be linear, they attribute the imperfect fit to an overestimate of maximum capillary pressure.

This study serves to extend and complement previous investigations, particularly investigating the effects of changing film thickness through a trio of methodologies.[9,15,16] Film thickness will be varied through deposition speed, applied thermal gradients, and particle volume fraction. In addition, significant particle deformation comes into play in the formation of latex films—this work will present complementary data of silica nanoparticles, with an emphasis on the comparison of crack spacing between the two chemistries. The use of oxide nanoparticles should remove some limitations and complexities that might confound conclusions. In addition, previous research into the cracking of nanoparticle thin films has primarily concerned the evaporation of pools of suspensions—this shares strong parallels with droplet evaporation and the "coffee ring effect." The use of convective deposition, where a suspension meniscus is pulled across a substrate, with particles drawn to an evaporative front and liquid thin film, enables significantly enhanced process control. In particular, this work will evaluate the transitions in cracking morphology with increasing, as well as decreasing, thin film thickness.

5.2: Materials and Methods

Convective deposition experiments are performed as described in Chapter 2. As an enhancement, some experiments are performed atop a Fisher Scientific Isotemp stirring hot plate. This allows the application of thermal gradients, which will increase thin film thickness by increasing evaporative flux, SiO_2 and polystyrene (PS) nanoparticles of comparable size are used in thin film formation. 80 nm SiO_2 nanoparticles are prepared through Stöber synthesis, paralleling the experimental techniques described in Appendix 9.6.1. 75 nm PS nanoparticles are prepared by emulsion polymerization and supplied by the Emulsion Polymers Institute.

Characterization via electron microscopy is performed as described in Chapter 2. Optical and confocal microscopy is performed using an Olympus IX71 optical microscope paired with a Visitech VTEye confocal system, in conjunction with a 100x objective. Profilometry is carried out using a Zygo Zemetrics ZeGAGE Interference Profilometer, with a 10x objective. Image analysis of optical and electron microscope imagery, as well as interference profilometer, data were carried out using ImageJ.

5.3: Experimental Results

A trio of methodologies is used to control nanoparticle thin film thickness, with increased thickness yielding larger crack spacing. Coating thickness is first tuned via suspension volume fraction, with higher volume fractions generating thicker thin films. Applied thermal gradients will increase evaporative flux and thus increase coating thickness. Finally, deposition speed, the speed at which the suspension is dragged across the substrate, will tune sample thickness. In these batch experiments, a single volume fraction and thermal gradient are applied to each sample. Thus thin films of homogeneous thickness are deposited. Contrastingly, deposition speed can be varied throughout a batch coating in order to systematically vary thin film thickness (Figure 5.1). Increasing nanoparticle thin film thickness, via slower deposition speeds, applied thermal gradients, or increased volume fraction, will limit sample transparency.

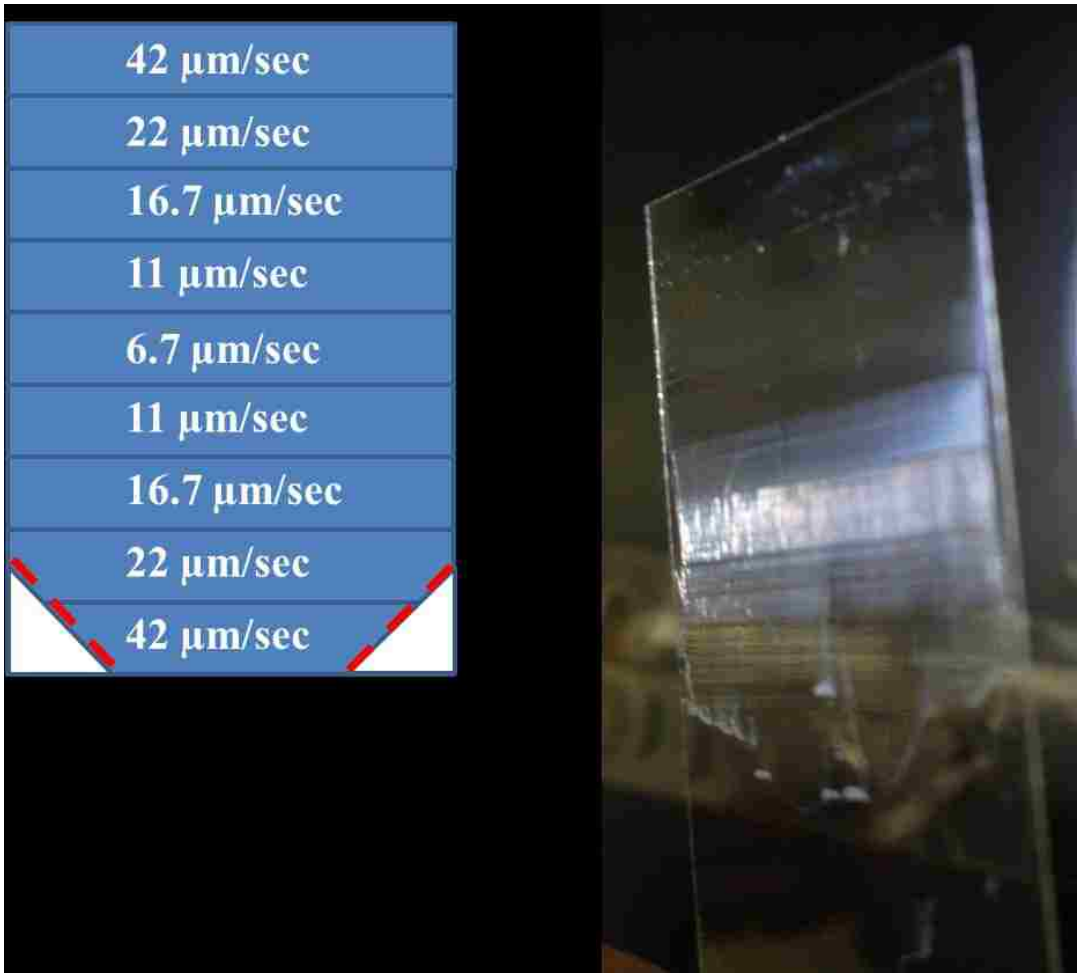

Figure 5.1: Variable-thickness nanoparticle thin film. Lower deposition speeds will yield thicker coatings. Note that thicker coatings exhibit decreased sample transparency.

5.3.1: Background and Film Thickness Calibration with Crack Spacing

The supposition that crack spacing scales with thin film thickness, and resulting increased drying stresses, is validated in the literature. Routh et al., 2004 use Vernier calipers to measure the macroscale crack spacing and film thickness in latex and silica systems.[14] Crack spacing in these systems spans 0.1 to 10 mm and film thickness spans 10 to 1000 μm (Figure 5.2). These data shows a semi-universal scaling of crack spacing with film thickness over a pair of particle chemistries and a range of particle sizes.

These data do not address small scale cracking and thinner particle coatings as a result of experimental limitations. Interference profilometry, in correlation with high resolution optical microscopy, are used to expand upon the data of Routh et al., over small lengthscales. These techniques provide micron to submicron-level detail. Figure 5.3 provides a methodological correlation of high-resolution optical microscopy and interference microscopy, as well a presentation of crack spacing data with thin film thickness. Note that the relation of monodisperse crack spacing with thin film thickness shows a strong linear correlation. This is at odds with the experimental data of Routh et a., 2004, where there data requires power law scaling to show a clear trend.[14] However, this clearly parallels the theory of Routh et al., (Equation 5.1-Equation 5.7) where a clear linear trend between relevant hydrodynamic length scale and crack spacing is expected. Also, note that a minimum crack spacing of ~2 μm is presented in Figure 5.3. That is the minimum observed spacing where cracks show significant length and monodisperse spacing. Below that lengthscale, analysis becomes increasingly complex as samples are characterized by small-scale subcracks.

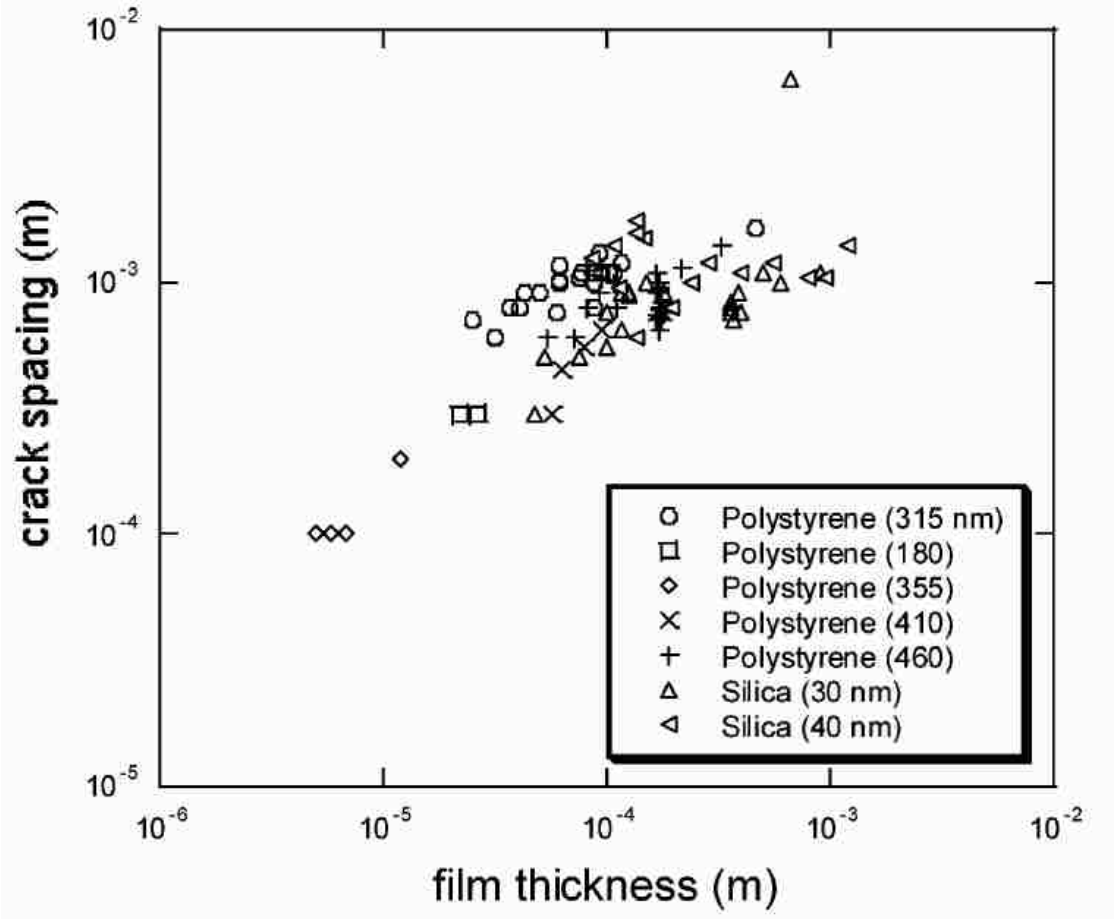

Figure 5.2: Data measured from dried latex and silica nanoparticle thin films. Crack spacing is compared with film thickness. Reprinted from Routh et al., 2004.

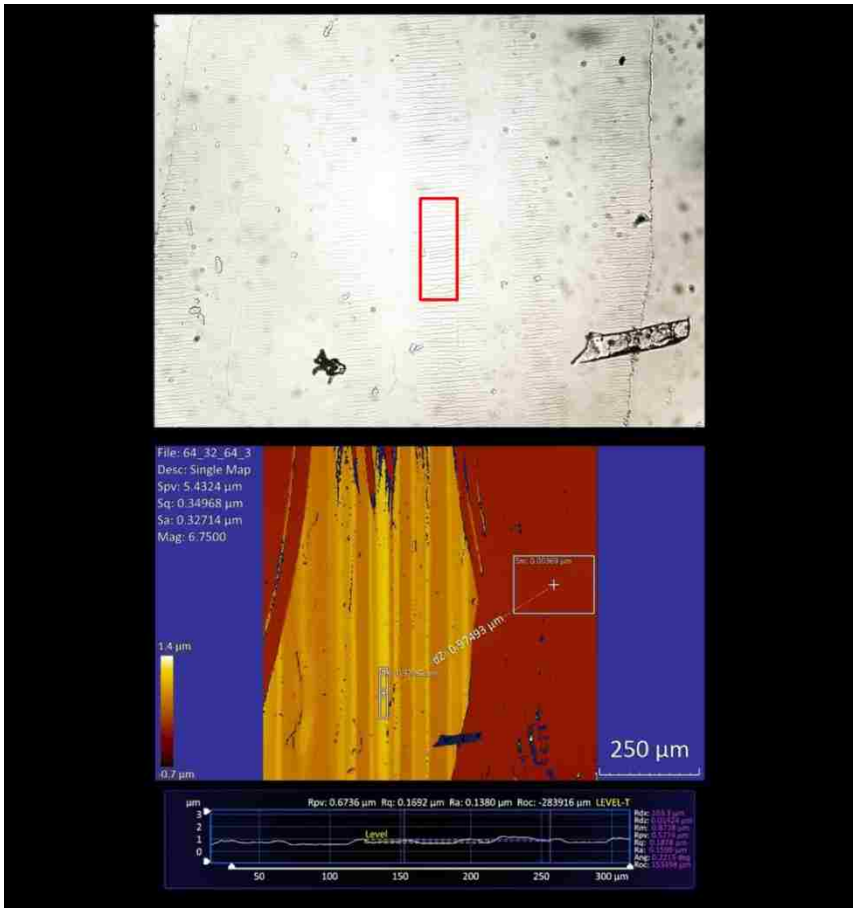

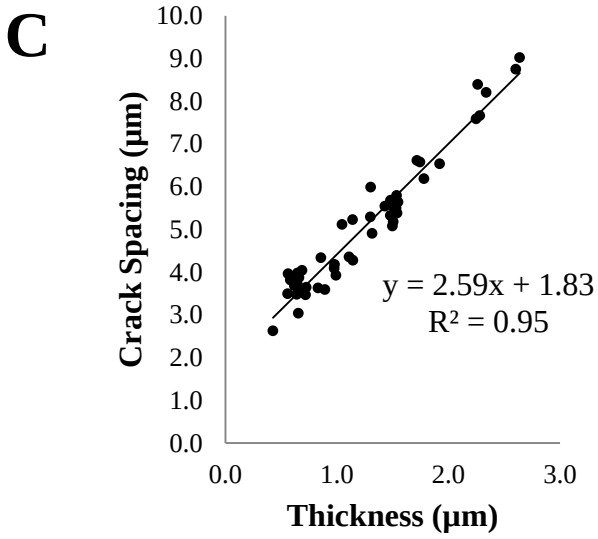

Figure 5.3: Methodological presentation of (A) high resolution optical microscopy and (B) interference profilometry to compare (C) crack spacing with nanoparticle thin film thickness. Note that this correlation is highly linear.

5.3.2: Particle Chemistry Comparison

Previous research into crack spacing in nanoparticle thin films primarily concerns latex films,[17,18] though some parallel research has been carried out with oxide systems.[14,19] As a final step in the formation of latex films, polymer particles soften and deform, and polymer chains reptate and interdiffuse. This guides the formation of a mechanically strong film. In order to deconvolute any specific "soft" particle interactions from the crack formation process, SiO_2 and PS particles of comparable size were deposited and resulting thin films were compared. Under a constant deposition speed of 41.7 μm/sec, 80 nm SiO_2/H_2O, at a volume fraction of 10.3%, and 75 nm PS/H_2O, at a volume fraction of 11%, were used in film formation. Figure 5.4 presents a side-by-side comparison of SiO_2 and PS particles deposited under parallel suspension and processing conditions. Thin film thicknesses, and crack spacing, were controlled through an applied thermal gradient (Figure 5.5).

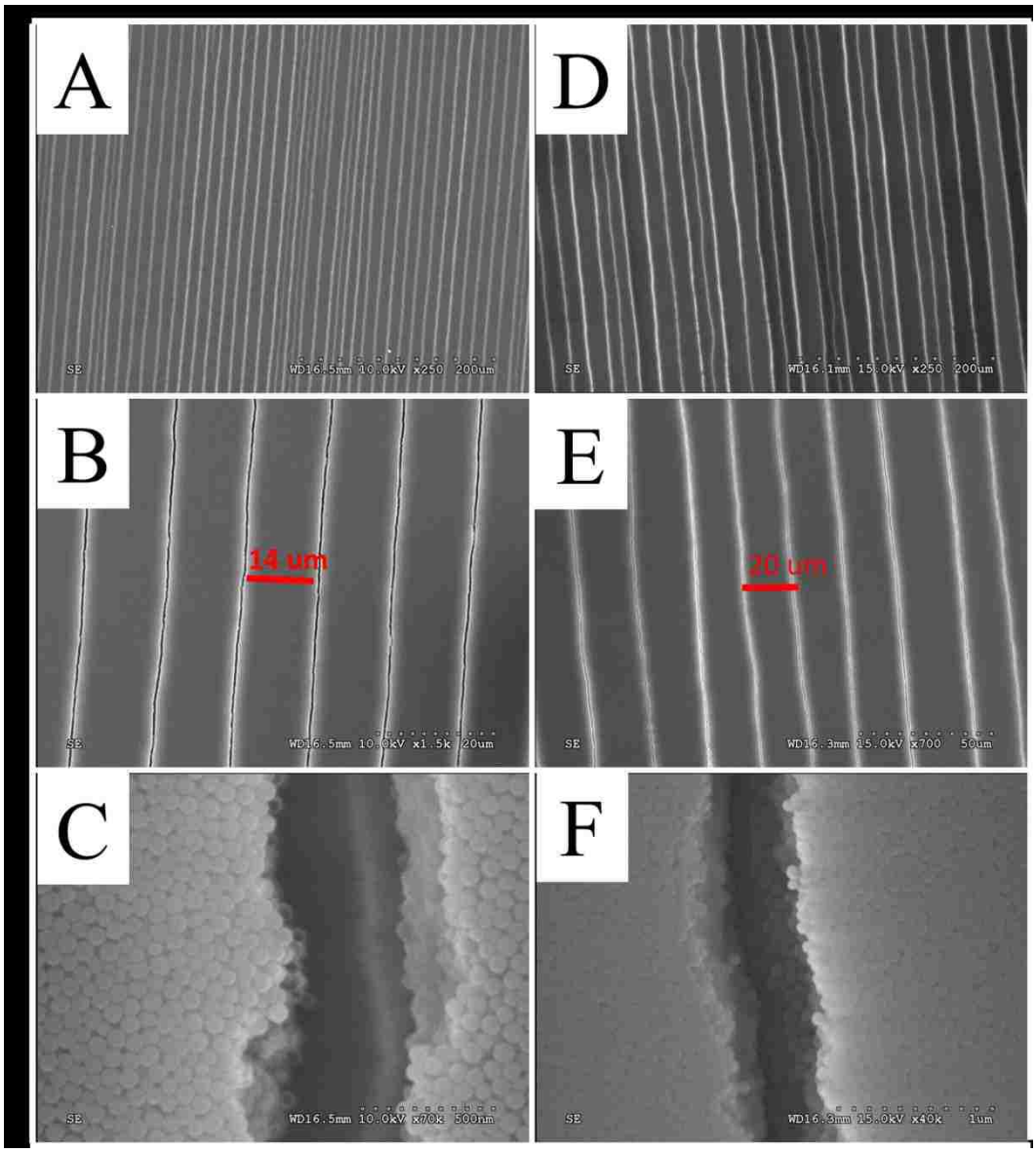

Figure 5.4: Side-by-side comparison of cracked 75 nm PS (A, B, C) and 80 nm SiO_2 (D, E, F) nanoparticle thin films deposited atop a 60°C hot plate. Varying magnification enabled macroscale (A, D), mesoscale (B, E) and microscale (C, F) analysis. Both SiO_2 and PS nanoparticles exhibit cracking, albeit of slightly different spacing.

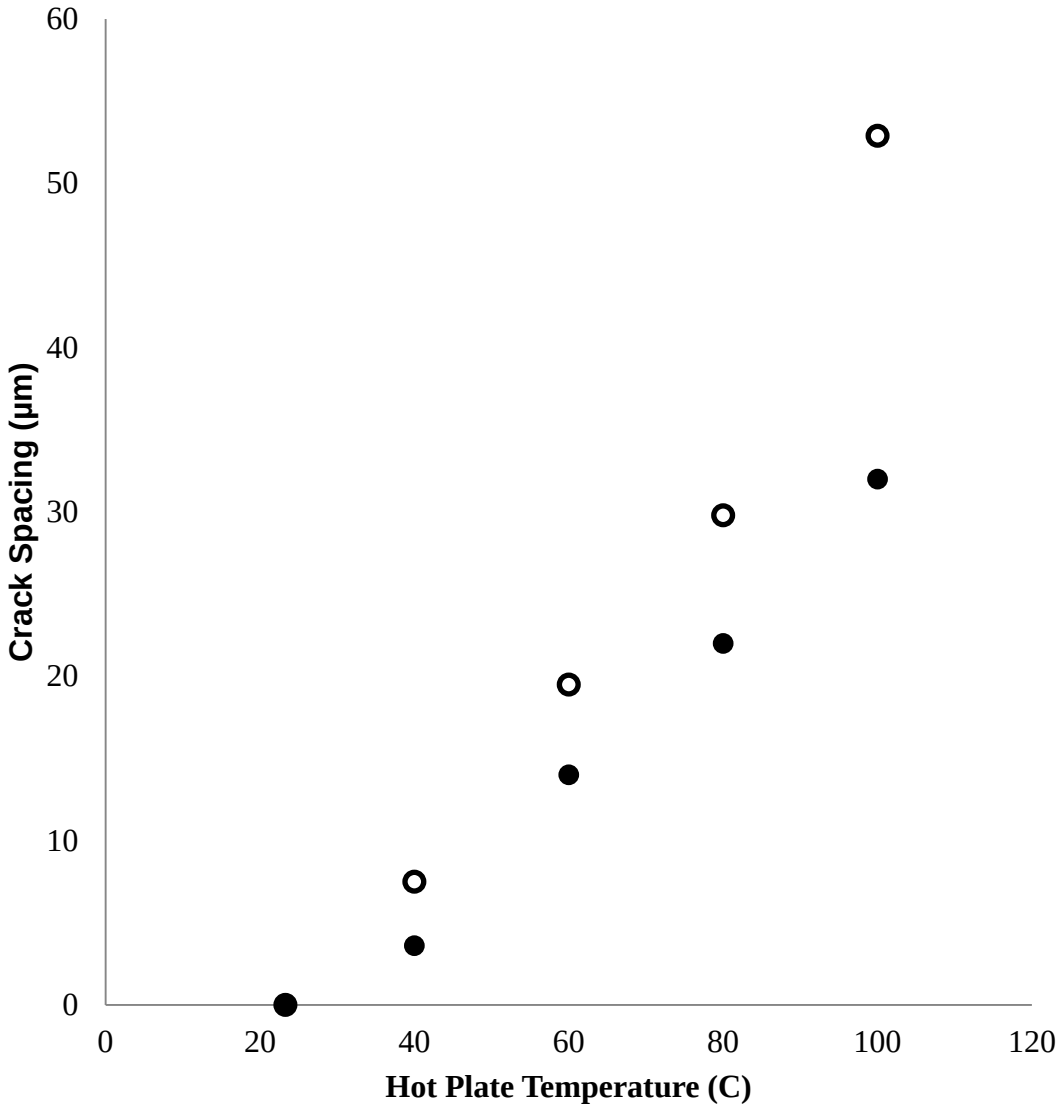

Figure 5.5: Crack spacing in SiO_2 and PS thin films as deposited through convective deposition. Black dots represent 11% 75 nm PS suspensions and white circles represent 10.3% 80 nm SiO_2 suspensions. Thus SiO_2 and PS particles are of comparable size and relative volume in suspension. Crack spacing is controlled through an increasing applied thermal gradient.

Note the very similar trends in crack spacing with comparable SiO_2 and PS suspension and processing characteristics. The "softer" PS particles do exhibit slightly smaller crack spacing, but both systems show highly controlled thin film morphology. The differences are subtle, and could also be due to minute differences in particle size and volume fraction. The fact that both systems show parallel cracking characteristics validates the following studies. Polystyrene and SiO_2 data will be presented in the forthcoming results.

5.3.3: Suspension Volume Fraction as a Mechanism to Control Cracking

Next, the effect of suspension volume fraction is characterized. 11% and 35% (v/v) PS suspensions are deposited with constant deposition speed, 41.7 μm/sec. Again, a hot plate is used to apply a thermal gradient to the drying thin film and thus increase crack spacing. As expected, higher suspension volume fraction yields thicker nanoparticle coatings. Under these experimental conditions, crack spacing from 35% PS suspensions appears to plateau around 140 μm. Note that this is not in fact a global threshold, and cracked thin films have been fabricated with spacing near 160 μm. Under these thickest conditions, coatings experience significant delamination from the substrate as the film dries (Figure 5.8).

In fact, with a volume fraction ratio of 35%/11% = 3.2, one could expect thin film thickness to scale accordingly. This theory is roughly borne out in practice, with crack spacing ratios as follows: 1.9(40°C), 3.3(60°C), 4.3(80°C), and 4.4(100°C). These data approach the 3.2 v/v ratio more strongly when the linear fit from Figure 5.3, even though this fit is generated for very thin films, is applied. Here, predicted thin film

thickness ratios are: 2.9(40°C), 3.6(60°C), 4.6(80°C), and 4.6(100°C). While these ratios are inexact, they are similar to the predicted results based on particle volume fraction. Confounding factors could include edge nonuniformities, as well as differences from the, extremely, thin film model versus experimentally generated films of varying thickness. Also, it is important to note that the absence of data under ambient temperature conditions, 23.3°C, is due to a complementary absence of cracking.

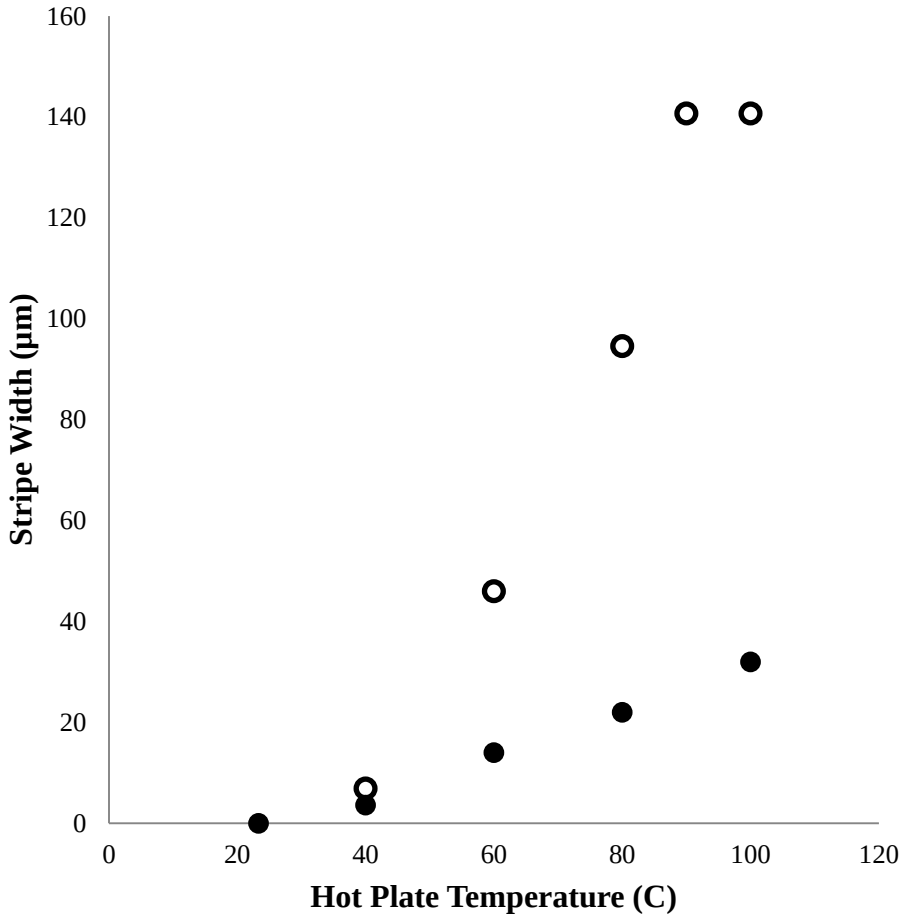

Figure 5.6: Crack spacing with varying PS suspension volume fractions of 11% (black dotes) and 35% (white circles). Note that, as predicted, increased suspension volume fraction yields thicker nanoparticle coatings.

Next, varying crack spacing, and thin film thickness, with changing deposition speed is presented. These methodologies parallel the macroporous membrane fabrication efforts as shown in Chapter 7.[20] The evolution of coating morphology with changing deposition speed, particularly with regards to enhanced particle convective and thin film thickness, is well understood.[21-24] These data serve to provide a quick validation of increased crack spacing with decreased deposition speed, without the addition of applied thermal gradients to the system. Data are presented for SiO_2 and PS nanoparticle systems, at moderate, 10.3%, and high, 35%, particle volume fractions (Figure 5.7). 10.3% SiO_2 suspensions are used to demonstrate the transition from a homogeneous, non-cracked, film, through a monodisperse cracking morphology (Figure 5.7A, Figure 5.7B). 35% PS suspensions are used to show a transition between morphologies of moderate crack spacing, 23 μm, and very thick spacing, ~160 μm (Figure 5.7E, Figure 5.7F). These wide cracks are sometime characterized by "subcracks," as demonstrated in Figure 5.7B and Figure 5.7F. Also, these wide cracks show some propensity to delaminate, where drying stresses minimize system energy by peeling the film from its substrate. This peeling is demonstrated at the microscale in Figure 5.7F, where higher pixel intensity correlates with increased height. In addition, a particularly pronounced example of this peeling, via conventional photography, is provided in Figure 5.8. These data clearly demonstrate the high level of morphological control provided through changing deposition speed.

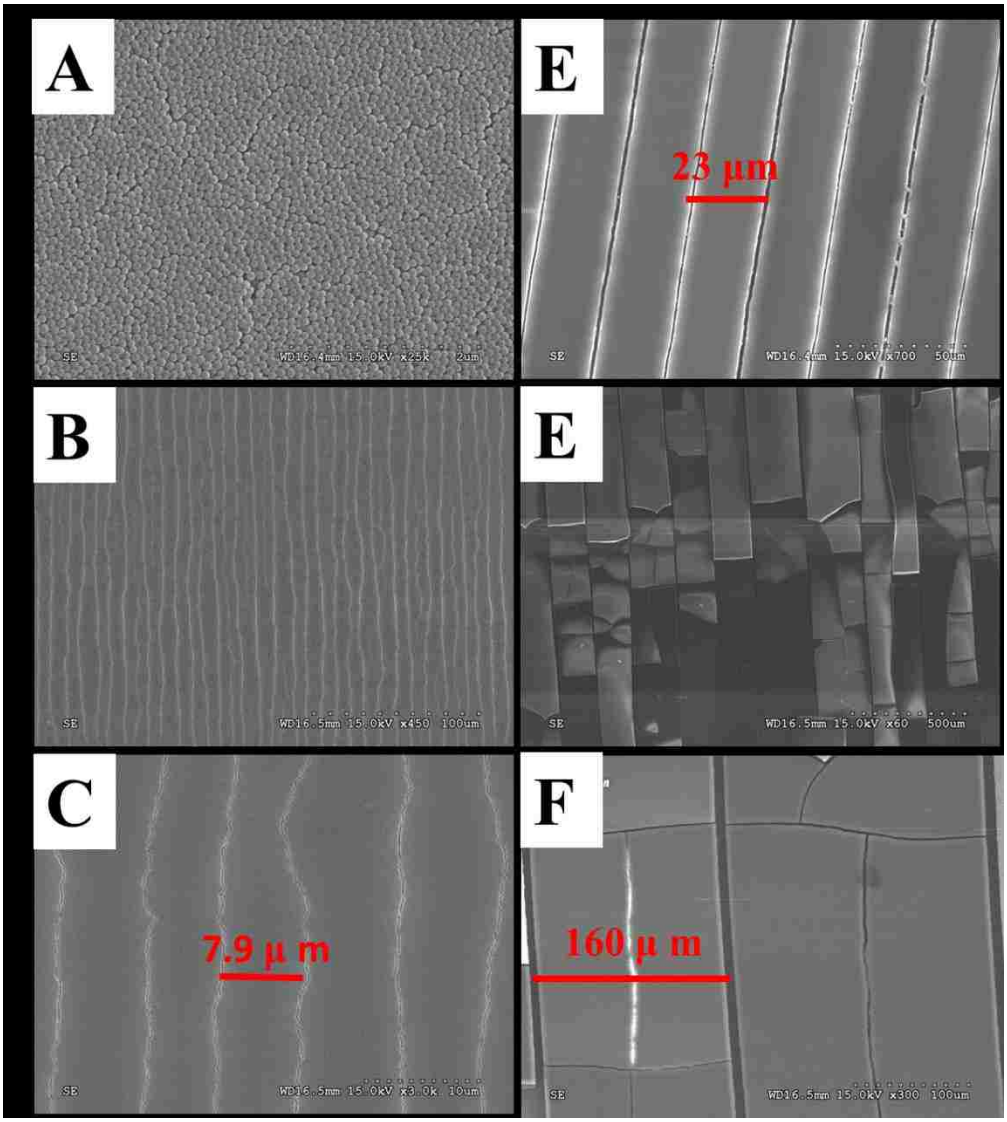

Figure 5.7: Nanoparticle thin films deposited from 10.3% SiO_2 (A,B,C) and 35% PS (D,E,F) (v/v) suspensions. No thermal gradient is applied in these systems. These data show the ability of changing deposition speed to control resultant thin film morphology. The left column demonstrates the transition from a (A) "crackless" homogeneous morphology, deposited at 42 µm/sec, to (B, C) monodisperse crack spacing at 7.9 µm, deposited at 16.7 µm/sec. The right column demonstrates a transition from (D) moderate crack spacing, 23 µm, deposited at 16.7 µm/sec, to (E, F) wide crack spacing at 160 µm, deposited at 6.7 µm/sec. Note that these widest cracks demonstrate some amount of "subcracking." Also, note that particularly thick samples, with wide crack spacing, display a tendency to delaminate from the substrate in order to minimize system stress upon drying.

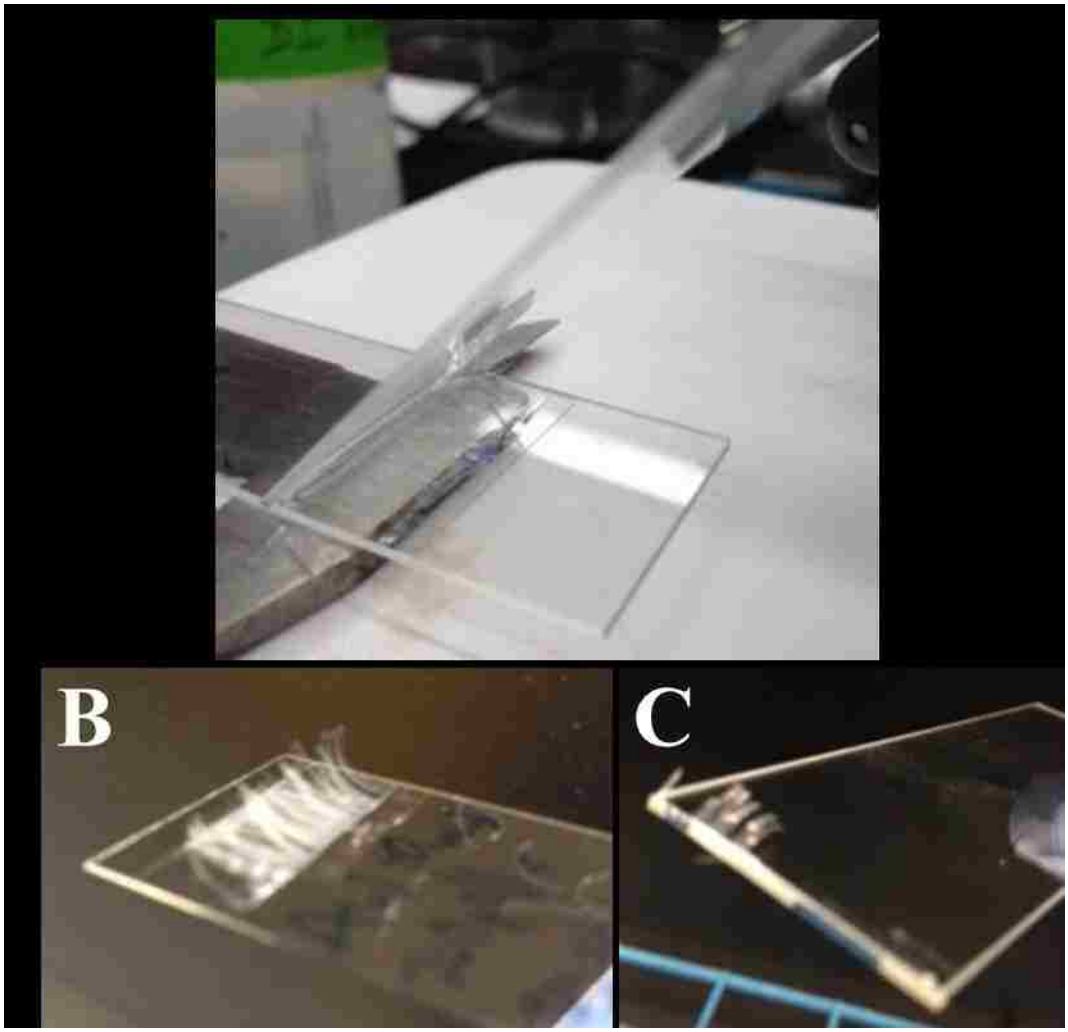

Figure 5.8: Photographs of delaminated thick nanoparticle cracks. (A) In-situ photography of experimental setup highlighting substrate and blade. (B) Substrate after coating completion. Note the delaminated, "peeling," cracks (C) Deposition blade. Some delaminated nanoparticle cracks wetted and adhered to the deposition blade.

5.3.4: Deposition Speed as a Method to Probe Transitions in Crack Spacing

This final section aims to probe and explain transitioning crack spacing with changing coating thickness. Deposition speed can be increased or decreased as shown in Figure 5.1—these speed changes will result in changing thin film thickness and crack spacing. Figure 5.9 provides data on variable speed coatings and highlights changing crack width and transition regions. This sample is initially quite thin (Figure 5.9A), and is subject to sequentially increasing thickness over regions of equal length. Upon reaching a prescribed thickness, deposition speed is increased to again thin the sample.

This coating starts and ends under fast enough deposition speeds so as not to exhibit cracks or significant large-scale crystalline defects (Figure 5.9A). In the transition from 16.7 to 11 μm/sec, cracks arise in a uniform front (Figure 5.9B). Crack spacing reaches a steady state value, under 11 μm/sec deposition speed, of 15 μm (Figure 5.9C). In the transition from 11 to 6.7 μm/sec, there is a starkly evident change in thickness and crack spacing (Figure 5.9D). Note the initial delamination at this transition point. At a deposition speed of 6.7 μm/sec, crack spacing reaches a steady state value of 40 μm (Figure 5.9E).

Next, the thinning condition will be presented (Figure 5.9E-H). The transition from 6.7 to 11 μm/sec exhibits significant stick-slip motion (Figure 5.9F). Here, crack spacing periodically varies between a larger and smaller value in the deposition direction, and also exhibits some lateral nonuniformity. Note that these increases and decreases in crack spacing do in fact correlate with increasing and decreasing film thickness, as confirmed by interference profilometry (Figure 5.3). Stick-slip motion

subsides and thin film morphology reaches steady state under a deposition speed of 11 μm/sec (Figure 5.9G). Crack spacing reaches a uniform value of 11 μm. Note that this is slightly thinner than the earlier 11 μm/sec condition—this difference is attributed to suspension depletion. As shown earlier, lower volume fraction will yield smaller crack spacing (Figure 5.6). In the transition from 11 to 16.7 μm/sec, significant "stick-slip" motion is observed, with correlative changes in crack spacing (Figure 5.9H). Again, at 16.7 μm/sec and faster speeds, coating do not exhibit cracking. It is important to note that stick-slip motion is observed under both thinning (Figure 5.9E-H) and thickening (Figure 5.9A-E) conditions. However, qualitatively, more exaggerated stick-slip transition regions are seen under thinning conditions, where coating speed is increased.

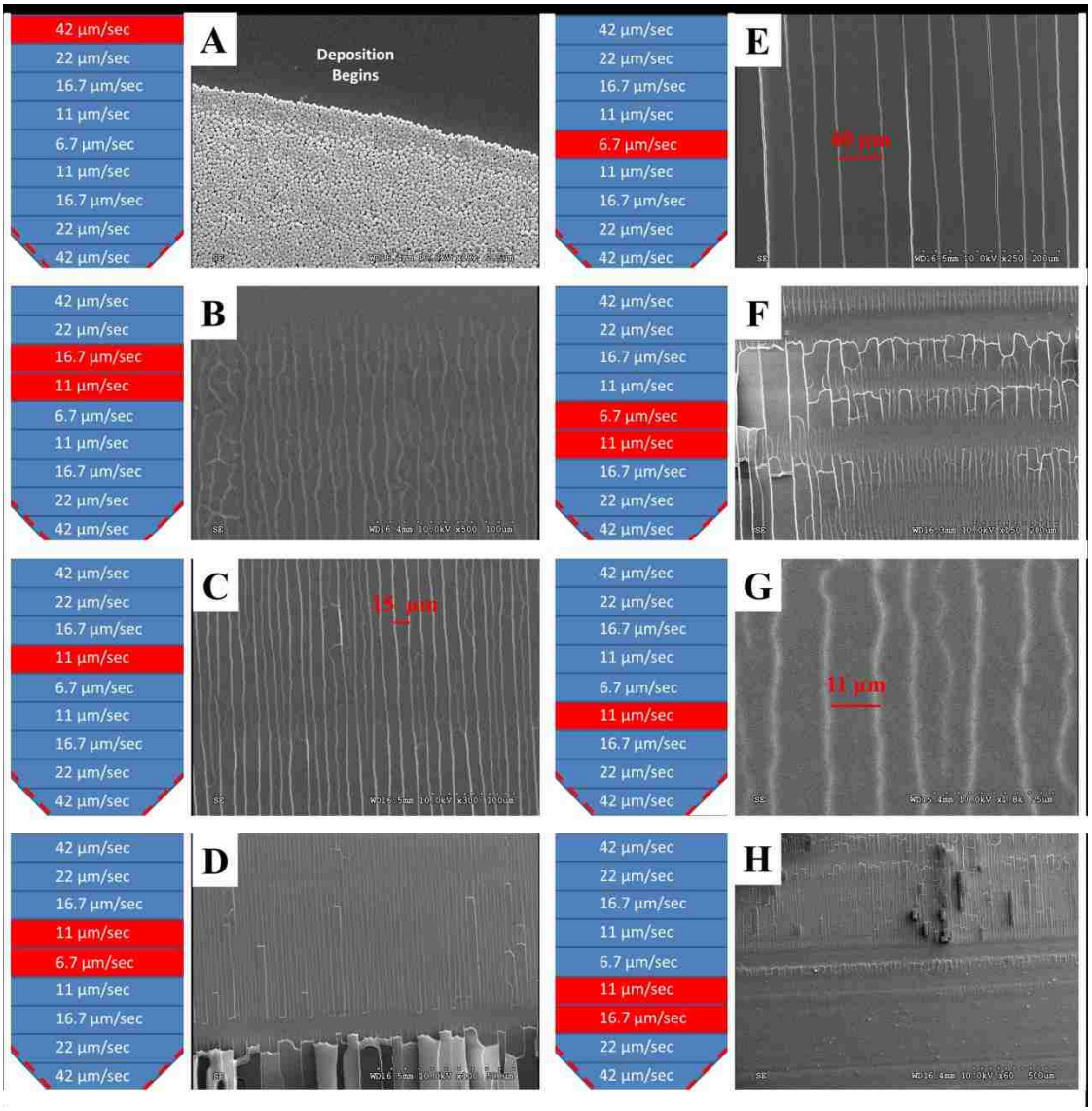

Figure 5.9: Data showing (A, B, C, D, E) increases and (E, F, G, H) decreases in crack spacing with changing film thickness (via deposition speed). In addition, transition regions (B, D, F, H) are highlighted. Especially in the thinning condition (E, F, G, H), with increasing deposition speed, stick-slip motion is observed, where crack spacing periodically varies. In both cases 16.7 µm/sec and faster speeds (A, B, H) do not exhibit cracking.

5.4: Conclusions and Impact

This work concerns deposited nanoparticle thin films. Increased coating thickness correlates with the onset and increased spacing between micro- to macroscale cracks. Coating thickness is varied through deposition speed, applied thermal gradients, and suspension volume fraction. In a significant process enhancement versus previous work, coating thickness is varied within individual experiments. This analysis from a batch to semi-batch methodology enables previously unattainable analysis of transition regions—in particular these results highlight the onset of stick-slip variability with changing coating thickness. Next steps could include complementary in-situ experiments to quantify crack formation mechanisms and timescales. Routh et al., by changing the timescales of evaporation and re-wetting latex films, cyclically control the formation and suppression of individual and aggregate cracks.[17,18] They demonstrate enormous plasticity in crack formation and evolution. Parallel experiments could be performed via in-situ confocal and optical microscopy, as well as interference profilometry.

5.5: References

1. Routh AF. Drying of thin colloidal films. *Reports of Progress in Physics*. 2013;76(046603):1-30.

2. Routh AF, Zimmerman WB. Distribution of particles during solvent evaporation from films. *Chemical Engineering Science*. 2004;59:2961-2968.

3. Patel MJ, Gundabala VR, Routh AF. Modeling film formation of polymer-clay nanocomposite particles. *Langmuir*. 2009;26(6):3962-3971.

4. Lee WP, Routh AF. Time evolution of transition points in drying latex films. *JCT Research*. 2006;3(4):301-306.

5. Gundabala VR, Lei C, Ouzineb K, Dupont O, Keddie JL, Routh AF. Lateral surface nonuniformities in drying latex films. *Aiche Journal*. 2008;54(12):3092-3105.

6. Konig AM, Bourgeat-Lami E, Mellon V, von der Ehe K, Routh AF, Johannsmann D. Dilational lateral stress in drying latex films. *Langmuir*. 2010;26(6):3815-3820.

7. Petersen C, Heldmann C, Johannsmann D. Internal stresses during film formation of polymer latices. *Langmuir*. 1999;15:7745-7751.

8. Routh AF, Russel WB. Deformation mechanisms during latex film formation: Experimental evidence. *Industrial and Engineering Chemical Research*. 2001;40:4302-4308.

9. Yow HN, Beristain I, Goikoetxea M, Barandiaran MJ, Routh AF. Evolving stresses in latex films as a function of temperature. *Langmuir*. 2010;26(9):6335-6342.

10. Lee WP, Gundabala VR, Akpa BS, Johns ML, Jeynes C, Routh AF. Distribution of surfactants in latex films: A rutherford backscattering study. *Langmuir*. 2006;22:5314-5320.

11. Gundabala VR, Routh AF. Thinning of drying latex films due to surfactant. *Journal of Colloid and Interfacial Science*. 2006;303(1):306-314.

12. Kleinert J, Kim S, Velev OD. Electric-field-assisted convective assembly of colloidal crystal coatings. *Langmuir*. 2010;26(12):10380-5.

13. Grosskreutz JC, McNeil MB. The fracture of surface coatings on a strained substrate. *Journal of Applied Physics*. 1969;40:355-359.

14. Lee WP, Routh AF. Why do drying films crack? *Langmuir*. 2004;20(23):9885-9888.

15. Lee WP, Routh AF. Temperature dependence of crack spacing in drying latex films. *Industrial and Engineering Chemical Research*. 2006;45:6996-7001.

16. Yow HN, Goikoetxea M, Routh AF. Effect of film thicknesss and particle size on cracking stresses in drying latex films. *Journal of Colloid and Interfacial Science*. 2010;352(2):542-548.

17. Dragnevski KI, Routh AF, Murray MW, Donald AM. Cracking of drying latex films: An ESEM experiment. *Langmuir*. 2010;26(11):7747-7751.

18. Goehring L, Clegg WJ, Routh AF. Plasticity and fracture in drying colloidal films. *Physical Review Letters*. 2013;110:0243301-1-0243301-5.

19. Dufresne ER, Corwin EI, Greenblatt NA, et al. Flow and fracture in drying nanoparticle suspensions. *Physics Review Letters*. 2003;81(22):4501-1-4501-4.

20. Weldon AL, Kumnorkaew PK, Wang B, Cheng XC, Gilchrist JF. Fabrication of macroporous polymeric membranes through binary convective deposition. *Acs Applied Materials & Interfaces*. 2012;4(9):4532-4540.

21. Kumnorkaew P, Ee Y, Tansu N, Gilchrist JF. Investigation of the deposition of microsphere monolayers for fabrication of microlens arrays. *Langmuir*. 2008;24(21):12150-12157.

22. Kumnorkaew P, Gilchrist JF. Effect of nanoparticle concentration on the convective deposition of binary suspensions. *Langmuir*. 2009;25(11):6070-6075.

23. Kumnorkaew P, Weldon AL, Gilchrist JF. Matching constituent fluxes for convective deposition of binary suspensions. *Langmuir*. 2010;26(4):2401-2405.

24. Wang B, Weldon AL, Kumnorkaew PK, Xu B, Gilchrist JF, Cheng X. Effect of surface nanotopography on immunoaffinity cell capture in microfluidic devices. *Langmuir*. 2011;27(17):11229-11237.

Chapter 6

Applications: Effect of Surface Nanotopography on Immunoaffinity Cell Capture in Microfluidic Devices

6.1: Introduction

Microfluidic cell isolation devices have recently found applications in tissue engineering,[1,2] clinical diagnosis,[3,4] and fundamental cell biology.[5,6] Immunoaffinity isolation based on specific cell surface markers attracts special attention due to its capability to distinguish cell types of similar physical properties in complex samples, for example, human blood.[4,7,8] Its ease of use makes it a good candidate for point of care settings.

Immunoaffinity cell capture generally takes one of two forms: target cells attach to either suspended magnetic beads[9] or interior surfaces of a microfluidic chip.[10] Cell–antibody interactions are more accurately controlled in the latter strategy, and as such yield higher capture efficiency and purity of target cells.[4] Toner's group has designed immunoaffinity microfluidics for reliable isolation of circulating cells at concentrations as low as 5 cells/mL from whole blood with average purity higher than 50%.[4,8] This

exceeds the performance of commercially available magnetic bead-based assays. These microchips have been shown to diagnose cancer,[4] infection,[11] and inflammatory[7] diseases with minimal sample handling.

To enhance cell interactions with antibody-functionalized device walls, several groups have employed capture beds with nanotopography. Wang et al. fabricated nanopillars to enhance contact frequency and duration of circulating tumor cells with functionalized substrates and increased capture yield by greater than 40%.[12] The King group deposited nanobeads and nanofibers in capillary channels to isolate stem cells and tumor cells.[13,14] Capture yield is increased by up to 100% in deposited versus smooth capillaries. While these studies suggest the positive effect of nanotopography on cell capture, nanopatterns studied contain either a single geometry or random structures that do not elucidate a detailed relationship. In a separate study, Tuttle et al. immobilized antibodies on surface-bound nanobeads 40 to 860 nm in diameter and tested their functionality by capturing antigen-coated fluorescent microspheres.[15] Specific capture increased continuously with the nanobead size. The results were suggested to stem from greater amounts of immobilized antibodies and an enhancement of collective antibody functionality on rough surfaces. Additionally, the Santore group investigated affinity between microbeads and patched charge capture surfaces with varying overall charge density and patch size.[16-18] Although these studies explored a variety of nanostructured geometries, the interaction of microbeads with rough or patterned surfaces may not translate fully to that of the cells. This study controls surface nanotopography, over a

greater range than that previously explored, and studies its influence on immunoaffinity capture of lymphocytes.

To create surfaces with reproducible and uniform nanotopography, smooth glass substrates are modified with a monolayer of close-packed, uniform-sized, silica nanobeads 100 to 1150 nm in diameter. These surfaces were incorporated as the base of microfluidic channels then functionalized with CD4 antibodies in order to capture CD4+ cells from human lymphocyte culture under continuous flow. In addition to depositing nanobeads with varying diameters, numerous flow rates and altered cell mechanical properties were evaluated in order to explore the mechanisms behind cellular adhesion with rough functionalized substrates.

6.2: Experimental Methods

6.2.1: Materials

Plain glass microslides (76 mm × 25 mm × 1 mm), ammonium hydroxide (NH_4OH, 28–30% and 29%), parafilm, Rhodamine B, and fetal bovine serum (FBS) were all purchased from Fisher Scientific (Pittsburgh, PA). Polydimethylsiloxane (PDMS) Sylgard 184 silicone elastomer kit, was purchased from Dow Corning Corporation (Midland, MI). 3-mercaptopropyl trimethoxysilane was obtained from Gelest Inc. (Morrisville, Pa). NeutrAvidin and *N*-[g-maleimidobutyryloxy]sulfosuccinimide ester (GMBS) were purchased from Pierce Protein Inc. (Rockford, IL). Biotinylated antihuman CD4 monoclonal antibody was obtained from Beckman Coulter (Brea, CA). Phosphate buffered saline (PBS), lyophilized bovine serum albumin (BSA), and RPMI-1640 cell media were obtained from Sigma Aldrich Chemical Co. (Milwaukee, WI). Penicillin–streptomycin (pen-strep) and Hoechst 33258 cell stain were received from Invitrogen (Carlsbad, CA). Ethyl alcohol (190 proof or 95%) was purchased from Pharmco-AAPER (Brookfield, CT). Ethanol (200 proof) was purchased from Koptec (King of Prussia, PA) and Pharmco-AAPER (Brookfield, CT). Tetraethyl orthosilicate (TEOS) (98%) was purchased from Sigma Aldrich (Milwaukee, WI) and Acros Organics (Pittsburgh, PA). SU8 photoresist was purchased from MicroChem (Newton, MA). Three-inch silicon wafers were purchased from Silicon Inc. (Boise, Idaho). Five hundred nanometer SiO_2 particles used to seed the core–shell semibatch synthesis were purchased from Fuso Chemical Co. (Japan).

6.2.2: Preparation of Silica Nanobeads

The particles used in this study have diameters between 100 and 1150 nm to cover the size range reported in the literature for cell capture enhancement. Silica particles within this size range form stable suspensions for coating by convective deposition. The spheres used in this study are referred to as nanoparticles or nanobeads in this paper, but are sometimes referred to as colloidal particles or microspheres in the literature. SiO_2 particles were prepared through batch, semi-batch, and continuous experiments taking advantage of core-shell Stöber synthesis as described in Appendix 9.6.1.

6.2.3: Preparation of Close-Packed Silica-Nanoparticle Substrates

Close-packed silica-nanobead substrates were prepared through convective deposition following the method reported in Chapter 2.[19]

A schematic of the convective deposition setup is shown in Chapter 2. For these experiments, the deposition blade angle was positioned 45° above the substrate as calibrated with a digital camera. Ten microliters of SiO_2/DI H_2O suspension was injected between the substrate and blade with a micropipette. The substrate was then linearly translated at the appropriate speed, as governed by specific suspension characteristics, for monolayer deposition.

Substrates covered with a smooth layer of TEOS were prepared as a control with identical surface chemistry but minimal roughness (root-mean-squared surface roughness < 2.0 nm, Appendix 9.6.2). Clean glass sides (root-mean-squared surface

roughness < 3.0 nm, Appendix 9.6.2) were soaked in an ethanol solution with TEOS for 15 min. Subsequently, slides were thoroughly washed with ethanol and blown dry with nitrogen.

6.2.4: Device Preparation

The nanoparticle-coated substrates were patterned in a 3 mm × 3 mm square region for cell capture. Beads outside the square capture region were removed with clean room adhesive tape. A microchannel was then bonded atop the substrate to enclose both the nanosphere patterned area and a bare glass control region.

Polydimethylsiloxane (PDMS) microchannels were prepared by pouring a 10:1 mixture of silicone elastomer base and silicone elastomer curing agent onto an SU8 mold patterned on a silicon wafer. Simple straight channels with dimensions 14 mm × 4 mm × 50 μm (L × W × H) were fabricated. PDMS was degassed and cured at 70 °C and microfluidic devices were cut out. Fluid inlets and outlets were drilled using a syringe needle. Nanobead-deposited substrates and microchannels were activated by oxygen plasma, then carefully aligned and heated for 5–10 min at 70 °C to produce permanent bonding. An image of a typical assembled device, with a schematic of the assembly process, is presented in Figure 6.1.

After assembly, the interior walls of the device, including the nanobead-deposited area and bare glass control region, were functionalized using a previously published method.[11] A 4% (v/v) solution of 3-mercaptopropyl trimethoxysilane in ethanol was injected into the device and allowed to incubate for one hour at room temperature. Next, the device was incubated with 0.01 μmol/mL GMBS in ethanol for

one hour at room temperature. NeutrAvidin was then immobilized to GMBS by incubating chamber surfaces with a 10 μg/mL NeutrAvidin solution in PBS (phosphate buffered saline) for at least one hour at 4 °C. Finally, 10 μg/mL of biotinylated antibody solution in PBS containing 1% (w/v) BSA was injected to react at room temperature for at least 15 min before cell capture experiments were performed.

6.2.5: Cell Culture and Live Cell Capture

Jurkat cells (human lymphocytes) were maintained following the ATCC protocol at a cell concentration of 10^5 cells/mL to 10^6 cells/mL using RPMI-1640 media supplemented with 10% (v/v) FBS and 1% (v/v) pen-strep. Cells were centrifuged and resuspended at 10^6 cells/mL in culture media prior to cell capture experiments. Cell suspension was delivered into the devices using a syringe pump at constant flow rates of 2 μL/min, 5 μL/min, or 8 μL/min for 15 min. These flow rates are within the optimal window for CD4+ T cell capture.[11] The sample injection time was chosen to ensure that target cells were not depleted from the suspension prior to reaching the downstream capture area. The numbers of cells captured in the patterned and bare glass regions of a given channel (Figure 6.1) were counted using a bright field microscope. The counts on bare glass served as an internal control to account for batch to batch variations in cell concentration and testing conditions.

As bare glass slides have slightly different chemistry versus silica beads synthesized by TEOS hydrolysis,[20] smooth TEOS coatings were also prepared, on glass substrates, as samples with minimal roughness. The normalized cell capture efficiency,

η, was obtained by taking the ratio of cell counts on silica beads versus those on smooth TEOS coatings using the following formula

$$\eta(R) = \frac{n_{nb(D)}}{n_{bg1}} \times \frac{n_{bg2}}{n_{TEOS}} \quad (6.1)$$

Where $n_{nb}(D)$ is the number of cells captured on nanobeads in the patterned region in Device 1,n_{bg1} and n_{bg2} are counts of cells captured on bare glass region within Device 1 and Device 2, respectively, and n_{TEOS} is the cell count from smooth TEOS-treated regions in Device 2.

6.2.6: Capture of Fixed Cells

In order to test the influence of the cell mechanical properties on capture, cells were centrifuged and resuspended in 1% glutaraldehyde in PBS (v/v) for 30 min. This glutaraldehyde fixation process cross-links proteins in the cell membrane and thus increases its modulus. The fixed cells were centrifuged, washed in PBS, and resuspended in culture media at a concentration of 10^6 cells/mL for capture. In a separate experiment, Jurkat cells were fixed with 1% glutaraldehyde in PBS for 30 min and then stained with Hoechst 33258 (0.5 mg/mL in PBS) for 10 min. After rinsing, the fixed and stained cells were mixed with untreated live Jurkat cells at a 1:1 ratio in culture media with a total cell concentration of 10^6 cells/mL. This cell mixture was also used for cell capture under selected bead size and flow rates. To test if glutaraldehyde fixation affected antibody–antigen binding, the same cell mixture was used for capture experiments in microchannels bonded to antibody-functionalized bare glass. The number of each cell type captured within the same imaging areas was counted and the two quantities compared.

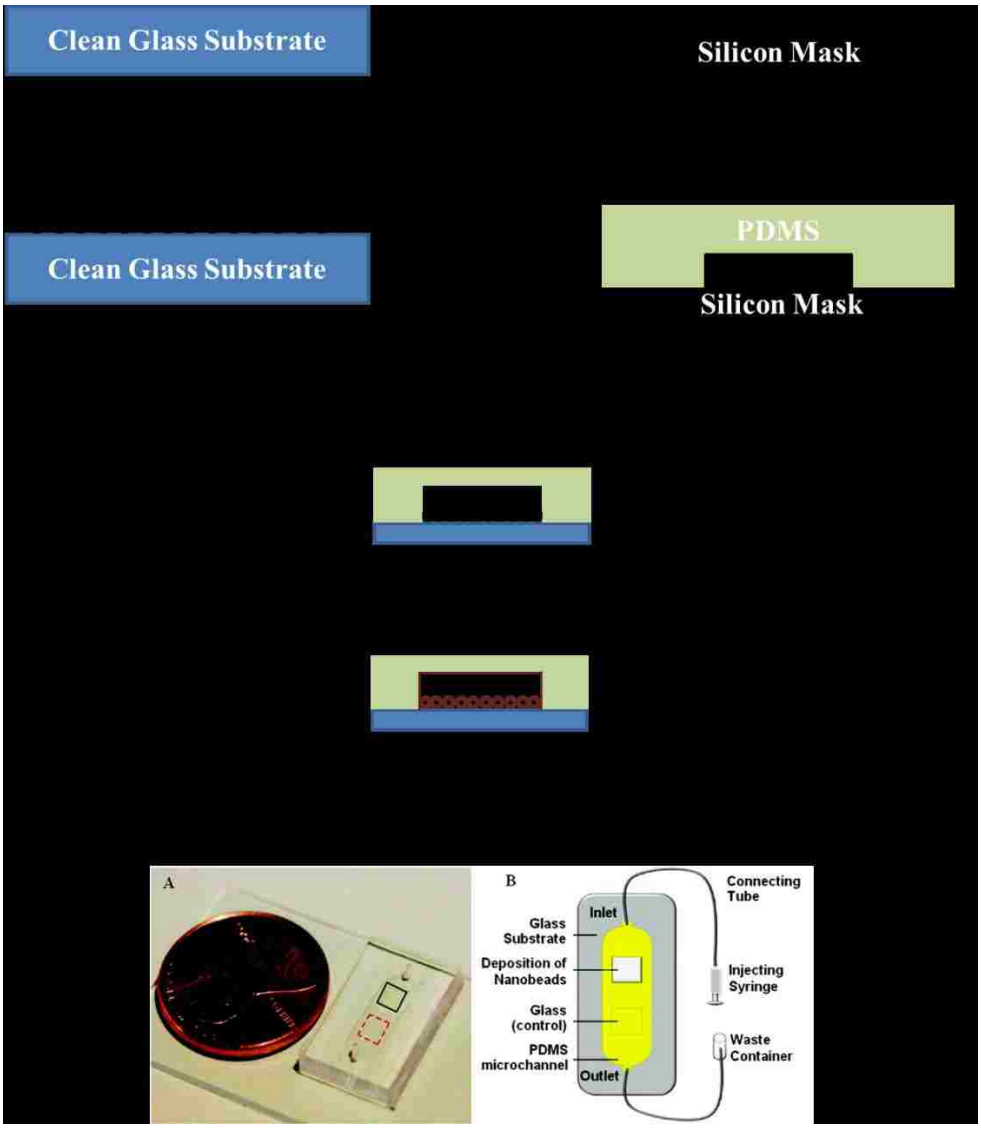

Figure 6.1: Cell capture microchip used in this study. This cartoon highlights the major steps in device assembly. (Left) A crystalline monolayer of particles is fabricated atop a glass substrate via convective deposition. (Right) In parallel, soft lithography is used to synthesize a PDMS microchannel. These components are activated through Oxygen plasma bonding and attached through heat treatment. The interior of the device is functionalized with a CD4 antibody for CD4+ T cell capture from Jurkat cell cultures (for more details, see text). The finished device is used for immunoaffinity cell capture trials. (A) Photograph of a typical microchannel. Deposited nanobead pattern (cloudy region in the black square) and a control region of bare glass (red dashed square) are enclosed in the same microchannel. (B) Schematic showing fully functioning device with nanobead-covered and control glass regions highlighted.

6.2.7: COMSOL Simulation

Flow above a layer of close-packed beads was simulated in *COMSOL Multiphysics 4.0* (COMSOL Inc., Burlington, MA). Assuming a 2D crystal structure, simulations are carried out atop a periodic cell of a hexagonal array of 1 μm spheres. A constant velocity is imposed three particle diameters from the substrate in order to investigate the near-field disturbance. The fluid is Newtonian and a volumetric flow rate of 2 μL/min renders a very small Reynolds number ($Re \ll 1$). Therefore, flow near the walls is self-similar and scales with bead size.

6.2.8: Cell Imaging by Confocal Microscopy

Antibody-immobilized cells on smooth glass substrate were imaged using a confocal laser scanning microscope (Visitech International, model vteye). The cells were stained by 0.16 mM Rhodamine B in the normal culture media for 10 min and imaged without further washing. The *z*-stack images were taken using 100x magnification and expressed as a 3D image with *ImageJ*.

6.2.9: Surface Characterization by Scanning Electron Microscopy (SEM) and Atomic Force Microscopy (AFM)

AFM measurements were carried out on a Nanoscale V AFM in tapping mode to characterize 100, 490, and 1150 nm individual particle roughness as well as the roughness of TEOS-coated and bare glass. Gwyddion was used for data analysis and visualization. Individual particle roughness values are documented as root mean squared (rms) roughness. SEM measurements were performed on all nanobead

depositions with iridium coating using a Hitachi 4300 instrument (Japan). The diameter and packing of nanobeads are documented in Figure 6.2.

6.2.10: Statistical Analysis

All cell capture experiments were repeated in at least 5 independent devices, except for Figure 6.6, where the experiments were repeated in at least 3 independent devices. The data were analyzed using two-tailed *t* tests. Two *p* values were calculated for the data points presented in Figure 6.3, Figure 6.5, and Figure 6.6: one from comparing the cell capture on nanobead surfaces to that on TEOS under the same flow rate; the other by comparing the cell capture on a particularly sized nanobead surface to its neighboring data point of a smaller nanobead diameter. When the *p* value between two data points was less than 0.1, their difference was considered statistically significant.

6.3: Results and Discussion

6.3.1: Preparation of Silica Bead Depositions

Close-packed silica–nanobead thin films were used to accurately control surface nanotopography in microchannels over a broad range of experimental conditions. The influences of these layers on immunoaffinity cell isolation were studied. Since the particle surfaces, glass, and TEOS-treated glass slides are all very smooth with an rms roughness less than a few nanometers by AFM measurements (Appendix 9.6.2), the surface roughness is mainly controlled by the radius of the particles. The arithmetic surface roughness is defined by the following equation:[21]

$$R_a = \sqrt{\frac{1}{n}\sum_{i=1}^{i=n} Yi^2} \tag{6.2}$$

Where R_a is the arithmetic surface roughness, n is the number of points along the top surfaces, and Y_i is the vertical distance of the ith point from the mean surface height. For close-packed nanobead depositions, R_a can be further expressed as:

$$R_a = \sqrt{\frac{1}{n}\sum_{i=1}^{i=n}\left(\int_{\theta=0}^{\theta=\frac{\pi}{2}} Rcos(\theta)\right)^2} = radius\ of\ nanobeads \tag{6.3}$$

Convective deposition was used to create ordered nanobead monolayers atop glass substrates. While humidity, particle size, suspension volume fraction, substrate speed, and blade angle all influence the packing quality of nanoparticles,[19] preliminary work showed that solely varying deposition speed was sufficient to obtain tune the deposition of hexagonally close-packed nanobead arrays. Particles were deposited from suspensions at 10.84–32.40% volume fractions in water. Optimized deposition speeds

for each particle size are summarized in Table 6.1. Close-packed morphologies of the deposited layers were verified with scanning electron microscopy (SEM). The corresponding nanoparticle layer morphologies are presented in Figure 6.2. The size range of nanobeads was chosen because they are on the same order of magnitude as the size of nanostructures on cell membrane, which was suggested to enhance cell capture previously.[12]

Even though the size of the nanobeads used in this study covers a broad range, the increased surface area for cell capture actually remains the same for all sizes and is independent of nanobead diameter as long as the beads have similar packing structure. This can be shown by the following calculation:

$$Total\ area\ for\ cell\ capture\ after\ nanobead\ deposition = \frac{Af}{\pi R^2} 2\pi R^2 = \frac{A\pi}{\sqrt{3}} \quad (6.4)$$

Where A is the surface area on the substrate covered by beads, f is the fraction of the substrate covered by beads, which is $\pi/(2\sqrt{3})$ for 2D hexagonal close-packing, and R is the radius of the nanobead. The capture surface area on the nanobead-covered substrates I~1.8 times of that on a flat substrate.

Size of SiO_2 Beads (±1 SD)	Concentration (v/v in DI H_2O)	Optimal Speed
100 ± 10 nm	12.84%	3 μm/s
309 ± 30 nm	12.84%	6 μm/s
319 ± 17 nm	11.80%	33 μm/s
407 ± 23 nm	10.84%	10 μm/s
460 ± 20 nm	26.50%	21 μm/s
490 ± 20 nm	25.90%	58 μm/s
700 ± 24 nm	32.40%	17 μm/s
928 ± 16 nm	15.20%	42 μm/s
1150 ± 24 nm	12.50%	67 μm/s

Table 6.1: Concentration and Optimal Deposition Speed of Nanobeads Used in This Study

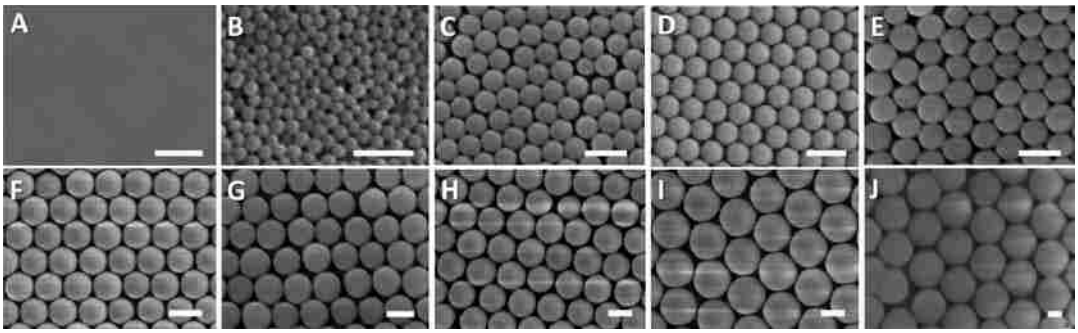

Figure 6.2. Scanning electron microscope images of close-packed particle arrays with diameters of (B) 100 nm, (C) 309 nm, (D) 319 nm, (E) 407 nm, (F) 460 nm, (G) 490 nm, (H) 700 nm, (I) 928 nm, and (J) 1150 nm. Image (A) shows a glass surface coated with a smooth layer of TEOS. All scale bars = 500 nm. Standard deviations of the particle sizes are summarized in Table 6.1

6.3.2: Live Cell Capture of Silica-Nanobead Substrates

Next, the silica nanobead deposited substrates were enclosed within PDMS microchannels and functionalized with CD4 antibodies to capture CD4+ T cells under continuous flow. Three different flow rates, 2, 5, and 8 μL/min, covering the optimal range for CD4+ T cell capture, were evaluated.[11] Jurkat cells, a human T lymphocyte cell line, were used for capture experiments, and 23.8% of the cells were found to be CD4+ via flow cytometry (Appendix 9.6.3). The total number of captured cells was enumerated as specific capture since the surface chemistry has been shown to yield greater than 95% purity.[11] The number of cells captured on the silica nanobead deposition was normalized to that on a functionalized smooth TEOS surface (approximating a continuous array of infinitely small silica beads) using the Equation 6.1. This normalization minimizes the effects of any run-to-run nonuniformity and allows direct comparison of capture efficiencies with different surface nanotopography.

Figure 6.3A shows a typical image of cells captured on the nanopatterned surface. Typically, ~50 cells/mm^2 were captured with 15 min sample delivery. Reversing the flow direction did not affect capture results, indicating that the capture difference in the up- and downstream regions was not due to target cell depletion. Figure 6.3B–D shows that nanopatterned surfaces generally improve capture efficiency versus smooth substrates; however, the two do not have a monotonic relationship. Statistically significant data sets are highlighted. Data points with * have a statistically different cell capture compared with capture on TEOS under the same flow rate with $p < 0.1$. Data points in red circles have statistically different cell capture as compared to

their preceding neighbor (neighboring data set of a smaller nanobead size) with $p < 0.1$. The cell capture efficiency profile strongly depends on flow rate. At 2 μL/min (wall shear stress of 5.5×10^{-5} N/m^2), the capture efficiency increases nearly continuously from 100%, the normalization value on smooth TEOS (control), to 160% on roughened surfaces with the largest beads (1150 nm). Interestingly, the capture efficiency dips on surfaces coated with 700 nm particles to the level of the control, smooth TEOS, samples. At 5 μL/min (wall shear stress of 1.385×10^{-4} N/m^2), the cell capture efficiency first climbs with increased surface roughness, and gradually decreases as bead size increases. An outlier to this trend is a significant decrease in capture efficiency with a 407 nm bead-patterned substrate—this yielded only 60% capture as compared with the smooth TEOS surface. The 8 μL/min (wall shear stress of 2.215×10^{-4} N/m^2) trend follows the 5 μL/min capture profile. The cell capture efficiency nearly doubles for the smallest deposited particles, then decreases with nanobeads greater than 700 nm in diameter. The capture profile shows two significant dips at 407 and 490 nm where the capture efficiencies are comparable to those on smooth surfaces. Thus, cell capture on rough surfaces is dependent not only on surface topography, but also on wall shear stress.

The complex capture profiles are not expected to result from increased surface area after nanobead deposition. The differences between TEOS and nanobead surfaces are likely due to surface area increase (an 80% increase in surface area with nanobead deposition), but differences between the various beads are not (surface area is independent of nanobead size under hexagonal close-packing). They are also likely not

a result of antibody surface chemistry or antibody density as different-sized beads were synthesized under the same TEOS hydrolysis reaction with only reaction time and reagent concentration varying. In addition, treating a monolayer of nanoparticle deposition with a TEOS solution followed with antibody conjugation does not change cell capture (Appendix 9.6.4); this also suggests comparable surface chemistry among the different roughness conditions.

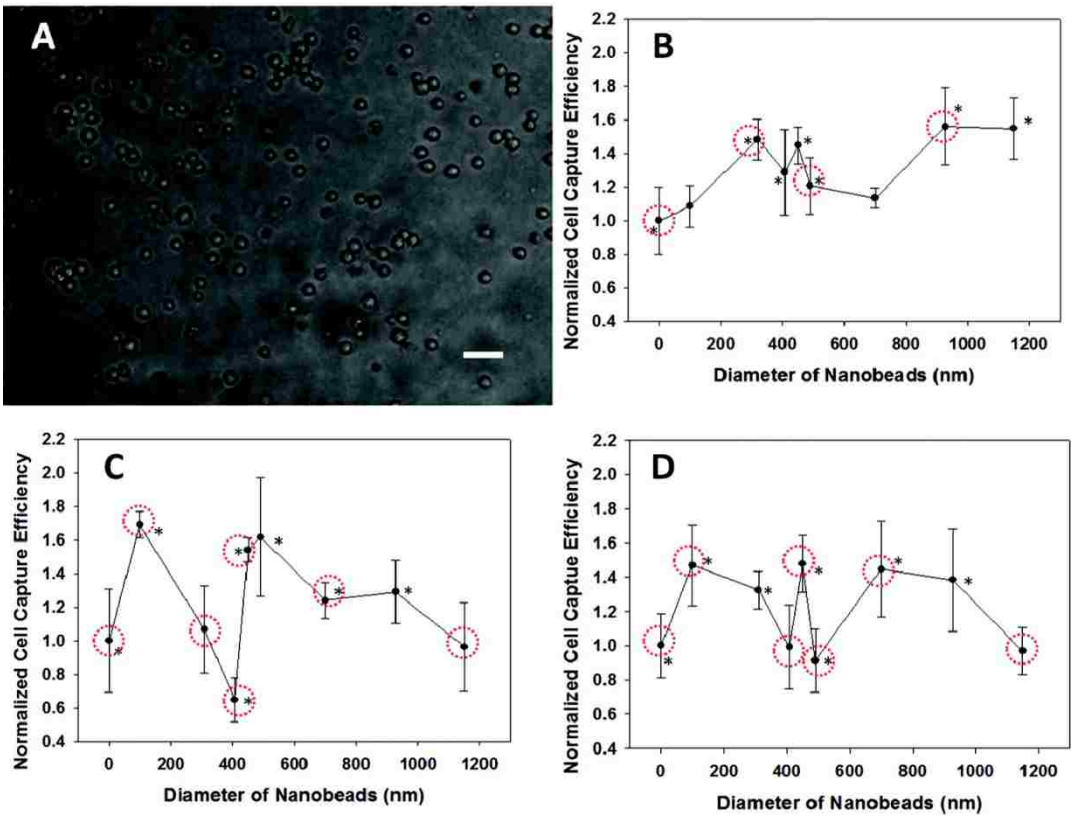

Figure 6.3: (A) Bright field image showing CD4+ cells captured on a surface patterned with 928 nm beads under 5 μL/min sample flow (scale bar = 50 μm). (B–D) Normalized capture efficiency on nanobead-covered substrates. Cell suspension flow rates were (B) 2 μL/min, (C) 5 μL/min, and (D) 8 μL/min. The numbers of cells captured on the silica nanobead surfaces were normalized to those on smooth TEOS-coated surfaces (approximating a particle layer of infinitely small particles) for direct comparison of capture efficiencies. Error bars show one standard deviation in 5–10 trials. Data points labeled with * have a statistically different cell capture compared with the capture on TEOS with $p < 0.1$, while data points in red circles have a statistically different cell capture compared to its preceding neighbor (neighboring data set of a smaller nanobead size) with $p < 0.1$.

Cell capture on rough surfaces under continuous flow could be influenced by cell movement near substrates, shear induced deformation, and increased capture surface area as proposed previously. Inertial migration of flowing cells, however, should not be a main contributor to the complex capture patterns as the Reynolds number Re is much smaller than 1 under all flow conditions. Numerical simulation (Figure 6.4) confirms that the flow is essentially undisturbed at heights roughly two bead-diameters from the bottom substrate. Even the largest particles deposited here (1150 nm in diameter) are much smaller than Jurkat cells (7–20 μm in diameter[22]) captured. As a result, cell movement under these near-Stokes flow conditions should not significantly undulate with surface topography or lead to any abrupt changes to cell migration at the dipping points in the capture efficiency curves. In addition, in these dilute cellular suspensions, multibody hydrodynamic interactions are also minimal. The only nonlinear behavior in this near-wall interaction is the elasticity of the cellular membrane. Thus it is hypothesized that mechanical deformation of cells on the cellular and subcellular level is the key factor contributing to the complex capture profiles observed.

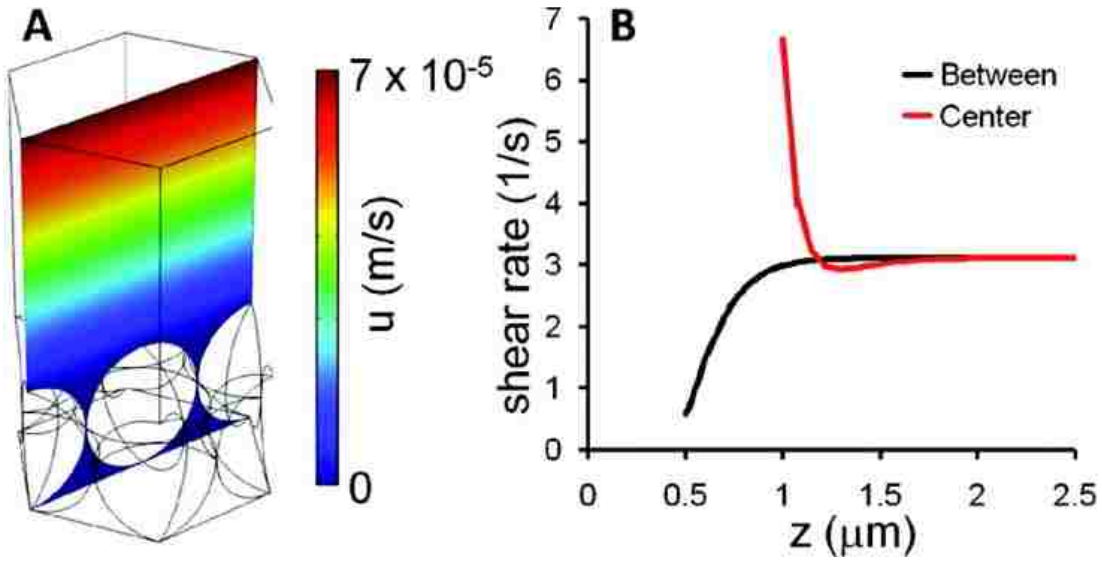

Figure 6.4: (A) Fluid velocity profile at a cross section parallel to the flow direction simulated by *COMSOL*. Velocities and shear rates correspond to 2 μL/min. Not far from the beads, the flow profile nears *Poiseuille* conditions and is essentially undisturbed by the bead patterns. The shear rate along the *z*-direction, above the bead center, and above the two bead contact point at various height points were computed and shown in (B). Greater than two bead diameters from the glass surface, velocity differences between the two points are effectively zero and the flow is no longer disturbed by the imposed roughness.

6.3.3: Capture of Glutaraldehyde Fixed Cells on Silica-Nanobead Surface

To evaluate the hypothesis that cell mechanical properties influence their capture, Jurkat cells were fixed with 1% glutaraldehyde and used in capture experiments under 5 μL/min flow. Glutaraldehyde cross-links amine groups and thus increases the Young's modulus of cells by more than an order of magnitude.[23] Figure 6.5 shows the normalized capture efficiency of fixed cells: capture efficiency increases slightly for the smallest nanobead layers then gradually decreases. With fixed cells, no dip in cell capture efficiency is seen, and the effects of surface topography are greatly dampened—no statically significant difference was found when neighboring data points were compared or when capture on nanobeads was compared to that on flat TEOS.

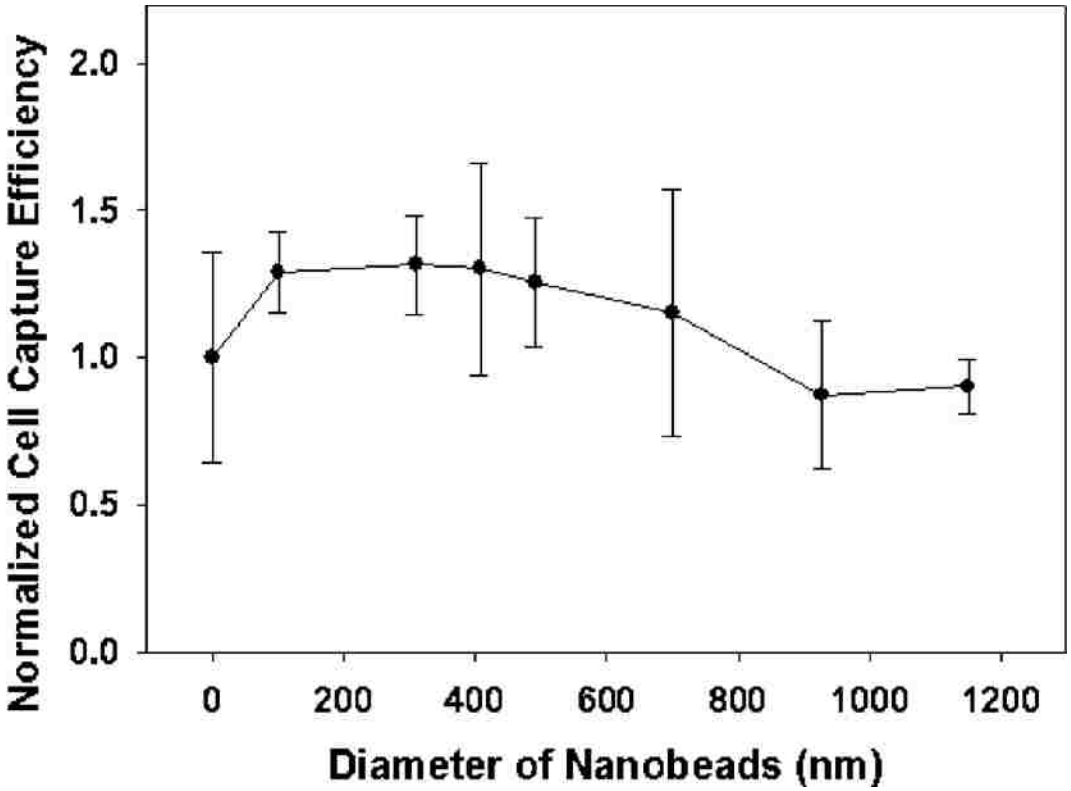

Figure 6.5: Capture of glutaraldehyde-fixed Jurkat cells from culture media onto nanobead-patterned substrates at 5 μL/min. Numbers of cells captured on nanobeads were normalized to those captured on flat TEOS-coated surfaces. The error bars represent 1 standard deviation as calculated from greater than four repeats of each condition. *P* value was found to be greater than 0.126 for every data point, either comparing with capture efficiency on TEOS or its preceding neighbor, indicating that capture on the various surfaces was not significantly different.

To further verify the different capture between live and fixed cells, live (triangles in Figure 6.6) and fixed (circles) Jurkat cells were mixed at a 1:1 ratio for capture on 490 nm beads under 5 μL/min (empty symbols) and 8 μL/min flow (solid symbols). As shown in Figure 6.6, the normalized capture efficientcy is consistent with the results in Figure 6.3 and Figure 6.5 using live or fixed cells alone under the respective conditions. In addition, capture of glutaraldehyde-fixed cells is much less sensitive to changes in surface roughness—under 5 μL/min flow, the *p*-value is 0.7597 when comparing the capture of fixed cells on 490 nm bead monolayers with that on smooth TEOS. There is a significant difference for live cell capture on the two surfaces ($p = 0.0002$). Live cell capture is also highly sensitive to the flow rate, as shown by the significant differences of capture efficiency at the two tested flow rates ($p = 0.00518$).

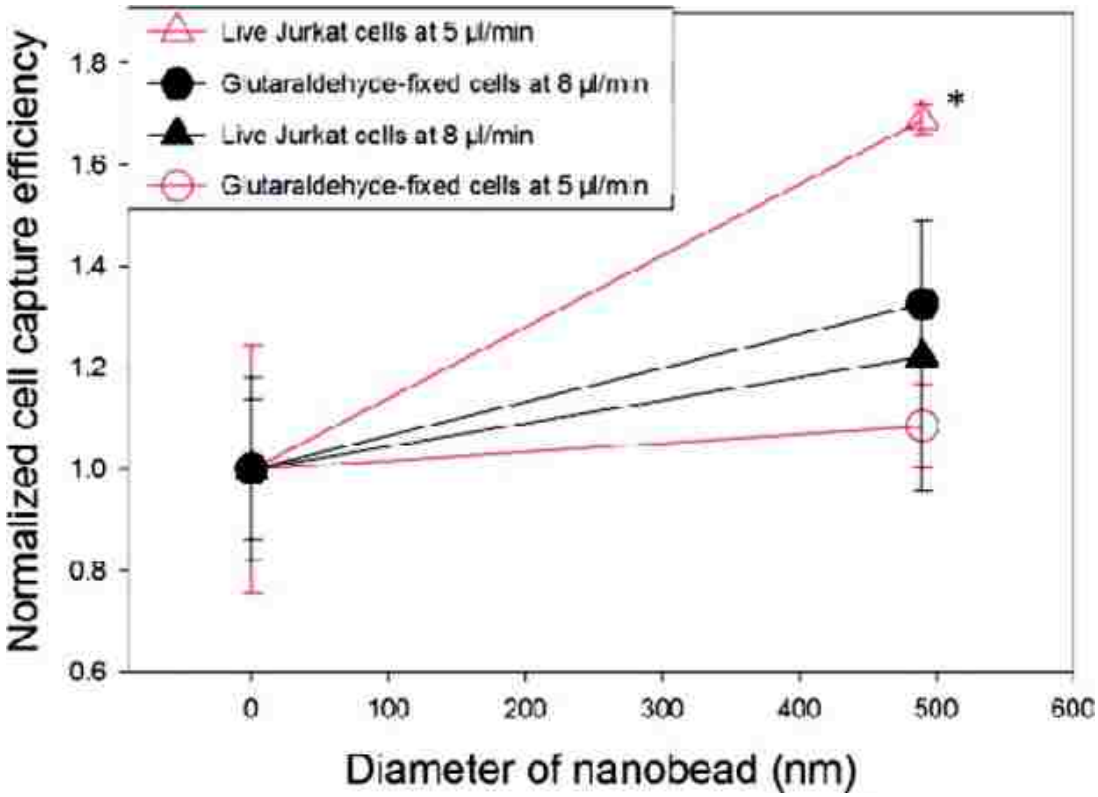

Figure 6.6: Capture of glutaraldehyde-fixed and live Jurkat cell mixture (1:1 ratio) from culture media onto 490 nm nanobead-patterned substrates at 5 µL/min and 8 µL/min. Numbers of cells captured on nanobeads were normalized to those captured on flat TEOS-coated surfaces. The error bars represent 1 standard deviation as calculated from greater than three repeats under each condition. Data points labeled with * have a statistically different cell capture compared with the capture on TEOS with $p < 0.1$.

To test if glutaraldehyde fixation interferes with antibody–antigen binding chemistry, Jurkat cells were fixed with glutaraldehyde then their nuclei were stained with Hoechst 33258. Afterward, fixed and stained Jurkat cells were mixed with live cells at a 1:1 ratio. The cell mixture was manually injected into a PDMS microchannel, bonded to functionalized bare glass, and incubated under static conditions for 15 min. The device was rinsed and captured cells were counted—Figure 6.7 shows a representative image. Average cell counts from multiple devices and imaging areas show that identical numbers of fixed and untreated cells were captured. This suggests that the different capture profiles of live and fixed cells are not due to altered antibody–antigen interactions.

Figure 6.7: Representative bright field image showing the capture of glutaraldehyde-fixed (blue) and live (gray) Jurkat cells mixed 1:1 in culture media on antibody-functionalized bare glass substrates under static incubation. Average cell counts from multiple devices and imaging areas show that identical numbers of fixed and untreated cells were captured. This indicates that the fixation procedure does not interfere with antibody–antigen recognition. Scale bar = 50 μm.

A direct outcome of glutaradehyde fixation is significant enhancement of cell moduli.[23] Live CD4+ cells have a flexible membrane undulating even in static culture medium (Appendix 9.6.5). The varying levels of shear deformation under different flow rates are expected to influence the interaction area between cells and antibody-coated substrates. Although shear deformation on the cellular level may contribute to flow rate dependent capture, it does not fully explain cellular interaction with regards to enhanced nanotopography—nanoparticles are an order of magnitude smaller in diameter than cells used in this study.

Instead, a more plausible explanation of the capture dependence on surface nanofeatures and wall shear stress may arise from protruding nanostructures on the cell membrane. The predominant features on the surface of human lymphocytes are microvilli[24] that consist of bundles of cross-linked actin filaments.[24] CD4 receptors, the target antigen in this study, are preferentially located on the microvilli ends.[25] Indeed, cell extensions, a few hundred nanometers in diameter, were observed tethering cells to antibody functionalized substrates (Figure 6.8), and indicating interactions between membrane nanostructures and the capture bed. With dimensions 300 to 400 nm in length, ~100 nm in width, and a spatial distribution of ~4/μm[2,24] microvilli are comparable in size to the nanobeads used in this study. This comparable scale suggests a physical complementarity between certain substrate nanotopographies and the cell surface in addition to specific antibody–antigen interactions. Complementary interactions with nanopillars have been reported to enhance capture yield of circulating tumor cells.[12] Optimal capture yield occurs with 6 μm or longer nanopillars which are

on the same length scale as the protrusion lengths of tumor cells.[12] In this system, while the amount of accessible antibody may increase continuously with the nanobead diameter,[15] the physical complementarity has a nonmonotonic dependence on the nanoparticle size. The interplay of these two factors may strongly contribute to the complex capture profiles on the nanostructured surfaces. Interestingly, the tethers observed in Figure 6.8 are much longer than the length of microvilli measured on unattached lymphocytes.[24] These long extensions may be a result of microvilli being stretched after initial tethering. The diameter of these extensions is also slightly thicker than those measured by AFM or SEM,[24] likely due to optical diffraction. Microvilli are highly dynamic and deformable, and susceptible to shear forces, in order to help cells contact and bind to patterned substrates.[26,27] Thus they can experience different shear deformation under varying experimental conditions and contribute to flow dependence in cell capture. While fixed cells also present microvilli,[24] their lack of dynamics and weak response to shear forces makes capture of fixed cells much less sensitive to surface topography.

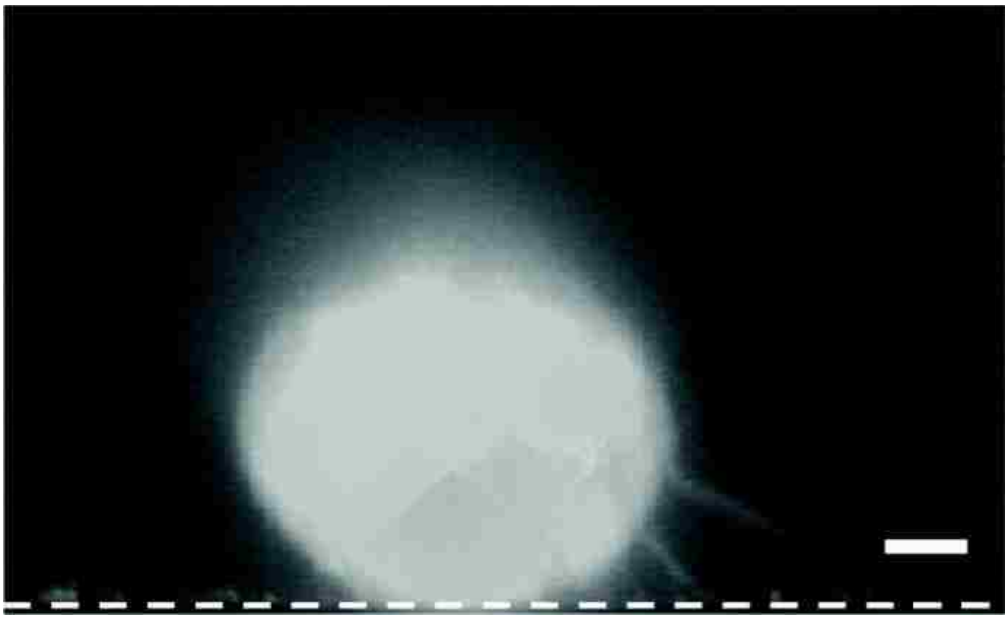

Figure 6.8: A confocal *Z*-stack image showing tethers from a Rhodamine B stained Jurkat cell to an antibody functionalized smooth glass substrate (scale bar = 2 μm). After cell capture from continuous flow on an antibody-treated smooth glass slide, the flow was stopped and confocal images were acquired. The fluid flowed from the right to the left for cell capture, and the substrate is located at the bottom of the image as indicated by the dashed line. The fuzziness of the membrane away from the substrate is a result of spontaneous membrane fluctuation.

6.4: Conclusions and Impact

Close-packed silica bead layers provide a powerful tool to systematically control surface roughness and enhance immunoaffinity cell capture under continuous flow. Interestingly, complicated cell capture efficiency profiles were observed across several flow rates and surface nanotopographies. Hardening cells through glutaraldehyde fixation significantly dampened this dependence. The nonmonotonic relationships between the capture efficiency and surface roughness under various flow rates are likely the results of complementarity and shear deformation of nanoprotrusions on the cell membrane. Future studies plan to extend the length scale and investigate the influence of substrate microstructures on cell capture. This relationship between surface topography and cell capture efficiency, once established, will enable more rational design of cell capture devices.

6.5: References

1. Plouffe BD, Radisic M, Murthy SK. Microfluidic depletion of endothelial cells, smooth muscle cells, and fibroblasts from heterogeneous suspensions. *Lab on a Chip*. 2008;8(3):462-472.

2. Gomez-Sjoberg R, Morisette DT, Bashir R. Impedance microbiology-on-a-chip: Microfluidic bioprocessor for rapid detection of bacterial metabolism. *J Microelectromech Syst*. 2005;14(4):829-838.

3. Du Z, Colls N, Cheng KH, Vaughn MW, Gollahon L. Microfluidic-based diagnostics for cervical cancer cells. *Biosens Bioelectron*. 2006;21(10):1991-1995.

4. Nagrath S, Sequist LV, Maheswaran S, et al. Isolation of rare circulating tumour cells in cancer patients by microchip technology. *Nature*. 2007;450(7173):1235-1239.

5. Liu Y, Guo S, Zhang Z, et al. A micropillar-integrated smart microfluidic device for specific capture and sorting of cells. *Electrophoresis*. 2007;28(24):4713-4722.

6. Faley S, Seale K, Hughey J, et al. Microfluidic platform for real-time signaling analysis of multiple single T cells in parallel. *Lab on a Chip*. 2008;8(10):1700-1712.

7. Kotz KT, Xiao W, Miller-Graziano C, et al. Clinical microfluidics for neutrophil genomics and proteomics. *Nat Med*. 2010;16(9):1042-1047.

8. Stott SL, Hsu C, Tsukrov DI, et al. Isolation of circulating tumor cells using a microvortex-generating herringbone-chip. *Proc Natl Acad Sci U S A*. 2010;107(43):18392-18397.

9. Neurauter AA, Bonyhadi M, Lien E, et al. Cell isolation and expansion using dynabeads((R)). *Cell Separation: Fundamentals, Analytical and Preparative Methods*. 2007;106:41-73.

10. Hashimoto M, Kaji H, Nishizawa M. Selective capture of a specific cell type from mixed leucocytes in an electrode-integrated microfluidic device. *Biosens Bioelectron*. 2009;24(9):2892-2897.

11. Cheng X, Irimia D, Dixon M, et al. A microfluidic device for practical label-free CD4+T cell counting of HIV-infected subjects. *Lab on a Chip*. 2007;7(2):170-178.

12. Wang S, Wang H, Jiao J, et al. Three-dimensional nanostructured substrates toward efficient capture of circulating tumor cells. *Angewandte Chemie-International Edition*. 2009;48(47):8970-8973.

13. Hughes AD, King MR. Use of naturally occurring halloysite nanotubes for enhanced capture of flowing cells. *Langmuir*. 2010;26(14):12155-12164.

14. Han WJ, Allio BA, Foster DG, King MR. Nanoparticle coatings for enhanced capture of flowing cells in microtubes. *ACS Nano*. 2010;4(1):174-180.

15. Tuttle PV, Rundell AE, Webster TJ. Influence of biologically inspired nanometer surface roughness on antigen-anti body interactions for immunoassay-biosensor applications. *Int J Nanomedicine*. 2006;1(4):497-505.

16. Kalasin S, Martwiset S, Coughlin EB, Santore MM. Particle capture via discrete binding elements: Systematic variations in binding energy for randomly distributed nanoscale surface features. *Langmuir*. 2010;26(22):16865-16870.

17. Kalasin S, Santore MM. Sustained rolling of microparticles in shear flow over an electrostatically patchy surface. *Langmuir*. 2010;26(4):2317-2324.

18. Santore MM, Kozlova N. Micrometer scale adhesion on nanometer-scale patchy surfaces: Adhesion rates, adhesion thresholds, and curvature-based selectivity. *Langmuir*. 2007;23(9):4782-4791.

19. Kumnorkaew P, Ee Y, Tansu N, Gilchrist JF. Investigation of the deposition of microsphere monolayers for fabrication of microlens arrays. *Langmuir*. 2008;24(21):12150-12157.

20. Tabatabaei S, Shukohfar A, Aghababazadeh R, Mirhabibi A. Experimental study of the synthesis and characerisation of silica nanoparticles via the sol-gel method. *Journal of Physics: Conference Series*. 2006;26:371-374.

21. Huang J, Hu G, Orkoulas G, Christofides PD. Dependence of film surface roughness and slope on surface migration and lattice size in thin film deposition processes. *Chemical Engineering Science*. 2010;65(23):6101-6111.

22. Deng JD, Schoenbach KH, Buescher ES, Hair PS, Fox PM, Beebe SJ. The effects of intense submicrosecond electrical pulses on cells. *Biophys J*. 2003;84(4):2709-2714.

23. Lulevich V, Zink T, Chen H, Liu F, Liu G. Cell mechanics using atomic force microscopy-based single-cell compression. *Langmuir*. 2006;22(19):8151-8155.

24. Majstoravich S, Zhang JY, Nicholson-Dykstra S, et al. Lymphocyte microvilli are dynamic, actin-dependent structures that do not require wiskott-aldrich syndrome protein (WASp) for their morphology. *Blood*. 2004;104(5):1396-1403.

25. Singer II, Scott S, Kawka DW, et al. CCR5, CXCR4, and CD4 are clustered and closely apposed on microvilli of human macrophages and T cells. *J Virol*. 2001;75(8):3779-3790.

26. Amieva MR, Furthmayr H. Subcellular-localization of moesin in dynamic filopodia, retraction fibers, and other structures involved in substrate exploration, attachment, and cell-cell contacts. *Exp Cell Res*. 1995;219(1):180-196.

27. Pospieszalska MK, Ley K. Dynamics of microvillus extension and tether formation in rolling leukocytes. *Cellular and Molecular Bioengineering*. 2009;2(2):207-217.

Chapter 7

Applications: Fabrication of Macroporous Polymer Membranes through Binary Convective Deposition

7.1: Introduction

Applications in biomedicine form one of the most important synthetic membrane market segments.[1,2] Nano- and microporous media with pore sizes comparable to bioparticles and biomolecules, i.e. mesopores (2–50 nm) and slightly larger, have found a wide range of utilities in biomedicine including biosensing,[3,4] targeted drug delivery,[5,6] immunoisolation,[7,8] dialysis,[9] tissue engineering,[10,11] bioseparation,[12,13] and bioanalytical[14] devices.

As size exclusion media, it is desirable to have membranes with pore sizes matching target sizes, from molecular to cellular scale, and high porosity. Conventional porous polymeric materials created by foaming, high internal phase emulsion (HIPE) polymerization, and phase separation[15] generally exhibit broad pore size distributions, random pore geometry, and are relatively thick.[16,17] As a result, these materials

generally possess poor size cutoff properties and low transport rates. Alternate synthesis methods, such as track etching by nuclear fission fragments, have been developed to improve pore size distributions, pore structure, and pore geometry of polymeric membranes. These, however, face limitations of low porosity and random pore distribution. Other approaches to improve the physical properties of the mesopores include lithography and focused ion beam etching,[17-19] but these usually require sophisticated clean room facilities and sometimes have very low throughput. Membranes fabricated thorough block copolymer self-assembly followed by selectively etching the sacrificial blocks exhibit excellent biofiltration selectivity.[20] However, the pore size is limited by the self-assembled domain size, which ties to the macromolecular radius of gyration and is usually less than a few tens of nanometers.[21,22] Furthermore, composition of the block copolymer membranes is limited to those capable of forming segregation structures. Inorganic membranes synthesized electrochemically (e.g., anodic aluminum oxide),[23-25] by nanoparticle templating (e.g., porous silica),[26] or by self-assembly[27,28] have desirable physical structures and are scalable, but stiffness and lack of ductility make them hard to handle. In this study, binary particle suspensions were deposited through convective deposition in order to fabricate membranes that are highly selective with uniform[29] and well-defined pore size,[30] mechanical integrity,[31] and high potential for functionalization[32] and therefore are resistant to fouling.[33] Most membrane fabrication techniques are limited by one or multiple of these factors and/or scalability whereas convective deposition is enormously versatile in each regard.[34]

Recently, a generic templating method has been proposed to fabricate porous membranes of versatile chemistry and with a broad range of pore sizes. The membranes are obtained through the selective removal of the porogen in a two-phase thin film.[35-37] The key step in this approach is to deposit particles controllably, which has been achieved with many methods including spin coating,[38] epitaxy,[39,40] optical tweezers,[41] electrophoretic assembly,[42] and convective deposition.[43-45] Of these approaches, convective deposition yields regular particle layers quickly, controllably, and repeatedly. Convective deposition has been used previously for the formation of solid and porous thin films. Dip coating is a widely used and accepted technique for thin film fabrication. Boudreau et al. have used convective deposition through dip coating to assemble and grow zeolite layers on glass.[46] Bohaty et al. fabricated membranes through dip coating of glass substrates with SiO_2 particle suspension.[47] Extending beyond the idea of dip coating, a notably slow process, as a means of convective deposition, Yuan et al. fabricated mesoporous SiO_2 thin films through rapid convective deposition with a linear motor-driven evaporating meniscus.[48] However, these thin films were very thin and thus required fabrication atop a support. Advantages to the fabrication of membranes through convective deposition include the low cost of materials and equipment, a highly repeatable and versatile fabrication process, as well as high porosity. By selecting appropriate matrix chemistry or surface modification post-fabrication, the membrane can be rendered resistant to fouling and resilient under backflushing or crossflow. Convective deposition gives large flexibility in terms of materials and the potential to functionalize membranes and enhance bioseparations. The

aforementioned research by Boudreau et al. as well as Bohaty et al. show the successful functionalization of assembled zeolite and SiO_2 films through silane treatments respectively.[46,47] Also, Lee et al. perform enantiomeric drug separations with antibody-functionalized alumina membranes and Létant et al. use biotin-functionalized silicon membranes to capture particles modeling viruses and bacteria.[13,49]

In this study, convective deposition was used to create crystalline thin films containing two types of particles, nanoparticles that remain as the polymeric membrane and larger microspheres that are sacrificed to form cavities and pores. A thin film consisting of ordered SiO_2 microspheres and polystyrene (PS) nanoparticles was codeposited with highly uniform local microstructure, long-range morphology, and film thickness. After melting the PS particles and etching away SiO_2, a continuous PS porous phase was obtained. This convective deposition process involves the translation of a meniscus of suspension across a glass substrate under a glass blade. Prior work on convective assembly studies the self-organization of particles and how factors like blade angle and hydrophobicity, as well as deposition speed and glass treatment, affect the resultant thin film.[50] This method was used to fabricate composite thin films by consecutive depositions of SiO_2 microspheres followed by polystyrene (PS) nanoparticle depositions in order to dramatically improve the light extraction efficiency of LEDs.[50] Lenhoff and Velev describe the gravitational sedimentation of template colloidal crystals. Infiltration of a second constituent, and subsequent removal of the template, leaves behind a porous structure.[51] Alternatively, as used in this study, both the oxide and polymer phases can be codeposited in a single step; these binary

depositions yield crystalline monolayers with long-range order only when microsphere and nanoparticle component fluxes are matched.[52,53] The key difference between this study and previous studies is that codeposition decreases the complexity of the membrane fabrication process, increases the ability to control membrane fill fraction, scales up easily, and is consistent over longer ranges than consecutive unary depositions.

The convective deposition of binary suspensions is an ideal method for the repeatable fabrication of membranes with uniform[29] and prescribed pore sizes,[30] ordered microstructure, targeted morphology, and customizable thickness. Through tuning the sizes of the larger and smaller constituents it is simple to optimize membrane pore size for particular applications. Advantages to the fabrication of membranes through convective deposition include the low cost of materials and equipment and the highly repeatable and versatile fabrication process. These membranes are highly porous while remaining mechanically strong.[31] They also hold a high potential for functionalization[32] and therefore are resistant to fouling[33] and are resilient under crossflow or backflushing. Most membrane fabrication techniques are limited by one or multiple of these factors and/or scalability, whereas convective deposition is enormously versatile in each regard.[34]

7.2: Materials and Methods

7.2.1: Suspension Preparation

The silica/polystyrene (SiO_2/PS) binary suspension used in these membrane fabrication experiments was produced through the combination of unary SiO_2 and PS suspensions, as described in Chapter 2 and 3. The PS suspension consisted of $2a_{nano}$ = 100 nm PS nanoparticles (Emulsion Polymer Institute, Lehigh University) in DI H_2O having ζ-potential of −59 mV ± 1 mV. Concentrated individual stock suspensions of SiO2 and PS were prepared (30% and 25%, by volume, respectively), dispersed using a sonic dismembrator (model 550, Fisher Scientific, Pittsburgh, PA), then used along with additional DI H_2O to make the 20% volume fraction $SiO_2$and 8% volume fraction PS colloidal suspension used in these experiments.

7.2.2: Substrate Preparation

Glass microslides (Fisher Sci. Plain Glass Microscope Slides Premium, 76 × 25 × 1 mm^3) were used as deposition blades and substrates. Blades and substrates were prepared as described in Chapter 2.

7.2.3: Convective Deposition

The experimental setup is described in Chapter 2. All experiments were performed at 50% ± 5% relative humidity and 24 °C. The blade angle was fixed at 45° and positioned 10 μm above the substrate for all experiments and 10 μL suspension volumes were injected between the blade and substrate for each experiment.

7.2.4: Polystyrene Melting

Polystyrene in convectively deposited thin films was melted using a Fisher Scientific hot place set at 250°C for 20 min.

7.2.5: Microstructural Analysis

Fabricated membranes were analyzed primarily through scanning electron microscopy on a Hitachi 4200 field emission SEM with some quick imagery performed on available optical and confocal microscopes. Relevant data presented here was gathered on the SEM at nominal horizontal orientation or tilted to show membrane height and intermediary structure. Pore sizes were measured from SEM imagery using ImageJ. Prior to electron microscopy samples were coated with Iridium using an EMS, Electron Microscopy Sciences, 575X Turbo Sputter Coater.

7.3: Results and Discussion

Aspects of convective deposition and etching were explored in order to fabricate robust membranes with high porosity and uniformly sized and spaced pores. In overview, colloidal crystal structures were first assembled on a glass substrate by convective deposition of a binary suspension of 1 μm silica (SiO_2) microspheres with 100 nm polystyrene (PS) nanoparticles. Previous research on the formation of microsphere monolayers and multilayer colloidal crystal self-assembly[50,52,53] gives a basis for these experiments. Melting the polymer nanoparticles forms the working membrane, providing a uniform, continuous scaffold around the SiO_2 microspheres. Next SiO_2 is etched from the colloidal crystal with KOH or HF. A simple flow diagram, pictured in Figure 7.1, provides a series of diagrams describing the membrane fabrication process. While in principle only a single crystalline layer would be needed to form a uniform membrane with controlled pore size, in practice such a layer is too thin and fragile to be easily handled or effectively used under real filtration conditions with a significant transmembrane pressure drop. The viability of this work is shown through proof of concept experiments as well as closer examination into multilayer and layer by layer depositions to fabricate membranes of controllable thickness. It is essential to maintain thickness and mechanical strength without losing repeatable crystal structure and consequent uniformly-sized and shaped pore/cavity sizes.

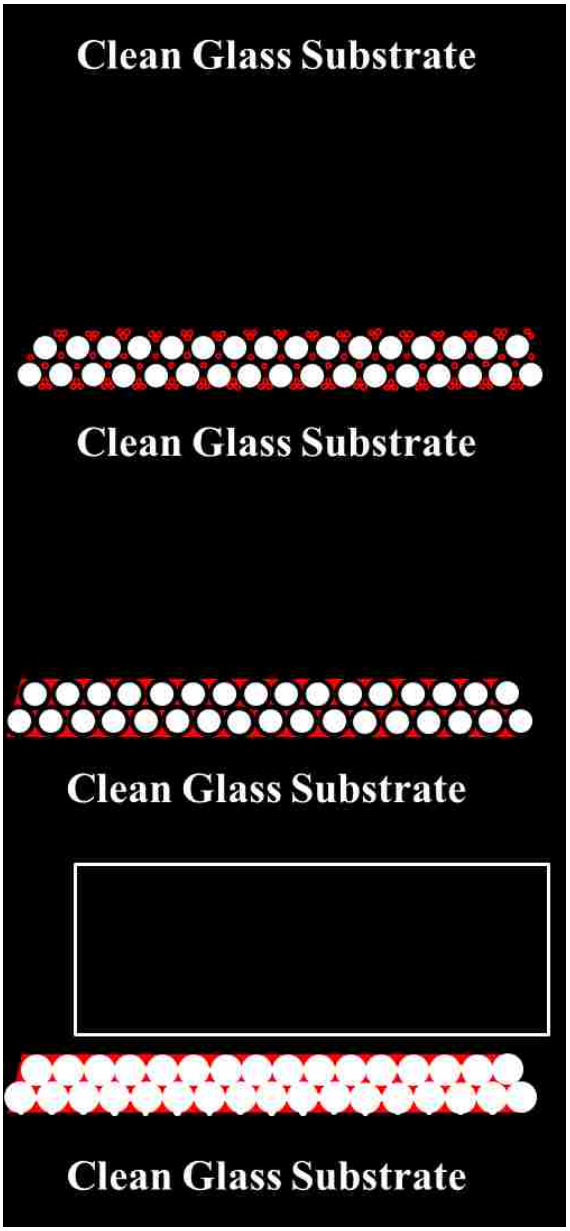

Figure 7.1: A simple flow diagram for the membrane fabrication process. Binary convective deposition is used to fabricate a highly ordered thin film of SiO_2 microspheres with Polystyrene (PS) nanoparticles filling the inter-microsphere voids. Heat treatment is used to melt the PS nanoparticles into a continuous phase polymer scaffold. Finally, chemical etching via KOH or HF is used to reform the SiO_2 template and detach the PS membrane from its glass substrate. Note that resultant membranes are mechanically strong, easy to handle (Figure 7.8), and have pores at the microsphere-microsphere and microsphere-substrate contact points.

7.3.1: Colloidal Crystal Formation

Membrane fabrication strategies focus around permutations of successive monolayer or multilayer depositions of binary suspensions. As shown previously, subsequent microsphere particle depositions align to fill the interstices of their base layer and grow the crystal.[50] Binary deposition gives the ability to deposit a two-phase layer, which is critical in the fabrication of these microporous membranes. Also, the addition of a smaller constituent alongside SiO_2 microspheres greatly enhances packing and thin film uniformity and makes for an enormously repeatable fabrication process.[52,53] Membranes were synthesized with thicknesses ranging from a single (monolayer) to six layers of SiO_2. The relationship between the deposited crystal thickness and deposition rates is coupled through a simple mass flux balance, Equation 7.1, first posed by Dimitrov and Nagayama[54] as

$$v_{mono} = \frac{J_e \beta}{2a(\phi^D)} \frac{\phi}{1-\phi} \tag{7.1}$$

Here, v_{mono} describes the substrate velocity for monolayer deposition that depends on J_e, solvent flux, $2a$, microsphere diameter, ϕ and ϕ^D, which are the suspension volume fraction and volume fraction within the deposited thin film respectively, and β, a parameter describing particle-surface interactions. $\beta \approx 1$ when particle–surface interactions are strongly repulsive—this is the case in this study where highly repulsive constituents and substrates are utilized. At faster deposition speeds than v_{mono}, the substrate translates faster than the crystal formation rate and results in submonolayer morphology. Conversely, at deposition speeds slower than v_{mono}, the rate of particles flowing to the crystal formation front exceeds the deposition velocity and a resultant

multilayer is formed. Previous work[50] shows that other factors such as the shape of the meniscus dictated by the blade angle α (as described in Chapter 2) also influence the deposition rate. Also, a schematic of the convective deposition experimental setup in provided in Chapter 2.

For these experiments, the monolayer deposition speed for the binary SiO_2/PS suspension was determined to be v_{mono} = 40.8 μm/s through confocal and scanning electron microscopy. The deposition speed can be altered to deposit crystalline multilayers of targeted thickness. For instance, depositing at one-half the monolayer velocity, ½ v_{mono}, will deposit two layers, 1/3 v_{mono} will deposit three, etc. Surprisingly, this holds although the primary mechanism for assembly during deposition changes between monolayer and multilayer deposition. Assembly in monolayer deposition is driven by capillary interactions of particles confined within a film of thickness on the order of the particle size. In multilayer deposition, the relatively thick film is filtered through the growing crystal and assembly primarily occurs due to pressure-driven 'steering'.[55] However, the most dense and ordered crystalline membranes are produced with depositions speeds close to v_{mono}. Multilayer depositions, as their name suggests, result from multiple particles flowing at once to the crystal formation front. The initial layers of particles formed on the substrate show high packing and long-range crystallinity; however, additional particles flowing in (arranging atop that first layer) have trouble arranging with maximal order. Two strategies, consecutive and multilayer depositions, were explored in combination and independently to increase membrane thickness. Multilayer depositions can be performed at any fraction of v_{mono} in order to

control layer thickness. Monolayer depositions can increase membrane thickness very controllably a single layer at a time. As a natural extension, particle multilayers can be deposited to thicken membranes in fewer steps. Samples fabricated at slightly faster deposition speeds than v_{mono} show somewhat less uniform crystallinity and more defects at the local level though they are still composed primarily of crystalline regions. With increasing speed, these submonolayer depositions show an increasing prevalence for void patches as well as particle patches, bands, and strings.

Particles were deposited at one, one-half, one-third, and one-sixth the monolayer deposition speed. In each case, the aim was to make a membrane six layers thick; thus depending on the deposition speed, six depositions for v_{mono}, three for ½ v_{mono}, two for 1/3 v_{mono}, and one for 1/6 v_{mono} were performed (Figure 7.2). This thickness was chosen to show the tunability of convective deposition as a membrane fabrication process and because these membranes were thick enough so as to be mechanically strong and easy to handle. One point to be considered is that, given the finite suspension volume in each experiment, controlling the flux so as to increase the number of vertical layers leads to a corresponding decrease in deposition length and resultant shorter membrane. Here, semibatch processing using a finite volume of suspension was employed. Ten microliters of SiO_2 suspension 20% volume fraction yield roughly 4 × 2.5 cm^2 depositions at v_{mono}, whereas those run at 1/6 v_{mono} were roughly 0.7 × 2.5 cm^2 in length.

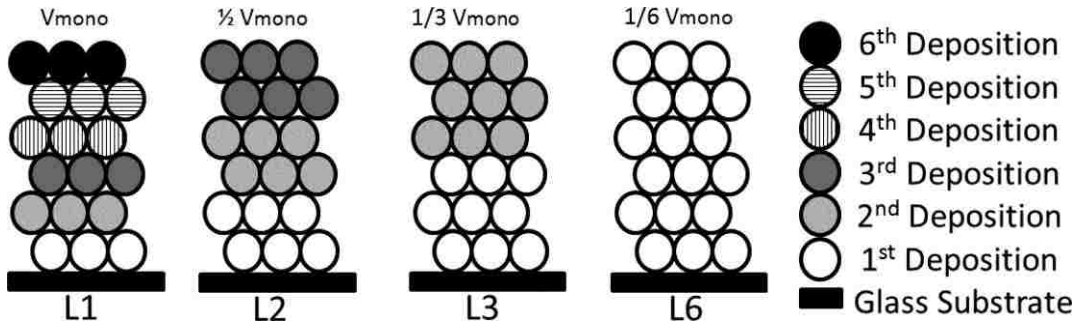

Figure 7.2: Sketch showing the deposition strategies developed through an understanding of the direct relationship between deposition speed and crystal formation rate. V_{mono} is the monolayer deposition speed determined to be 40.8 μm/s From left to right, L1 comprises six consecutive monolayer depositions at v_{mono}, L2 comprises three consecutive bilayers deposited at ½ v_{mono}, L3 comprises two consecutive trilayers deposited at 1/3 v_{mono}, and L6 comprises a single six-layer deposition deposited at 1/6 v_{mono}. Note L1, L2, L3, and L6 have identical thickness but may vary in structural periodicity and crystallinity.

7.3.2: Template Etching and Membrane Fabrication

To convert microsphere crystal assemblies into membranes, SiO_2/PS thin films were treated with Potassium Hydroxide (KOH) or Hydrofluoric Acid (HF). Using KOH as an etchant, usable well-ordered membranes are fabricated under all deposition conditions. Even in depositions with significant defects or disorder, the membrane will still be composed of cavities and pores of equal size and thus will have identical separations capability with regard to size selectivity, as shown in Figure 7.3F. Figure 7.3A shows a binary monolayer deposition of SiO_2/PS with a second PS monolayer deposition. Note the crystalline structure of the particles. Occasional line and point defects do form but, by and large, a hexagonal close-packed microstructure is maintained. Here an additional 8% volume fraction PS/DI H_2O deposition was performed atop the SiO_2/PS thin film demonstrating the ability to form a fully connected continuous membrane in the event PS was not uniformly distributed through the SiO_2 crystal or was not present in sufficient quantities to fully cover the SiO_2 microspheres. The nanoparticles flow uniformly into the interstices and show that additional depositions do not disrupt the base layer. This additional deposition ended up being unnecessary as sufficient PS is deposited with both multilayer and consecutive binary depositions to form mechanically robust membranes. This unary PS deposition step is omitted from all subsequent membrane fabrication experiments.

Increasing the thickness of SiO_2/PS thin films while maintaining uniform pore size and membrane morphology is next explored. Figure 7.3B–D shows membranes fabricated through a single binary deposition at $1/6v_{mono}$. Note the differences in

crystallinity between the bottom and top layers of the thin film. The bottom layer is very well-ordered and crystalline but moving vertically through the deposition there is an increasing degree of nonuniformity. The top layer shows smaller crystalline regions without the long-range order of their lower neighbors. The result is a semi-unconnected network of SiO_2 microspheres that renders the process ineffective for fabricating a working membrane. Figure 7.3C–E has been etched for <12 hours with 30% KOH/DI H_2O at 80 °C. In Figure 7.3C, where the PS is unmelted in an attempt to enhance the etching of interior SiO_2 microspheres, only a slight recession of the SiO_2 microsphere surface is found. As the process continues in Figure 7.3D, the microspheres etch to the degree that they become free-floating, exit, and leave behind resultant void regions in the PS membrane.

The microspheres maintain their spherical shape under etching indicating that etching proceeds uniformly from all sides rather than in a purely top-down format (Figures 7.3F, 7.3G). These samples have been etched for 17 hours with 40% KOH/DI H_2O at 90 °C. In Figure 7.3F the SiO_2particles have recessed significantly; Figure 7.3G shows the same behavior but highlights the fact that the particles are in fact freestanding in their cavities. Here multiple SiO_2 nanoparticles have recessed, detached, and lifted off only to redeposit in single void. Images (F) and (G) in Figure 7.3 highlight the size exclusion properties of these membranes and the robustness of the pores during the etching process. The particles are effectively filtered and not allowed to pass through. For an application of virus separation from blood cells, cellular constituents larger than these shrunken particles would be stopped, whereas the virus components, on the order

of a hundred nanometers or smaller, could easily pass through. Figure 7.4 describes two potential mechanisms for etching. In the first, etching proceeds through a top-down process where SiO_2 microspheres in the top, exposed, layers etch initially. Only when the exposed microsphere is sufficiently etched away can the KOH flow to microsphere-microsphere contact point and begin to etch the next microsphere. However, that the SiO_2 microspheres, collected in that PS cavity, remain monosized during the etching process as they shrink sufficiently to escape their original PS cavities indicates that a second mechanism governs the etching process. That the melted PS is essentially nonpermeable indicates that the etchant creeps along the sides of the microspheres and thus etching most likely proceeds simultaneously in all layers at once. A possible explanation of this is the fact that SiO_2/KOH surface energy is much lower than SiO_2/PS surface energy and thus KOH selectively wets along the microsphere/scaffold interfaces and flows from microsphere to microsphere under a faster time scale than the etching itself (Figure 7.4). Aided by the increase in surface energy, the entire surface area of the microspheres is simultaneously etched inward. Crude contact angle of 40% KOH/DI H_2O measured on glass are roughly <10°, whereas the observed wetting angle of PS on the microspheres as calculated from SEM imagery is roughly 40°. As a side note, the increase in SiO_2 microsphere etching is due to the longer etching time and higher temperature. It is not due to the increase in KOH concentration.[56]

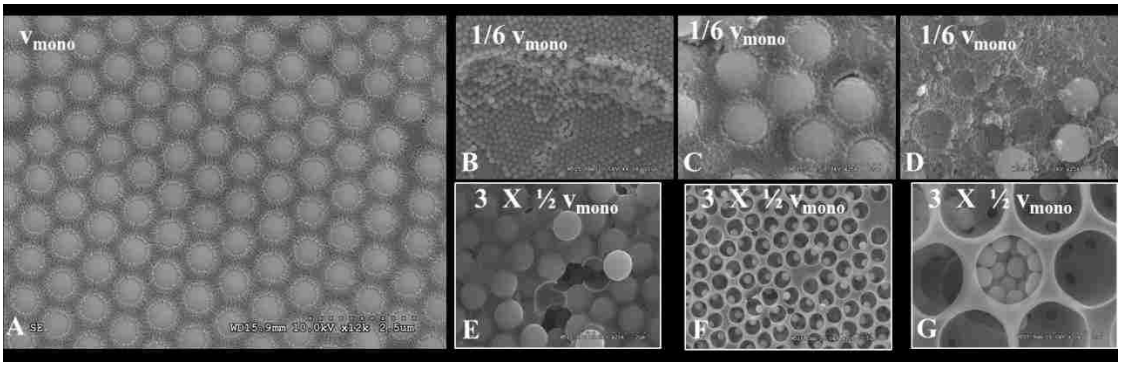

Figure 7.3: (A) Well-ordered single layer of SiO_2/PS, (B–D) unmelted SiO_2/PS layers deposited at 1/6 v_{mono}, L6, (E–G) melted SiO_2/PS layers deposited at 1/2v_{mono}, L2, as well as (C–G) progressive partially etched samples. (B) Image showing progressive multilayer morphology with underlying highly ordered layers in a razor-scratched sample. (C)-(E) have been etched in 30% KOH for <12 h at 80°C without melting PS. (C) and (D) show partially etched samples with unmelted PS. Notice that in (C), the SiO_2 spheres are beginning to etch away, and in (D) and (E), the partially etched spheres have etched to the degree that they can lift off from the layer. (E) shows a sample partially etched similarly to (C) and (D) with similar microsphere liftoff but from a melted PS scaffold. f and g represent incomplete etching under 17 hours 40% KOH etching at 90°C with a melted PS scaffold. (F) shows the recedence of the SiO_2 microspheres under etching sitting in each cavity with the cavities' associated pores in view as well. (G) shows that the etched SiO_2microspheres are in fact free-floating having washed out of a number of neighboring cavities and redeposited into a single void.

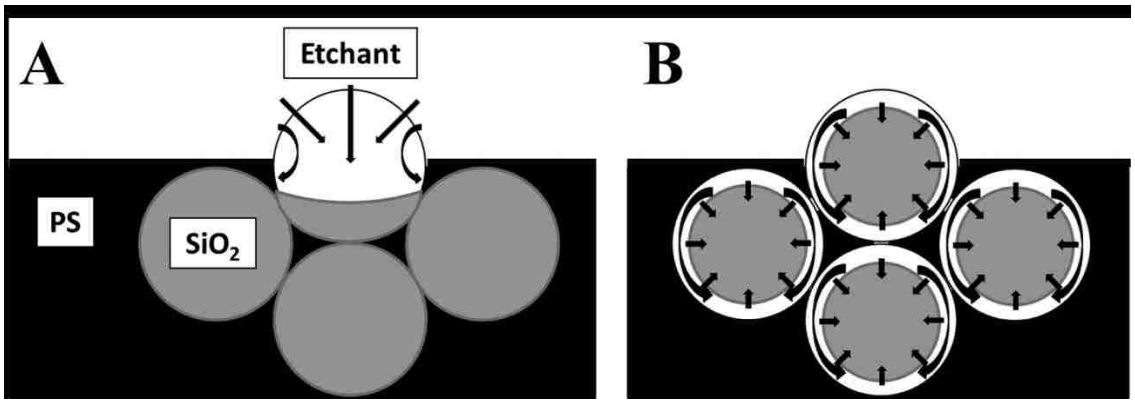

Figure 7.4: Sketch showing two alternative mechanisms by which SiO_2/PS membranes might be etched. (A) Top-down etching process whereby the underlying SiO_2 microspheres will not be etched until their top neighbors have receded sufficiently. (B) Method where the etchant works its way around the microspheres, flows through pores, and etches multiple layers simultaneously. The microspheres recede inward uniformly from all sides and are freed to liftoff and potentially leave their cavities. Imagery in Figure 7.3 supports method b as the mechanism of etching.

Optimizing suspension characteristics should provide great control over membrane pore size. To validate this hypothesis, contrasting membranes were synthesized with 1 μm SiO_2/100 nm PS and 0.5 μm SiO_2/100 nm PS. For each membrane, two types of pores were evaluated: microsphere–microsphere intercavity pores and microsphere–substrate pores (see Appendix 9.7.1, Figure 9.7.1). As expected, the larger particles yielded larger pores. One micrometer SiO_2/100 nm PS exhibit 141 ± 10 nm (one standard deviation) intercavity pores and 200 ± 8 nm pores at microsphere-substrate contact points. 0.5 μm/100 nm PS exhibit 103 ± 5 nm intercavity pores and 149 ± 8 nm pores at microsphere–substrate contact points. Obviously the smaller pores will govern membrane selectivity. The difference in pore sizes stem from the differently sized interstices between microspheres and their neighbors versus microspheres and the substrate—it is hypothesized that a combination of nanoparticle packing and polystyrene wetting ability on SiO_2/glass within these angles governs the difference. In addition to particle size, constituent composition can be varied. Preliminary trials with polyethylene glycol (PEG) MW 575 and MW 258 were performed. Crystalline SiO_2/PEG layers can be deposited, with the PEG cured under UV, but a higher degree of heterogeneity in the deposition and initial trials to selectively remove the SiO_2 phase generated lower quality films. The success of PS trials does give validity to the potential of future research into alternative polymers.

Figure 7.5 highlights the robustness of this membrane fabrication technique. Here all membranes have been fully etched with 40% KOH for >24 h at 90 °C and subsequently rinsed with DI H_2O. These images show the strength of repeating layers of

pores in a multilayer membrane. The large and deep defect regions, excellent for showing underlying layers and presented in images a and b in Figure 7.5 respectively, are not typical of mono- and multilayer depositions. These defects, created in the sample preparation process, are presented to show uniform lower layers and cavities. Close inspection shows that the enormous stress of fracturing the membranes, in Figure 7.5A, has affected only the top two, fifth, and sixth, membrane layers; the untouched underlying pore array in Figure 7.5A is the fourth layer. Figure 7.5B shows a deeper defect, also near the fracture zone, and shows that layer defects are compensated by their underlying neighbors such that neither the integrity of the membrane nor its separations capabilities will be impaired. Figure 7.5C specifically shows a point defect, in the original deposition, with the crystalline layer below obviating any potential filtration issues. This robustness and mechanical stability to the fabricated membranes will contribute to their longevity and long-term effective filtration. Specifically, in presence of a defect or membrane stress, the low propensity for that crack to propagate will both limit decreased membrane effectiveness and prevent catastrophic failure.

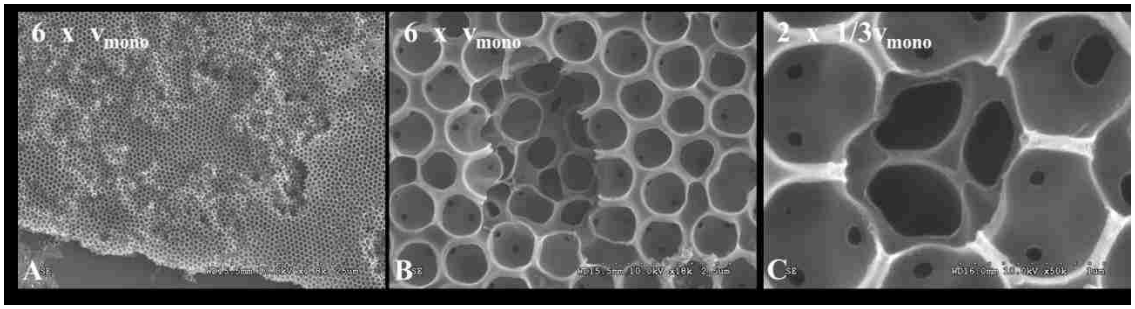

Figure 7.5: SEM Images showing the robustness of this membrane fabrication process. (A, B) Synthesized through six consecutive depositions at v_{mono}, L1; (C) synthesized with two depositions at $1/3v_{mono}$, L3. All three images show that in the sparse defect regions, supporting underlayers obviate any potential weaknesses of the membrane. Note that samples a and b were scratched with a razor in order to evaluate membrane interior and the especially large amounts of nonuniformity in the top layers is a product of that scratching process.

Figure 7.6 shows membranes fabricated under optimal conditions. Note the higher order of the topmost layers as compared with the slower multilayer depositions. These membranes, fabricated through multilayer and monolayer depositions, have identical pore and cavity sizes; however thin films fabricated through multiple consecutive monolayer depositions show the highest crystallinity and packing and thus would be expected to have the highest resolution selectivity in filtration applications. The membranes presented in Figure 7.6 are fabricated through six consecutive depositions at v_{mono}, 24+ hours of 40% KOH etching at 90 °C, and four DI H_2O water washes/soaks. These membranes are presented at progressively lower magnifications in order to highlight first, the regular orientation of the pores, and second, the high crystallinity and low number of defects across the membrane. Note that the submonolayer patchiness in the top layer is a product of the consecutive depositions. In depositions on bare glass or other hydrophilic flat surfaces, a monolayer deposition deposits exactly that: a single layer of particles with very long-range order and high crystallinity.[50,53,57,58] To confirm the regularity of the membrane interior, Figure 7.6D shows a fractured membrane, fabricated through two consecutive depositions at 1/3 v_{mono}, viewed on a tilted SEM stage. It highlights the interior structure of the membrane including partial voids along the fracture plane. These images show the mechanical stability of the membranes in that the membranes fracture cleanly without fingers or cracks extending inward from the fracture line. Also note that this fracturing method of snapping the substrate and thin film disrupts the structure of the topmost membrane layers far less than the razor-scratching membrane presented earlier.

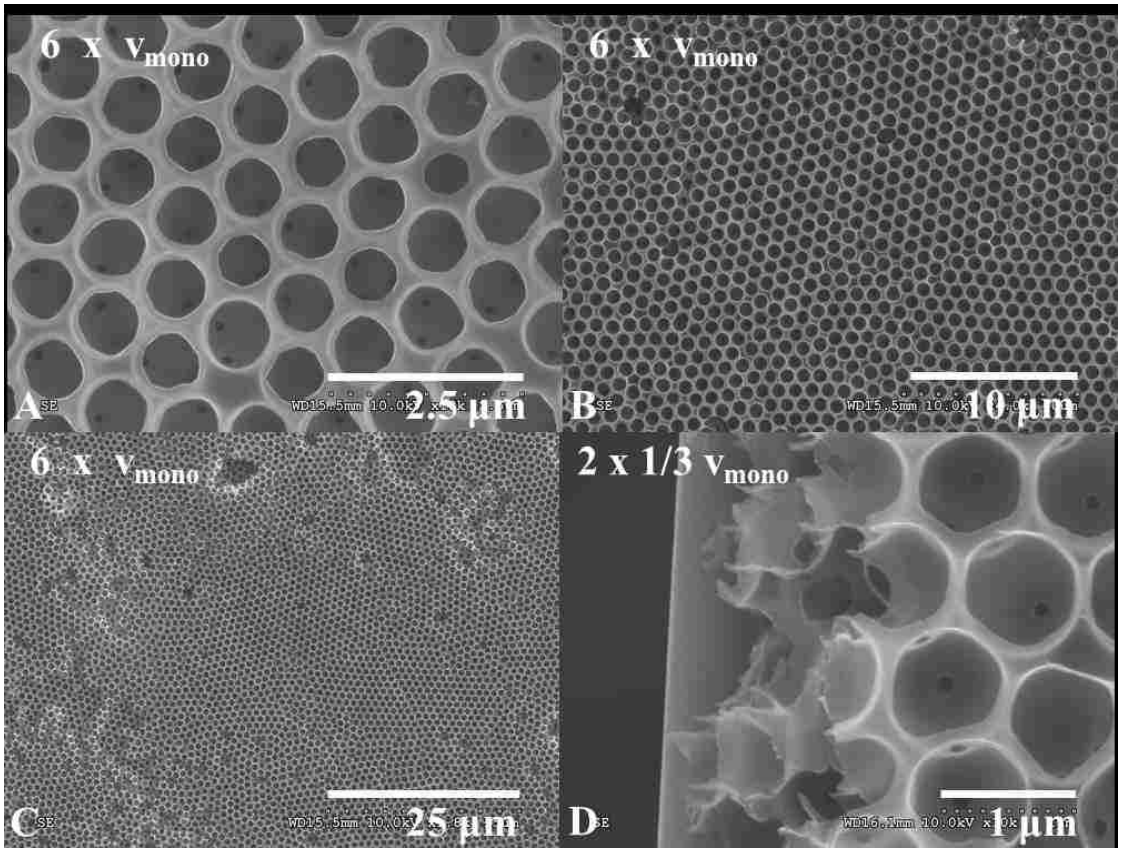

Figure 7.6: (A–C) Fully-etched membranes at progressively lower magnifications fabricated with six consecutive depositions at v_{mono}, L1, etching with 40% KOH/DI H_2O for 24+ hours at 90 °C, and four water bath washes/soaks. In (A), note the pores connecting the topmost sets of cavities to their neighbors underneath at points where SiO_2 microspheres previously touched. In (B) and (C), note that even in defect regions, where the uppermost layer or two exhibits submonolayer characteristics as a product of the somewhat rough surface of underlying crystalline SiO_2, the underlying layers maintain the integrity of the membrane. (D) Interior of a membrane fabricated with two 1/3 v_{mono}, L3, depositions. This sample is placed atop a glass slide and the slide and membrane are snapped in half. The SEM stage is tilted in order to highlight the membrane interior. Note the visible cavities with their pores in the interior of the membrane. Also note that the infrastructure of the membrane is intact; this highlights the mechanical strength of the PS membranes.

KOH etching successfully produced robust, uniform membranes; the only downside to KOH etching is the higher temperature and long time necessary to successfully remove SiO_2 microspheres. As such the next step was to look into a stronger etchant. HF is a very strong SiO_2 etchant and thus warranted an investigation into its comparable efficacy as a fabrication strategy versus KOH. Two disadvantages to using HF as an etchant are that HF etches so rapidly that the etching process is not as easily revealed and that safety/environmental concerns surrounding use of HF are magnified. HF etching was carried out by pipetting a droplet of HF atop the deposition, leaving it for one minute, then rinsing several times with ethanol. First, to show the validity of this approach, a monolayer of particles is deposited from a purely SiO_2 suspension. Etching this layer (Figure 7.7A) shows the ability to selectively etch SiO_2. Figure 7.7B shows a double layer deposited from a binary SiO_2/PS suspension with PS subsequently melted. HF can be used to selectively spatially etch SiO_2 without degrading PS. Here, a portion of the bilayer thin film is etched with fingers of PS extending into the void region where the membrane was fractured. Figure 7.7C presents a top-down view of an etched SiO_2/PS bilayer with long-range order. The inset shows an etched monolayer. Images d and e in Figure 7.7 highlight the monodispersity and regularity of the membrane as well as pore locations stemming from SiO_2 contact points. Figure 7.7D presents etched thin films where microspheres cavities are highly covered with polystyrene. Images e and f in Figure 7.7 also show the PS wetting around each of the SiO_2 microspheres and that impact on the resulting membrane morphology—the PS wets higher directly above microsphere contact points than in-

between. In addition, one advantage of depositing SiO_2 alongside a polymer onto glass is that the membranes are easy to handle because that glass substrate, SiO_2 itself, etches along with the microspheres. This causes membranes to delaminate from that base and float to the top of the KOH bath for simple recovery. Figure 7.8 presents a photo of a typical 6-layer membrane removed from its etchant bath then placed atop an aluminum support for SEM analysis in order to demonstrate typical membrane size and mechanical robustness. Convective deposition as a process is highly scalable, and thus so will be membrane size.

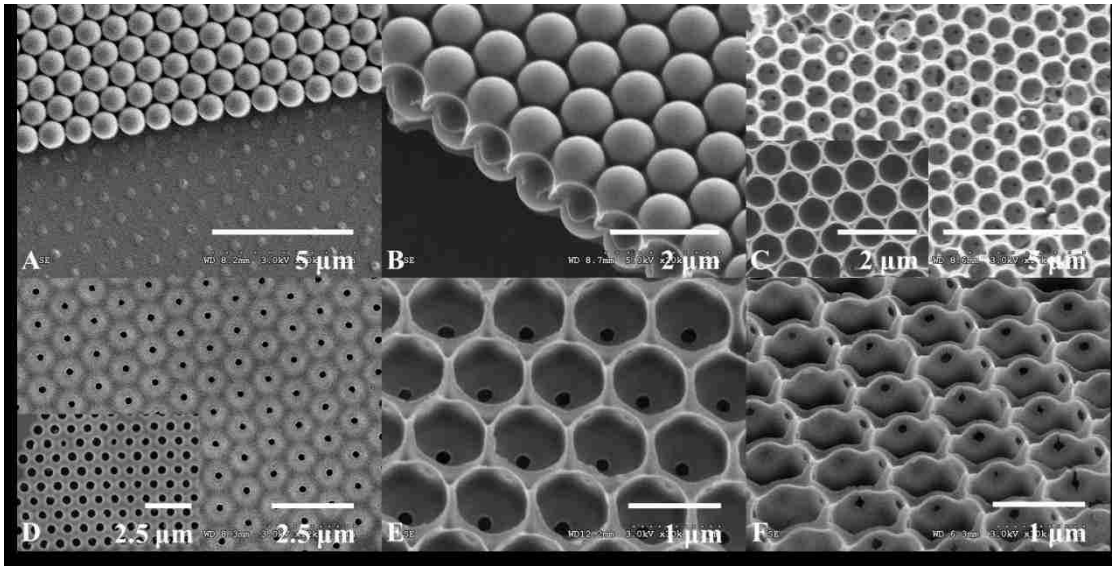

Figure 7.7: SEM imagery showing the validity of this membrane-fabrication approach. Samples were etched for 1 min while at room temperature. (A) SiO_2 monolayer partially etched using HF. (B) Binary SiO_2/PS bilayer etched and showing fingers of PS bracketing the SiO_2 voids. All other images show monolayer depositions. (C) Top-down views of membranes with some pores visible. (D–F) PS membranes highlighting the interconnecting cavity pores and PS wetting around the SiO_2 microspheres on a tilted SEM stage.

Figure 7.8: Photo showing a six-layer membrane, synthesized through three depositions at ½ v_{mono}, prepared for SEM analysis. Membranes are mechanically strong enough to be easily handled.

In a given membrane, there are two types, and sizes, of pores. Where microspheres contacted one another, cavity–cavity pores are formed. Where microspheres contact the substrate, cavity–substrate pores are formed. The pore size ratio is determined by a simple geometric relation of smaller to larger constituents which determines the available angles for smaller particles to pack into the interstices of the larger particles (Equations 7.2 and 7.3). Experimentally, 1 μm SiO_2 microspheres coupled with 100 nm PS nanoparticles yield substrate-cavity pores with 200 ± 8 (1 standard deviation) nm diameter, cavity–cavity pores with 141 ± 10 nm diameter and a resulting pore size ratio of 1.42 ± 0.12. Membranes were fabricated with 500 nm SiO_2 and 100 nm PS and exhibited substrate–cavity pores with 149 ± 7 nm diameter, cavity–cavity pores with 104 ± 5 nm, and a resulting pore size ratio of 1.45 ± 0.11. With identical size ratios, k = 0.1, 0.2, Equation 7.3 yields pore size ratios of 1.40 and 1.39, respectively—these ratios correlate very well with the experimental data. For a more in-depth look at this theory, see Appendix 9.7.1.

$$k = \frac{R_2}{R_1} = particle\ size\ ratio \tag{7.2}$$

$$Pore\ Size\ Ratio = \frac{\tan^{-1}\sqrt{2k+k^2}}{2\tan^{-1}\frac{\sqrt{k}}{2}} \tag{7.3}$$

These membranes can be easily functionalized for cell, viral, or other bioparticle capture depending on need. Convectively deposited SiO_2 microspheres have already been successfully functionalized with antibodies for cell capture experiments.[59-61] Similarly, PS and other polymers can be labeled with antibodies for targeted biomolecular immobilization.[62,63] Coupling this ability to functionalize membrane

constituents with the materials flexibility and tunable pore size gives an enormously versatile membrane fabrication process. Obviously, for filtration experiments factors such as internal concentration polarization and fouling will come into play. One unique advantage of the rapid convective deposition is that this process is scalable by varying the sizes of the blade and substrate and volume of suspension. Additionally, it can easily be modified into a continuous process for industrial applications by continuously pumping suspension into the corner flow between the blade and substrate.

7.4: Conclusions and Impact

This study investigated the use of binary convective deposition to fabricate macroporous membranes with highly ordered pores of a narrow size distribution. One of the greatest strengths of convective deposition as a method for membrane fabrication is the sheer versatility and tunability of the process. Stepping back from the aforementioned variations that show the huge variety of fabrication techniques and the robustness of the convective deposition technique for the fabrication of multilayer thin films, very small variations in materials can yield enormous flexibility. Binary SiO_2/PS suspensions were convectively deposited with subsequent selectively removal of SiO_2 with KOH and HF. Through depositions with monolayer and multilayer morphologies, membranes of definable thickness with controllable pore and cavity sizes are fabricated. The issue of uniform pore size that so plagues many macroporous membranes of intermediate size is a nonissue with this strategy, and the mechanical stability and physical robustness of these membranes makes them easier to handle than their more fragile counterparts. These membranes are hugely versatile and highly repeatable; they highlight proven techniques that have the potential to enormously enhance separations capabilities to target specific cells, viruses, and other receptor-laden bioparticles. Having already machined a suitable testing platform, the next step is to test the efficacy of these membranes with nanoparticle and pseudovirus suspensions.

7.5: References

1. Burnouf T, Radosevich M. Nanofiltration of plasma-derived biopharmaceutical products. *Haemophilia*. 2003;9(1):24-37.

2. Christy C, Vermant S. The state-of-the-art of filtration in recovery processes for biopharmaceutical production. *Desalination*. 2002;147(1-3):1-4.

3. Desai TA, Hansford DJ, Leoni L, Essenpreis M, Ferrari M. Nanoporous anti-fouling silicon membranes for biosensor applications. *Biosensors & Bioelectronics*. 2000;15(9-10):453-462.

4. Baker LA, Choi Y, Martin CR. Nanopore membranes for biomaterials synthesis, biosensing and bioseparations. *Current Nanoscience*. 2006;2:243-255.

5. Zhang K, Wu XY. Temperature and pH-responsive polymeric composite membranes for controlled delivery of proteins and peptides. *Biomaterials*. 2004;25(22):5281-5291.

6. Park YJ, Ku Y, Chung CP, Lee SJ. Controlled release of platelet-derived growth factor from porous poly(L-lactide) membranes for guided tissue regeneration. *Journal of Controlled Release*. 1998;51(2-3):201-211.

7. Desai TA, Hansford D, Ferrari M. Characterization of micromachined silicon membranes for immunoisolation and bioseparation applications. *Journal of Membrane Science*. 1999;159(1-2):221-231.

8. Risbud MV, Bhonde RR. Suitability of cellulose molecular dialysis membrane for bioartificial pancreas: In vitro biocompatibility studies. *Journal of Biomedical Materials Research*. 2001;54(3):436-444.

9. Clark WR, Hamburger RJ, Lysaght MJ. Effect of membrane composition and structure on solute removal and biocompatibility in hemodialysis. *Kidney International*. 1999;56(6):2005-2015.

10. Lopez CA, Fleischman AJ, Roy S, Desai TA. Evaluation of silicon nanoporous membranes and ECM-based micro environments on neurosecretory cells. *Biomaterials*. 2006;27(16):3075-3083.

11. Norman J, Desai T. Methods for fabrication of nanoscale topography for tissue engineering scaffolds. *Annals of Biomedical Engineering*. 2006;34(1):89-101.

12. Malik DJ, Webb C, Holdich RG, et al. Synthesis and characterization of size-selective nanoporous polymeric adsorbents for blood purification. *Separation and Purification Technology*. 2009;66(3):578-585.

13. Létant SE, Hart BR, Van Buuren AW, Terminello LJ. Functionalized silicon membranes for selective bio-organism capture. *Nat Mater*. 2003;2(6):391-396.

14. van de Merbel, N. C. Membrane-based sample preparation coupled on-line to chromatography or electrophoresis. *Journal of Chromatography A*. 1999;856(1-2):55-82.

15. vandeWitte P, Dijkstra PJ, vandenBerg JWA, Feijen J. Phase separation processes in polymer solutions in relation to membrane formation. *Journal of Membrane Science*. 1996;117(1-2):1-31.

16. Adiga SP, Curtiss LA, Elam JW, et al. Nanoporous materials for biomedical devices. *Jom*. 2008;60(3):26-32.

17. Ulbricht M. Advanced functional polymer membranes. *Polymer*. 2006;47(7):2217-2262.

18. van den Boogaart MAF, Kim GM, Pellens R, van den Heuvel, J. P., Brugger J. Deep-ultraviolet-microelectromechanicaI systems stencils for high-throughput resistless patterning of mesoscopic structures. *Journal of Vacuum Science & Technology B*. 2004;22(6):3174-3177.

19. Bwana NN, Leigh P. Synthesis of highly ordered nanopores on a photoresist template for applications in nanofabrications. *Journal of Nanoparticle Research*. 2008;10(2):353-356.

20. Yang SY, Ryu I, Kim HY, Kim JK, Jang SK, Russell TP. Nanoporous membranes with ultrahigh selectivity and flux for the filtration of viruses. *Advanced Materials*. 2006;18(6):709-712.

21. Thurn-Albrecht T, Steiner R, DeRouchey J, et al. Nanoscopic templates from oriented block copolymer films. *Advanced Materials*. 2000;12(11):787-791.

22. Olson DA, Chen L, Hillmyer MA. Templating nanoporous polymers with ordered block copolymers. *Chemistry of Materials*. 2008;20(3):869-890.

23. Li AP, Muller F, Birner A, Nielsch K, Gosele U. Hexagonal pore arrays with a 50-420 nm interpore distance formed by self-organization in anodic alumina. *Journal of Applied Physics*. 1998;84(11):6023-6026.

24. Li FY, Zhang L, Metzger RM. On the growth of highly ordered pores in anodized aluminum oxide. *Chemistry of Materials*. 1998;10(9):2470-2480.

25. Lee W, Schwirn K, Steinhart M, Pippel E, Scholz R, Gosele U. Structural engineering of nanoporous anodic aluminium oxide by pulse anodization of aluminium. *Nature Nanotechnology*. 2008;3(4):234-239.

26. Yuan ZY, Su BL. Insights into hierarchically meso-macroporous structured materials. *Journal of Materials Chemistry*. 2006;16(7):663-677.

27. Wu YY, Cheng GS, Katsov K, et al. Composite mesostructures by nano-confinement. *Nature Materials*. 2004;3(11):816-822.

28. Yamaguchi A, Teramae N. Fabrication and analytical applications of hybrid mesoporous membranes. *Analytical Sciences*. 2008;24(1):25-30.

29. Wickramasinghe SR, Bower SE, Chen Z, Mukherjee A, Husson SM. Relating the pore size distribution of ultrafiltration membranes to dextran rejection. *Journal of Membrane Science*. 2009;340(1-2):1-8.

30. Black CT, Guarini KW, Breyta G, et al. Highly porous silicon membrane fabrication using polymer self-assembly. *J Vac Sci Technol B*. 2006;24(6):3188-3191.

31. Tsai H, Huang D, Ruaan R, Lai J. Mechanical properties of asymmetric polysulfone membranes containing surfactant as additives. *Ind Eng Chem Res*. 2001;40(25):5917-5922.

32. Athens GL, Ein-Eli Y, Chmelka BF. Acid-functionalized mesostructured aluminosilica for hydrophilic proton conduction membranes. *Adv Mater*. 2007;19(18):2580-2587.

33. Bouhabila EH, Aim RB, Buisson H. Fouling characterisation in membrane bioreactors. *Separation and Purification Technology*. 2001;22-3(1-3):123-132.

34. Unnikrishnan S, Jansem H, Berenschot E, Elwenspoek M. Wafer scale nanomembrane supported on a silicon microsieve. *Micromechanics Europe*. 2007;16(18):127-130.

35. Eyal AM, Hadju K, Hazan B, Edelstein D. Pore formation, premeabliity, and permselectivity in porogen derived membranes. *Journal of Applied Polymer Science*. 1992;46:1621-1629.

36. Wu S, Frederic KJ, Talarico M, Kee DD. Porous polymer monolith templated by small polymer molecules. *The Canadian Journal of Chemical Engineering*. 2009;87:579-583.

37. Baniel A, Eyal A, Edelstein D, et al. Porogen derived membranes. 1. concept description and analysis. *Journal of Membrane Science*. 1990;54:271-283.

38. Jiang P, McFarland MJ. Wafer-scale periodic nanohole arrays templated from two-dimensional nonclose-packed colloidal crystals. *J Am Chem Soc*. 2005;127(11):3710-3711.

39. van Blaaderen A, Hoogenboom JP, Vossen DLJ, et al. Colloidal epitaxy: Playing with the boundary conditions of colloidal crystallization. *Faraday Discuss*. 2003;123(Pages 1-421):107-119.

40. Lee W, Chan A, Bevan MA, Lewis JA, Braun PV. Nanoparticle-mediated epitaxial assembly of colloidal crystals on patterned substrates. *Langmuir*. 2004;20(13):5262-5270.

41. Biancaniello PL, Crocker JC. Line optical tweezers instrument for measuring nanoscale interactions and kinetics. *Rev Sci Instrum*. 2006;77:113702-113702-10.

42. Hayward RC, Saville DA, Aksay IA. Electrophoretic assembly of colloidal crystals with optically tunable micropatterns. *Nature*. 2000;404(6773):56-59.

43. Dimitrov AS, Nagayama K. Steady-state unidirectional convective assembling of fine particles into 2-dimensional arrays. *Chemical Physics Letters*. 1995;243(5-6):462-468.

44. Shimmin RG, DiMauro AJ, Braun PV. Slow vertical deposition of colloidal crystals: A langmuir-blodgett process? *Langmuir*. 2006;22(15):6507-6513.

45. Diao JJ, Hutchison JB, Luo GH, Reeves ME. Theoretical analysis of vertical colloidal deposition. *J Chem Phys*. 2005;122(18):184710-1-184710-5.

46. Boudreau LC, Kuck JA, Tsapatsis M. Deposition of oriented zeolite A films: In situ and secondary growth. *Journal of Membrane Science*. 1999;152(1):41-59.

47. Bohaty AK, Abelow AE. Nanoporous silica colloidal membranes suspended in glass. *J Porous Mater*. 2011;18(3):297-304.

48. Yuan Y, Burckel DB, Atanassov P, Fan H. Convective self-assembly to deposit supported ultra-thin mesoporous silica films. *Journal of Materials Chemistry*. 2006;16(48):4637-4641.

49. Lee SB, Mitchell DT, Trofin L, Nevanen TK, Söderlund H, Martin CR. Antibody-based bio-nanotube membranes for enantiomeric drug separations. *Science*. 2002;296(5576):2198-2200.

50. Kumnorkaew P, Ee Y, Tansu N, Gilchrist JF. Investigation of the deposition of microsphere monolayers for fabrication of microlens arrays. *Langmuir*. 2008;24(21):12150-12157.

51. Velev OD, Lenhoff AM. Colloidal crystals as templates for porous materials. *Current Opinion in Colloidal & Interface Science*. 2000;5:56-63.

52. Kumnorkaew P, Gilchrist JF. Effect of nanoparticle concentration on the convective deposition of binary suspensions. *Langmuir*. 2009;25(11):6070-6075.

53. Kumnorkaew P, Weldon AL, Gilchrist JF. Matching constituent fluxes for convective deposition of binary suspensions. *Langmuir*. 2010;26(4):2401-2405.

54. Dimitrov AS, Nagayama K. Steady-state unidirectional convective assembling of fine particles into 2-dimensional arrays. *Chemical Physics Letters*. 1995;243(5-6):462-468.

55. Brewer DD, Allen J, Miller MR, et al. Mechanistic principles of colloidal crystal growth by evaporation-induced convective steering. *Langmuir*. 2008;24(23):13683-13693.

56. Seidel H, Csepregi L, Heuberger A, Baumgartel H. Anisotropic etching of crystalline silicon in alkaline-solutions .1. orientation dependence and behavior of passivation layers. *J Electrochem Soc*. 1990;137(11):3612-3626.

57. Kumnorkaew P, Gilchrist JF. Effect of nanoparticle concentration on the convective deposition of binary suspensions. *Langmuir*. 2009;25(11):6070-6075.

58. Prevo BG, Velev OD. Controlled, rapid deposition of structured coatings from micro- and nanoparticle suspensions. *Langmuir*. 2004;20(6):2099-2107.

59. Cheng X, Irimia D, Dixon M, et al. A microfluidic device for practical label-free CD4+T cell counting of HIV-infected subjects. *Lab on a Chip*. 2007;7(2):170-178.

60. Cheng X, Liu Y, Irimia D, et al. Cell detection and counting through cell lysate impedance spectroscopy in microfluidic devices. *Lab on a Chip*. 2007;7(6):746-755.

61. Wang B, Weldon AL, Kumnorkaew PK, Xu B, Gilchrist JF, Cheng X. Effect of surface nanotopography on immunoaffinity cell capture in microfluidic devices. *Langmuir*. 2011;27(17):11229-11237.

62. Lunov O, Syrovets T, Loos C, et al. Differential uptake of functionalized polystyrene nanoparticles by human macrophages and a monoclinic cell line. *ACS Nano*. 2011;5(3):1657-1669.

63. Peterman JH, Tarcha PJ, Chu VP, Butler JE. The immunochemistry of sandwich-ELISAs: IV. the antigen capture efficiency of antibody covalently attached to bromoacetyl surface-functionalized polystyrene. *Journal of Immunological Methods*. 1988;111:271-275.

Chapter 8

Summary and Future Outlook

8.1: Summary

Convective deposition is a highly robust and scalable technique for the formation of particle thin films with targeted morphology and microstructure. It is hugely versatile, and is rapidly developing to that point that most any substrate can be coated with most any particle constituent. This thesis concerns the development of convective deposition from fundamental and application-driven perspectives. Of course, both of these foci include process enhancements.

Fundamentally, submonolayer coatings, and varying defect analysis provides significant insight the physics of convective deposition. Varying submonolayer coatings, and the morphological dependence on blade angle, suggests two very different mechanisms for particle deposition. Depending on the shape of the meniscus, particles do or not have times to order, before reaching the evolving crystal front. Defect work concerns the coatings of microspheres and nanoparticles. Instability-driven streak formation in microsphere suspension depositions has plagued the field of rapid convective deposition since its inception. While significant process enhancements have

been made to suppress these defects, there is very little convention understanding as to how and why streaks occur. This work clearly demonstrates that streak formation is a result of surface tension gradients through the meniscus and thin film. Drying nanoparticle films are susceptible to uniform cracking in the drying direction. This work demonstrates clearly that volume fraction, formation rate, and applied thermal gradients can influence thin film thickness and crack spacing. Convective deposition provides a significant enhancement in research ability with this field. Prior experiments were limited to drying droplet systems. In contrast, convective deposition allows the probing of in-situ transitioning crack morphologies with changing thin film thickness. Also, layer-by-layer deposition shows a clear ability to minimize defects.

The addition of nanoparticles to suspension and the application of lateral vibration are significant process enhancements in convective deposition. Nanoparticle addition, in the transition to binary convective deposition, suppresses native instabilities and defects, and by extension increases coating order and packing density. The application of lateral vibration enables the formation of monolayer crystalline coatings at faster formation rates. In addition, it significantly improves process robustness by allowing the deposition of monolayer coatings under a wider range of conditions. Both enhancements will be of critical importance in scale-up efforts and device applications.

Convective deposition has significant potential for device performance enhancement. While its ability to enhance optical technologies is well-established, this thesis presents a pair of biomedical device enhancements. Ordered particle arrays are used to controllably enhance surface roughness in immunoaffinity cell capture devices.

Convective deposition-modified devices exhibit enhanced relative cell capture of up to 60% versus a flat substrate. In addition, the binary deposition of SiO_2 microspheres alongside PS nanoparticles enables the fabrication of macroporous polymer membranes with highly monodisperse pore size and robust mechanical properties. In addition, theory and experimentation are provided that show tunability in pore size design.

8.2: Future Outlook

Convective deposition is an exciting and evolving field, with significant opportunity for enhancement. It has been shown to significantly improve multiple device technologies at the laboratory scale. Significant challenges lie in wait in the scale up of convective deposition, both engineering and scientific. Convective deposition will need to be scaled up to a continuous process while continuing to apply developed process enhancements. Particle suspension and mixing will need to be maintained over long timescales.

In addition, further research into defect suppression strategies is necessary. Already, ongoing work probes the ability of surfactants to control streaking and gross thin film morphology. Also, transitions in cracking nanoparticle morphology would benefit from addition quantification and analysis. In addition, binary liquid phases could continue to probe the Marangoni flows within convective deposition—in this case preferential evaporation of one phase would drive the formation of surface tension gradients and resultant flow. Finally, vibration-assisted convective deposition is moderately understood, and only with large amplitudes. Smaller-scale vibration, on the lengthscales of the particles themselves, could act at thermal noise to anneal crystalline defects very effectively.

Chapter 9

Appendix

Appendix 9.6.1: Preparation of Silica Micro and Nanoparticles: Methods and Techniques

In order to facilitate the enhancement of the following biomedical device technologies, it was necessary to gain expertise in SiO_2 core-shell particle synthesis.[1] The following section provides a brief snapshot of reactor design and synthesis techniques explored.

SiO_2 particles of diameters 100 nm, 309 nm, 319 nm, 407 nm, 460 nm, 490 nm, 700 nm, 928 nm, and 1150 nm were synthesized through a variety of robust synthesis methods and used in cell capture experiments.[2-4] This section presents a broader catalogue of synthesized particles in an attempt to clarify particle synthesis strategies. Particles synthesized include:

TEOS	NH_3	H_2O	Seed Size (nm)	Final Diameter (nm)	Process	References
0.2M	0.2M	17M	-	100	Batch	Wang 2003[2]
0.2M	0.6M	17M	-	300	Batch	
0.2M	1.2M	17M	-	460	Batch	
0.2M	1.4M	17M	-	480	Batch	
0.2M	1.6M	17M	-	490	Batch	
0.04M	2.45M	1.58M	-	309	Batch	Zhang 2003[3] Adaptation
.29M	1.9M	6M	-	407	Batch	Jiang, UI/MIT Recipe[4]
0.2M	1.2M	17M	-	328	Batch	Wang 2003[2] Seed Growth
4.25g			328	404	Semi-Batch	
6.375g			404	452	Semi-Batch	
10.625g			404	471.4	Semi-Batch	
14.875g			471.4	526.1	Semi-Batch	
19.125g			526.1	554.7	Semi-Batch	
0.2M	1.2M	17M	-	400	Batch	Wang 2003[2]
0.106M	1.2M	17M	-	319	Batch	Wang 2003[2] Adaptation
.074M	2.27M	5.22M	-		Continuous	Zhang 2003[3] Continuous
4.7g			-	700	Continuous	
8.46g			-	969.3	Continuous	
0.2M	1.2M	17M	500	928	Semi-Batch	Wang 2003[2] 500nm seed
4.25g			928	1150	Semi-Batch	
8.5g			1150	1301	Semi-Batch	
12.75g			1301	1375	Semi-Batch	
0.2M	1.2M	17M	1000	*	Semi-Batch	Wang 2003[2] 1 um seed
4.25g			*	1938	Semi-Batch	
8.5g			1938	2144	Semi-Batch	
0.2M	1.2M	17M	1375	*	Semi-Batch	Wang 2003[2] 1.375um seed
4.25g			*	1865	Semi-Batch	
8.5g			1865	2107	Semi-Batch	
12.75g			2107	2151	Semi-Batch	
*Particles Not Sized						

Table 9.6.1: Catalogue of SiO_2 Particles Synthesized through Batch, Semi-batch, and Continuous Semi-batch Synthesis Strategies.

For batch processes, NH_4OH, DI water (when applicable) and ethanol were mixed initially. TEOS and ethanol, also pre-mixed, were added to the ammonia solution to start the particle synthesis reaction. The batch production methods used limit the sizes of synthesizable particles. For particles larger than 500 nm in diameter a core-shell methodology was used. Microspheres of overlapping sizes were synthesized in order to bridge the gap between smaller particles synthesized in single batch reactions and larger particles synthesized in core-shell semi-batch reactions. Core particles were initially synthesized using the batch process with [TEOS] = 0.2 M, [DI H_2O] = 17.0 M, and [NH_3] = 1.2 M. A 100 mL solution of equal parts of NH_4OH/EtOH/H_2O and TEOS/EtOH was prepared and used to repeatably synthesize particles 328 nm in diameter. At this juncture additional TEOS/EtOH (200 proof) was added daily to progressively form shells around seed SiO_2 particles. TEOS additions were of equal mass to the initial TEOS quantity, 4.25 grams, in solutions as shown. Particle growth proceeds nearly linearly with TEOS addition with consistent reagents as shown in the compilation of two parallel trials (Figure 9.6.1). With reagent variation (different chemical suppliers and lot numbers) particle synthesis and growth became somewhat less repeatable.

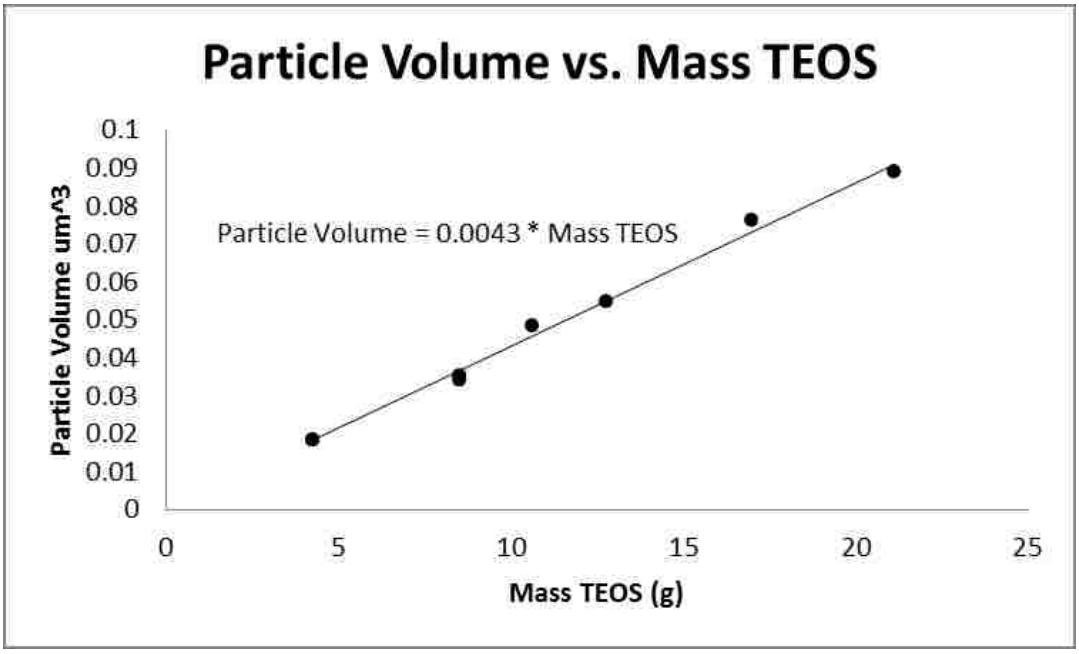

Figure 9.6.1: SiO_2 seeds 328 nm in diameter were synthesized through a batch process following the recipe from Wang 2003.[2] Additional TEOS was added daily to linearly increase particle volume.

Seeing an upper limit to our initial core-shell synthesis we performed identical experiments, but in addition to the 50 mL initial volume of NH_4OH/H2O/EtOH we added 300 μL of 46% volume fraction 500 nm SiO_2/EtOH. The purpose of this was to start with a larger core for the hydrolyzing SiO_2 to form a shell atop. Here, with our initial conditions and 4.25, 8.5, and 12.75 grams TEOS, added at 4.25 grams/day, particles grew to 928 nm, 1150 nm, 1301 nm, and 1375 nm. Once more there is a linear relation between particle volume increase and the mass of TEOS added (Figure 9.6.2). One limit on both of the preceding strategies relates to SiO_2 growth h location. Initially the vast majority of SiO_2 synthesis takes place at the surface of seed particles. However, as additional shells are added, more secondary nucleation events take place where new particles are formed and they have a cumulatively detrimental effect on the linearity of seed particle growth as the additional TEOS in the continued presence of H_2O and NH_3 causes these particles to grow as well. Initially these particles are incredibly easy to remove through centrifugation, but as the size distribution grows it becomes harder to post-process the synthesized particles into a monodisperse suspension.

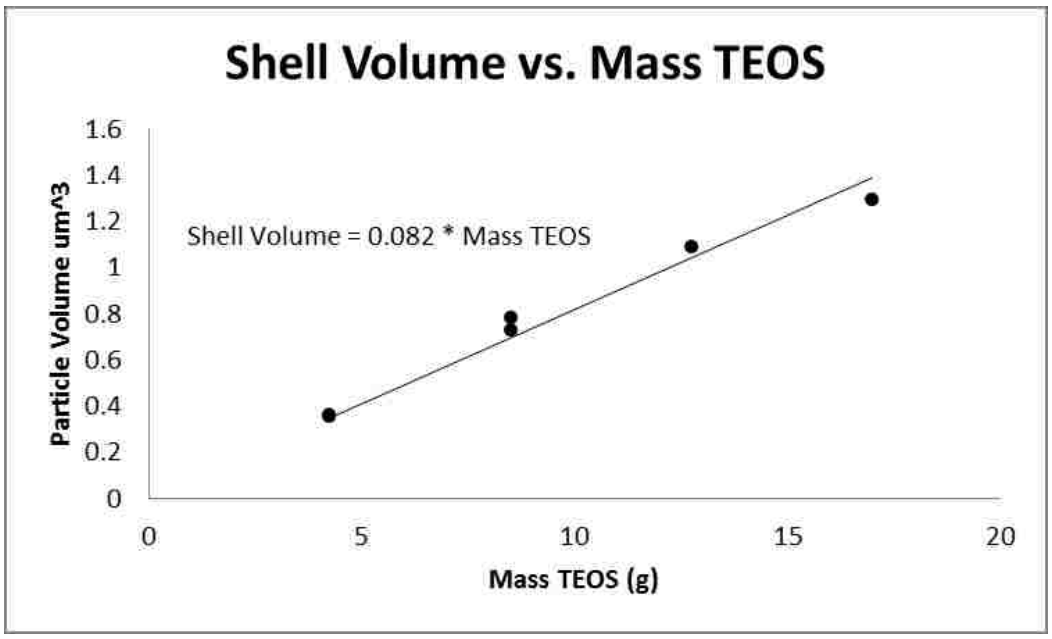

Figure 9.6.2: Seeded growth Wang 2003[2] reagents with 500 nm SiO_2 seeds. Shell volume (total volume minus initial seed volume) scales quite linearly with mass of TEOS added.

In an effort to investigate the upper limits to this core-shell methodology we performed similar synthesis experiments with 1.0 μm (Fuso) and 1.375 μm (largest particles synthesized previously) seed SiO_2 microspheres. With a seed addition of 300 μL of 1.0 μm SiO_2/EtOH at 40% volume fraction to the initial NH_4OH/DI H_2O/EtOH, 2 and 3 TEOS additions yield 1.938 and 2.144 μm SiO_2 microspheres. With a seed addition of 300 μl 1.375 μm SiO_2/DI H_2O at 28% volume fraction, 2, 3, and 4 additions yield 1.865, 2.107 and 2.151 μm SiO_2 microspheres. Note that the different slopes in Figures 9.6.1 and 9.6.2 stem from the numbers of seed particles. The number of spontaneously forming particles in the batch processes without seeds is much larger than the number of 500 nm seeds added to spur larger growth—larger growth on the individual seeds is observed when there are fewer cores for shells to form atop.

Using a continuous core-shell synthesis process, seeds were first prepared by the addition of 1 mL TEOS ([TEOS] = .074 M) and 4 mL 200 proof ethanol to 46 mL 200 proof ethanol and 9.0 mL NH_4OH ([NH_3] = 2.27 M). After two hours an additional 5 mL TEOS/20 mL ethanol solution was fed continuously at 0.1 ml/min to yield 700nm SiO_2 microspheres. Separately, using the same seeding process, an 8 mL TEOS/36 mL ethanol solution was fed continuously at 0.1 mL/min to yield 969 nm SiO_2 microspheres. All experiments were carried out at room temperature in sealed vessels under moderate stirring. Post-synthesis, the particles were centrifuged and had their solvent replaced with ethanol a minimum of three times and DI H_2O a minimum of three times. Centrifugation times were based on the terminal particle settling velocity in order to remove both excess reagents and any smaller secondary constituents formed as

byproducts in our reactions. For deposition, particles were suspended in DI H_2O and brought to an appropriate volume fraction based on their size.

Appendix 9.6.2: SiO_2 Particle Surface Roughness via Atomic Force Microscopy

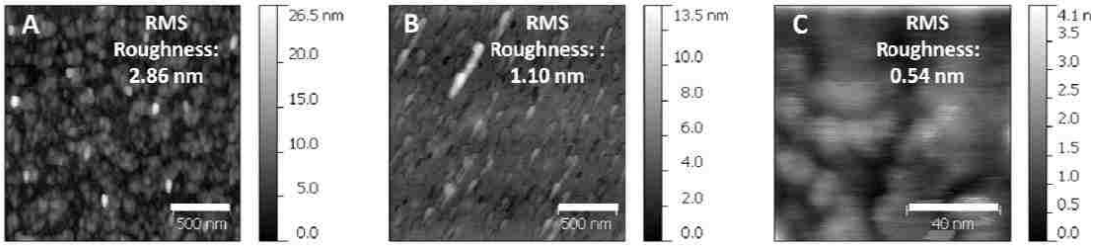

Figure 9.6.3: Atomic force microscope (AFM) measurements carried out on a Nanoscale C AFM in tapping mode to characterize 1150 nm individual particle roughnesses as well as the roughness of TEOS-coated and bare glass. Gwyddion was used for data analysis and visualization. The images are: A) bare glass surface, B) TEOS coated glass surface, and C) surface of an 1150 nm bead. For all surfaces, the root mean squared (RMS) roughness is less than a few nanometers. As the values are comparable to surface immobilized antibody molecules, the instrinsic roughness on the flat surfaces or individual beads are not expected to have a differential effect on capture. Instead, gross roughnesses of spherical particle monolayers dictate cell capture profiles as discussed in the paper.

Appendix 9.6.3: CD4+ Analysis via Flow Cytometry

Flow cytometry analysis (BD FACSCanto II flow cytometer, BD Biosciences, Rockville, MD) was performed to quantify the percentage of CD4+ cells in the Jurkat cell culture. Jurkat cells were incubated with Alexa Fluor 488-CD4 antibody (1:100 dilution, clone RPA-T4, BD Pharmingen, Rockville, MD) or FITC-goat anti-human IgG (H+L) (0.013mg/mL, LOT92662, Jackson ImmunoResearch, West Grove, PA) in 1% BSA/PBS for one hour. Afterwards, the cells were washed with buffer, centrifuged and resuspended in 1% BSA/PBS for flow cytometry analysis. Then the data was analyzed by FACSDiva software (BD Biosciences, Rockville, MD). As shown in Fig. 9.6.4, 23.8% of Jurkat cells are CD4+.

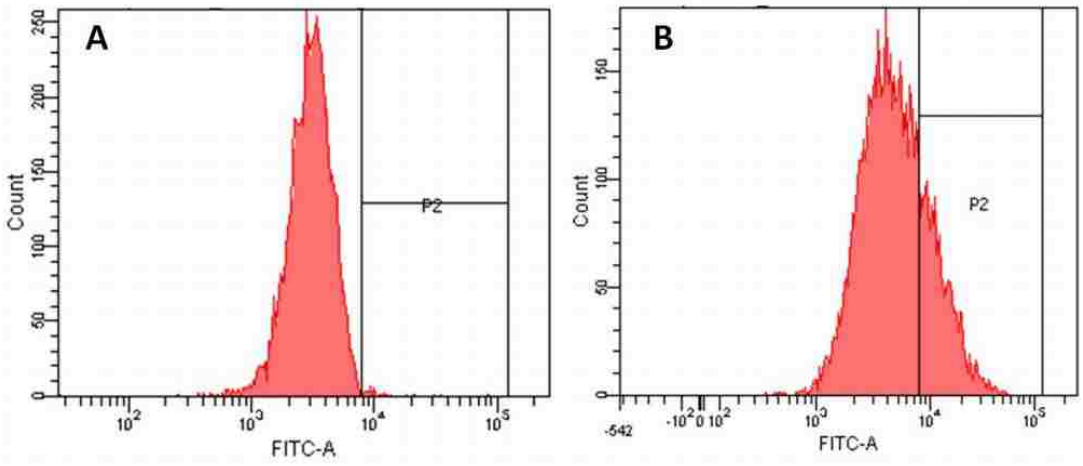

Figure 9.6.4: (A) Flow cytometer histogram showing FITC fluorescence intensity of IgG-FITC stained Jurkat cells versus cell count. A gating of 0.1% population was performed. (B) Flow cytometer histogram showing fluorescence intensity of CD4-AF488-stained Jurkat cells versus cell count. In order to evaluate the expression of CD4 on Jurkat cells, IgG-FITC stained cells were used as the negative control. Using the same gating as in (A), 23.8% of the Jurkat population was found to be CD4 positive. In both analyses, a total of 10,000 events were recorded.

Appendix 9.6.4: Cell Capture Surface Chemistry Comparison

To confirm that the surface chemistry is comparable between the nanobeads and planar TEOS, we deposited 490 nm silica beads on clean glass and further dipped half of the deposition into a TEOS solution in ethanol (same as used in creating the planar TEOS coating) for 15 min. After assembly into a microchannel and functionalizing the surface with CD4 antibody, live jurkat cells were flowed into the channel at 5μl/min for 15 min. After a washing step by PBS, the numbers of cells on the nanobead deposition coated or non-coated by TEOS in the same device were compared. Five repeats yielded an average ratio of 1.03 with standard deviation of 0.08 (number of cells on non-coated to TEOS coated regions). This suggests that the chemistries between TEOS-coated planar surface and beads synthesized using TEOS hydrolysis are comparable.

Appendix 9.6.5: Cell Membrane Dynamic Motion

A real time video:

(http://pubs.acs.org/doi/suppl/10.1021/la2015868/suppl_file/la2015868_si_001.avi) showing the dynamic membrane motion of a Rhodamine B stained Jurkat cell after immobilization onto a glass substrate by CD4 antibody. Even in the absence of flow, the cell membrane is observed to be flexible and fluctuating spontaneously.

Appendix 9.7.1: Membrane Pore Size Theory

These membranes are characterized by two types of pores: cavity-cavity and substrate-cavity. Cavities are defined as the spherical void spaces within the membranes formerly occupied by the SiO_2 microspheres. Upon HF or KOH etching these cavities are connected by pores formed at the former microsphere-microsphere contact points. The second, and much less populous, type of pore comes from the "bottom" layer of microspheres deposited, along with polystyrene nanoparticles, directly atop the glass substrate (Figure 9.7.1). The available angle for nanoparticles to pack into the interstices where microspheres touch one another is larger than the available angle where microspheres contact the substrate—this larger angle yields smaller void spaces and, by extension, smaller pores. This modeling work makes a two-dimensional approximation of the three-dimensional reality. This approximation is valid because of the spherical symmetry of the particles involved.

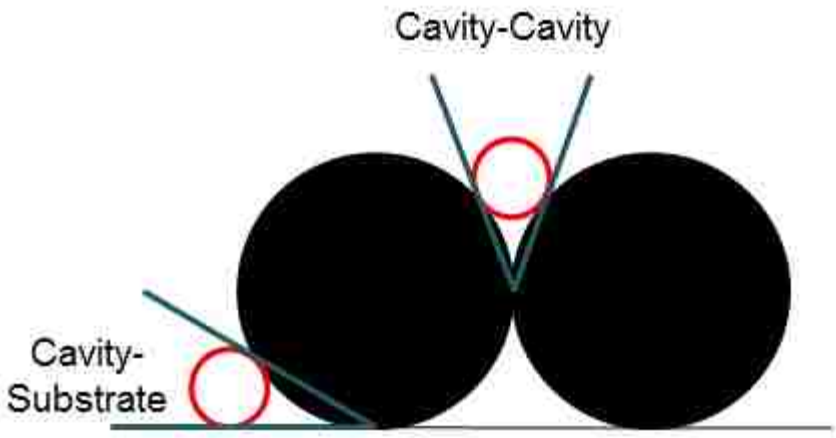

Figure 9.7.1: Diagram describing nanoparticle packing, in two dimensions, near the two different pore formation locations: microsphere-microsphere and microsphere-substrate contact points. Black signifies SiO_2 microsphere while red circles signify polystyrene nanoparticles. Nanoparticles, and subsequently melted polystyrene, have a larger angle within which to pack, and thus yield smaller pores, where microspheres contact one another.

The angles into which nanoparticles can pack, as shown in Figure 9.7.1, can be calculated through simple geometry as shown. First, the substrate-cavity pores, as shown in Figure 9.7.2.

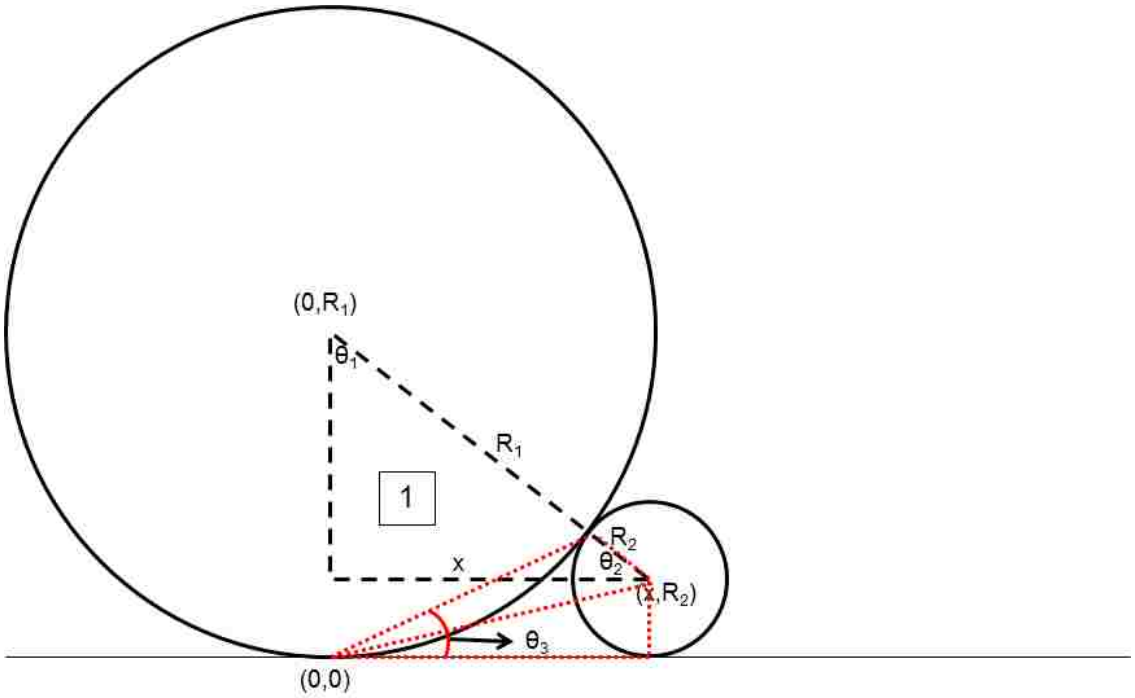

Figure 9.7.2: Two-dimensional representation of nanoparticle packing into the substrate-microsphere interstice with the necessary geometric relations highlighted. Subsequently, the smaller, polystyrene, nanoparticles will be melted to form a continuous phase with their neighbors and the larger, SiO_2, microsphere will be etched away through HF or KOH treatment.

First, right triangle 1 is fully characterized:

$$x^2 + (R_1 - R_2)^2 = (R_1 + R_2)^2$$

$$x = 2\sqrt{R_1 R_2}$$

Also,

$$\tan\frac{\theta_3}{2} = \frac{R_2}{x}$$

Thus

$$\theta_3 = 2\tan^{-1}\frac{R_2}{x}$$

And

$$\theta_3 = 2\tan^{-1}\frac{R_2}{2\sqrt{R_1 R_2}}$$

This means that for, for the particle size ratios investigated:

1.0 μm/ 100 nm: $\theta_3 = 17.97°$

500 nm/ 100 nm: $\theta_3 = 25.21°$

The microsphere-microsphere nanoparticle packing condition, yielding cavity-cavity pores, is shown in Figure 9.7.3.

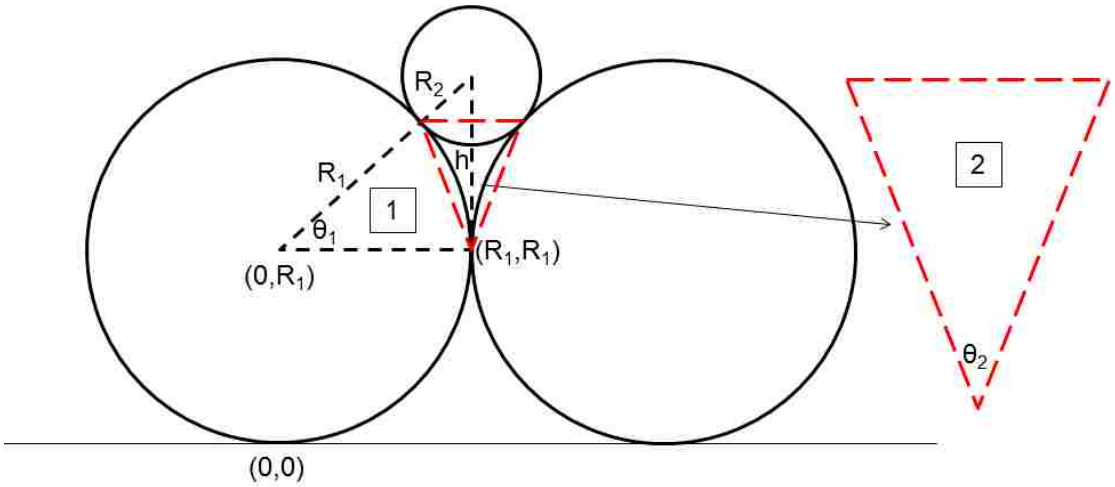

Figure 9.7.3: Two-dimensional representation of nanoparticle packing into the microsphere-microsphere interstice with the necessary geometric relations highlighted. Subsequently, the smaller, polystyrene, nanoparticles will be melted to form a continuous phase with their neighbors and the larger, SiO_2, microsphere will be etched away through HF or KOH treatment.

First, similarly to the previous case, right triangle 1 is characterized as follows:

$$h^2 = (R_1 + R_2)^2 - {R_1}^2$$

$$h = \sqrt{2R_1R_2 + {R_2}^2}$$

And

$$\tan\theta_1 = \frac{h}{R_1} = \frac{\sqrt{2R_1R_2 + {R_2}^2}}{R_1}$$

Thus

$$\theta_1 = \tan^{-1}\frac{\sqrt{2R_1R_2 + {R_2}^2}}{R_1}$$

Understanding $\theta_1 = \theta_2$

$$\theta_2 = \tan^{-1}\frac{\sqrt{2R_1R_2 + {R_2}^2}}{R_1}$$

This means that for, for the particle size ratios investigated:

1.0 μm/ 100 nm: $\theta_3 = 24.62°$

500 nm/ 100 nm: $\theta_3 = 33.56°$

Taking the ratio of the cavity-cavity available angle and the substrate-cavity available angle for nanoparticle packing yields a result that is easily comparable with experimental data.

$$Available\ Space\ Ratio = \frac{Cavity - Cavity, \theta_2}{Cavity - Substrate, \theta_3}$$

$$Available\ Space\ Ratio = \frac{\tan^{-1}\frac{\sqrt{2R_1R_2 + {R_2}^2}}{R_1}}{2\tan^{-1}\frac{R_2}{2\sqrt{R_1R_2}}}$$

Nondimensionalizing,

$$k = \frac{R_2}{R_1} = particle\ size\ ratio$$

$$Pore\ Size\ Ratio = \frac{\tan^{-1}\sqrt{2k + k^2}}{2\tan^{-1}\frac{\sqrt{k}}{2}}$$

Experimentally, cavity-cavity pores were measured from SEM imagery using ImageJ. Images analyzed include those presented within the bulk of this paper. Cavity-substrate pores were measured from SEM imagery as well. These pores were determined either by viewing the top of a SiO_2-etched monolayer deposition (Figure 9.7.4, full image) or by viewing the underside of an etched membrane that has lifted off (Figure 9.7.4, inset). Results were consistent with both methods.

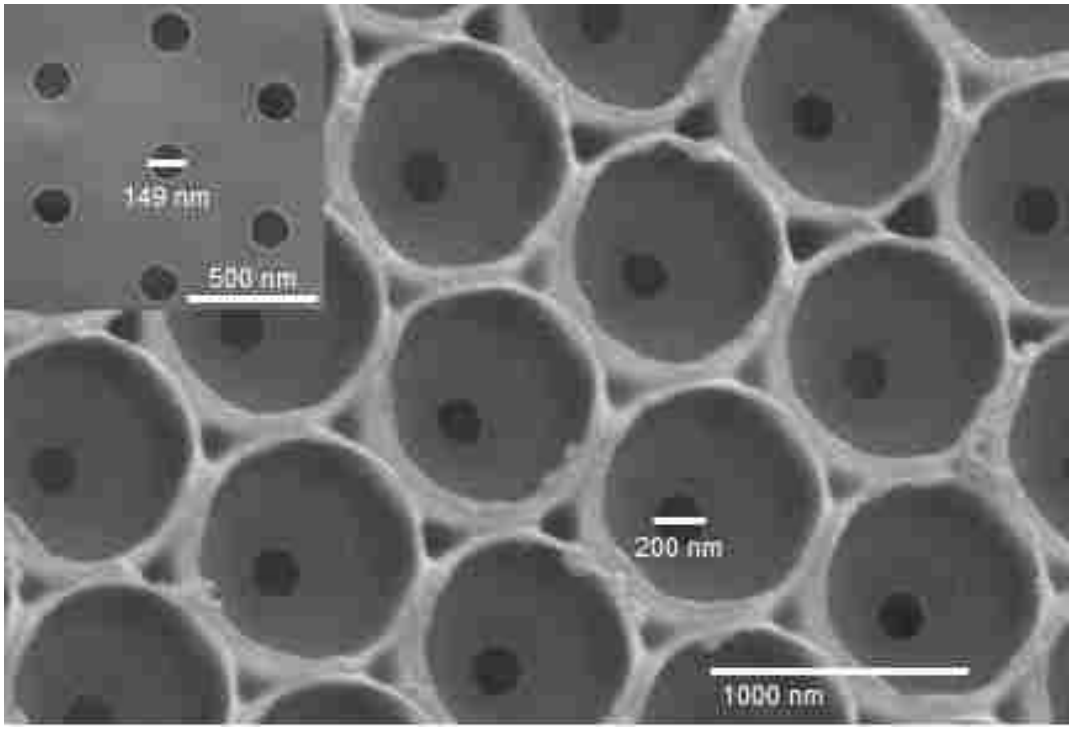

Figure 9.7.4: Examples of the two methods used to evaluate cavity-substrate pore sizes from SEM imagery. (Full Image) Representative SEM image of a monolayer 1 μm SiO_2 / 100 nm polystyrene deposition, with PS melted and SiO_2 etched, highlighting 200 ± 8 nm cavity-substrate pores. (Inset) Representative SEM image of the underside of a 6-layer 500 nm SiO_2 / 100 nm PS membrane, with PS melted and SiO_2 etched, with 149 ± 8 nm cavity-substrate pores. Results were consistent between both techniques as pores were simply viewed from either side.

Comparing theoretical calculations for the cavity-cavity/cavity-substrate pore size ratio with experimental data yields a strong correlation as shown below:

Theoretically,

For 1 μm SiO_2/100 nm PS (k=0.1):

Cavity-Cavity, θ_3: 24.62°

Cavity-Substrate, θ_3: 17.97°

Pore Size Ratio: 1.37

For 500 nm SiO_2/100 nm PS (k=0.2):

Cavity-Cavity, θ_3: 33.56°

Cavity-Substrate, θ_3: 25.21°

Pore Size Ratio: 1.33

Experimentally,

For 1 μm SiO_2/100 nm PS:

Cavity-Cavity Pore Diameter: 141 ± 10 nm

Cavity-Substrate Pore Diameter: 200 ± 8 nm

Pore Size Ratio: 1.42 ± 0.12

For 500 nm SiO_2/100 nm PS:

Cavity-Cavity Pore Diameter: 103 ± 5 nm

Cavity-Substrate Pore Diameter: 149 ± 8 nm

Pore Size Ratio: 1.44 ± 0.11

Thus it is concluded that it is in fact the geometric space into which nanoparticles pack that determines the pore size ratio in the macroporous membranes fabricated here.

Appendix 9.9.1: Ethanol/Water Droplet Experiments

Marangoni effects will obviously play a role in ethanol/water experiments. Water has a higher surface tension, ~71 mN/m, as compared with ethanol, ~22 mN/m, and thus will flow away presumably to the interfaces of the meniscus and thin film. This inhomogeneous distribution of liquids in the suspension will affect control over the evaporation rates and surface tensions and could blunt the changing evaporation at the interfaces as water preferentially flows in that direction. Preliminary experiments, similar to those described throughout this thesis, could be used to drag of pure ethanol/water mixtures across a substrate using the convective deposition apparatus. Optical microscopy could be used to evaluate the uniformity of the thin liquid film. Specifically, experiments could evaluate any waviness at the three-phase contact line.

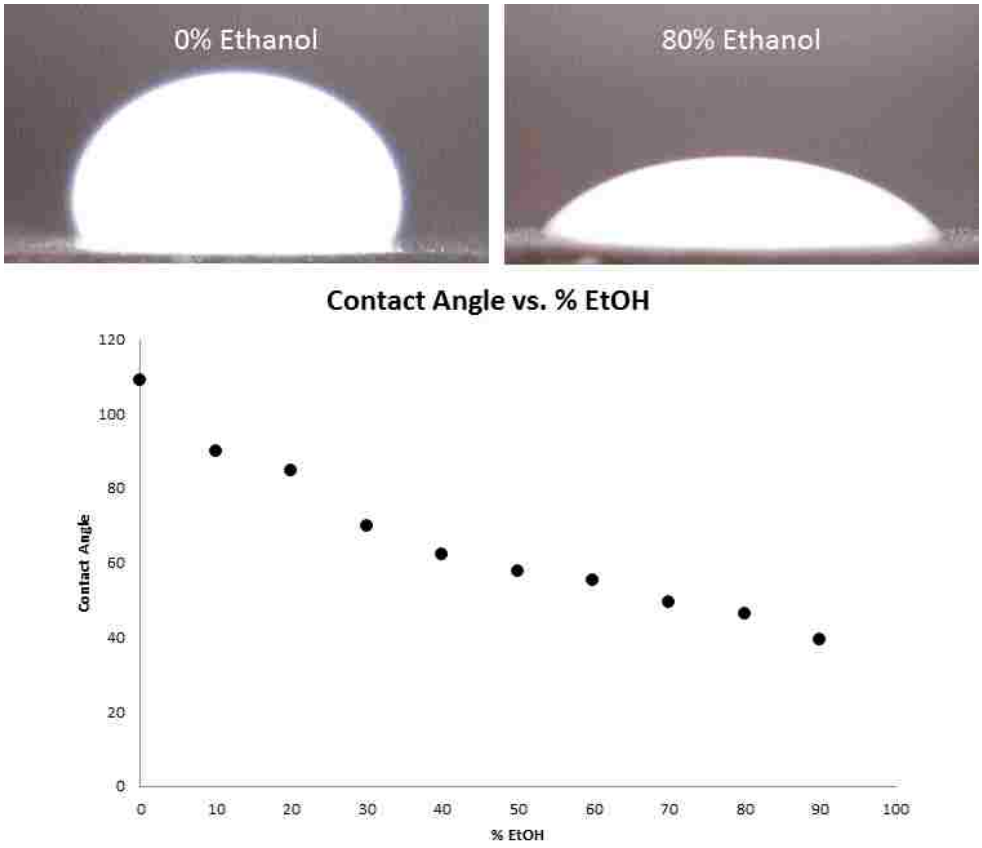

Figure 9.9.1: (Top) Representative images of 20% SiO_2 suspension with the liquid phase composed of pure DI H_2O (left) and 80% ethanol/20% DI H_2O (right) on parafilm. (Bottom) Suspension contact angle versus % ethanol in the liquid phase.

Appendix 9.9.2: References

1. Weldon AL, Kumnorkaew PK, Wang B, Cheng XC, Gilchrist JF. Fabrication of macroporous polymeric membranes through binary convective deposition. *Acs Applied Materials & Interfaces*. 2012;4(9):4532-4540.

2. Wang W, Gu BH, Liang LY, Hamilton W. Fabrication of two- and three-dimensional silica nanocolloidal particle arrays. *J Phys Chem B*. 2003;107(15):3400-3404.

3. Zhang JH, Zhan P, Wang ZL, Zhang WY, Ming NB. Preparation of monodisperse silica particles with controllable size and shape. *J Mat Res*. 2003;18(3):649-653.

4. Jiang S. Recipes for stober silica particles. http://mit.edu/sjiang2/www/Resources/stober_recipes.pdf 2011.

Vita

Alexander L. Weldon was born in Portland, Oregon to Marcelle Anderson and Tim Weldon. He was raised in nearby Helvetia with a younger sister, Erin Weldon. He attended grade school at West Union Elementary School, then 6^{th}-12^{th} grade at St. Mary of the Valley Grade School and Valley Catholic Middle and High School. He graduated high school in 2004, with a few notable honors including his induction as a National Merit Scholar and SAT Composite Index of 1600/1600. In addition, he competed as a Llama showman, earning Top 5 National Placements and Rankings in a number of performance categories, and the National Championship in Youth Judging.

In 2004, Alex moved back East to attend Princeton University in New Jersey. He attained a Bachelor of Science and Engineering (B.S.E) in Chemical Engineering, along with Certificates in Engineering Biology and Materials Science. While at Princeton he completed a pair of Internships at Intel Corporation as a part of the Intel Honors Internship Program (iHip). After completing his first rotation as a technician in Non-Copper Metrology, he carried out EUV test mask development and modeling within Components Research. Within Components Research he earned Intel Corporation's highest honor, an Outstanding rating. In addition, he traveled to University of New South Wales in Sydney, Australia, to carry out Practicum Research with Professor Vicki Chen. He researched and optimized novel cleaning techniques for PES ultrafiltration membranes. Finally, he completed year-long Senior Thesis with

Professor Celeste Nelson at Princeton. Here, he elucidated the bulk and microscale properties of collagen gels for use in designing polymer scaffolds for tissue engineering.

In June, 2008, Alex graduated Princeton University with his Bachelor's degree and moved to Bethlehem, Pennsylvania to pursue his doctorate in Chemical Engineering at Lehigh University. Within the first semester, Alex and Professor James F. Gilchrist teamed up to further investigations into convective deposition. Alex has a strong interest in biomedical technologies, and was fortunate to work within a pair of device–driven collaborations with Professor Xuanhong Cheng (M.S.E., BioE, Lehigh) and her student Bu Wang. Together they developed immunoaffinity cell capture devices with varying nanotopography, for the capture and diagnosis of HIV+ and neoplastic cells, and macroporous polymer membranes for use in viral filtration. Alex also had the extreme pleasure of managing a pair of full-time interdisciplinary teams of undergraduates through the Biosystems Dynamics Summer Institute, supported by the Howard Hughes Medical Institute. Throughout the following years, he worked in the Gilchrist lab with fellow doctoral students Pisist Kumnorkaew, Changbao Gao, Bu Xu, Tanyakorn Muangnapoh, Tharanga Perera, Midhun Joy, Kajun Ding, and Kedar Joshi and postdoc Eric Daniels.

Throughout his graduate studies, Alex published seven papers and gave 18 oral and poster presentations. 12 of these were invited talks and poster sessions. Awards earned at Lehigh included Wenzel and University Fellowships on arrival in 2008, the Graduate Student Champion award from 2011-2012, the Rossin Doctoral Fellowship from 2012-2014, the Kenneth A. Earhart Award for Excellence in Colloid Research

(Emulsion Polymers Institute) in 2012, the Society of Plastics Engineers Polymer Nanocomposites Conference Top Poster Award in 2013, and the distinction of being honored as a finalist for the Stout Dissertation Award in 2014.

Alex maintained a vibrant life outside of the lab. He served for several years within various official capacities within the Chemical Engineering Graduate Association (ChEGA) at Lehigh University—these responsibilities culminated in his tenure as President during the 2011-2012 academic year. In 2012, he established a Graduate Student Seminar Series for the Chemical Engineering Department at Lehigh as well as a professional Brown Bag lunch series. He maintained extreme levels of physical condition throughout graduate school. He led the Lehigh Graduate Student Running Club for several years, winning his age division in some races and competing in races ranging from 5k sprints to a 50 mile trail ultramarathon. In addition, he competed in the CRASH-B Indoor Rowing World Championships in Boston, MA twice. In 2011 he earned 43rd, with a 2k time of 6:15.9, and in 2012 he earned 36th, with a 2k row time of 6:09.5. Throughout graduate school he trained and competed in Crossfit. He competed in numerous competitions individually and as a member of South Mountain Crossfit's competition team. In addition, he competed in several 12 and 24-hour backpacking endurance races as a member of the Endurance Multisport Extreme Team. On a shorter timescale, he won the Lenape Survival Challenge with partner Ryan O'Rourke. He, obviously, has a strong love of the outdoors and loves hiking in the Delaware Water Gap and surrounding areas.